CRANFIELD UNIVERSITY

Iordan Doytchinov

# ALIGNMENT MEASUREMENTS UNCERTAINTIES FOR LARGE ASSEMBLIES USING PROBABILISTIC ANALYSIS TECHNIQUES

School of Aerospace, Transport and Manufacturing
Precision Engineering

PhD
Academic Year: 2014 - 2017

Supervisors: Dr. Xavier Tonnellier, Dr Heather Almond
2017

CERN-THESIS-2018-001
/ /2018

CRANFIELD UNIVERSITY

School of Aerospace, Transport and Manufacturing

Precision Engineering

PhD

Academic Year 2014 - 2017

Iordan Doytchinov

# ALIGNMENT MEASUREMENTS UNCERTAINTIES FOR LARGE ASSEMBLIES USING PROBABILISTIC ANALYSIS TECHNIQUES

Supervisor: Dr. Xavier Tonnellier, Dr Heather Almond
2017

This thesis is submitted in partial fulfilment of the requirements for the degree of Doctor of Philosophy (PhD)
***(NB. This section can be removed if the award of the degree is based solely on examination of the thesis)***

© Cranfield University 2017. All rights reserved. No part of this publication may be reproduced without the written permission of the copyright owner.

## ABSTRACT

Big science and ambitious industrial projects continually push forward with technical requirements beyond the grasp of conventional engineering techniques. Example of those are ultra-high precision requirements in the field of celestial telescopes, particle accelerators and aerospace industry. Such extreme requirements are limited largely by the capability of the metrology used, namely, it's uncertainty in relation to the alignment tolerance required. The current work was initiated as part of Maria Curie European research project held at CERN, Geneva aiming to answer those challenges as related to future accelerators requiring alignment of 2 m large assemblies to tolerances in the 10 µm range. The thesis has found several gaps in current knowledge limiting such capability. Among those was the lack of application of state of the art uncertainty propagation methods in alignment measurements metrology. Another major limiting factor found was the lack of uncertainty statements in the thermal errors compensations applied to assembly's alignment metrology. A novel methodology was developed by which mixture of probabilistic modelling and high precision traceable reference measurements were used to quantify both measurement and thermal models compensation uncertainty accurately. Results have shown that the suggested methodology can accurately predict CMM specific measurement uncertainty as well as thermal drift compensation made by empirical, FEM and FEM metamodels. The CMM task specific measurement uncertainties made at metrology laboratory were validated to be of maximum 7.96 µm (1σ) for the largest 2 m assemblies. The analysis of the results further showed how using this method a 'virtual twins' of the engineering structures can be calibrated with known uncertainty of thermal drift prediction behaviour in the micrometric range. Namely the Empirical, FEM and FEM Metamodels uncertainties of predictions were validated to be of maximum: 8.7 µm (1σ), 11.28 µm (1σ) and 12.24 µm (1σ).



Keywords:

Precision alignment measurements, uncertainty modelling, accelerator components fiducilisation

*“…My Sword I give to him that shall succeed me in my Pilgrimage…”*

- *John Bunyan, Piligrim’s Progress, Section X, part 2 [1678]*

# ACKNOWLEDGEMENTS

Firstmost I would like to thank the people from the European Union for providing the financial support and trust for the PACMAN project and for this PhD thesis in the form of the grant agreement PITN-GA-2013-606839 part of 7th Framework Programme, Marie Curie actions.

The research leading to this thesis has been coordinated and guided by CERN and Cranfield University under the PACMAN project (CERN, 2017b) framework. Thus it would have not been possible without the kind guidance and open hearts and minds of numerous colleagues, friends and souls along my path during last few years. Hereby in this non exhaustive list I would like to thank them for being part of my journey and pilgrimage of thought.

To: Petya Georgieva for the kind warmth inside my heart

To: Kostadin Doytchinov for the inspiration, his kind heart and numerous advice among numerous time zones around the world that led me follow his pilgrimage.

To my supervisors being the true wizards that took me as their apprentice: Dr Bertrand Nicquevert for endlessly reading discussing and advising me on my work shaping it and putting the mind, heart and encouragements in my final months. Dr Michele Modena for introducing me and guiding me through my first and last steps at CERN. To Prof. Paul Shore for the initial guidance and light of thought that served always as an example. To Dr Paul Compley for taking on with the lead and asking the right questions. To Dr Xavier Tonnelier and Dr Heather Almond for taking the responsibility of guiding me and the thesis through its final stage. To Dr Nuria Catalan Lasheras for helping and listening when it was hard. To Dr Helene Mainauld Durand for leading this magnificent project and guiding our research. To Ahmed Cheriff and his team for bearing with my unusual experiments at the always CERN metrology laboratory. To Xavier Gontero and the cheerful and Witt technicians of magnet laboratory at ISR8.

To Dr Eugen Trapet a magician of his own right for the kind dinner at his home in the Basque country and conversation that taught me and inspired me of learning the true value of understanding uncertainties.

To the people of DMP and the great secondment in the Basque country that helped on developing my methods. Gratitude and thanks to Daniel.Cambell, Dr John Baldwin, Dr Kim Summerhays for their guidance and help used for CMM uncertainties studies. To Dr Alex Skordos for his critical support and helpful advice on the use of heat flux sensors.

To my friends and colleagues from the PACMAN giving it it's light. For all the conversations help advices and laughter: Claude Sanz, Solomon Kamugasa, Vasileios Vlachakis, Dr Giordana Severion, Domenico Caiazza, Peter Novotny and David Tshilumba

*To the one who would learn, take forward and contribute to the ideas in this work being my true rewarder*.

# TABLE OF CONTENTS

# LIST OF FIGURES

# LIST OF TABLES

# LIST OF EQUATIONS

## LIST OF ABBREVIATIONS

| | |
|---|---|
| AS | Accelerating structures |
| BIPM | Bureau International des Poids et Mesures |
| BPM | Beam Positioning Monitoring |
| CTE | Coefficients of Thermal Expansions |
| CLIC | Compact Linear Collider |
| DFR | Dimensional Frame of Reference |
| EDM | Electrical Discharge Machining |
| EM | Empirical Models |
| FEA | Finite Element Analysis |
| FPS | Full Parametric Space |
| GD&T | Geometric Dimensioning & Tolerancing |
| GPS | Geometrical product specifications |
| HPC | High-Performance Cluster |
| LHC | Large Hadron Collider |
| LHS | Latin Hypercube Sampling |
| LPU | Law of Propagation of Uncertainties |
| LSL | Linear Scaling Law |
| MB | Main and Drive Beam |
| MBQ | Main Beam Quadruple |
| MC | Monte Carlo |

| | |
|---|---|
| MPE | Maximum Permissible Error |
| NE | Nominal Expansion |
| NIST | National Institute of Standard and Technology |
| NPL | National Physics Laboratory |
| NTC | Negative Temperature Coefficient |
| PRT | Platinum Resistance Thermometers |
| PTB | Physikalisch-Technische Bundesanstalt |
| PUMA | Procedure for Uncertainty MAnagement |
| RF | Radio Frequency |
| RSS | Route sum of the squares |
| SBC | Simulation By Constraints |
| TLS | Thermal Load Sensors |

# 1 INTRODUCTION

## 1.1 Large assemblies precision alignment challenges

Large-scale scientific and industrial research projects require state of the art engineering to fulfil the desired requirements. In such projects, micrometre accuracy of assembly and alignment of large components can be critical. Alignment of large structures is defined as the procedure where large components or assemblies are dimensionally arranged in a manner into a superstructure to deliver certain desired function at a given tolerance. Large can be defined as any component or assembly larger than 0.5 m as defined by (Stahl, 2013). This process can be performed actively by the use of actuators and guidance system (Glassman *et al.*, 2016) or passively by the reliance on well-designed kinematic features and tight manufacturing tolerances (Slocum and Donmez, 1988). Examples of large-scale high precision assembly projects (and related references) that utilise those techniques and have common challenges in the field of scientific research, industry and military can be seen as shown in **Figure 1-3**

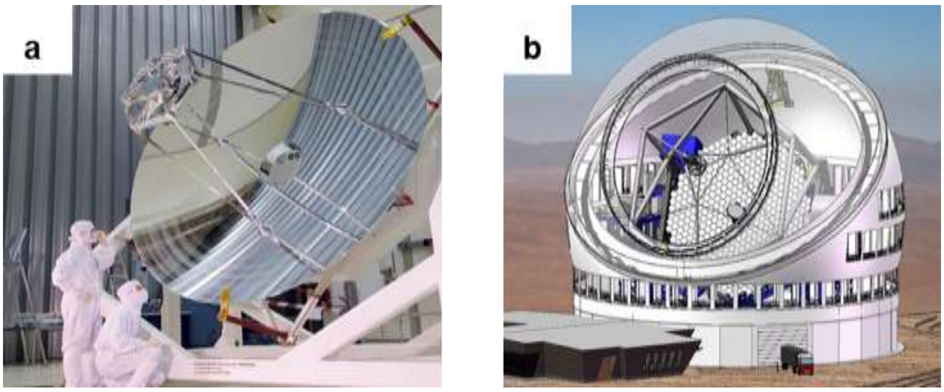


**Figure 1: Celestial and Earth Telescopes: a) Herschel space observatory** (Fransen, Doyle and Catanzaro, 2011)**; b) Thirty Meter Telescope** (Nelson and Sanders, 2008)

Both active and passive alignment rely on high accuracy measurements of features location used to guide the process. In metrology, a reference for the required accuracy of measurement is the so-called “golden rule” as stated in

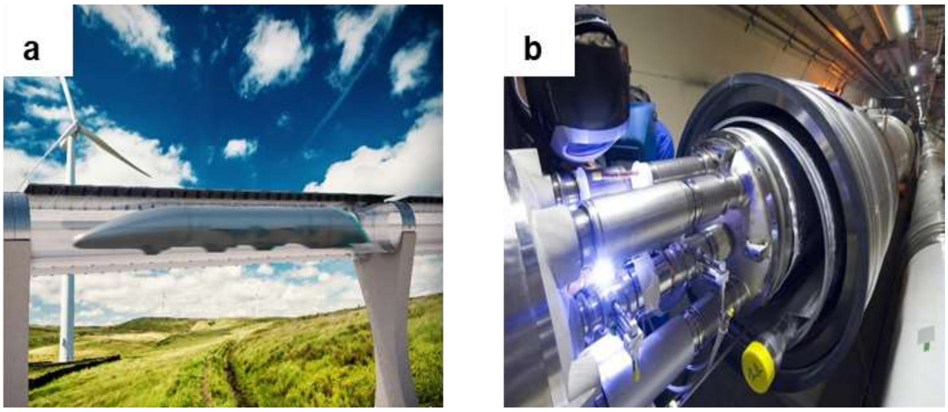


**Figure 2: Future high-speed earth transport projects** (Musk, 2013) **and Accelerators/Large scientific experiments** (Bottura *et al.*, 2006)

(ISO, 2012, 2013b). Measurements have to be with uncertainty of up to 10 % of the tolerance zone for which they are used to qualify (Knapp, 2001; ISO, 2013b). If this ratio is achieved, engineers can rely on the metrology applied and use it for the alignment procedures. For state of the art scientific or industrial research projects, this ‘rule’ might not be suitable. Required tolerance with respect to metrology uncertainty zone ratio can be close to one to one. A summary of metrology equipment qualifications and respective limit of tolerance studied (according to ‘golden rule’) are shown In **Table 1**.

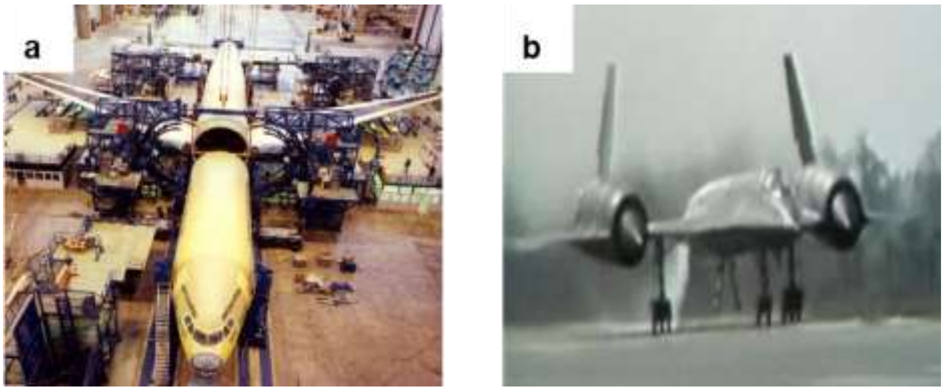


**Figure 3: Aerospace: a) Airbus factory assembly challenges** (Saadat and Cretin, 2002)**, b) Blackbird SR 71 thermal expansion challenges** (Merlin, 2009)

**Table 1: Metrology systems for geometrical location measurement and their expected performance according to manufacturers.**

| **Metrology system** | **Maximum Permissible Error (MPE)** (ISO, 2009) | **Lowest verified tolerance ranges**<br>"golden rule ratio" - 10/1 (Tolerance/MPE) [10] |
|---|---|---|
| *Laser tracker:* | ± [15 μm + 6 μm/m] (Hexagon metrology, 2009) | ± [150 μm + 60 μm/m] |
| *Photogrammetry:* | ± [50 μm to 100 μm] at 1 m to 2 m (Luhmann *et al.*, 2013) | ± [500 μm to 1000 μm] |
| *CMM's :* | ± [0.3 μm to 1.9 μm + 1 to 7 μm/m] (Carl Zeiss AG, 2017; HexagonAB, 2017) | ± [3 μm to 19.9 μm + 10 to 70 μm/m] |

Currently, highest accuracy alignment metrology for meter range structures can be delivered by Coordinate Measurement Machines (CMM) (Hocken and Pereira, 2016). Maximum Permissible Errors (Committee for Guides in Metrology, 2008; ISO, 2009) for CMMs are quoted as low as 1.3 μm (for a system capable of measuring up to 1.2 m object) (HexagonAB, 2017) to 8.9 μm (for a system capable of measuring up to 3 m sized object) (Carl Zeiss AG, 2017). The quoted best-achieved measurement capabilities are only valid within very tightly controlled environmental conditions (temperature, vibration, measurement procedure applied and more). This high measurement performance is achieved at the cost of lengthy measurement procedures performed at specialised CMM systems and laboratories frequently limited to components of up to 2 m to 3 m. Even with this high metrology performance, the (alignment tolerance/measurement uncertainty) ratio for future projects such as Compact Linear Collider (CLIC) (CLIC (Collaboration), 2012) can be close to one.

Alignment tolerance requirements can be as low as 7 μm to 12 μm @ 1 σ for up to 2 m objects (CLIC (Collaboration), 2012).

When large assemblies need to be aligned to micrometric accuracy, not only the knowledge of metrology equipment performance is critical but also its and the measurand dimensional stability during and after measurement. Thermal effects can create dimensional changes in assemblies in the order of 8 μm to 25 μm per m per °C for most common materials used (Steel, Aluminium, Titanium and other alloys). These contributions effects have to be considered in the uncertainty budget and compensated when necessary (Stahl, 2013). Several examples are found in various domains such as celestial and earth telescopes, future high-speed earth transport projects and aerospace. A challenge in supersonic aerospace is the consideration of thermal expansion in components precision components alignment due to air friction heating effects. An extreme example is the design of Blackbird SR-71 spy aircraft. Due to Mach 3+ cruise speed and high friction heat generated (up to 450 °C airframe surface temperature), the designers had to assemble and align components with consideration for the expected thermal expansion. This had a big impact on the aircraft airframe at take-off environment. Large expansion gaps (of up to 4 mm/m) in the fuel tank were letting fuel leaking through the seals on the runway (Merlin, 2009) **Figure 3**, **b)**.

Thermal gradients between the top of the aircraft airframe and the bottom were created due to the depletion of fuel in the tanks which itself acted as a heat sink. This further caused dimensional variations in the airframe that reportedly altered the aerodynamic characteristics during flight (Merlin, 2009). Another example of thermal issues in large objects assembly and alignment example is coming from challenges in a future project of high-speed transportation, the Hyperloop (Musk, 2013; Taylor, Hyde and Barr, 2016). One of the enabling factors for the project success is the ability to cope with the vacuum pipes alignment and thermal deformations caused by sun radiation and internal heat loads. Those can cause significant drift in the dimensions of the tube used to guide the train boogies (up to 0.8 mm per 30 m single steel pipe segment for 10 °C thermal gradient). Such large dimensional changes can have a critical impact on the tubes alignment and thus high-speed train boogies (travelling more than 1000 kph). This can cause additional structural stresses and vibrations due to the required thermal joints interfacing between each 30 m tubular segments. Understanding and compensating accurately for any such thermal effects in high precision assembly and alignment can be critical for project realisation.

An additional challenge for large-scale state of the art research and engineering projects is their complexity, high economic value. Their practical realisation requires industrial and international decentralisation. This puts great challenges in the coordination and standardisation of manufacturing and metrology practices. A direct example from industry is the A380 aircraft developed by Airbus Europe. Components for the aircraft were manufactured in several member states of the EU and finally integrated in Toulouse France. The final integration had to rely on length and angle measurements having less than 50 μm errors for up to 50 m long components. All components coming from different countries and manufacturers with different internal work practices and process. Such undertakings would not have been possible without the traceability to a common reference and standards. This being the international SI (BIPM, 2006) unit system the and the realisation of the meter standard (Vollard, 2005).

Particle accelerators are another example where state and beyond state of the art solutions for all the upper stated challenges can be critical for a project relisation. The Compact Linear Collider (CLIC) future accelerator study and it is beyond state of the art requirements initiated the current thesis as revieled in the following chapter.

## 1.2 Compact LInear Collider (CLIC) accelerator study

### 1.2.1 Future particle accelerators

One of the future goals of accelerator physics is the ability to study particle beam collisions at the highest possible energy and event rate of collision. The current physical design of the machines limits the maximum possible acceleration gradient of the particles. To increase the physics energy and thus the probability for discoveries, length of future machines needs to be increased. The second important requirement, event rate of collision is proportional to Luminosity which can be seen defined in **Eq.(1-1)**

$$N_{colision\ event} \propto L\ (Luminosity)\ where$$

$$L\ (Luminosity) \propto \frac{f_{rep} N_e^2}{\sigma_x \sigma_y} \qquad \textbf{(1-1)}$$

Where $\sigma_x \sigma_y$ [nm] is the transverse particle beam size, $f_{rep}$ [Hz - MHz] is the repetition rate of bunches of particles accelerated and $N_e^2$ [nC] is the beam charge. Thus achieving high event rate of particle collision an accelerator must have as high as possible Luminosity. This would imply that the particle beam cross section size ($\sigma_x \sigma_y$ ) has to be as small as possible and the frequency of events ($f_{rep}$) as high as possible. Circular colliders, such as the Large Hadron Collider (LHC), can have really high frequency [MHz] of events. This is due to the possibility of inserting and circulating numerous particle bunches within the ring colliding repetitively and continuously at the interaction point. Thus those machines can achieve high Luminosity with beam cross sections in the current state of art for LHC of the order of 16 μm at Collison point (Wenninger, 2007) with alignment requirements in the range of 100 μm up to 1 mm. This was achieved using the current state of the art techniques. However, for future circular and linear accelerators that may not be the case. Linear accelerators design implies that particles have only one try/shot per beam bunch before they meet at the interaction point. They act as particle guns using only their available length for each bunch acceleration. Thus, in order to reach higher luminosities, smaller beam sizes (in the nm region cross section (CLIC (Collaboration), 2012)) and longer machines (~50 km) will be among the design requirements. Beyond state of the art circular colliders (such as The Future Circular Collider (CERN, 2017a)) would have really high luminosity requirement thus needing beam cross section close to the linear accelerator requirements ( ~50 nm region at interaction point). Thus size of future colliders would need to be in length of the order of 50 km to 100 km  with colliding beams cross section in the nm region.

This, however, would require extremely tight specifications for components assembly and alignment (i.e. beam focusing magnets, accelerating structures) to be realised. This will ensure successful collision at the impact location (the particle detector) (Redaelli, 2004) as shown in **Figure 4**.

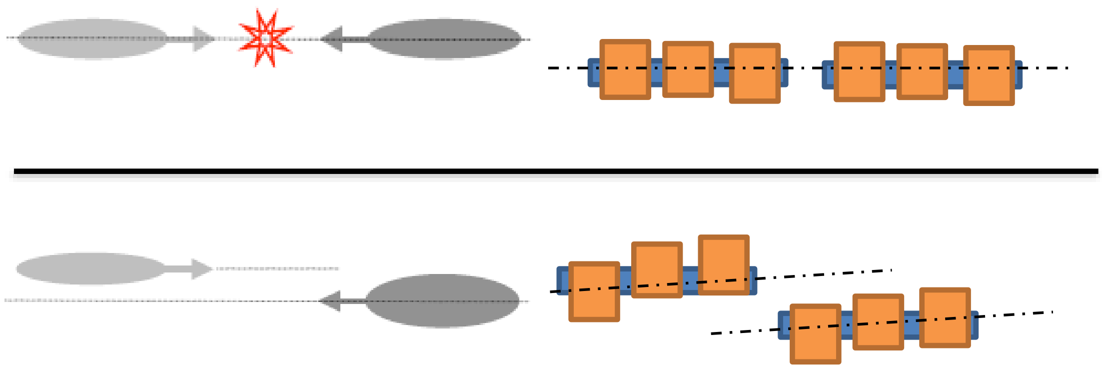

**Figure 4:** ***Top:*** **Beam bunches collide due to successful alignment of accelerator active components.** ***Bottom:*** **Beam bunches missing collision due to unsuccessful alignment of accelerator components.**

The relative accuracy of assembly and alignment required can be compared with the analogy of aiming, aligning and stabilising two rifle barrels at more than 10000 km targeting to collide two 2 cm bullets in a pre-determined location in mid-air.

Alignment of accelerator components can be split into two phases: pre-alignment and beam based alignment. In the first stage, 'pre-alignment' concerns all alignment aspects before launching the first beam within the accelerator. In this phase the active components (focusing and accelerating) are aligned to sufficient tolerance, so the beam can pass for the first time (see **Figure 8**). Pre-alignment itself consist of two separate phases: 'fiducialisation' and 'tunnel alignment'. Fiducialisation phase concerns the measurement of the spatial 3D location of the components electrical and magnetic axes with respect to the zero coordinate reference frame part of each assembly. The zero reference frame is defined by the location of fixed to the assembly physical reference marks called fiducials **Figure 5**.

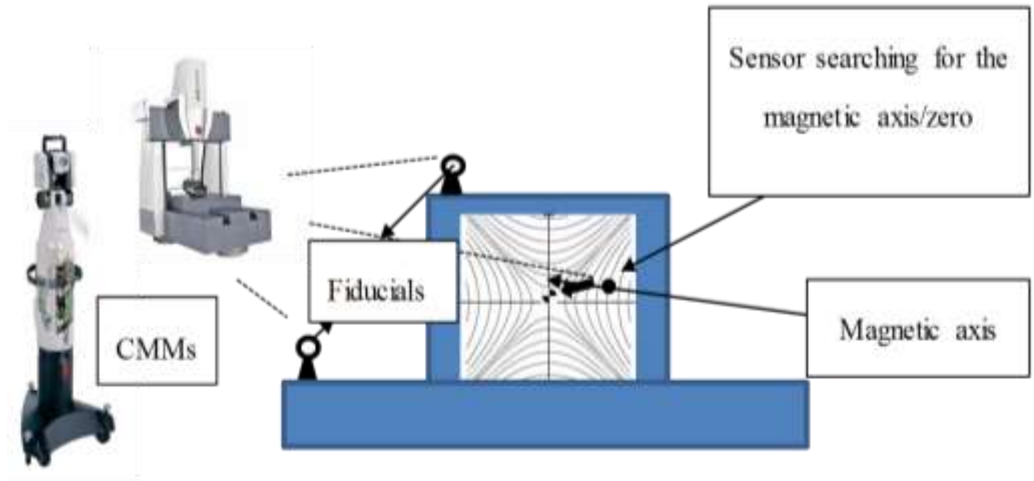


**Figure 5: Schematic of magnet assembly cross-section. Measurement of electromagnetic axis with respect to fiducials (pre-alignment) in quadrupole magnet**

In the tunnel alignment stage, this information is used to align each assembly with respect to a common tunnel frame of reference (i.e. long overlapping stretched wire or another mean such as a laser to create this stable global reference (Mainaud Durand, 2016)). Each assembly fiducials, and thus magnetic axis, has to be adjusted with respect to the global reference. This initially is done by reliance of high precision mechanics, achieving 0.2 mm to 0.3 mm of alignment tolerance. Next step would be to use 5 degree of freedom high precision actuators in order to further align each active component magnetic or electric axis. This has to be done up to tolerance of 14 μm to 17 μm (1 σ), depending on the component type. These requirements lead to a target uncertainty of alignment measurements of 12 μm at 1σ for various magnet assembly sizes from 0.6 m to more than 2 m in length (see **Figure 8**).

The difference between the targeted measurement uncertainty (12 μm at 1σ) and CLIC alignment tolerance zone (14 μm to 17 μm at 1σ) is due to the extra budget required for the magnet to magnet alignment reference system based on capacitive Wire Positioning Sensors (WPS). The WPS system links each assembly reference frame with the global tunnel reference known as the stretched wire [2]. These demanding requirements have to be achieved for a large number of modules, assembled and measured by several companies and laboratories located in CERN member states around the world. (see **Figure 8**). Once each active assembly is aligned to the desired tolerance the beam based alignment can begin. In this phase, the high precision actuators use so-called Beam Positioning Monitoring sensors (BPMs) information in real time to align, stabilise and focus the beam to the highest fidelity and thus luminosity (Mainaud Durand and T.Touze, 2006). This procedure is comprised of three stages "one to one steering" allowing for the first pass of the beam through the machine. "Dispersion-free steering" an optimisation of the BPM sensors and quadruple magnets location by variation of beam energy. "Minimisation of acceleration structures offsets" by the use of Wakefield monitors and assembly girders actuators.

Currently, the biggest challenges fur future projects lie within the first stage: pre-alignment and especially fiducialisation. Small errors due to measurements performed at that stage could be magnified across the large accelerator lengths through the other active (via precision actuators) alignment process and lead to miss-collision of the particle beams **Figure 4**. To master this challenge a metrology capable of aligning metre plus size active components (magnets, accelerating structures and BPM at large manufacturing scale with uncertainties in the micrometre range is required.

In this work, these challenges of large-scale metrology and uncertainty evaluation are addressed as part of a study on the alignment of one of the future particle accelerators concepts: CLIC (Compact Linear Collider) **Figure 6** (CLIC (Collaboration), 2012).


**Figure 6: Artistic Impression of CLIC (48.3km long) under the Jura Mountains France next to Geneva, Switzerland courtesy to CERN**

Extremely low alignment measurement uncertainties of the order of 10 μm and below state of the art need to be achieved on up to 20 000 sub-assemblies, of 0.5 m to 2 m length each. Those would be subject to varying thermal conditions during their alignment process in 48.3 km long underground tunnel. CAD impression of such two-metre module can be seen in **Figure 7**.

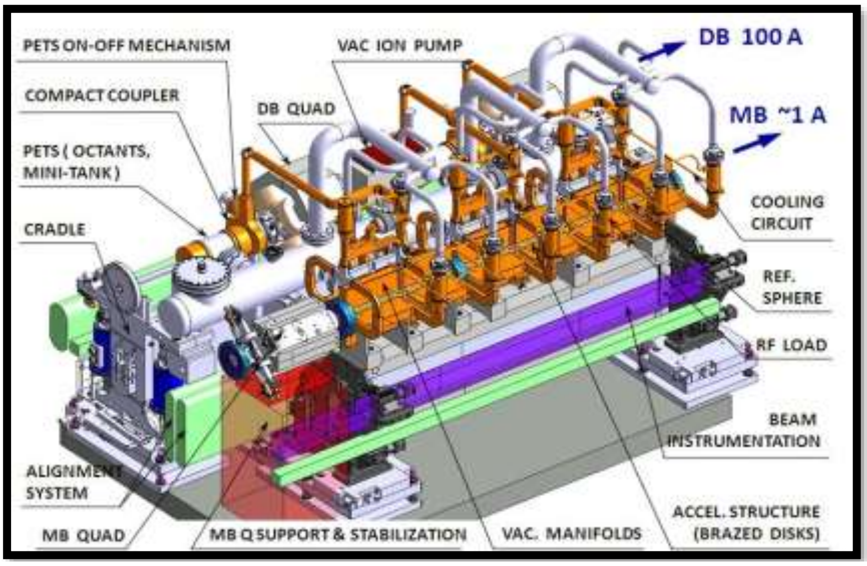


**Figure 7: One of 20 000 units, 2 m sub-assembly "two-beam modules" as referred in CLIC documentation** (CLIC (Collaboration), 2012)**.**

Each of this two-metre modules will be assembled from numerous components from which the most critical are the focusing magnets or Main and Drive Beam Quadrupoles (MB Quad and DB Quad), the beam accelerating structures (AS) and Beam Positioning Monitors integrated into the MBQ. The specification is even more challenging as the aligning reference is the electromagnetic null or so-called active magnetic axis (Bottura *et al.*, 2006; Arpaia *et al.*, 2015) of each magnet with respect to each consecutive one.

Those measurements are later used for the alignment procedure via precision actuators at nominal operating conditions of the accelerator within the tunnel. Thermal conditions during operation could vary significantly causing internal thermal gradients critical for the assembly's alignment. Temperatures of more than ten °C differential between metrology and machine actual operation in an underground tunnel. This causes large deformations and thus drift in the magnet alignment measurements. Therefore, accurate metrology and thermal drifts compensations are among the alignment challenges that need to be addressed for the realisation of the CLIC accelerator.

### 1.2.1 The PACMAN project

The current PhD work was part of the Particle Accelerator Components Metrology and Alignment to the Nanometre-scale (PACMAN) EU project which aimed to address the current state of art issues of accelerator pre-alignment (CERN, 2017b). Before the PACMAN project, the possibility of achieving real alignment measurements uncertainties for such large industrial sized project had not been studied.

The CLIC beam studies estimated that to achieve the desired luminosity, an elliptical beam with cross section semi-major axis sizes: $\sigma_x\sigma_y$ = 60 nm x 0.7 nm must be aligned and focused. As defined in CLIC Conceptual Design Report (CDR) (CLIC (Collaboration), 2012), the required pre-alignment measurement of electromagnetic axis with respect to fiducials coordinate system must be done to 12 µm uncertainty for magnet alignment. Those values are equal to the maximum value a measurement could lie from a true value at probability of one sigma (1 σ) or 68 % (**Figure 8**).

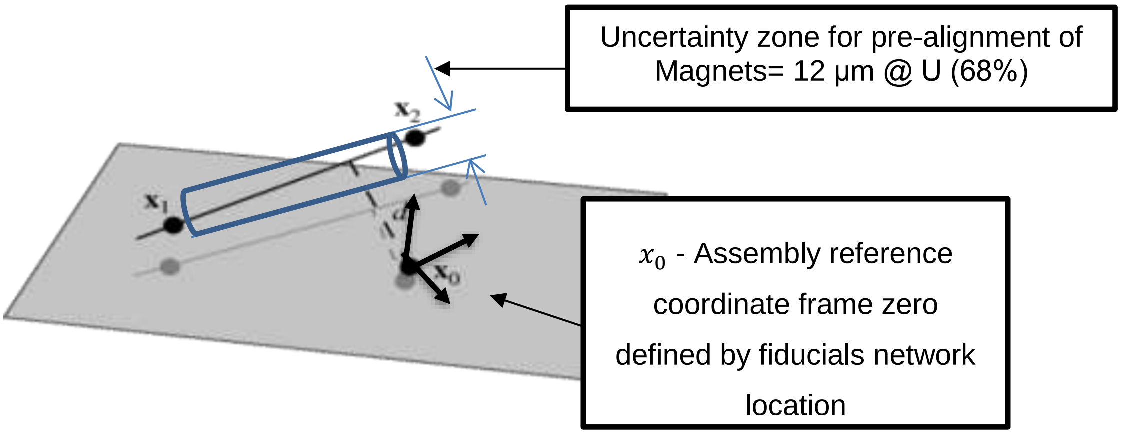


**Figure 8: The electromagnetic axis represented as line through 2x coordinates in space, and the global reference as coordinate system defined by the fiducials**

The current state of the art in accelerators component alignment is based on historical considerations and experience gained with the alignment work done for CERN (Bottura *et al.*, 2006) and others across the globe accelerator projects. The best alignment performance quoted for similar size assemblies are in the range of 50 µm + (Bottura *et al.*, 2006) with no expansion coefficient k (σ level) but rather quoted as RMS errors. An exception is a work done for the LHC (Dupont, Missiaen and Winkes, 2004) where metrology performance was stated at 1 σ but in the region of 100 µm +. However, none of the existing state-of-the-art work was done following the international standards of uncertainty propagation and quantification thus stating traceable to SI unit uncertainty statements (**2.1.2**) rather than error budget estimates (**2.2.3**). CLIC tight alignment tolerance was never required or reached. This is believed to be an issue for future accelerators having tolerances at the limit and beyond of currently available metrology methods for this assembly sizes. This limitation was the main driver behind the PACMAN project initiation. The project studied the integration, design and calibration of a multi-sensorial coordinate measurement system being able to perform the required alignment measurements at one place and time. The system created by the PACMAN team has four different sensorial elements used in series to perform the alignment measurement. All were integrated into the bed of industrial bridge type Coordinate Measurement Machine (CMM).

The four measurement systems are as follows:

*<u>Stretched wire magnetic axis measurement:</u>* A stretched wire system was used for location of the magnetic axis of a magnet by best fitting a stretched wire with known minimum sag to it **Figure 9**.


**Figure 9: Example of stretched wire metrology system used for fitting a wire to components electrical or magnetic axis or for studying the field quality (courtesy of CERN)** (Arpaia *et al.*, 2015; Caiazza, 2015; Mainaud Durand *et al.*, 2016)**.**

*<u>Stretched wire RF (Radio Frequency) axis measurement</u>.* A stretched wire system is used for locating the electric zero of BPM sensor. This was done by best fitting stretched wire known position to the electric centre. The electric axis measurement system was designed to utilise the same mechanical hardware as the magnetic axis measurement system with different electronic instrumentation and method used for this specific measurement **Figure 9**. The systems were developed by the PACMAN PhD students (Caiazza, 2017) and (Zorzetti, 2017)

*<u>CMM non-contact wire location measurement</u>*. This measurement was used for locating the stretched wire axis (defined by the stretched wire system) in space with a CMM non-contact head. It translates the coordinates of the magnetic and electric axis to the CMM frame of reference. The instrument was developed by the PACMAN PhD student (Sanz, 2018).

*CMM tactile measurement of reference datum on the assembly.* Leitz Infinity CMM system (HexagonAB, 2017) was used for measurements integration and location of a global measurement datum on the PACMAN magnet assembly. This was done by exchanging the non-contact head with a tactile probe on the CMM. This referenced the knowledge of the stretched wire sensor and thus of the electromagnetic axes to the global assembly datum set by a system of fiducials **Figure 10**.

**Figure 10: Left CMM (Leitz Infinity). Right CAD impression of the integrated pre-alignment system with the magnet assembly**

These measurements were performed in class 1 metrology thermal environment with a temperature variation of ± 0.1°C evaluated according to (ISO, 2015) standard. Minimum test current within the coils, required for magnetic measurements and no water cooling was used to minimise any possible thermal perturbations of the measurement environment.  Compensations of CMM alignment measurements for both magnetic axis and spherical reference fiducials drift was studied consequently of initial alignment measurements. This was done by series of thermal cycles and reference measurements validated against Probabilistic Empirical and Finite Element compensation models. This work was done by the author of the current PhD thesis (Doytchinov, 2017) submitted to Cranfield University, UK.

## 1.3 Research motivation

CLIC challenges raised the following questions and thus research motivation in the field of precision alignment addressed by the current work:

- How to achieve alignment measurements with accurate uncertainty statements in the micrometric range for meter sized objects at large and international production scale? A challenge for future large-scale accelerator and engineering projects.
- How to accurately evaluate the uncertainty contribution of the thermal effects on the alignment measurement uncertainties? How to compensate them if necessary with a known and valid uncertainty of the compensation?

The present work was motivated on contributing to the knowledge of creating and validating a methodology that can be applied to answer the current state-of-the-art challenges stated. This was achieved by providing accurate and traceable alignment measurements with specific uncertainties including for thermal effects compensation. It is claimed that such methodology provides a tool for solving common challenges in the area of large-scale high precision alignment.

## 1.4 Thesis structure

*Chapter 1:* In chapter one an introduction to the challenges of current and future large assembly's precision alignment problem is given. The domain of engineering is defined as the one covering state of the art projects requiring the assembly of meter range objects to micrometre accuracy. Examples of current and future common challenges are given in the field of large telescopes, aerospace engineering and big science projects. Metrology performance vs desired assembly tolerances is put as one of the limiting factors in this field of engineering. The chapter then introduces a current alignment challenge in the field of future particle accelerators and the latest project on which the current thesis is based, aiming to resolve them. The chapter finally summarises the current PhD work research motivation aiming to resolve the challenges in the domain of accelerator alignment and thus contribute to large assemblies high precision assemblies in general.

*Chapter 2:* In this chapter, a review of the relevant state of the art literature is given. The review starts from defining the basic concepts in uncertainty analysis, relating them to the internationally agreed definitions, rules and standards (JCGM, 2008a). The capabilities and limitations of those state of the art uncertainty analysis standards and methods are discussed. The chapter introduces one of the latest expansions of the state of the art uncertainty methods (BIPM, 2008) based on probabilistic Bayesian analysis as possibly the best method for tackling efficiently complex uncertainty analysis problems. Later in the chapter the state of the art of how uncertainty analysis in precision manufacturing and measurement machines Is discussed. Showing that currently manufacturing precision systems lag behind in the application of state of the art uncertainty analysis methods. The chapter then looks deeper into the concrete case of alignment of accelerators. It reviews state of the art in the field and current gaps in knowledge and challenges. Finally, the chapter defines a gap of knowledge in both accelerator alignment and precision engineering in general.

*Chapter 3:* In this chapter, the focus of the current thesis is defined as an aim and hypothesis which if proven can answer the defined in previous chapter gaps of knowledge.

*Chapter 4:* In this chapter, a new methodology aiming at answering the outlined in the previous chapter hypothesis is defined. The methodology is split into two separate sub-methods that aim at answering the two major challenges: quantifying accurately the measurement uncertainty and having uncertainty statements on any systematic error compensation models applied such as the one for thermal errors.

*Chapter 5:* In this chapter, a summary of the experimental setups equipment and applied procedures is outlined. Here all the experimental setups and measurement systems are described in greater detail with further references given. Their measurement performance and the methods used for its quantification is defined as well. Beside measurement equipment, the key software tools used are described with given references. Second part of the chapter describes in greater detail the specific procedures applied for the uncertainty analysis and mathematical modelling.

*Chapter 6:* In this chapter, the studies significant results and findings are summarised in the form of various graphs and tables. In the first part, the results linked to the alignment measurements uncertainty analysis are outlined. In the second part, the results linked to thermal deformation modelling uncertainty are outlined

*Chapter 7:* In this chapter, a discussion of the thesis results is made. In the first part, an explanation of the findings related to CMM measurement uncertainty is made. In there the results confirm some of the gaps in knowledge and limitations of existing practices. Further, it shows how the suggested methods answer the exiting gap of knowledge related to alignment measurements uncertainty analysis. In the second part, the results related to uncertainty analysis of thermal deformation models are discussed and findings outlined. There a critical comparison of empirical, Finite Element Modelling and metamodeling is made. Further, it is shown how the findings confirm the hypothesis and can answer gaps in knowledge not only in precision alignment but precision engineering as a whole.

*Chapter 8:* In this chapter, the findings from the discussions are summarised as a conclusion that shows the direct contribution to knowledge in the field of metrology and precision engineering. Further conclusions related to the CLIC project and alignment challenges is summarised.

*Chapter 9:* In this chapter, a future work recommendation is given. Namely current research work has found some additional gaps of knowledge that need to be answered if further increase alignment accuracy is required. Suggestions as well are made for further verifications and studies for alternative application of the proven in this thesis methodology.

# 2 LITERATURE REVIEW

## 2.1 Uncertainties and their propagation

A precision system, manufacturing machine tool or measurement, is designed with the view of delivering a desired specific function. For metrology systems, this is a measurement with a related certificate of the measurement truthfulness – the uncertainty statement. Uncertainty is the doubt one has on the validity of measurement as best described in (JCGM, 2012) as the "parameter, associated with the result of a measurement that characterizes the dispersion of the values that could reasonably be attributed to the measurand". The internationally recognised model for the propagation of various errors to final metrology system uncertainty is outlined In (JCGM, 2008a). This mathematical model is based on the Bayesian theorem and describes the final measurement uncertainty as Gaussian or t-shifted probability density propagated as a function of all possible error contributors. Detail illustration of the methodology for evaluation of uncertainty according to (JCGM, 2008b) are shown in **Figure 11**.

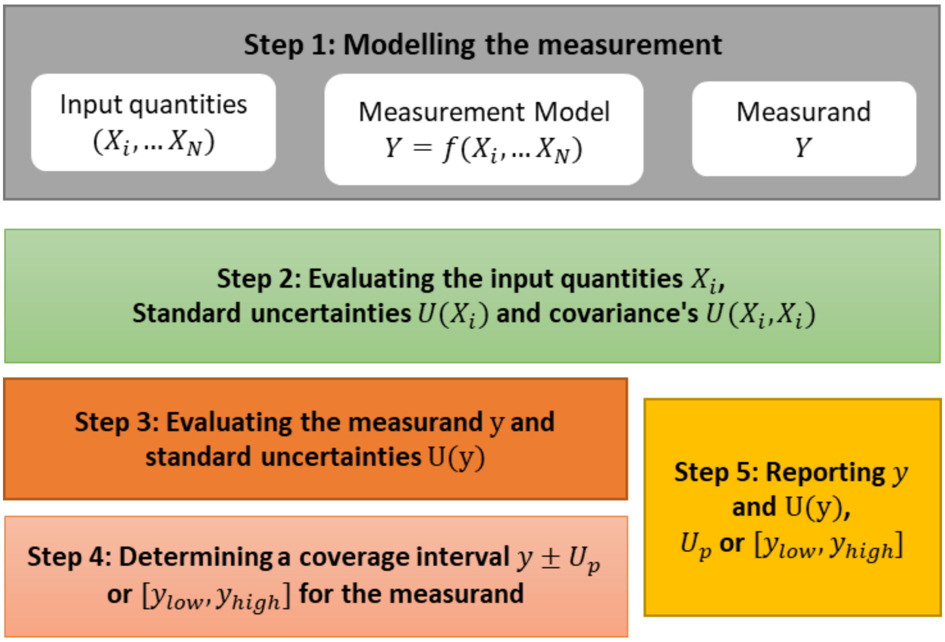


**Figure 11: Graphical sketch of the GUM model steps as presented in** (JCGM, 2008b)**.**

The first step (step 1 in **Figure 11**) is to describe the measurement model. This would include defining what exactly the measurand is $\boldsymbol{Y}$ (Is it length, form, mass, time etc.). Next step woud be to describe all possible influencing paramters ($X_1, X_2, \ldots, X_n$). Final step is to define a model of the measurement describing how the various parameters influence the measurand $\boldsymbol{Y}$. The model is defined as the mathematical description of cause and effect describing $Y$=$f(X_1, X_2, \ldots, X_n)$. For example measurand $\boldsymbol{Y}$, has the following function **Eq.(2-1)** of $X_1, X_2, X_3$.

$$Y = \frac{X_1(X_2 + X_3)}{{X_3}^2} \qquad \textbf{(2-1)}$$

**Figure 12** shows how the three influencing parameters $\boldsymbol{X_1}, \boldsymbol{X_2}, \boldsymbol{X_3}$ and their measurement uncertainties $\boldsymbol{u}(\boldsymbol{x_1}), \boldsymbol{u}(\boldsymbol{x_2}), \boldsymbol{u}(\boldsymbol{x_3})$ propagate through the measurement model $\boldsymbol{f}(\boldsymbol{x})$ to the final Measurand $y$ and its measurement uncertainty $\boldsymbol{u}(\boldsymbol{y})$.

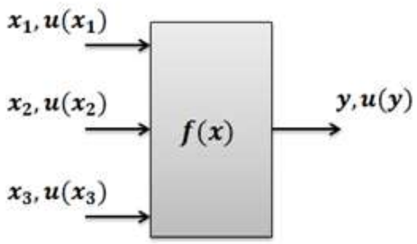


**Figure 12: Graphical sketch of the GUM model as presented in** (Couto, Damasceno and Oliveira, 2013)

Once the measurement model is complete, the standard uncertainties ($\boldsymbol{u_1} \ldots \boldsymbol{u_i}$) associated with all input quantities ($\boldsymbol{X_1} \ldots \boldsymbol{X_i}$) must be evaluated (step 2 in **Figure 11**). In step 2, an estimation of their probability distribution and probability density functions (PDF - function that describes the relative likelihood for a random variable to take on a given value) (JCGM, 2012) is made. This is achieved using Type A or Type B evaluation. In Type A analysis the evaluation of uncertainty contributor probability distribution is done via statistical analysis of series of observation. For example, this can be the standard deviation of a repeatability study. The uncertainty u(x) due to repeatability of a set of (n) measurements of the quantity (x) can be expressed by the standard deviation of the mean as shown in **Eq.(2-2), Figure 13.**

$$u(x) = s(\bar{x}) = \frac{s(x)}{\sqrt{n}} \quad \textbf{(2-2)}$$

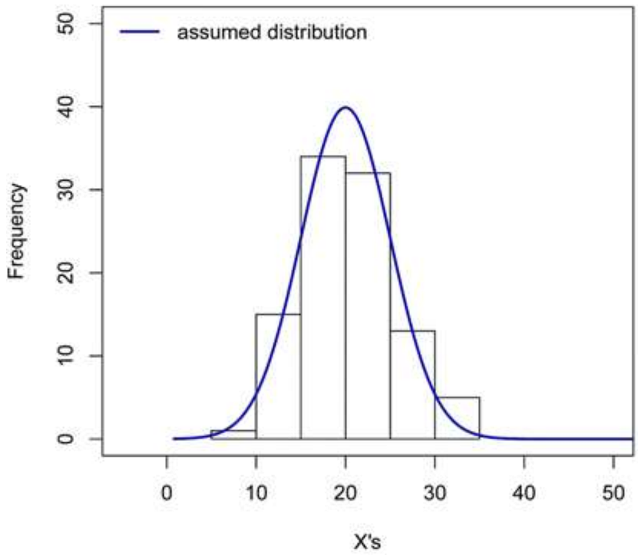


**Figure 13: Example of Type A uncertainty analysis defining PDF from frequency of measurand samples.**

Where in **Eq.(2-2)** $\boldsymbol{s(\overline{x})}$ is the standard deviation of the mean, s(x) is the standard deviation of the sample and n is the number of measurements.

In cases when it is not possible to perform Type A evaluation, Type B can be chosen, for example when the system is not available or not economical to be tested. In Type B evaluation, the uncertainty is defined by a theoretical distribution which is selected by the metrologist. An uncertainty PDF which represents at best the behaviour of the real system is chosen. For example, a digital calliper final digit reading, (with a decimal resolution due to rounding equal to a) could be anywhere between $(a_{-})$ and $(a_{+})$ **Figure 14**.

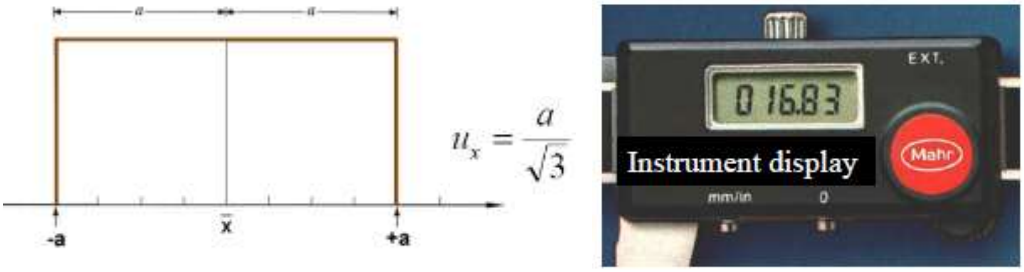


**Figure 14: Rectangular probability distribution assigned for calliper resolution rounding uncertainty contributor. The resolution of the calliper is 2a = 0.01 m.**

Thus we accept that for our measurement it is equally probable a true value to lie in our measurement interval $(a_{-})$ to$(a_{+})$. Such interval can be described by uniform PDF or so called rectangular probability **Eq.(2-3)**

$$X_i = \frac{(a_{-} + a_{+})}{2} \tag{2-3}$$

With associated variance **Eq.(2-4)**

$$U^2(x_i) = \frac{(a_{-} + a_{+})^2}{12} \tag{2-4}$$

If the difference between the bounds $(a_{-}\ to\ a_{+})$ is denoted by 2a, then:

$$U^2(x_i) = \frac{a^2}{3}\ or\ U(x_i) = a/\sqrt{3} \tag{2-5}$$

Which gives the standard uncertainty $U(x_i)\ =\ a\ x\ (d)$ where (d) is called the distribution coefficient and in the case of rectangular probability density function is calculated to be $1/\sqrt{3}$.Examples of three frequently used Type B assumptions can be seen in **Figure 15**.

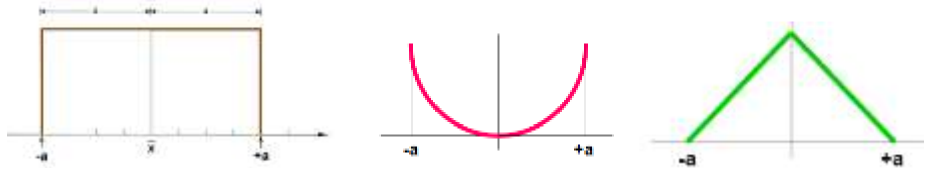


**Figure 15: Rectangular, U shaped, Triangular Type B assumptions for the PDFs of different types of uncertainties.**

Depending on the assumption made (rectangular, triangular, U-shaped or other) their associated standard uncertainties would be calculated to be different (a function of the area under the PDF).

Once Type A or Type B evaluation methods are performed, and associated standard uncertainties are evaluated for each input $(X_1, X_2, \ldots, X_n)$, the best guess for $C_n$ and $u\left(x_i, x_j\right)$ should be calculated, where:

$$c_n = \frac{\partial f}{\partial x_n} \qquad \textbf{(2-6)}$$

are the sensitivity coefficients on how (Y) will be influenced by small variation *U*($x_n$) and:

$$u\left(x_i, x_j\right) = cov\left(x_i, x_j\right) \qquad \textbf{(2-7)}$$

$$and \quad u\left(x_i, x_j\right) \in 0 \; to \; 1 \qquad \textbf{(2-8)}$$

$u\left(x_i, x_j\right)$ is the correlation coefficient between each two uncertainties $(x_i, x_j)$. It defines how they influence each other. If there is full dependance i.e. corelation of $x_i$ with $x_j$ then $u\left(x_i, x_j\right) = 1;$ if there is no dependance i.e. corelation at all then $u\left(x_i, x_j\right) = 0$.

In this stage, all the evaluated standard uncertainties and their sensitivity and correlation coefficients are propagated (step 3 in **Figure 11**) to final 'combined standard uncertainty'= $(U_c)$ which is the combined function of all 1 sigma uncertainty contributors **Eq.(2-9).**

$$U_c = f(u_1, u_2 \ldots, u_n) \qquad \textbf{(2-9)}$$

This can be done in several ways. In traditional GUM (JCGM, 2008a), the method suggested is the Law of Propagation of Uncertainties (LPU) see **Eq.(2-10).**

$$U_c{}^2(y) = \sum_{i=1}^{N} c_i^2 u^2(x_i) + 2\sum_{i=1}^{N-1}\sum_{j=i+1}^{N} c_i c_j u\left(x_i, x_j\right) \quad \textbf{(2-10)}$$

Alternatively, to this law three other methods are proposed in (BIPM, 2008; JCGM, 2008a) which propagate not only uncertainties but distributions as well: a) analytical integration, b) numerical integration or c) numerical simulation using Monte Carlo methods. The first two rely on the available analytical model of the measurement. Another limitation is the high mathematical rigour required in more complex measurement models. This might be limiting factor for the practical application of those (a, b) methods. The LPU propagation law can be defined as follows:

This law **Eq.(2-10)** Is derived by expanding the measurement model in a Taylor series and simplifying the expression by considering only the first-order terms. This assumption holds as long as the uncertainties are a minimal number in comparison to the values of their corresponding quantities (measurand values).

Once the combined uncertainty $U_c$ is known, the Expanded Uncertainty $U_p$ should be evaluated (step 4 in **Figure 11**). Expanded Uncertainty is as defined in (JCGM, 2012) a product of the combined standard uncertainty and expansion coefficient ($\mathrm{k_p}$) **Eq.(2-11)**. **Eq.(2-10)** describes an interval that contains only one standard deviation (68% confidence interval).

$$\mathrm{U_p} = \mathrm{k_p} U_c(y) \quad \textbf{(2-11)}$$

Where $(k_p)$ is defined as 'the coverage factor', and is a constant that expands the uncertainty to the desired level of confidence by the metrologist (1,2 or 3 σ) Alternately if the uncertainty analysis is based on Type A assumptions the output PDF is accepted to be best described by Student's t distribution (Moffat, 1988; Leito, Jalukse and Helm, 2017). Student's t is a distribution that resembles normal distribution however its PDF shape is dependent on the number of measurement samples performed. Those are quantified under a control parameter called degrees of freedom equal to one minus the number of measure df = (1-N). At high degree of freedom (large number of measurements > one hundred) the Students t distributions matches the shape of normal distribution. However at lower degree of freedom the shape changes with lowering probability density around the mean distributed evenly among the tails of the PDF **Figure 16** (Left – Normal Distribution, Right Students t)**.**

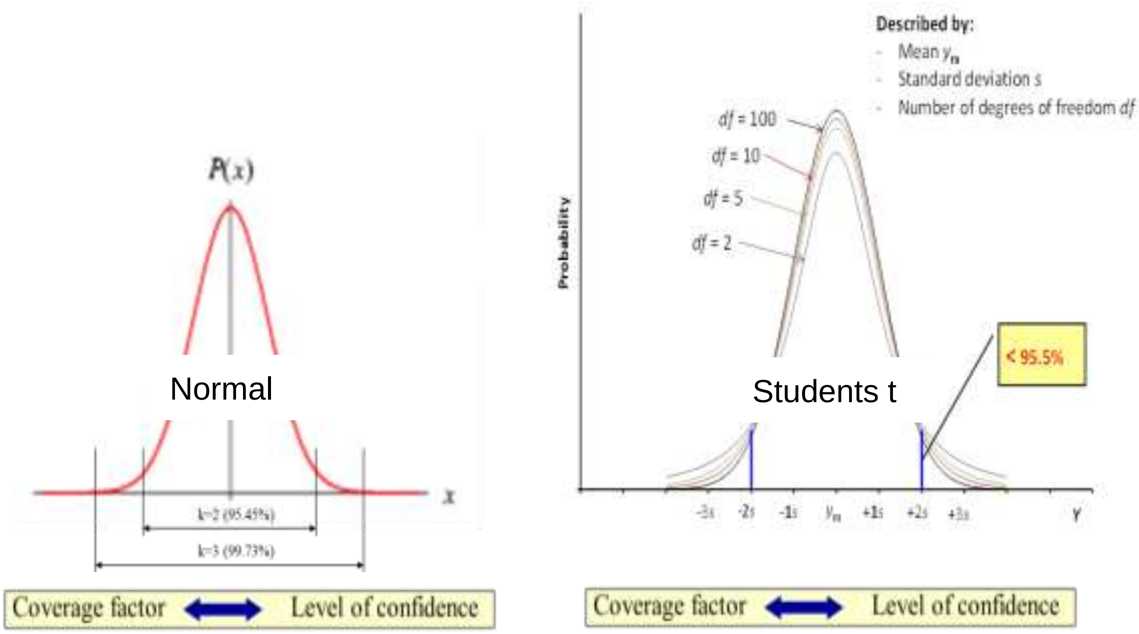


**Figure 16: Coverage factor influence on level of confidence** (Leito, Jalukse and Helm, 2017)**, Left Normal; Right Students t distributions**

The coverage factor constant can be derived from tables linking it to the degree of freedom control parameter.

When multiple uncertainty sources are propagated effective degree of freedom function of the degree of freedom of each uncertainty contributor has to be calculated $v_{eff}$ ($v_{eff} \rightarrow \mathrm{k_p}$). It can be calculated by using Welch-Satterthwaite formula **Eq.(2-12).**

$$V_{eff} = \frac{u_y^4}{\sum_{i=1}^{N} \frac{u_{x_i}^4}{v_{x_i}}} \quad \textbf{(2-12)}$$

Where $v_{x_i}$ are the degrees of freedom of the *i*'th input uncertainty contributor, $u_{x_i}$ is its standard uncertainty and $u_y$ is the combined standard uncertainty (Satterthwaite, 1946; Welch, 1947).

Step 5): Once all of those steps are completed the result Y, and the associated uncertainty and coverage interval can be stated (**Eq.(2-13)**).

$$Y = y \pm U_p \tag{2-13}$$

### 2.1.1 Monte Carlo method for uncertainty's propagation

However mathematically sound, the GUM (JCGM, 2008a) is cumbersome and difficult to implement, even impossible in some more complex cases. The three main limitations as defined in (Couto, Damasceno and Oliveira, 2013) are the following:

- The LPU law is defined by using Taylor approximations truncating the higher order terms. If a system presents a strong element of nonlinearities this assumption might not be correct enough to estimate the uncertainty output. This is because some of the information would be lost with the truncation of the higher order terms.
- In GUM central limit theorem (MIT, 2003) is accepted to hold for the final uncertainty PDF. Thus it is assumed that the final uncertainty has approximately normal distribution or t-shaped one. In reality, many of the contributor's uncertainties might not be symmetric thus the final uncertainty might not tend to Student's t or normal distribution. This might make the statement of uncertainty produced in this way inadequate.
- Once the standard uncertainty is evaluated, it is required to calculate the effective degrees of freedom by the Welch-Satterthwaite formula to expand it to greater intervals. The analytical evaluation of the effective degrees of freedom in various situations is not a completely solved problem thus not always adequate to adopt.

Due to these limitations, the international standardisation committee has come with a supplement to the standard - GUM Supplement 1 (BIPM, 2008). It is the application of Monte Carlo (MC) method for the propagation of the various errors to the measurand uncertainty. The MC (Metropolis and Ulam, 1949; BIPM, 2008) is a method for the propagation of distributions (PDFs) of the various error sources to the final output PDF which is used to define the model uncertainty. This is done by performing random sampling from input parameters distributions and propagating them through the measurement model. In contrast to LPU, this method is not based on the analytical propagation of standard uncertainties but the direct numerical propagation of distributions. This allows the information of the various uncertainty's PDF to propagate to its final uncertainty PDF which can be of any regular or irregular/nonlinear shape. This can be seen in **Figure 17** where the various control parameters PDFs ($g(x_1)$,$g(x_1)$, $g(x_1)$,…) are propagated by MC sampling through the measurement model $f(x)$ to the final measurands PDF $g(y)$.

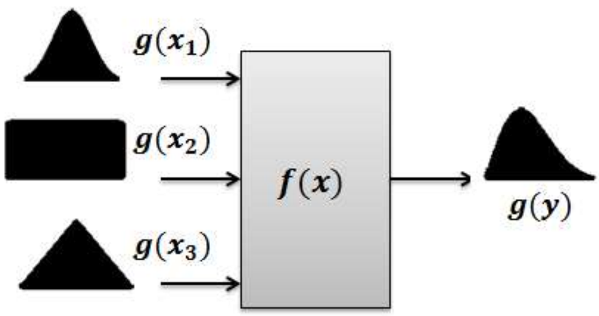


**Figure 17: Graphical impression of the GUM model steps as presented in** (Couto, Damasceno and Oliveira, 2013)

This gives a better and more realistic/accurate propagation of uncertainty, especially in more complex non-linear systems as commented in GUM Supplement 1.

Another significant advantage of the MC method is the ease with which it can be applied to various measurement models. With MC unlike with GUM LPU, one can numerically or empirically propagate the PDF of the various uncertainty factors avoiding the complex analytical work required with LPU.

The validity of MC model depends on how accurately the PDFs of the various contributors are representing reality. As in any simulation, the output is as accurate as the input parameters provided. In general, as discussed in (Couto, Damasceno and Oliveira, 2013), the greater the number of simulation trails the greater is the convergence of the results. This can be optimised, and GUM supplement 1 (BIPM, 2008) has suggested a formula (**Eq.(2-14)**) for selecting an optimum number of iterations with relation to the confidence interval probability p, where $0 \leq p \leq 1$.

$$M > \frac{10^4}{1-p} \tag{2-14}$$

For example, if coverage probability of 95 % is required then p=0.95 and M must be higher than 200,000 iterations. Once the simulation is already complete, the standard uncertainty is commented as the standard deviation of the final generated combined uncertainty PDF. The coverage interval is then determined as the shortest 100 % coverage interval of the combined uncertainty PDF (BIPM, 2008; Couto, Damasceno and Oliveira, 2013). The intrinsic requirement for such high number of simulation iteration makes the MC method, although accurate, highly computationally expensive. This can be limiting in situations where the measurement model is complex and thus computational intensive. However adaptive, sampling procedures (as Latin Hypercube Sampling (LHS) (Iman and Conover, 1980; Florian, 1992; Manteufel, 2000), Central Composite (Box and Wilson, 1992), Full Factorial (Fisher, 1992) and other techniques used in response surface methodology (Khuri and Mukhopadhyay, 2010; Myers, Montgomery and Anderson-Cook, 2011)) can be applied in order to study the optimum convergence number of trials to an accurate measurement model output PDF. In this way, the required sample size can be significantly reduced.

Adaptive sampling schemes can efficiently distribute samples across input model parameters PDF ‘design space’. In this way, an output probability density function with probabilistic significance can be propagated with a minimum number of model iterations/samples. One of the most optimal schemes suggested for the case is the LHS technique (Iman and Conover, 1980; Florian, 1992; Manteufel, 2000) **Figure 18**.

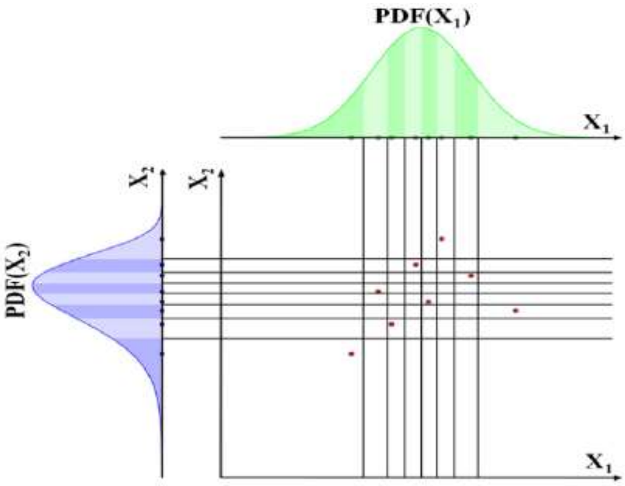


**Figure 18: Illustration of Latin Hypercube Sampling Technique distribution of samples for a case with two variables and eight samples** (Youssef *et al.*, 2013)

This sampling algorithm is particularly effective for the larger amount of input variables. It forces equal distribution of samples among parameters space represented by each parameter PDF, done in a way that none of the samples would overlay within the available design space. A visual example of such sampling distribution for two parameters can be seen **Figure 18.** Studies have shown (Manteufel, 2000) that if MC requires $x$ iterations for minimum error in predicting a confidence interval, then LHS requires $\sqrt{X}$ iteration (see **Eq.(2-15)**).

$$X_{LHCsamples} > \sqrt{X_{MCsamples}} > \sqrt{10^4 \frac{1}{1-p}} \quad \textbf{(2-15)}$$

Where p is the desired coverage interval probability. Thus meaningful results at one σ expansion interval can be achieved with several hundred sampling iterations.

### 2.1.2 Metrological traceability of uncertainty statements

The second main attribute to uncertainty statements beside accurate error sources propagation is its traceability to international standards. By metrological traceability is meant "property of a measurement result whereby the result can be related to a reference through a documented unbroken chain of calibrations, each contributing to the measurement uncertainty" (JCGM, 2012). By calibration is meant where the metrology method and instrumentation are validated against more accurate reference being a measurement tool or an artefact acting as a standard with documented and known uncertainty. Once a relationship is established from the metrological tool or procedure to the reference standard, the results can be used to define its accuracy and thus its uncertainty. Lower the uncertainty of the reference standard of measurement unit, the higher, the capability of calibration of the metrology system studied. The standards of lowest uncertainties available are the international definitions of the units of measurements. Those are realised and held within the "International Bureau of Weights and Measures or Bureau International des Poids et Measures" BIPM (BIPM, 2017). This is the intergovernmental organisation which has the mission of holding and distributing around the national metrology laboratories the most accurate definition of the SI units of weights and measures. In order of true traceability to be achieved, each measurement should possess a calibration certificate linked by an unbroken chain of measurements to the ultimate definition of the unit at BIPM. Such calibration chain can be seen as an illustrated example for the unit of a meter in **Figure 19**.

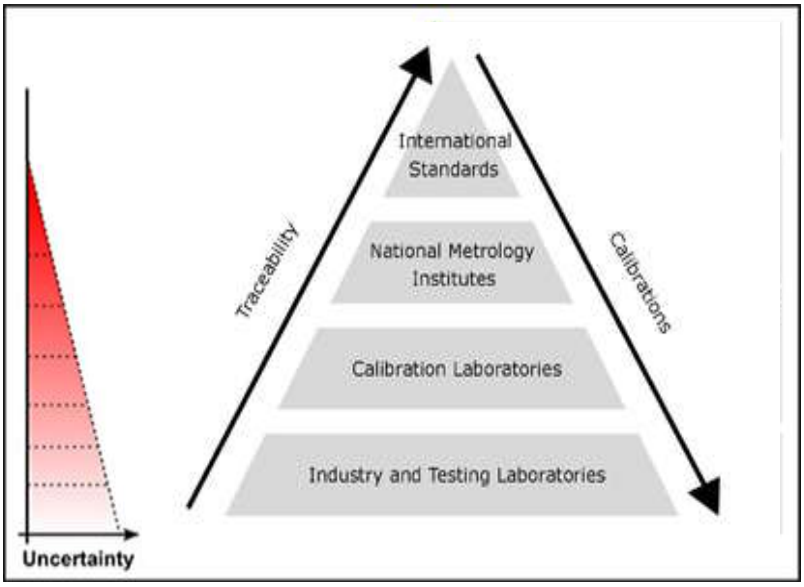


**Figure 19: Schematic representation of uncertainty and the chain of references linked to the source – the international standards as defined by BIPM**

As shown in **Figure 19** the lowest uncertainty is given by the international standards realisation. For distance dimensions, for example, this is the SI unit of meter held by BIPM (BIPM, 2006). In there the most accurate experimental knowledge of the unit is defined as a function of the fundamental physical constant of the speed of light $c_o$ and the second **s** *"the length of the path travelled by light in vacuum during a time interval of 1/299792458 of a second"* (BIPM, 2006). Where a second is further defined as *"The second is the duration of 9 192 631 770 periods of the radiation corresponding to the transition between the two hyperfine levels of the ground state of the caesium 133 atom"* (BIPM, 2006). From there the knowledge of the meter is distributed to the national metrology institutes among the countries such as National Physics Laboratory (NPL) ('*National Physical Laboratory*', 2017) in the UK or Physikalisch-Technische Bundesanstalt (PTB) Germany ('*Physikalisch-Technische Bundesanstalt*', 2017). This can be done by practical experimental realisation of the units within the national laboratories. Those realisations are accepted s so called *"primary standards"*. They are used as calibration reference for calibrating more practical and transferable to other Calibration laboratories so called *“secondary standards”*. This is done via high precision comparators and making appropriate corrections for the non-ideal methods and conditions. A meter secondary standard for example can be defined by calibrating the length of extremely dimensionally stable artefact. At this stage, this secondary standards artefacts are distributed as reference master artefacts among calibration laboratories with increased uncertainty with respect to the SI unit definition at the BIPM. As final step in the calibration chain, the secondary standards can be used for the calibration of so called working standards – gauge blocs and other type of artefacts such master parts that can be distributed among industry and other testing laboratories. Those have as well higher uncertainty with respect to the “secondary standards”. An example for such unbroken chain achieving traceability can be seen as outlined for CMM in (Trenk, Franke and Schwenke, 2004) Error! Reference source not found.**.**

In there a primary standard is calibrated via stabilised lasers of up to uncertainty of 0.3 μm. From there secondary CMM calibration standards such as ball plate are calibrated and distributed to laboratories with high precision calibration CMMs with increased uncertainty of the calibrations close to 1 μm. The high accuracy CMM’s in their hand can be used to calibrate ‘master parts’ or artefacts that are further used in industry for the determination of the quality inspection on site CMM’s and machine tools. This increases the uncertainty even further from 4 μm to + 30 μm depending on task, conditions and system studied at hand. The ability to perform accurate metrology is directly linked to the successful establishment of such traceability chain. Thus knowing the exact uncertainty of one’s measurements with respect to the ultimate definition of the SI unit standards.

## 2.2 Error budgets, coordinate measurements and accelerator alignment uncertainties

### 2.2.1 Error budgeting for precision machines

In precision engineering literature, ‘error budgeting’ is described as a deterministic process that helps to understand and evaluate machine performance. It can be accepted as a specific application of errors and uncertainties analysis as applied to precision machine system design. Error budgeting can be a useful analysis tool to predict of the total expected error of the machine system at the design stage. It gives a deeper understanding of how the various subsystems influence the final function of the machine, It can also be used iteratively during and after the design stage as an optimisation tool (Thompson and D.C., 1988; Slocum, 1992; Thompson and Fix, 1995; Homann and Thornton, 1998; Walter and M, 2002; Dornfeld and Lee, 2008; Schöck *et al.*, 2013; Thompson, Youden and Hampshire, 2013). For a targeted total-error of the system, the error budget estimation can be used to study and set individual sub-system error limits. Such study can estimate which subsystems are most influential toward the total error budget and thus most important for detail estimation, compensation and minimisation. The error budget evaluation final aim is to understand how trade-offs can be made between the various subsystems, to help decide in which area to concentrate the system analysis and design effort to meet the final target most economically (Thompson and Fix, 1995). This same core methodology can be seen applied in state of the art works done in different fields of science and engineering such as astrometry science (Nelson and Sanders, 2008; Schöck *et al.*, 2013, 2014), ultra-precision machine tools (Slocum, 1992; Thompson and Fix, 1995; Homann and Thornton, 1998; Walter and M, 2002; Dornfeld and Lee, 2008) and metrology (Thompson and D.C., 1988; Thompson, Youden and Hampshire, 2013). The error budgeting method can be seen as a specific application of the GUM standard adopted as a tool for precision systems design. The general methodology is set by first stating and understanding what the final function of the system should be and what is the targeted final specification for this function. For example for machine tools this would be the location accuracy of the end-effector in Cartesian X, Y and Z. Once this is well-defined, all possible error contributors have to be identified, classified and evaluated appropriately according to the system architecture investigated. This can be done by sorting uncertainties in sub-error or categories budgets as shown in **Figure 20.**

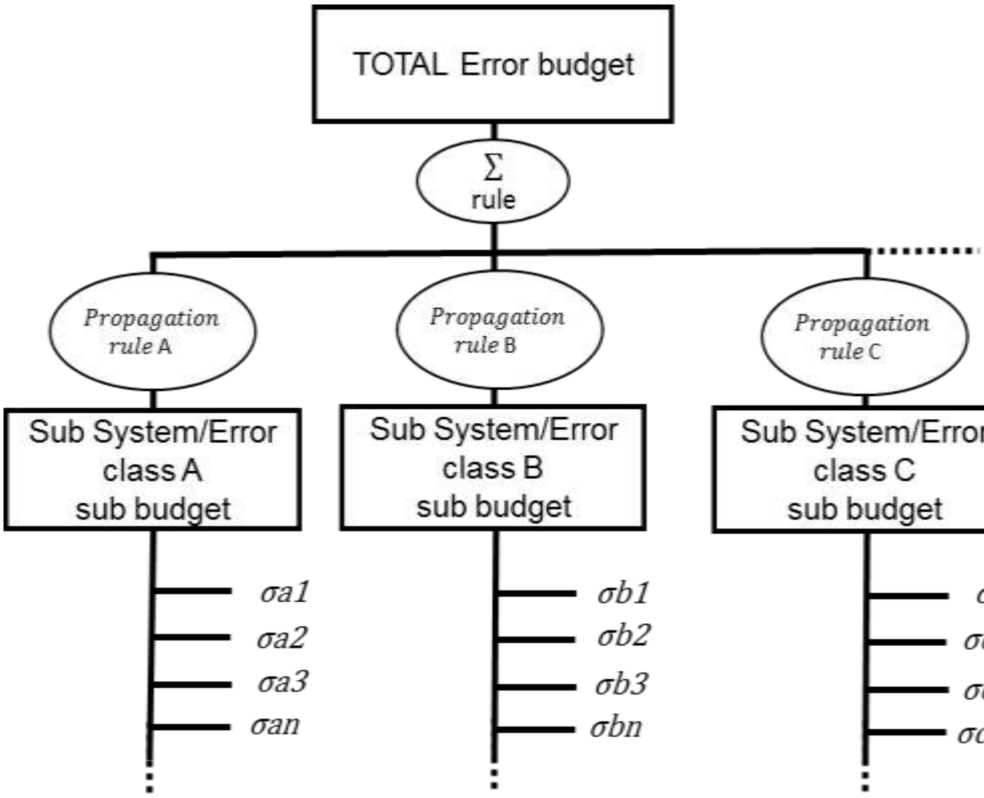


**Figure 20: Example of error budgeting top down architecture for sorting of the uncertainties**

The classification helps divide the complex system studied into smaller sub error classes which could help the designers to understand the nature of the error sources and their impact on the final desired function. Such classification would be specific to the machine or metrology system studied. Once the measurand and subsystems/class and error sources are defined and evaluated next step would be to select propagation and summation rules. Propagation rules would depend on the nature of the system/machine studied and its required function. For example, for a machine tool or CMM, the propagation rule would be the kinematic equations (homogeneous matrix transformations) that transfer machine degrees of freedom errors to end effector Cartesian X, Y and Z location error (Siciliano *et al.*, 2010).

Finally, the errors of the subsystems are summed to the total error by a summation rule chosen by the designers. A good example of that architecture can be seen work **Figure 21** (Thompson, Youden and Hampshire, 2013).

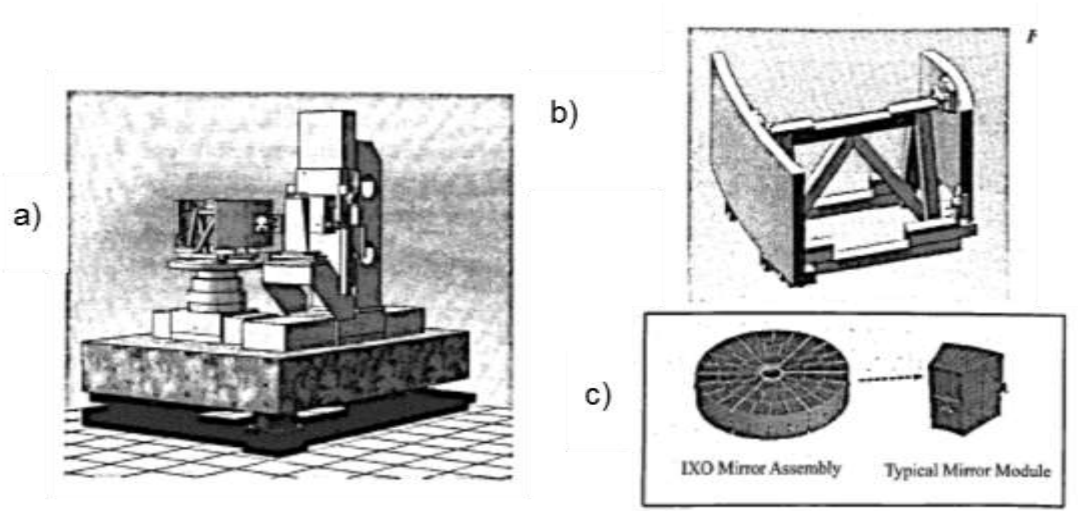


**Figure 21: a) The measuring system, b) Measured component – sub assembly of IXO Mirror Assembly, c) Example of the assembly in which those precision modules fit** (Thompson, Youden and Hampshire, 2013)

In this paper, the error budgeting as applied to the design of a specialized precision tactile measuring machine evaluating the geometrical shape of ultra-precision manufactured components for X-Ray Telescope Mandrel(Thompson, Youden and Hampshire, 2013). The metrology system aim was to determine the mirror sub-assemblies shape. The quality of the measurement was determined by the accuracy of the system end effector measuring location in X, and Y Cartesian coordinates with respect to its base. Various error sources such as positioning accuracy, straightness and Abbe offsets, thermal errors were included as contributors to the Y, and X associated errors as a function of stated manufacturers of used components specifications.

In this example as well as with (Thompson and D.C., 1988; Slocum, 1992; Thompson and Fix, 1995; Homann and Thornton, 1998; Walter and M, 2002; Dornfeld and Lee, 2008; Schöck *et al.*, 2013; Thompson, Youden and Hampshire, 2013), the final step of the method is the addition of the uncertainties. First, the propagation within the sub-budgets themselves was done and later on to the

Total or combined expected error of the desired final function. In (Thompson, Youden and Hampshire, 2013) errors are propagated via (as referred in the paper): 'RMS sum'. This was defined equivalently to $(\frac{1}{\sqrt{3}})\frac{(\sum E_i^2)^{1/2}}{2}$ which the RMS is multiplied by a distribution correction factor for uniform or square distribution = $(\frac{1}{\sqrt{3}})$ . Here the authors have deviated from the standard and by using RMS instead of RSS (root sum of the squares) for estimation of the uncorrelated uncertainties. With this propagation expression, they were determining a typical error for their sample set and not following the propagation rules of uncertainties as defined by GUM. As discussed later by D.C. Thompson (Thompson and Fix, 1995; Thompson, Youden and Hampshire, 2013) one of the greatest difficulties in their work and in error budgeting for predicting the absolute system performance was the lack of following mathematically sound and proven combinatorial rule for propagation/summation of the individual errors. They further discussed that the propagation method used is fundamental to the validity and accuracy of the total error prediction related with the system final function. If the direct arithmetical sum is done of the Peak to Valley (P-V) expected errors, then it would be too pessimistic: 913 nm predicted versus the 417 nm maximum error measured (Thompson and Fix, 1995). By P-V is referred to the amplitude given by the largest possible unknown variation of input parameter quantifying its possible error. It is highly unlikely that all the maximum of the errors would occur and correlate positively at the same time. If RSS or Root of the Sum of the Squares rule is used (this is a simplified version of the GUM Gaussian shaped uncorrelated uncertainties propagation equation) the result could be too optimistic in believing that the errors would be entirely uncorrelated and their distribution would be a Gaussian one 105 nm predicted versus 417 nm measured (Thompson and Fix, 1995). In the same work a rule named after it's author 'Hocken's rule' was applied as compromise by taking the mean between P-V and RSS as the predicted uncertainty. Using 'Hocken's rule' a remarkably good correlation between the predicted uncertainties and the real machine data is seen, having predicted 509 nm versus the measured 417 nm. However, the author's comment that they are not convinced in its case to case robustness. In the same paper a greater, care for assigning distributions to the various uncertainties is taken. This was done by correcting the P-V value of the errors anticipated by multiplying it by correction factor related to designer chosen distribution (similar to GUM Type B) analysis. This care of mathematical soundness in their analysis can be one of the factors that led to their successful use of the 'error budget' method. As a validation they have, used artefact manufactured and calibrated by a 3rd party using interferometry technology. It proved that the system performance was better than the specification given for their tactile system to measure.

Examining state-of-the-art work (summarised in analysis table drafted in Appendix **A.1**) it can be concluded that the error budgets are a helpful tool for precision system designers. It helps for system performance evaluation and optimisation. However, they were not considered as an absolute tool for system final function uncertainty qualification. The reason for this, as suggested by the authors, is the lack of common and mathematically sound error propagation method and rules applied. One of the biggest and most challenging error contributors identified commonly for all precision systems were the thermal errors. Compensation and estimation techniques can be seen applied, however up to the unknown and often not satisfactory results. Those types of errors are still not completely understood and present one of the greatest issues to precision systems performance.

### 2.2.2 Uncertainty in coordinate measurement machines

ISO Acceptance and re-verification tests

Series of standards were designed under the name of ISO 10360 for acceptance and re-verification of CMM systems by metrology laboratories and manufacturers **Table 2**.

**Table 2: ISO 10360 series standards (September 2017)**

| Standard | Name |
|---|---|
| ISO 10360-1:2000 | Vocabulary |
| ISO 10360-2:2009 | CMMs used for measuring linear dimensions |
| ISO 10360-3:2000 | CMMs with the axis of a rotary table as the fourth axis ISO |
| ISO 10360-4:2000 | CMMs used in scanning measuring mode |
| ISO 10360-5:2010 | CMMs using single and multiple stylus contacting probing systems |
| ISO 10360-6:2001 | Estimation of errors in computing Gaussian associated features |
| ISO 10360-7:2011 | CMMs with imaging probing systems |
| ISO 10360-8:2013 | CMMs with optical distance sensors |
| ISO 10360-9:2013 | CMMs with multiple probing systems |
| ISO 10360-10:2016 | Laser trackers for measuring point-to-point distances |
| ISO/WD 10360-11 | Computed tomography |

A CMM system can be checked against a reference, to validate if it is within working specification. This is done by comparing calibrated to low uncertainty high precision artefacts against measurements by the CMM system. For classical kinematic type CMM systems the Cartesian bridge type kinematics, this is done by evaluating the system sensor head (contact or non-contact) probing errors and of the complete system length measurement errors.

For the probe measurement errors qualification, a 25 evenly distributed point measurements of a high precision reference sphere of known shape are performed. The biggest deviations between the sphere calibration (for shape and radius) and measurements are used as a qualification of the probe system error. For CMM length measurement qualification a set of material standards of known sizes (step gauge or gauge block artefacts) are measured again by the CMM system. The difference between the calibration certificate for each of the distance and the CMM studied is calculated and plotted as a function of length. Finally, a CMM system is passed or failed depends if it meets a set of the manufacturer criterion: The Maximum Permissible Error (MPE). This is the maximum allowed error which if measured above (following ISO 10360 procedures) qualify a system as uncelebrated. This can be a fixed number. A number function of length or combination of both: **Figure 22**

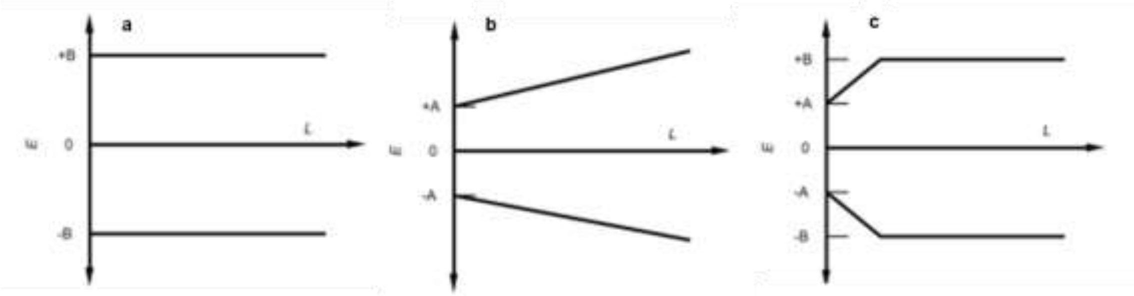


**Figure 22: CMM maximum permissible error of indication** (Flack, 2011)**: a) for fixed value; b) as function of length; c) mixture**

*Where A* is a positive constant and supplied by the manufacturer [μm]; *K* is a dimensionless positive constant supplied by the manufacturer; *L* is the measured size [mm], and *B* is the maximum permissible error, as stated by the manufacturer[μm].

ISO standards aim is to unify to a common base similar versions of national standards. Viable national standard alternatives that are still widely used are the USA (ASME B89.4 series) and Germany (VDI 2617).

However, ISO 10360 does not provide the means of quantifying the CMM systems uncertainty. As discussed in (Gestel, 2011), ISO 10360 and the MPE qualifications are often misused as the expected uncertainty of a CMM.

Interpretation of uncertainties

ISO 14253-1 (ISO, 2013b) standard provides the tools with which a decision on acceptance or rejection of a geometrical component can be made on a given tolerances. In this standard, the measurement uncertainty of the CMM is taken into account and can affect the conformance and nonconformance with specification tolerance zones (**Figure 23**).

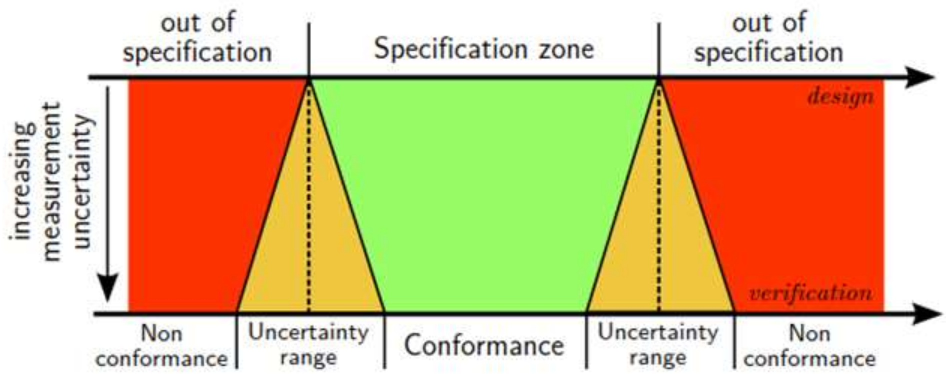


**Figure 23: Conformance range and measurement uncertainty's** (Gestel, 2011)

If the measurement uncertainty is placed at the end of the specification zone limits, it would affect the conformance and nonconformance ranges. If measured results with its actual uncertainty added lies within the new corrected conformance range, it is accepted as within specification. If it lies within the new non-conformance range, then it is out of specification. If however, it lies within the uncertainty range, no decision can be made using (ISO, 2013b). Thus according to the standard, the correct knowledge of the uncertainty range, (i.e. the uncertainty of the measurement system) is critical for making the correct decision of conformance or non-conformance. In this standard, as a general recommendation, the ratio between the Specification zone and the Uncertainty range is recommended as 1/10.

ISO 14253-2 (ISO 14253-2, 2011) concentrates on the evaluation of the uncertainties in measurement and acts as a practical interpretation of the GUM standard. An iterative method for dealing and quantifying the uncertainties in measurement defined as “the Procedure for Uncertainty Management” (PUMA) (**Figure 24**).

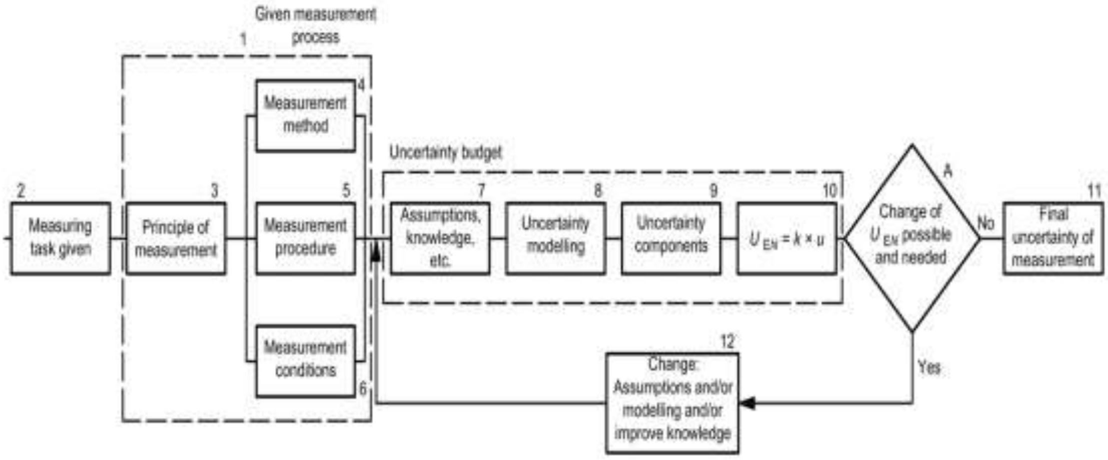


**Figure 24: Uncertainty evaluation simplified process diagram according to PUMA method** (ISO 14253-2, 2011)

As with the GUM and error budgets, the measurand is first defined followed by the complete evaluation of all error contributors to the measurement process. Those are later propagated through the measurement model, and a statement of uncertainty is given at the end. However, in PUMA, a strategy of cost efficiency about the debt of the analysis is taken. In the first step, uncertainties from various error sources are overestimated and taken in their worst possible case. This procedure aims to achieve accurate enough uncertainty statement for making a conformance/non-conformance decision with a minimum investment of resources in studying the CMM system uncertainties. If the evaluated uncertainty is not satisfactory, i.e. still large regarding the specification zone studied, further uncertainty budgeting is performed, defining more accurate the uncertainty contributors and making the measurement model more accurate.

However, no accurate validation of the predicted uncertainty is made against traceable to the unit of meter reference. The measurement model can be inaccurate and omit important error sources that are not well-understood. Thus an uncertainty predicted by the method can be small concerning the specification zone but inaccurate. This can lead to wrong acceptance of measurement that is in fact non-conforming. If most accurate and valid statement of uncertainty is needed, the so-called 'task specific uncertainty' has to be evaluated.

Task-specific uncertainty via probabilistic modelling of the CMM

The "task-specific uncertainty", as defined in the field of coordinate measurement, is a complete uncertainty statement that takes into account all the uncertainty sources associated with all the details of the measurement process (Wilhelm, Hocken and Schwenke, 2001). Such statements can be produced by several methods: *expert judgement*, *sensitivity analysis*, *analysis by substitution via calibrated objects*, *measurement history* and *computer simulation*. A good intercomparison of those methods is presented In (Summerhays *et al.*, 2004; Gestel, 2011).

*Expert judgement* method relies on the availability of a highly experienced and skilled metrologist with really good knowledge of the GUM standard and the CMM system used. His long-term experience with the system being analysed and his critical judgement are applied to provide a task-specific statement of uncertainty. This method relies on the skills and intellectual honesty of a metrologist and is usually applied to situations where there is no existing standard reference, and it is not possible to apply any other method.

*Sensitivity analysis* method is a purely mathematical method defined at GUM (JCGM, 2008a) that relies on the existence of measurement model. In this method, all uncertainty contributors' magnitudes are evaluated. Then the impact of each error contributor and its correlation to the measurement output is mathematically evaluated. It is directly applicable only if accurate analytical model of the measurement exist.

*Analysis by substitution* method (ISO, 2011a) is a purely experimental method. It relies on the existence of calibrated master artefact that geometrically represents perfectly the measurand. Such artefact should be calibrated to significantly lower uncertainty than the system used to qualify. By comparing the calibration results and the CMM system measurements both bias and variance (if numerous measurements are performed) can be evaluated. Thus the task-specific uncertainty evaluated. Due to the need of the creation of such artefact and its accurate calibration, this method is expensive, complex, time-consuming and not flexible to any changes in the measurand shape.

*Measurement history* method relies on the analysis of continuously repeated measurements over time of the measurand. It relies that large enough number of samples would reduce significantly the variance of the measurement process by the use of the mean of the samples. However, this method does not perform any comparison to a known standard or reference of the 'true' value. Thus it stays 'blind' for any possible bias errors.

*Computer simulation* (ISO/TS and ISO, 2008) method is based on the availability of computer model of both the measuring machine, measurand and the measurement strategy. This approach follows directly GUM Supplement 1 (BIPM, 2008). By this, all possible error sources need to be identified and then virtually propagated by Monte Carlo method through the measurement, CMM and measurand models. If the models are complete and accurate both bias and variance can be evaluated as an accurate representation of the measurement uncertainty. This is the most flexible powerful and economic method of all as argued by (Phillips *et al.*, 2003; Summerhays *et al.*, 2004; METROSAGE, 2009; Gestel, 2011). The accuracy of this method would be directly linked to the completeness and accurate representation and validation of the CMM, measurand and procedure models. This technique can be seen applied to different types of CMMs: Cartesian (Summerhays *et al.*, 2004; Trenk, Franke and Schwenke, 2004), Serial kinematics (Ostrowska, Gąska and Sładek, 2014), laser trackers (Huo, Maropoulos and Cheng, 2010). The basis of its successful validation is the availability of more accurate reference standard (ISO/TS and ISO, 2008). For laser trackers used for large distances (10 m – 100 m) measurements, this can be a significant challenge and limitation.

A CMM model consist of a 3D kinematic description of the structure errors degrees of freedom done via homogeneous transformation matrices as shown in (Okafor and Ertekin, 2000). Those are the 21 parametric errors for Cartesian bridge type architecture machine as explained in (J . Soon et al., 1992; Schwenke *et al.*, 2008). They consist of 18 rigid body errors (6 DoF errors x 3 axes of the Cartesian machine) and three errors of perpendicularity between each axis. These errors are for a fixed non-articulating touch probe (**Figure 25**).

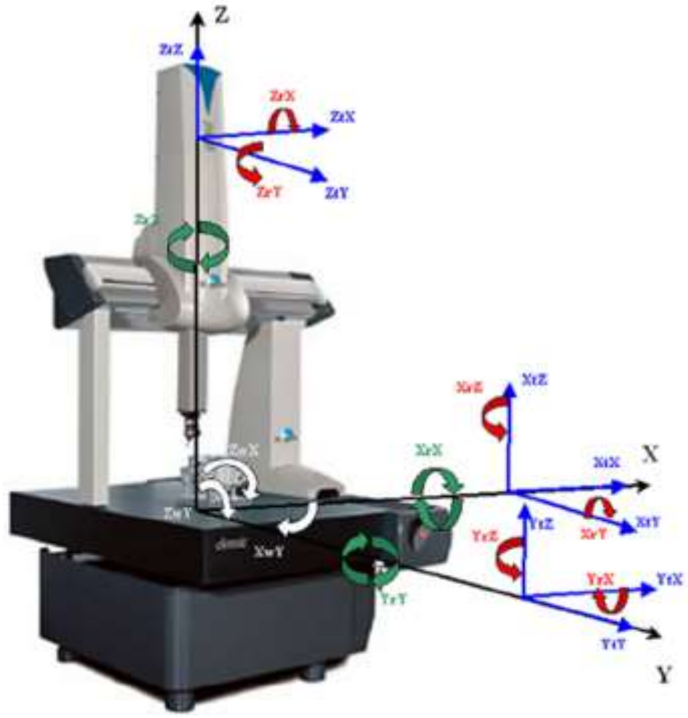


**Figure 25: Diagram of the 21 parametric errors on Cartesian CMM** (Habib, 2016)

If an articulating touch probe is used, additional homogeneous matrix model that adds the additional DoF to the error propagation is required. Each machine has a unique set of such errors which are a function of the quality of its design, manufacturing techniques applied, materials used and several other operational factors. Their combined effect is defined as the uncertainty contributor due to the CMM hardware. External effects as measurement targets form errors, thermal effects or sampling strategy have to be as well considered within such model.

The model of the measurand consists of a representation of the possible shape errors and geometrical stability. The size of such error contributors can be determined either by Type A or Type B uncertainty analysis **2.1**. This is important as shape error can significantly contribute to the task-specific measurement uncertainty. If an object is assumed to be circular, but its actual shape deviates, then large measurement errors could occur depending on the sample size and location. For example, if only three samples are taken on an object, its diameter can largely deviate from the original shape and two different radii estimated based on the two extreme measurement possibilities (Phillips *et al.*, 1998; Weckenmann, Knauer and Kunzmann, 1998; Ramesh, Mannan and Poo, 2000) (as shown in **Figure 26**).

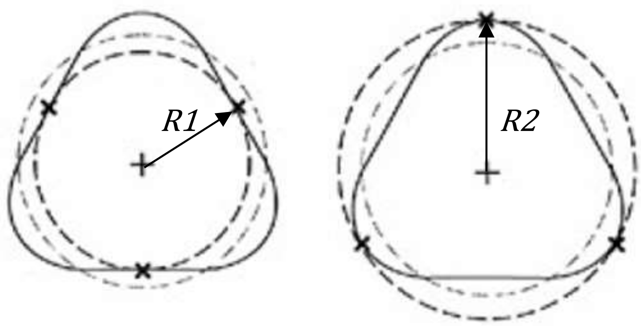


**Figure 26: Measurand form error influence on measurement result** (Summerhays *et al.*, 2004)

Dimensional stability is seen more challenging to predict. Application of simple linear thermal drift corrections are seen as the most frequently applied correction in state of the art (Phillips *et al.*, 1997). This is a challenging topic developed in detail at the following sub-chapter of the literature review.

Several commercial and research software exist for task-specific uncertainty evaluation of Cartesian CMM. The two most notable pioneering works on which state-of-the-art, is based, are the Virtual CMM initially developed at PTB (Germany) (Trenk, Franke and Schwenke, 2004), and Simulation by Constraints initially developed at NIST (USA) (Phillips *et al.*, 1997). The main difference in the two approaches is the way in which the various error contributors (Geometrical CMM errors, Form errors, Extrinsic factors) Probability Density Functions are estimated. For example, the Virtual CMM method relies on full and detailed parametric study of the various errors named Full Parametric Space (FPS). This can be performed using several techniques by substitution of known geometry of calibrated artefacts, laser interferometry and triangulation, or even statistical history error database creation (Trapet and Wäldele, 1991; Schwenke *et al.*, 2008). This, however, involves complex, expert knowledge demanding procedures and specialised equipment available at national institutes and Metrology R&D centres rather than commercial metrology laboratories. However, the method of Simulation By Constraints (SBC) takes a different approach. It uses already available information of the machine performance in the form of the standard tests machine qualifications such as ISO 10360 series (**Table 2**) where: MPEE, MPEml, MPEms, MPEmf (ISO draft/FDIS, 2010). That quantification of the machines are used to backwards map possible state space for the 21 rigid bodies parametric errors. Visual example for the possible error states area for 2 of the 21 errors can be seen in **Figure 27**.

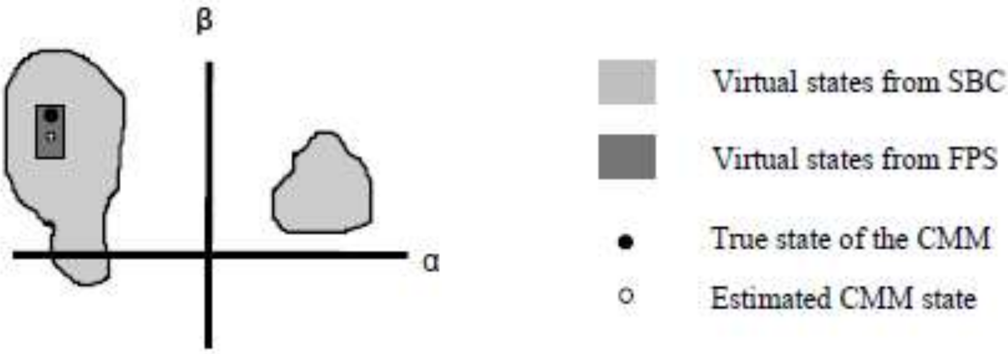


**Figure 27: Schematic of 2-dimensional state space of possible CMM error map** (Phillips *et al.*, 1997)

Following the method of inverse kinematics analysis (Kucuk and Bingul, 2006), the mathematically possible input parameters states that can combine to the output PDF can be matematicaly evaluated and described by (PDFs)s. To perform this methodology, a reference knowledge of the possible end effector location error states is required. This can be found from standard evaluation tests such as the one defined by ISO 10360 (**Table 2**) series where errors between calibrated value and CMM are measured. The solution of such kinematics problem is not linear, and there are a large amount of possible kinematic error states that can combine to the measured errors. Thus the SBC method would create large input parameter error states (PDFs) in comparison to the FPS and the true error state of a CMM **Figure 27**. Thus models calibrated by this method would be expected to overestimate the modelled uncertainty. The SBC method has the advantage of being able to map possible error states of a CMM model requiring only a standardly available calibration data (i.e. ISO 10360 tests) for any metrology laboratory and machine. Validation of this method for the application of alignment measurements can provide a tool for efficient and accurate estimation of the uncertainties. This will be further studied in chapter **6.1**.

### 2.2.3 Uncertainty estimations in accelerator fiducialisation

In state of the art literature about accelerator alignment (Pagano *et al.*, 1984; Farkhondeh *et al.*, 1991; Fischer *et al.*, 1992; Zangrando and Walker, 1993; Chida, Ohnishi and Matsui, 1995; Trbojevic *et al.*, 1998; Turner and CAS-CERN Accelerator School, 1998; Egawa *et al.*, 1998; Vasserman, 2000; Dupont, Missiaen and Winkes, 2004; Slac, 2005; Temnyjh, 2005; Temnykh, 2005; Wolf *et al.*, 2005; Di Marco, 2005; Loulergue, 2005; Pérez *et al.*, 2005; Bottura *et al.*, 2006; Zachary Wolf *et al.*, 2007), the most important process is knowing the electromagnetic axis location (of the active components) with respect to the physical references used for their alignment. The process referred as 'fiducialisation'. This process follows two separate steps **(Figure 5, page 8)**:

1) Measurement or definition of the magnetic axis with a sensor, i.e. (Colloidal Cell, Harmonic Coils, Stretched Wire, Pulsed Wire, Vibrating Wire, Hall plates).

2) Measurement of the location of the magnetic sensor in the spatial frame of reference created by the fiducial targets mounted on the assembly.

A summary and comparison of stated accelerator alignment measurement uncertainties of different state-of-the-art methods were reported by the TE department of CERN (Bottura *et al.*, 2006). Their study found measurement performance statements in the ranges of 13 µm to 60 µm for 1.13 m to 4 m sized assemblies. This included the combined errors of both geometrical survey and magnetic measurement. In general, the measurement performances reported were found to be used in a 'loose' sense in a similar way to error budgets as the best case scenario achieved not as uncertainties. No ISO or GUM standards were followed. Based on the reviewed literature, a common practice, in building the uncertainty budget, was to use the Maximum Permissible Error (MPE) for length measurement from CMM manufacturers as a quantification of the geometrical survey uncertainty, this practice can lead to wrong assumptions for the task-specific uncertainty (Gestel, 2011). For projects studied in (Bottura *et al.*, 2006), this was considered as an adequate assumption of their measurements as their targeted alignment budgets were in the range of 100 µm – 1000 µm for meter sized magnet assemblies. In **Figure 28,** one can see a summary of quoted alignment measurement uncertainty is a function of the magnets length as

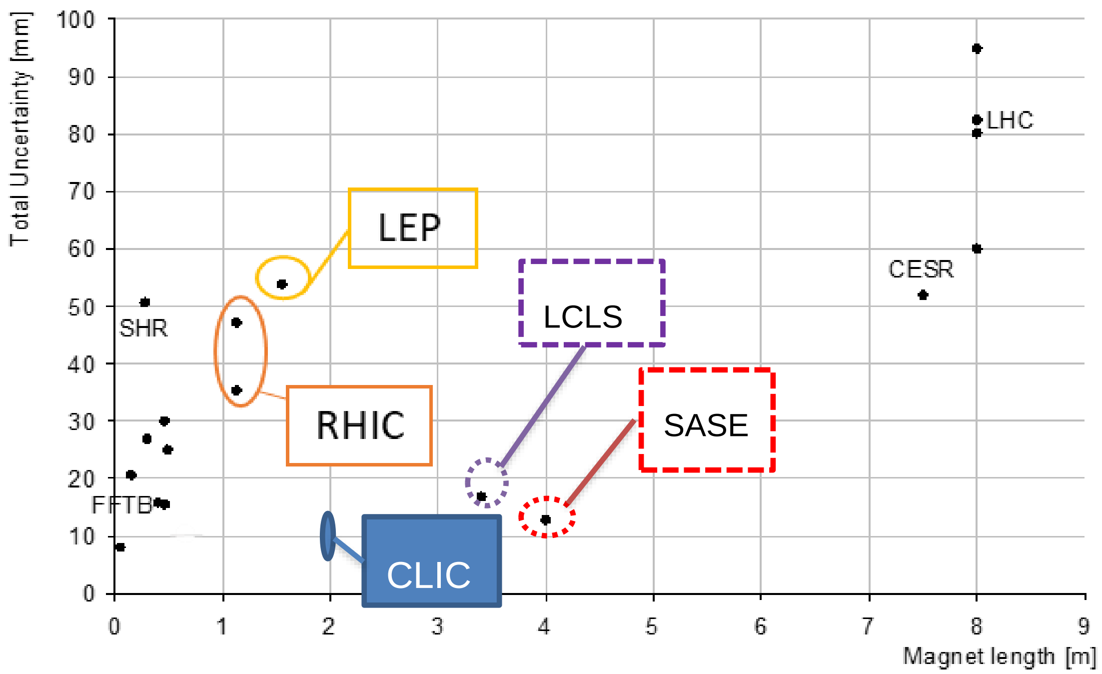


**Figure 28: Magnet lengths VS state alignment performance as presented in** (Bottura *et al.*, 2006)

studied in (Bottura *et al.*, 2006). The lowest alignment uncertainties for meter sized objects was stated for LEP (Pagano *et al.*, 1984) and RHIC (Trbojevic *et al.*, 1996)  accelerator magnets alignment and were in the range of 35 μm to 55 μm. Detail summary in the form of a table of the study can be seen in **A.6**. Those uncertainties were not evaluated according to GUM and used MPE as a qualification of the coordinate metrology.

Moreover, a general disregard of the thermal error influence quantifications can be seen. Exemption can be seen in one of the latest state-of-the-art work performed for smaller magnets (0.64 m) done for  Spring – 8 machine at Japan Synchrotron Radiation Research Institute (JASRI), (Fukami *et al.*, 2016; Zhang, Mitsuda and Kajimoto, 2016). Authors observed a high amount of correlation (0.89 correlation coefficient) between actual magnet temperature and location of the magnetic axis and thus the important influence of thermal drift axis alignment. They reported magnetic axis drift of about 2 μm per 1°C of magnet thermal drift, however, did not follow GUM standards and did not provide a statement of alignment measurement uncertainty including or with corrections for the thermal effects. In their discussion, a suggestion for minimisations of the thermal axis drift (at laboratory only) was made by controlling the magnet and environment temperature below 0.1°C of absolute thermal stability. No discussion of how thermal drift effects would influence actual in tunnel alignment was made.

In the alignment of permanent magnet undulators at Linac Coherent Light Source (LCLS) at SLAC, USA  (Zachary Wolf *et al.*, 2007) and (Ruland *et al.*, 1999) a significantly low for the size (nearly 4 m) alignment measurement errors were reported (13 μm to 17 μm). In their work statements of repeatability and measured error were only quoted without any absolute and traceable to international standards uncertainty evaluation following (GUM methods). Thus being impossible to trust such statements as real uncertainty evaluations. Those were performed as bespoke measurements on a limited number of small-scale components. It is interesting to observe that their repeatability (error measurement) results were significantly lower than the one achieved at lower sized magnets. One reason for this results might be the fact that they were aligning permanent magnets with no internal heat sources at thermally stable laboratory environment. Thus having minimum thermal effects during alignment measurements. No corrections for possible thermal drifts during machine operation were added to their alignment budgets.

In the work done for the Brazilian Synchrotron Light Laboratory – LNLS (Leãoa *et al.*, 2016), CMM alignment measurements errors of both contact and non-contact probe heads were evaluated using a calibrated artefact. The alignment measurement uncertainty target for the 1.8 m assembly was 40 μm. A 0.9 m long invar alloy beam was machined and calibrated to an uncertainty of 2 μm. The length measurement errors calibration vs measured were evaluated combining non-contact and tactile sensors. Single length measurement errors between the artefact calibration and various metrology equipment were found within the MPE stated by the manufacturers. The authors discussed the importance on achieving traceability to a common reference standard and the current lack of stated traceable results in the state-of-the-art. They claimed achieving traceability by trusting the MPE calibration certificate of the one of the high accuracy CMMs used for calibration of their artefact. However, no estimation of the full 'task specific uncertainty' was seen performed. The uncertainty propagation due to measurement datum's, thermal effects, targets form error and others were not evaluated and included. The fixed size and shape of the artefact restricted the study to assemblies having fiducial targets of the same shape and dimensions. Later in his PhD thesis work (Leãoa, 2017) proposed alignment quantification parameter called Profile Alignment Parameter for Particle Accelerators (PAPPA). This parameter aimed to apply existing ISO standard (ISO/TS-17450-2) for the quantification of alignment performance. This parameter defined the alignment quality as a tolerance zone created by two fitted to measurements lines. One by the highest two measurements and one by the lowest two measurements in sample envelope of magnets axis location. The tolerance zone was further increased by considering uncertainties of the measured samples. This qualification of alignment performance however again did not follow GUM standard and did not describe the alignment measurement process as a model thus propagating its variances and biases to a task-specific alignment measurement uncertainty. Thus it could provide misleading results either overestimating or underestimating the task-specific measurement uncertainty. The proposed alignment quality parameter performance was not validated via traceable to the meter reference.

## 2.3 Thermal effects compensation and associated uncertainty

Dimensions are inherently linked to the temperature at which they are stated. The measured result used at different thermal state, than the one obtained inherently have an error proportional to the expansion or contraction of the materials used in the assembly and of its mechanical design (California *et al.*, 1965), (California *et al.*, 1965; ISO/TR, 2003; Bryan and Doiron, 2011). The dimensional drift of the alignment targets of interest can be defined as Nominal Expansion ($NE$). The knowledge of $NE$ or any arithmetic compensation applied for its correction in alignment metrology can be defined as $U_{NE}$. Nominal Expansion of solids and assemblies can be generalised In the following steps as discussed in (Bryan, 1967; Weck *et al.*, 1995; Ramesh, Mannan and Poo, 2000; J.W. Li, W.J. Zhang. G.S. Yang S.D. Tu, 2008) **Figure 29**.


**Figure 29: Relationship between heat transfer and deformation/Nominal Expansion**

Heat Transfer between the body/bodies and environment (including internal heat sources) causes changes in the thermal field of the measurand. The change in the thermal field/state is related to internal material stresses that cause dimensional deformation among the body/bodies of the measurand. Any change from the heat transfer state present during metrology will create changes in the thermal field of the measurand thus causing it to drift away from its nominal dimensions. These thermal and thus dimensional changes from nominal conditions can be classified in three general ways: *Uniform temperature changes other than one at metrology*; *Static temperature gradients deviating from metrology temperatures* and *Dynamic thermal variation/gradients* (Bryan and Doiron, 2011).

Change in thermal conditions via heat transfer (Convection, Conduction, Radiation) during alignment after metrology would cause a change in the thermal state/field of the assembly **Eq.(2-16)**:

$$T_{field} = f(\Delta Q_{state}) = f(Conduction, Convection, Radiation) \quad \textbf{(2-16)}$$

Change in the thermal field would cause internal strain and thus expansion in the various components of the assembly constrained in a way dictated by the mechanical assembly design. The combined effect of all assembly components nominal expansions $(NE_i)$ (as guided by the assembly mechanical constraints) would define the final drift of the metrology frame. The metrology frame drift can be defined as the drift of a alignment feature (fiducial) $B_i$ with respect to zero reference datum $A_i$. In the case of magnets $A_i$ can be the magnetic axis and $B_i$ can represents an alignment fiducial mounted on the assembly. Any drift of the location of $A_i$ with respect to $B_i$ would be due to the combined function of all assembly components dimensional drift defined as $NE_{A-B_i}$ – (*Nominal Expansion of $A_i$ with respect to $B_i$*) **Eq.(2-17)**:

$$NE_{A_i-B_i} = \sum_{i=1}^{n} NE_i = \sum_{i=1}^{n} f\left(\frac{\Delta L_i}{L_i}\right) = \sum_{i=1}^{n} f(\alpha_{L_i} * \Delta T_{field_i}) \quad \textbf{(2-17)}$$

Thus to understand and quantify the process the change In thermal conditions via heat transfer$\Delta \mathrm{Q}_{\mathrm{state}}$, materials expansion coefficients $\overline{\alpha_{L}}_{component_i}$ and nominal expansion $NE_{A-B}$ of metrology frame have to be evaluated (ISO/TR, 2003).

ISO/TR 16015 (ISO/TR, 2003) discusses the importance of monitoring the thermal effects on measurand pieces and the importance of evaluation of any such systematic error and the assessment of the associated uncertainty. In this report, however, emphasis on measurand as single components and not complex assembly having internal thermal gradients is taken. The work addresses the combined use of experimental drift evaluation and thermal measurement used to quantify the effects of thermal drifts and some basic mathematical compensation of direct measurements, and it does not discuss models, and ways of predicting the dimensional drift effects as a function of the change of thermal loads post metrology and during alignment procedures.

Prediction for Nominal Expansion (NE) can be done via three different families of models: *Analytical*, *Numerical* or *Empirical* (based on experimental data).

### 2.3.1 Analytical prediction of Nominal Expansion

Most simple analytical model for NE is the Linear Scaling Law (LSL) that is widely used in metrology for simple corrections on single unconstraint piece/element measurement:

$$NE_{x\ or\ y\ or\ z} = LSL = \ [\ \alpha * L * \Delta T]_{x\ or\ y\ or\ z} \pm U_{LCL} \tag{2-18}$$

Where

$\alpha$ = average Coefficient of Thermal Expansion CTE for particular temperature interval.

$L =$ Length of measurand metrology loop in the coordinate direction measured.

$\Delta T =$ Temperature deviation from measurement/reference temperature and

$U_{LCL}$ = The uncertainty of LSL prediction (directly proportional to the uncertainty of knowing $(\alpha, L, \Delta T)$).

This law **Eq.(2-18)**, however, assumes that the thermal expansion is a linear phenomenon. Such approximation could be made with a minimum error for a single unconstrained component studied at various thermal steady state. However, this assumption can break for complex constrained assemblies where thermal deformation due to induced thermal gradients could be highly nonlinear.

State of the art review of analytical models applied for machine tool thermal error compensation was studied by (J.W. Li, W.J. Zhang. G.S. Yang S.D. Tu, 2008). The review showed that a major challenge in this approach was the accurate physical and mathematical description of both *heat transfer* and *deformation phenomena*. Because of the high complexity of structures such as the machine tools, models are rarely created for a complete assembly. Models reviewed were highly bespoke and applied to more simple structures and components part of the assemblies. From the literature reviewed no detail uncertainty studies according to the international GUM standard (Committee for Guides in Metrology, 2008) have been performed. Analytical approach to modelling is seen as not viable for modelling complex assemblies and thermal loading conditions.

### 2.3.2 Empirical prediction of Nominal Expansion

Empirical models for steady state thermal drift rely on the assumption that discrete thermal measurements on the assembly components can be representative for the local for the assembly thermal field and thus can be mathematically linked to the thermal drift of other points of interest (J.W. Li, W.J. Zhang. G.S. Yang S.D. Tu, 2008) **Eq.(2-19)**.

$$NE_{x\ or\ y\ or\ z} = f(\overline{\Delta T}) \qquad \textbf{(2-19)}$$

Thus the mathematical relationship between the inputs (measured temperature at various locations on the assembly) and the outputs (the dimensional drift) can be performed by several methods such as Polynomial Regression Analysis (Fan, Yang and Yang, 2013), Artificial Neural Networks (Fines and Agah, 2008), Kriging (Zhang, Zhu and Liew, 2014) and more. State-of-the-art works summarised in (J.W. Li, W.J. Zhang. G.S. Yang S.D. Tu, 2008) showed that application of such models for machine tools claim achieved reduction of the thermal errors ( the difference between the presumed by the author's true form of the object and the one measured) to 75-95 %. Most accurate models were experimentally proven to predict CNC machine tool drift with minimal errors of up to 3 μm (Ramesh *et al.*, 2003). Although there are promising results seen in state of the art, two gaps of knowledge should be outlined.

First, no uncertainty analysis of the error prediction models was seen to be performed following international standards such as GUM (Committee for Guides in Metrology, 2008), second empirical models were only valid for a particular assembly and conditions for which lengthy complex and time-consuming experiments were performed. This is an inherited drawback of the empirical modelling which does not provide any knowledge to machine designers for any different than the experimentally studied assemblies or unknown/unpredicted thermal conditions.

A famous historical case underlying this drawback was the Challenger space shuttle disaster caused by an O-ring component failure (Rogers *et al.*, 1986). As found by the presidential commission, the unique thermal conditions of cold weather (lowest recorded ambient temperature minus 5 °C previous lowest of 12 °C) have caused the unpredicted failure of the O-ring component. No test was performed to establish effects of such low temperature as it was unexpected to occur during a lunch day in the warm USA state of Florida. Calibration tests were not performed with temperatures below 4 °C thus no exact knowledge for o-ring behaviour was available for this conditions.

### 2.3.3 Finite Element Method prediction of Nominal Expansion

When direct analytical or empirical models are not available or economically and time-wise viable for application, numerical modelling methods based on analytical equations such as the Finite Element Method (FEM) can be applied. For thermo-mechanical modelling, those require a CAD design of the assembly, knowledge of the materials characteristics as well as initial and boundary conditions. As studied in (J.W. Li, W.J. Zhang. G.S. Yang S.D. Tu, 2008), FEM can be successfully applied as a general prediction and sensitivity tool by engineers but rarely achieving minimum error between experimental result and model prediction lower than 15 % (J.W. Li, W.J. Zhang. G.S. Yang S.D. Tu, 2008). No complete analysis of the sources of FEM models uncertainty or errors was performed based on GUM (Committee for Guides in Metrology, 2008) standard. Some recent advances in the application of FEM for thermal drift prediction can be seen in the so-called “Hybrid-Approach” (Ross-Pinnock, Yang and Maropoulos, 2015; Ross-Pinnock and Bingru Yang Glen Mullineux, 2016). Using this approach, an integration of real-time measurements and Finite Element Analysis (FEA) modelling are integrated. Thermal measurements on set location across the assembly were used as the input boundary conditions. Geometrical measurements on discrete locations on the assembly during the thermal drift were made, and the FEM calculated deformation shape of the assembly was corrected to match more closely the measured discrete locations. Results showed that the smallest errors between FEM predictions and metrology measurements for deformations were in the order of 20 μm for total deformations of around 200 μm to 300 μm.

One of the main advantages of the 'hybrid' approach is its flexibility to more complex assemblies and application to unknown recorded changes in the environment. However, in those works, no uncertainty analysis of the FEA model was performed but discussed as missing point and future work.

It is a general practice to use FEA modelling as an initial design tool and not for accurate prediction. Research teams in NIST have underlined the importance of providing uncertainty statements of any deterministic FEA models predictions. Further (Fong *et al.*, 2006; Fong, Filliben and Heckert, 2008), it is suggested that uncertainty of FEM can be evaluated following an international standard such as GUM, GUM – Supplement 1 and NIST. SOP No. 29 (BIPM, 2008; Committee for Guides in Metrology, 2008; NIST, 2014). Deterministic FEA models use mean values (taken from literature or experiments) for input. Thus the final FEM model result output is a single value.  In Probabilistic FEM the control parameters are not accepted as single values rather as Probability Density Functions (PDF). The uncertainty in model control parameters is represented by a PDF describing it. Monte Carlo or other optimised sampling techniques (such as Latin HyperCube (Iman and Conover, 1980)) can be applied to propagate the Input parameters PDF in the form of virtual experiments an output PDF **Figure 30**.

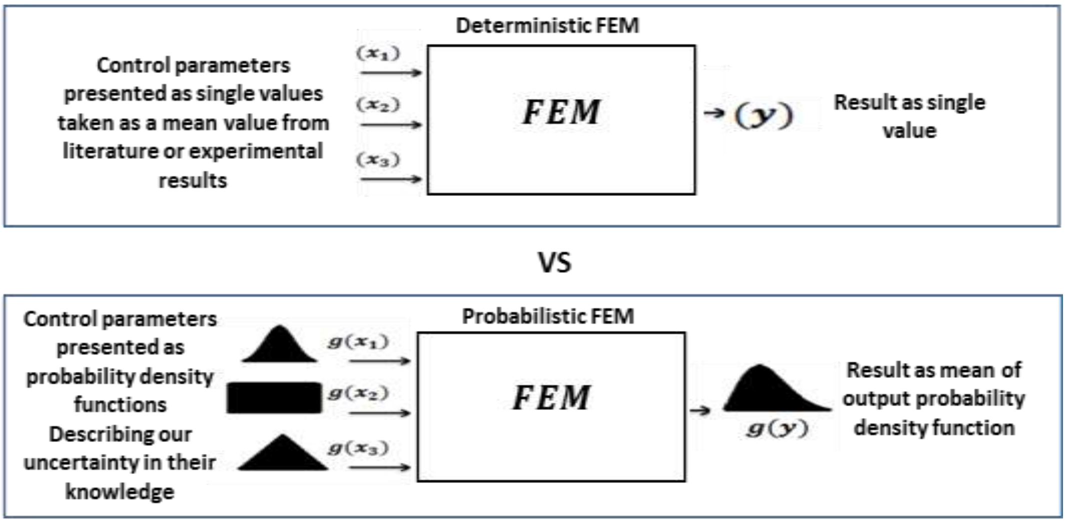


**Figure 30: Difference between Probabilistic and Deterministic FEM schematic**

The mean of the output distribution is accepted as the most likely output result and its standard deviation as quantification of the prediction uncertainty. The authors show a significant difference of up to 74 % between deterministic FEM models results and probabilistic. They claim that, in critical applications for accuracy, deterministic models can be unsafe and challenged in court as they provide a common overestimation to the prediction (mostly applicable in fatigue and failure analysis) and no proven statement of uncertainty. However, in those works, experimental proof for the accuracy of prediction was missing. Although the approach was demonstrated as feasible and useful, all the studies were performed for simplified models not related to thermal drift, i.e. such as cantilever beam natural frequency or beam fatigue predictions and validated only against their analytical solutions used as a reference.

Another relevant study that compared FEM modelling prediction accuracies and experimental results, was performed for the Herschel-Space Observatory assembly and alignment (Fransen, Doyle and Catanzaro, 2011). The alignment distance between two of the main mirrors of the telescope had to be compensated due to the thermal gradients between the assembly/alignment temperature on earth and actual operational temperature in space. This study was initiated after a large discrepancy between predicted and measured telescope focal distances was found at final tests in the cryogenic test facility. The main goal of the alignment team was to predict and compensate any thermal drift of the focal length of the telescope. Their maximum allowed discrepancy was up to ± 3mm deviation of the focal length calibration for more than 230 K difference between calibration and real operation in space. FEM models predicted final focus drift of the assembly of about minus 1.7 mm while experimental results gave the value of minus 11.7 mm. The large spread in CTE parameter of material properties taken was found causing this large discrepancy. A mean value of the materials CTE used measured by several laboratories, was selected without assessing the possible bias caused by the uncertainties of those measurements. Probabilistic FEM studies proved a high correlation between the prediction result and the bias caused by the uncertainties of the CTE measurements performed by different laboratories. A similar conclusion was reached by Doiron in NIST (Doiron, 2001, 2006).

CTE is very dependent on the details of the makeup of the material and the uncertainty of the measurement performed for its statement. Real material samples CTE can vary by more than 10 % (Doiron, 2001, 2006) with respect to the reference data given in material textbooks. The importance of considering models control parameters uncertainties and the possible bias that can be caused if a model of a system is accepted deterministic.

### 2.3.4 FEM Meta modelling (response surfaces)

Probabilistic FEM has emerged as a powerful tool for sensitivity analysis. However, one significant disadvantage is its high computational costs. Hundreds of iterations of complex FEM models are required to achieve statistically meaningful results. This limits the application of the method in optimisation studies and real-time modelling applications. To answer those gaps, the method of FEM meta-modelling and response surfaces is emerging as demonstrated in (Most and Will, 2008). The approach is to use the discrete sample points of the solution state space done by the Probabilistic FEM and to best fit multidimensional surfaces represented by analytical equations. An empirical model based on virtual samples is created as shown in **Figure 31**.

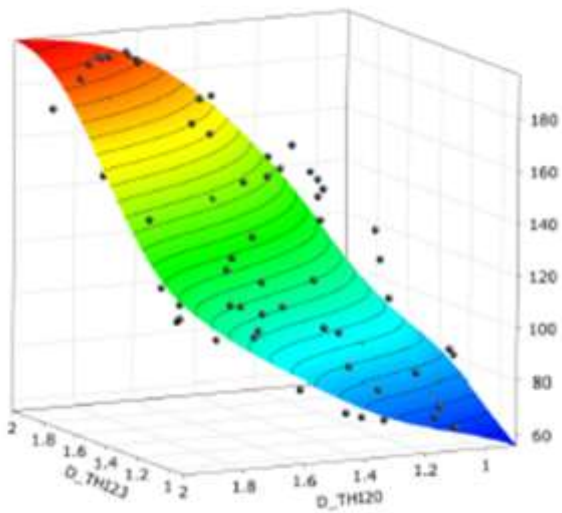


**Figure 31: Example of three dimensional response surface fitted to Probabilistic FEM responses data as shown in** (Most and Dynardo GmbH, 2010)

With this approach, the computationally heavy Probabilistic FEM is represented by simple analytical field function. This can allow powerful optimisation and real-time modelling. A disadvantage of this modelling technique is the missing statement of uncertainty. As it is a model based on a model, it is presumed that it would be less accurate than the Probabilistic FEM. However, no critical evaluation of its uncertainty with respect to real system responses following GUM has been reported. In the work of (Most and Will, 2008), an optimisation technique ‘Meta Model of Optimal prognosis’ for an optimisation of the response surface fit to represent better reality was proposed. However, again with a missing statement of traceable uncertainty.

The availability of a method to provide a traceable and accurate statements of the uncertainty of this powerful modelling technique can significantly increase its use and capabilities.

### 2.3.5 Modal thermal analysis

Thermal modelling technique uses modal analysis to define thermal 'modal' shapes of an assembly or component model. It can be seen emerging in the field of machine tool thermal control and deformation (Matsuo *et al.*, 1986; Weck *et al.*, 1995; Bueno, R.; Arzamendi, J; Almandoz, 1997; Morishima *et al.*, 2015). Step function temperatures changes and consequent drift responses are measured. Those can be explained by a model based on exponential functions with different time constants or by solving numerical FEM model in modal form for thermal deformations instead of the natural frequency of dynamic analysis. Thus temperature field distributions can be decomposed into "thermal modes" in a similar way as vibrations modes are studied in the structural modal analysis. A visual analogy of the two can be seen in **Figure 32** on next page (Bueno, R.; Arzamendi, J; Almandoz, 1997).

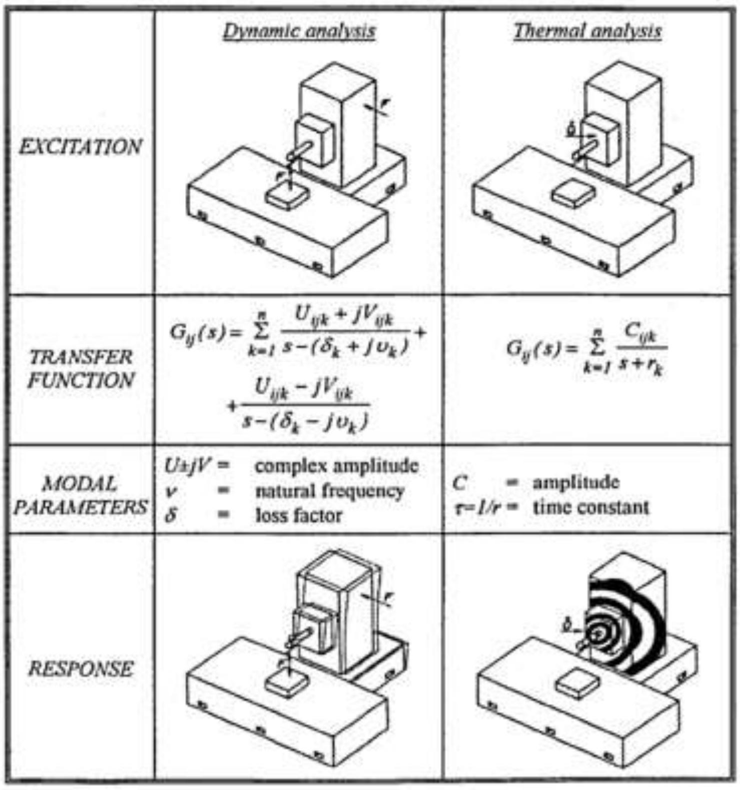


**Figure 32: Analogy between dynamic and thermal modal analysis as seen in** (Bueno, R.; Arzamendi, J; Almandoz, 1997)

As with dynamic analysis, in thermal modal analysis displacement can be described by the combination of several dominant modes. For machine tools, such dominant modes would be unique to the structure of the system studied. Based on those conclusions, performing thermal modal analysis can be used to evaluate an optimal number of thermal sensors and their mounting location. The number of thermal sensors should be equal to the number of modes of high importance. Their locations should be positioned in such a way to detect their response with the highest sensitivity. With this information input and output, responses can be mapped using classical numerical or empirical techniques to optimum performance.

However, promising this methodology is, its performance on thermal error compensation also has not been observed evaluated according to international uncertainty standards (GUM, GUM – Supplement 1 and NIST. SOP No. 29) with statements of uncertainties associated with the prediction made.

## 2.4 General conclusions

The literature review performed has found several gaps of knowledge. Those can be considered as limiting factors in achieving alignment of large assemblies with traceable uncertainty statements in the micrometric range and will be addressed in the PhD thesis.

1) No work was found to estimate the task-specific uncertainty of alignment measurements at required by CLIC magnets (12 μm, 1 σ) for up to 2 m assemblies subject to thermal loads variations electromagnets. For 1 m to 2 m sized magnets, alignment performance was observed varying between 35 μm to 55 μm for electromagnets and 13 μm to 17 μm for permanent magnets in thermally controlled environment. None of the alignment error budgets reviewed can be accepted as tracable task-specific uncertainty.

2) No work was found to fully apply state-of-the-art uncertainty budgeting and evaluation methods such as GUM, GUM Supplement 1 (BIPM, 2008; Committee for Guides in Metrology, 2008) in the domain of large scale and high precision systems alignment and integration. There is some misuse of metrology equipment qualification tests results (i.e. ISO-10360-2) as uncertainty quantification of CMMs measurements in error budgets for alignment (Bottura *et al.*, 2006). The task-specific uncertainty of alignment metrology including the dimensional stability of the measurand during alignment measurements was really observed in literature. In general no practice of estimating and including the 'Test uncertainty" (Salsbury, Corporation and Boulevard, 2003) has been observed. Commonly no expansion intervals (k) - **2.1** (Bottura *et al.*, 2006) ,as expected for uncertainty statements, can be seen quoted in the reviewed literature.

3) No validated method for correcting thermal errors with the ability to provide an accurate and traceable statement of uncertainty for the thermal errors compensations made (Bottura *et al.*, 2006; Fong *et al.*, 2006; Fransen, Doyle and Catanzaro, 2011; Ross-Pinnock, Yang and Maropoulos, 2015; Ross-Pinnock and Bingru Yang Glen Mullineux, 2016). No methodology of providing

valid uncertainty statements for empirical models that have been proven as most accurate in literature. Work done for the light controlled factories project (Ross-Pinnock, Yang and Maropoulos, 2015) has shown how online thermal measurements can be mixed with FEM for compensation thermal drift. However a lack of uncertainty evaluation of the FEM modeling has been observed although discussed as possible future line of research. Work performed for Herschel-Space observatory (Fransen, Doyle and Catanzaro, 2011) and at NIST for virtual FEM Metrology (Fong *et al.*, 2006) have shown the potential of Probabilistic FEM on the evaluation of uncertainty sources. However, the approach has not been observed applied and validated for real assemblies drift prediction with associated uncertainty.

# 3 AIM AND OBJECTIVES

## 3.1 Aim

The aim of this PhD is to define, study and validate an uncertainty budgeting methodology capable of accurately determining a specific alignment measurement uncertainty in the micrometric region for large meter range sized objects. Studing the litterature, gaps of knowledge and work on the PACMAN project has lead to the following Hypothesis:

*Specific alignment measurements uncertainty can be evaluated by a mixture of reference measurements traceable to the unit of meter and probabilistic error propagation of modelling techniques applied for both metrology and thermal compensation models.*

## 3.2 Objectives

In order to study the proposed hypothesis two major objectives with related task were defined:

(1) To evaluate and validate the task specific measurement uncertainty (Utask specific MEASURE – **Eq.(4-3)**) for defining the location of magnetic axis in the coordinate reference frame of CLIC, T1 type magnet assembly measured at a laboratory thermal conditions.

(2) To evaluate and validate a methodology that can accurately predict (with valid uncertainty statement $U_{NEmodel}$ - **Eq.(4-4)** in the micrometre region) a drift of the assembly metrology frame due to non-uniform steady state thermal gradients. Achieve this by following a mixture of reference thermal and drift measurements and probabilistic modelling for the CLIC T1. To validate methodology with respect to international uncertainty evaluation standards (GUM, Supplement 1 and ISO 15530-4 (BIPM, 2008; ISO/TS and ISO, 2008)).

# 4 METHODOLOGY

In this chapter, methodology followed in the PhD thesis is presented. First, in **4.1,** the methodology for evaluation of alignment uncertainty is generalised as function two major contributors: task-specific measurements uncertainty and thermal drift compensations. In **4.2** and **4.3** the sub methodologies applied for the evaluation of the two major contributors are detailed.

## 4.1 Alignment measurement uncertainty

The lowest uncertainty of dimensional measurements is achieved at the temperature at which the standard of the unit meter is defined (20 °C) (Ted Doiron, 2007). However, if dimensions are required to be stated at another temperature, then CMM's can be calibrated to do so via reference artefacts traceable to the meter standard (Trapet and Wäldele, 1991; Trapet, 2010, 2012). Measurements performed at a stable temperature different than 20 °C would have an inherent increase in uncertainty. This would be due to the increased dimensional uncertainty of the artefact used for the CMM's scales calibration with respect to the meter standard. Traceable reference artefacts are calibrated at 20 °C in the National Institutes. At any different temperature, their dimension can drift from the calibrated one, thus influence the artefact calibration uncertainty (Doiron, 2001, 2006; ISO, 2009). This can be minimised via thermally stable artefacts (extremely low CTE coefficient and low uncertainty of its knowledge - manufactured by materials such as Zerodur® (SCHOTT AG, 2017) or Carbon-Fibre) thus having a minimal increase of measurement uncertainty (Trapet and Wäldele, 1991; Trapet, 2010, 2012). It is up to the metrologist to decide (based on cost/accuracy targets) at what stable temperature/environment conditions their CMM would be calibrated, and alignment measurements would be performed.

For large-scale projects such as CLIC, CMMs can be of bespoke design or with unique calibration for measuring at the particular environment and thermal conditions close to the operational one. This strategy relies on the stability of the thermal state of the CMM and the measurand. Any drift in the thermal state of the

CMM or the measurand would cause a dimensional error of the measurement proportional to the differential expansion between the assembly being measured and the CMM (California *et al.*, 1965). Any drift of the thermal state of the assembly posterior to the measurements and during alignment procedures would cause drift in the measurement results proportional to the nominal expansion of the measurand itself. Thus to know the uncertainty traceable to the meter (**2.1.2**), all error sources including the thermal drifts have to be monitored both during metrology and posteriorly during alignment procedures of the large assemblies.

In the current methodology it is accepted that the alignment assemblies are thermally stabilised during the period of precision alignment without experiencing any *dynamic thermal variation/gradients.* This assumption is made as first the active alignment procedures as related to CLIC would take a short period relative (minutes) to the large thermal constant of the assemblies (hours due to their high thermal inertia function of their large size and mass). Second, it is accepted that the accelerator machine would be already tuned to its optimal operational conditions - temperature when alignment procedures are initiated. Thus, only *static temperature gradients deviating from measurement temperature* are to be considered for the measurement corrections.

The alignment uncertainty strategy was split in two phases (**Figure 33 –** top and bottom). First to perform alignment measurements in a laboratory at a set stable temperature conditions **Figure 33 -** top.

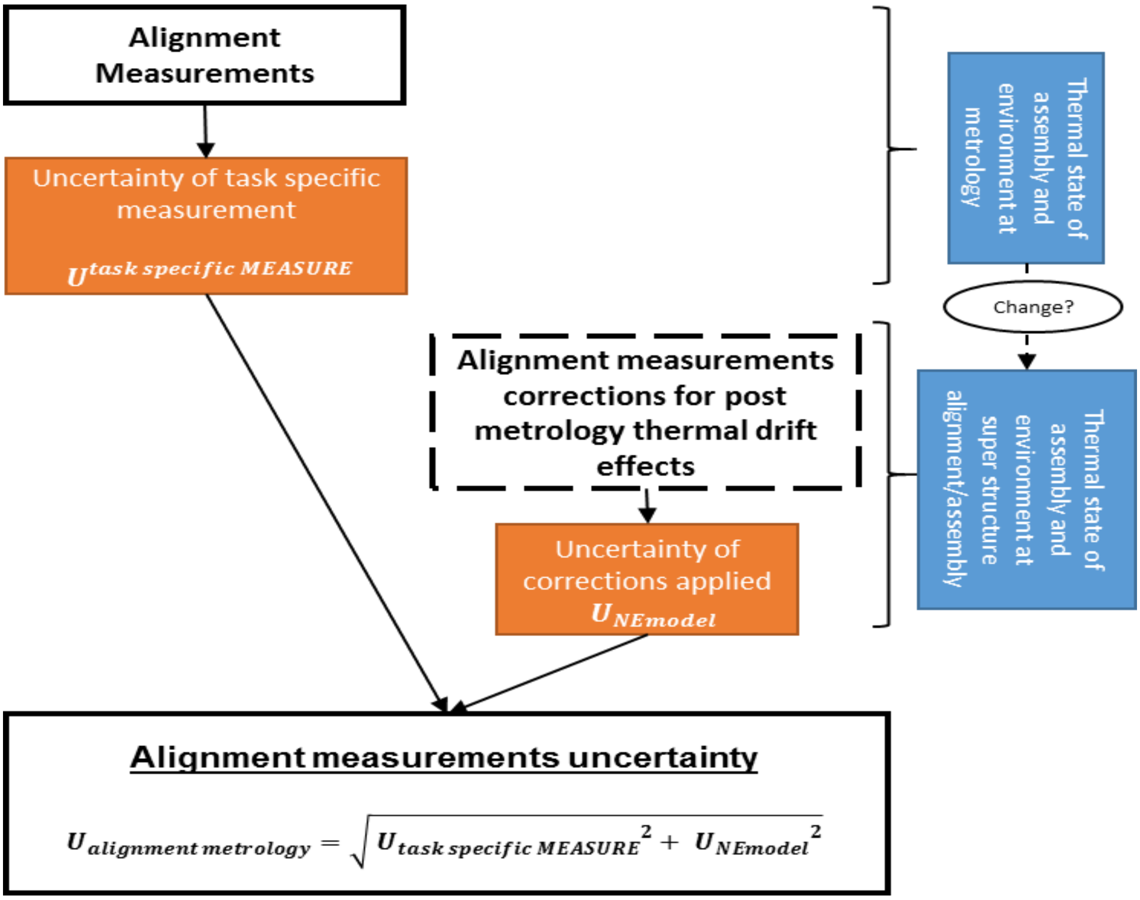


**Figure 33: Alignment measurement uncertainty evaluation general methodology**

The alignment measurements task-specific uncertainty ($U_{task\ specific\ MEASURE}$) was then evaluated in accordance to international standard GUM, Supplement 1 (BIPM, 2008). This was done by a mixture of reference thermal, dimensional measurements and probabilistic modelling software, at the environment of the metrology laboratory. They were used to estimate, variance and bias estimates of the measurements which combined defined ($U_{task\ specific\ MEASURE}$). Bias was defined as the difference between the probabilistic measurement model (PDF) mean and the conventional truth value set by the calibrated known artefacts dimensions, shape and location. The variance was defined as the one σ result of the probabilistic Monte Carlo models of the CMM measurements **Figure 34**.

Following metrology, the thermal assembly state was varied to match the expected thermal gradients during alignment procedures.

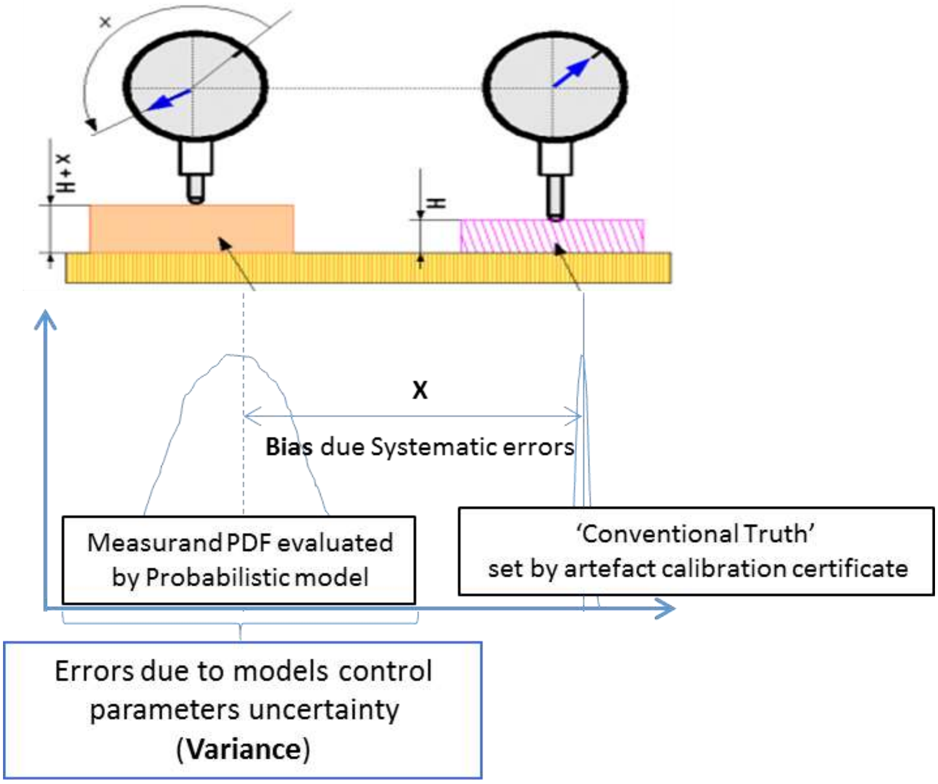


**Figure 34: Bias and Variance estimated by a mixture of probabilistic modelling and comparison to a known reference represented by an artefact**

Models using the measured thermal loads as input were applied to correct the alignment measurements bottom part of **Figure 33**. The uncertainty of the corrections ($U_{NE\ model}$) was evaluated in accordance to international standard GUM, Supplement 1 (BIPM, 2008). This was done by the use of probabilistic versions of the thermal compensation models establishing their variance. Reference measurements between the model's prediction and real assemblies measured deformation provided the bias of the thermal compensation models. Thus the real behaviour of an assembly deformation was taken as reference artefact of the truth **Figure 34.**

Key in both main steps of the method was to obtain traceability through the known standard representation of the truth **Figure 34**. The final alignment measurement uncertainty was quoted as the uncorrelated sum of the metrology task-specific uncertainty and the uncertainty of the thermal drift corrections applied **Eq.(4-1)**. They were later estimated following the same methodology as a function of both evaluated Variance (by probabilistic modelling) and Bias by reference measurements.

$$U_{alignment\ metrology} = \sqrt{U_{task\ specific\ MEASURE}{}^2 + U_{NEmodel.}{}^2} \tag{4-1}$$

and

$$U_{task\ specific\ MEASURE};\ U_{NEmodel.} = f(Bias, Variance) \tag{4-2}$$

In the two subchapters **4.2**, **4.3**, the methodology for the evaluation of $U_{task\ specific\ MEASURE}$ and $U_{NE\ model}$ is explained in detail.

## 4.2 Uncertainty of task-specific alignment measurements

Three principal error sources categories affect the alignment measurement uncertainties for the magnet assemblies. They are the uncertainties of the ***Magnetic Measurement System*** ($U_{magnetic\ measurment}$), the ***CMM*** ($U_{cmm\ specific}$) uncertainties and the ***Magnet Assembly*** ($U_{ass.\ stability}$) dimensional stability during measurement **Figure 35.** They were evaluated as uncorrelated and giving the final task specific measurement uncertainty ($U_{task\ specific\ MEASURE}$) as shown in **Eq.(4-3)**.

$$U_{task\ specific\ MEASURE} = \sqrt{U_{cmm\ specific}{}^2 + U_{ass.\ stability}{}^2 + U_{magnetic\ measurment}{}^2} \tag{4-3}$$

The ***Magnetic Measurement System*** uncertainty was given by the magnetic measurement metrologist expert of the team. There is no existing international standard for the definition of the magnetic axis. Thus it relied on the expert judgement of the magnetic measurement expert that qualified the uncertainty performance of the system.

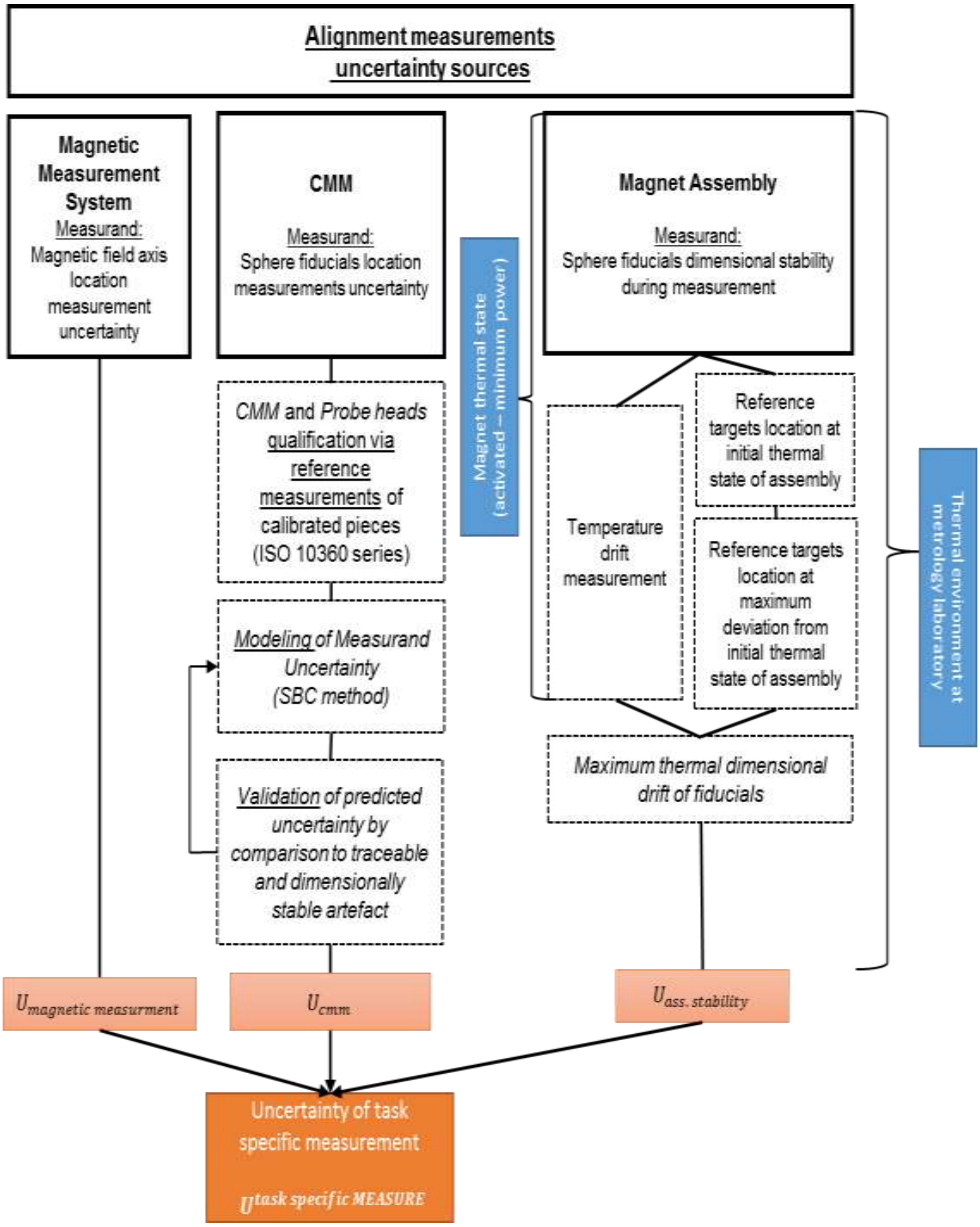


**Figure 35: Working method of evaluating task specific alignment measurement uncertainty for a large magnet assembly**

7The ***CMM*** task-specific uncertainty of the fiducials was evaluated by the application of probabilistic CMM modelling software. The first step was to perform standard tests such as the one suggested in ISO 10360 series. By those standard series, measurements of the CMM against the calibration of reference artefacts such as reference spheres and step, gauges were used. In this way, the repeatability, the form error of the probe heads, the maximum permissible errors, location and of the CMM's used was quantified. Using this data, a software based on the Simulation By Constraints (SBC) method was calibrated to model the CMM task-specific location measurement uncertainty. This model was validated against traceable to the meter (**2.1.2**) standard dimensionally stable tetrahedron artefact **Figure 36** (Trapet, 2015a).

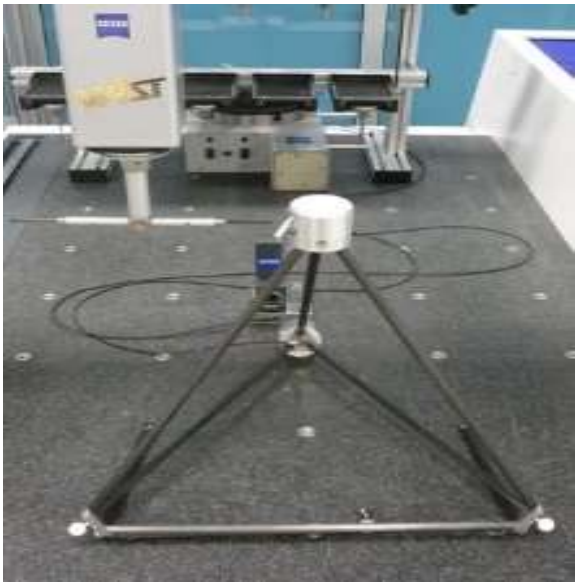

**Figure 36: Traceable tetrahedron Carbon-Fibre artefact** (Trapet, 2015a)

The artefact was calibrated by a metrology institute and part of an international inter-laboratory uncertainty study (Trapet, 2015a). By comparing the uncertainty regions predicted by the model and the real 3D location errors measured by the CMM, the uncertainty model was successfully validated (see - **6.1.1**) following (ISO/TS and ISO, 2008) suggested rule described in **5.2.3.** If validation was not successful, then the CMM model had to be revised for any misrepresented systematic errors.

***Magnet assembly*** dimensional stability was evaluated with the use of dimensional and thermal measurements. Thermal drift of the assembly was continuously monitored during the alignment measurement made. Main sources of error were the internal heat sources caused by ohmic heating of the resistive magnet coils. Reference targets were mounted stably on the CMM granite. Their location was measured with respect to the fiducials targets part the assembly. Initially at the start of the alignment measurements with the magnet being switched off. Then the magnet was switched on the minimal power required for magnetic measurement for this magnet (4 A), and the alignment measurements were performed. At the end of the alignment measurements, the location of the reference targets was measured again. The maximum 3D distance drift between the stable mounted on the CMM granite reference targets and the assembly fiducials was used to quantify the magnet assembly stability. Detail of the procedures applied can be seen in chapter **5.2.2**.

This sub methodology fullfiled objective one (see **3.2**) by following a set of defined tasks:

a. *Apply a probabilistic uncertainty modelling for the CMM coordinate measurements applicable for large industrial scale environment.*

   i. *Calibrate Simulation By Constraints based CMM uncertainty model following ISO 10360-(2,5,7-9)* ***2.2.2*** *standard tests and validate its uncertainty prediction with the use of reference measurements of traceable calibrated artefacts following ISO 15530-4* (ISO/TS and ISO, 2008) *standard.*

   ii. *Use the validated model to evaluate CLIC T1 assembly alignment measurements uncertainty*

   iii. *Extrapolate the model to assess the measurement uncertainty of the biggest CLIC T4 modules measured with CMM large enough to accommodate them.*

b. *Evaluate the thermal effects due to the low-powered magnet part of T1 assembly studied in the PACMAN project and to extrapolate results for T4 assembly family.*

## 4.3 Thermal drift compensation and associated uncertainty

Thermal drift compensation and related uncertainty were studied on both a single aluminium component and a more complex magnet assembly as shown in **Figure 37** and method diagram in **Figure 38**.

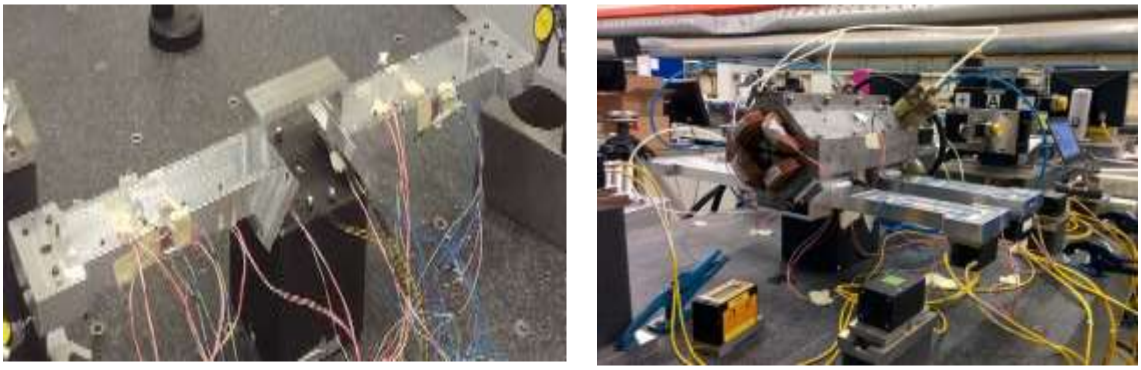

**Figure 37: Representative measurands studies. Left: Single component (beam part of magnet assembly). Right: Magnet assembly.**

They were considered as two representatives of possible alignment measurands. The single component is a more simple case of one object, one material. The Magnet assembly as a more complex case of multiple assembled and constrained objects. They were considered representative due to several features. First, their dimensions were chosen to be close to CLIC magnets metrology loop sizes being aligned and of the same material. Second, the magnet assembly had the sufficient multiple components complexity but of simplified geometry, allowing the proof of principle with minimised complexity and computational costs. Both were initially stabilised at the thermal state expected during metrology (See **Figure 38**).

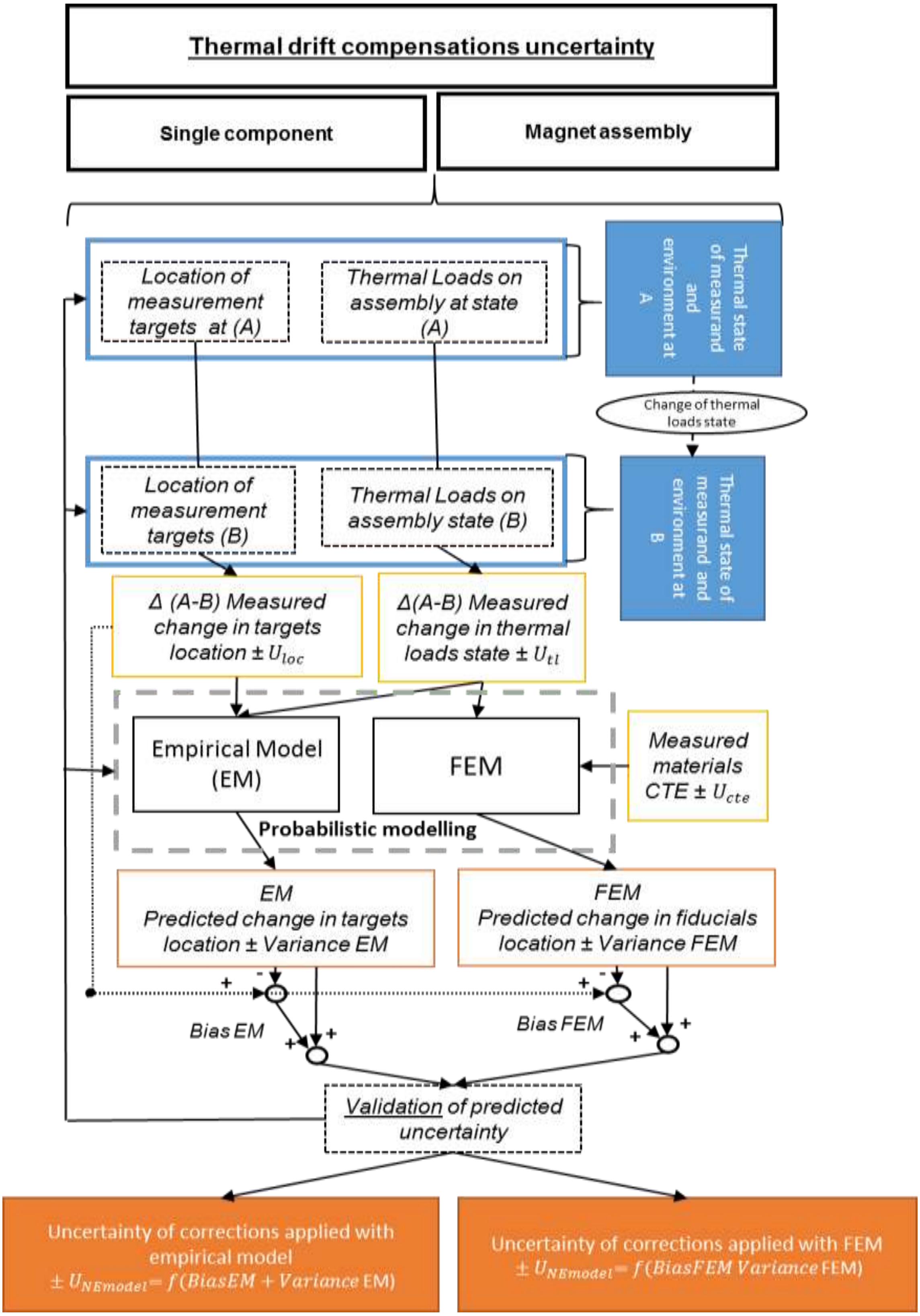


**Figure 38: Visual diagram summarising working method for evaluation of thermal drift and associated uncertainty after fiducialisation**

At this thermal state (A) the spatial location of the measurement targets (fiducials) and the thermal loads were measured. Following, a change in the thermal state of the measurands was introduced by a change in the thermal loads. The measurands were then stabilised at new thermal state (B). The difference in temperatures of the measurands between state (A) and (B) were at a maximum of 10°C to 15°C.

Once the measurands were stabilised at the new thermal state (B), both the spatial location of the fiducial targets and the new thermal loads were measured. The drift in the location of the targets and the drift in the thermal loads between (A) and (B) was estimated with quantification of the uncertainties of both ($U_{loc}$ - for the drift measurement and $U_{tl}$ – for the thermal loads drift measurement). Prior to the experiments, samples of the materials of the measurands were studied. Samples were taken from the exact material slab from which the single component and the components part of the magnet assemblies were machined. From those samples, the Coefficient of Thermal Expansion was estimated via dilatometry with an evaluated uncertainty of it is estimation ($U_{cte}$).

Following this experimental series, the change in targets location and change in thermal loads was used for the creation of Empirical Models (EM). The change of the thermal states and the evaluated CTE coefficients were used for the creation of FEM models. Probabilistic versions of both the EM and the FEM models were created. The Probability Density Functions (PDFs) quantifying the uncertainties in the evaluated input parameters were used as probabilistic models input ($U_{loc}$, $U_{tl}$ and $U_{cte}$). The output of the Probabilistic models was PDFs quantifying the most likely change in targets location. The mean of PDF was used as the most likely expected value. The PDFs one σ defined a *Variance* of the model as a function of the input parameter uncertainties.

The next step was to quantify the *Bias* of a model prediction. The real measured change in target location from the experiments was subtracted from the predicted mean value of the probabilistic models. The result was the bias or error difference between the actual measurand behaviour and the predicted one. The final predicted modelling uncertainty was taken as a sum of the *Bias*, *Variance* and uncertainty of the drift measurements.

The final step was to validate those predicted uncertainties. This was done by comparing a predicted targets drift with measured by independent means drift as suggested in (ISO/TS and ISO, 2008). The drift measured by independent means was found to lay within the predicted uncertainty region. If however, this would not have been the case then the Probabilistic models and calibration measurements would have had to be further studied and revised for unknown and unaccounted errors.

Finally, the uncertainty of the prediction model was quoted as a function of the evaluated *Bias* and the modelled *Variance* **Eq.(4-4).** Detail of this procedure can be seen in chapter **5.2**.

$$U_{NEmodel} = f(Bias + \ Variance) \qquad \textbf{(4-4)}$$

As a summary, according to this methodology, the alignment uncertainty was considered as the uncorrelated sum of the fiducialisation task-specific uncertainty and of the uncertainty related to the thermal drift compensation models applied following it. It is claimed that the probabilistic version of the measurement model or the thermal error compensation can be used for the evaluation of their variances. This can be combined with experimental evaluation of the probabilistic models bias errors. Further in the thesis in chapters **2.4** and **6** this methodology is tested by validating the predicted uncertainty regions to known references by independent measurement means (ISO/TS and ISO, 2008).

This sub methodology applied fullfiled objective two (**3.2**) by following a set of defined tasks:

a. *Create empirical models of the magnetic axis, and reference fiducials drift.*
    iv. *Evaluate/calibrate the most relevant parameters for the empirical models of assembly.*

v. *Assess and study the uncertainty of the empirical models via the Monte Carlo method and reference measurements of bias as a function of different measurement and setup/ conditions errors/uncertainties.*

vi. *Validate empirical models and their uncertainty prediction against validation measurements traceable to the meter international standard ISO 15530-4* (ISO/TS and ISO, 2008)*.*

b. *Create a Probabilistic FEM model for prediction of the fiducial target drift at various expected thermal conditions.*

vii. *Evaluate/calibrate the relevant input parameters and errors of the FEM prediction.*

viii. *Assess and study the uncertainty of the FEM models via probabilistic methods and reference measurements of bias as a function of different input parameters errors/uncertainties.*

ix. *Validate the probabilistic FEM prediction and its uncertainty statement against in a traceable to the meter manner. To do this by applying international metrology standard ISO 15530-4* (ISO/TS and ISO, 2008) *in the field of FEM analysis.*

# 5 EXPERIMENTAL EQUIPMENT AND PROCEDURES

In this chapter, the experimental equipment used is described in detail. The details on the procedures applied for the modelling and experiments performed are explained.

## 5.1 EXPERIMENTAL EQUIPMENT

### 5.1.1 CLIC T1 module

The CLIC T1 magnet module is representative of the shortest CLIC Main Beam Quadruple (MBQ) series (CLIC (Collaboration), 2012; Vorozhtsov and Modena, 2012) 0.42 m being the active length of focusing magnet yokes. Currently, at CERN, it is the only manufactured prototype of a complete CLIC magnet assembly module (**Figure 39**).

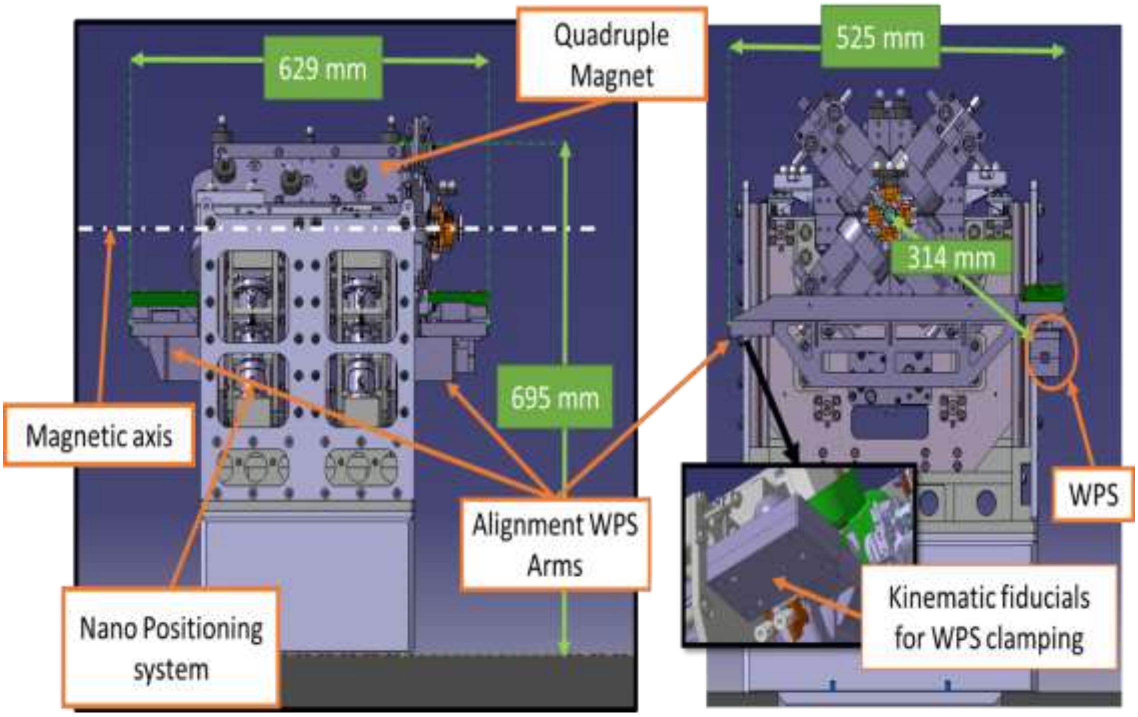


**Figure 39: CLIC T1 Module Left: Side view. Right: Front view**

It consists of an integrated resistive Quadruple magnet, a Nano-positioning system and an Alignment Wire Positioning System (WPS) ‘arms’. The Alignment WPS arms are aluminium structures that interface the MBQ magnet with the global reference system, which is a stretched carbon fibre wire (CLIC (Collaboration), 2012; Durand *et al.*, 2012; Mainaud Durand *et al.*, 2014; '*Wire Position Sensor*', 2017). At each end of the alignment WPS arms, there is a capacitive non-contact sensor mounted on three spheres kinematic bed (Mainaud Durand and T.Touze, 2006; '*Wire Position Sensor*', 2017). The system is further described in detail at **5.1.8**.

The alignment metrology for each quadrupole consists of knowing the location of the MBQ magnetic axis in the spatial reference frame created by the WPS kinematic spheres **Figure 40**.

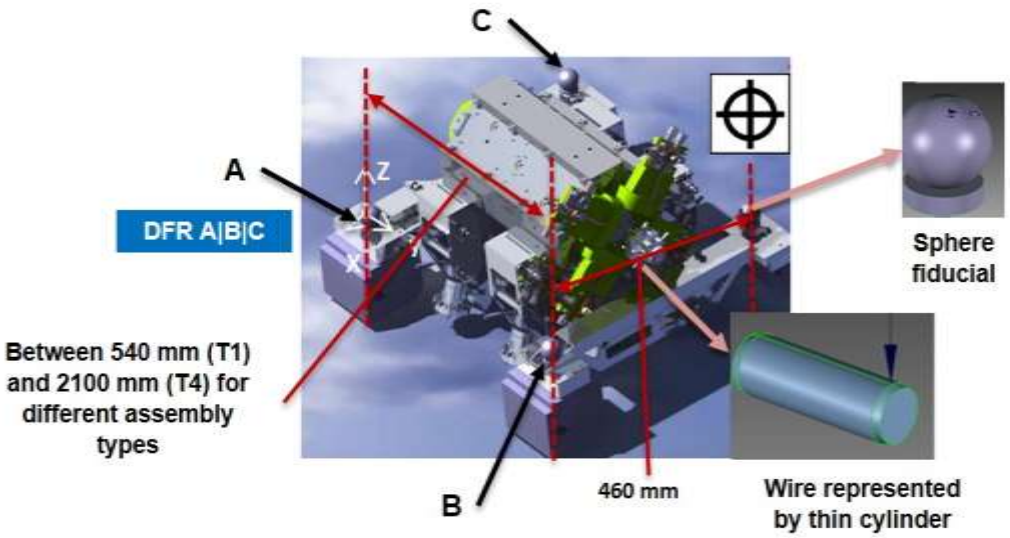


**Figure 40: MBQ T1 assembly alignment metrology GPS task**

The measurements task was defined in Geometric Product Specification (GPS) (ISO, 2011b, 2017) language as location tolerance. Uncertainty of each fiducial location was defined as a sphere tolerance zone. This tolerance zone was evaluated with respect to Dimensional Frame of Reference (DFR) defined by another three spheres, each used s location datum in 3D space. The uncertainty of a thin (100 μm) cylinder representing the magnetic measurement reference wire was defined as a cylindrical tolerance zone to the same three sphere DFR used for fiducial location uncertainty estimation

CLIC T1 assembly CAD and GPS task were used as input to CMM uncertainty modelling software (see **5.1.11**). The physical assembly itself was used in series of CMM measurements campaigns within Leitz Infinity CMM (see **5.1.7**). CMM and thermal measurements were used for the determination of the assembly thermal stability, and PACMAN integrated system repeatability **Figure 41** .

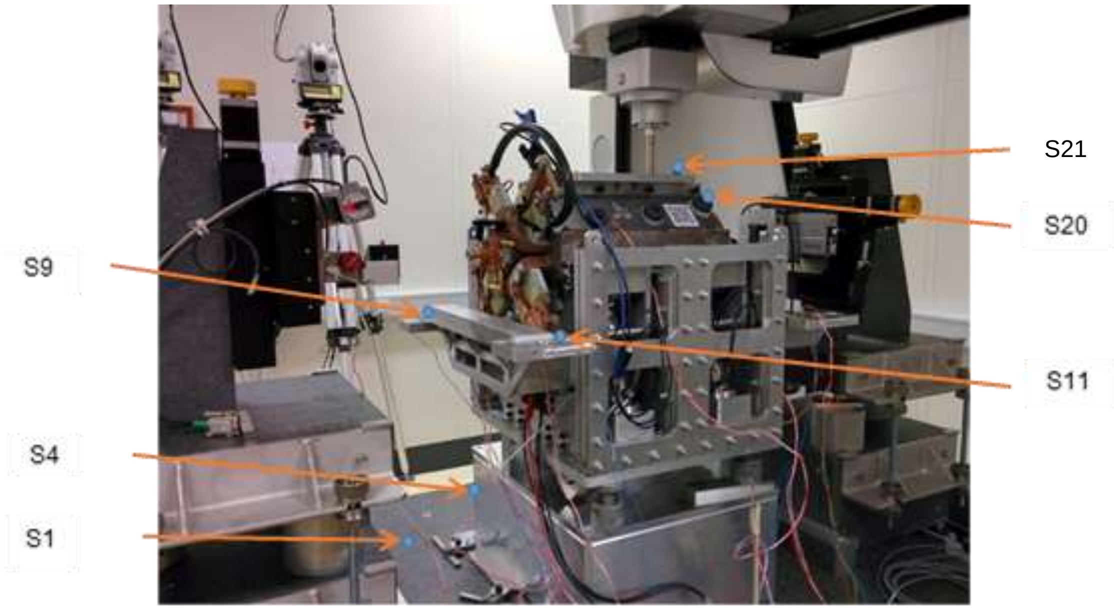


**Figure 41: CLIC T1 magnet assembly integrated within CMM**

Where S1 – S21 represent relative locations of spheres and thermal sensors (S1, S4 mounted on the granite; S9,S11 mounted on the alignment aluminium bridge component part of the assembly; S20,S21 mounted on the top of the steel magnet). In there, S1 to S4 spheres are mounted on the granite; S9 to S11 are mounted on the alignment aluminium bridge part of the assembly; S20 to S21 are mounted on the top of the steel magnet. Thermal sensors (including air front measurement sensors and assembly surface temperature) were mounted next to the installed fiducials.

### 5.1.1.1 CLIC T1 alignment measurement procedure

A full set of CMM alignment measurements on the assembly took a complete work day. After the initial measurement, the weekend was used to allow the system to stabilise. During the second measurement day, the magnet was switched on (**6.1.2**, **Figure 85 -** green line). A minimum required current (for axis measurement) of four amperes was selected by the magnet expert (D.Caiazza). No water cooling was provided to the magnet as water cooling is required only at high amperage operational rates (∼ 120 Amperes) due to Joule heating effect in the resistive coils. The second reason for not providing passive water cooling was that it could create a thermal gradient (between the coolant in the coils and the ambient air temperature) and act as a concentrated heat source within the assembly.

### 5.1.2 Tetrahedron artefact

The CMM Simulation By Constraints (SBC) uncertainty prediction model was validated against a calibrated artefact, as part of an international metrology inter-laboratory study (Trapet, 2015a). This study was supported by Entidad Nacional de Acreditación ENAC (Trapet, 2015a) and involved 19 metrology laboratories worldwide including CERN metrology laboratory. A traceable and dimensional stable tetrahedron artefact with calibration certificate was circulated among the international laboratories. This artefact has arms of 0.5 m length, made of carbon fibre with a CTE of 1 µm/m/K. Fiducial spheres are made to shape tolerance equivalent to grade 5 according to ISO-3290 sphericity precision with 0.127 µm maximum roundness error. The artefact calibration uncertainty of the distances was quoted as 0.7 µm at 2σ. A complete artefact survey was performed and

**Figure 42: Carbon fibre tetrahedron artefact used for CMM uncertainty model validation** (Trapet, 2017)

repeated three times using a Leitz Infinity CMM within the CERN Metrology laboratory. The exact measurement procedure can be seen detailed in (Trapet, 2015b).

### 5.1.3 Magnet assembly

CLIC T1 assembly was considered too complex and thus computationally expensive for the task of validating the methodology for thermal drift compensation prediction uncertainties. It consisted of numerous aluminium and steel components with complex interfaces. This could cause the presence of additional control variables (such as numerous interface heat transfer coefficients) and parameters that would not contribute to the process understanding and method validation. A simplified magnet assembly was designed, machined and assembled with the purpose of studying the thermal drift and the accuracy of compensation methodologies with a minimum amount of uncontrolled error sources. The assembly consisted of the original quadrupole magnet sub assembly with the addition of two aluminium alignment arms **Figure 43**.

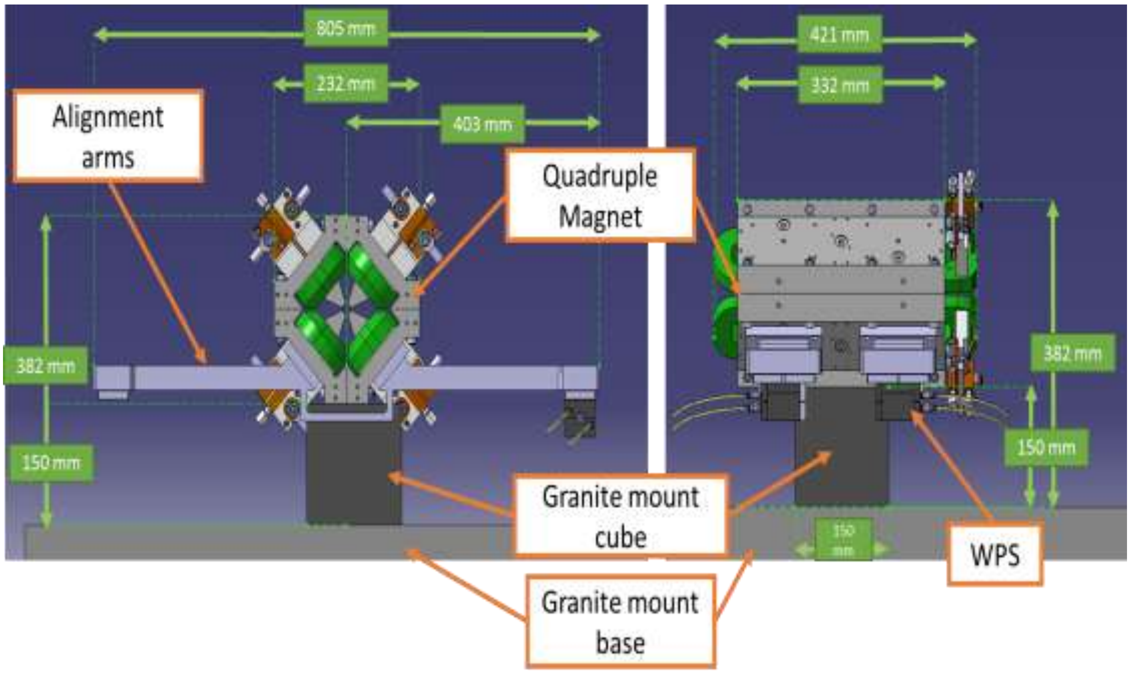


**Figure 43: Magnet assembly components Left: front view. Right: side view**

Their purpose was to mimic the function of the complex multi-component alignment arms present at CLIC T1 assembly. They were used as the alignment link between the magnet and the tunnel alignment reference being a carbon fibre stretched wire (Mainaud Durand and T.Touze, 2006). This was done by a kinematically assembled Wire Positioning System sensor (**5.1.8**) at the end of the alignment beam. The alignment arms were designed to bolt directly to the available on the magnet threads and with length equal to the total metrology loop (being the distance path of rigid bodies from the WPS sensor to the magnetic axis (**Figure 39**) present on CLIC T1. The magnet sub-assembly together with the alignment arms and their WPS sensors were mounted via Granite mount cube (6 high precision sides, 150 mm long (Microplan-gorup, 2017; Microplan-group, 2017)) to the Granite mount base of the CMM (**Figure 43**) .

The magnet assembly was studied both inside CERN accelerator tunnel laboratory (**Figure 44, a)**) and inside several different CMM systems (**5.1.7**) at CERN Metrology laboratory (**Figure 44, b)**). Thermal Load Sensors (TLS) were installed among and around the magnet assembly. Three sensors were installed on each of the assembly sub-components faces – side, top bottom. They consisted of local to installation point surface, thermal air probes and heat-flux sensor **5.1.5**. TLS were installed as well on the granite mount cube, granite mount base and water thermal control system Inlet and outlet **5.1.6**. As an alternative to the CMM measurement, a WPS system with stretched carbon fibre wire as a reference was integrated within the CMM. It was used as an alternative independent system that can measure the thermal drift in the micron level uncertainty as detailed in **5.1.8**. Reference precision spheres fiducials were

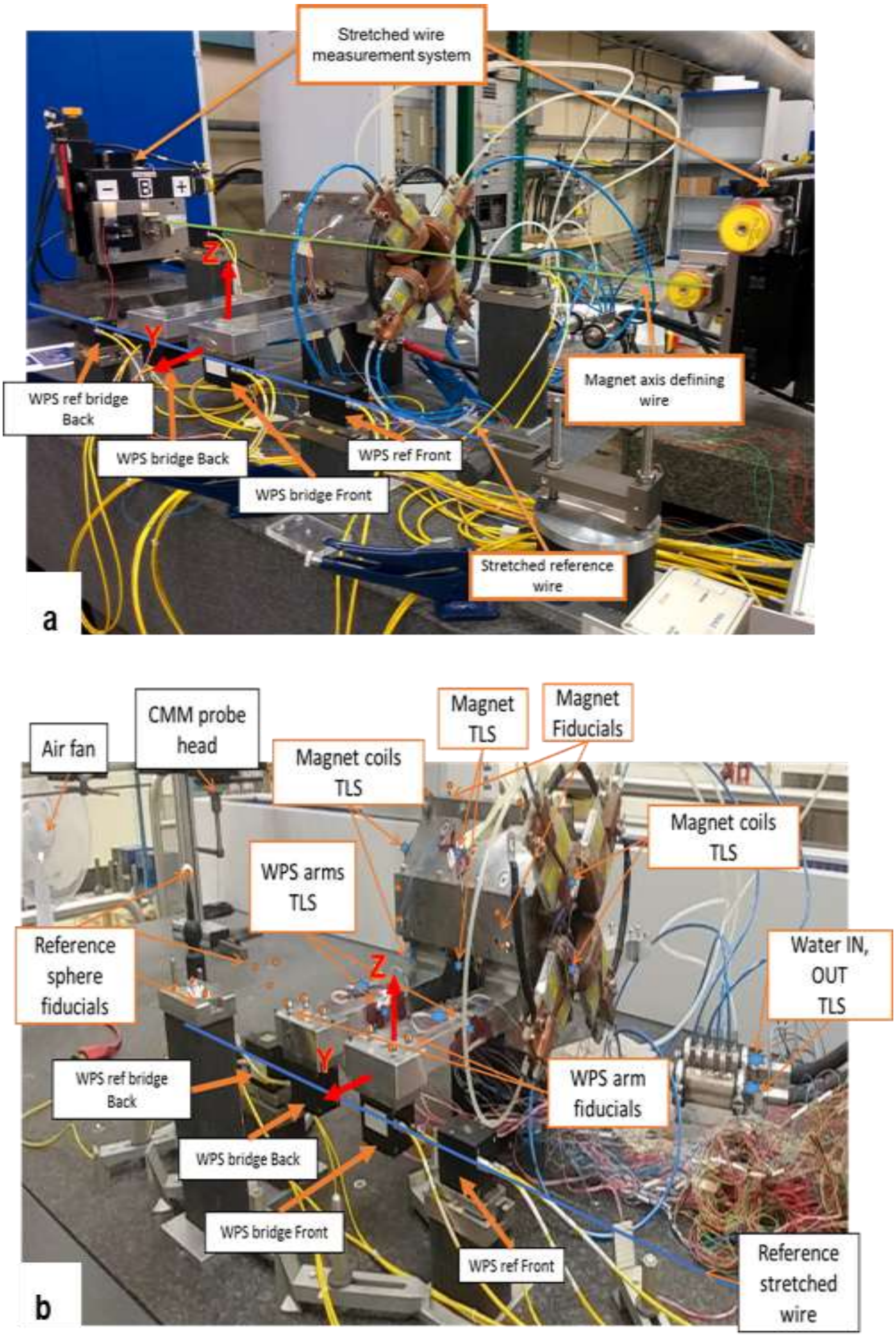


**Figure 44: a) Experimental setup for creating mapping model of WPS bridges drift inside accelerator tunnel laboratory b) Experimental setup validating WPS bridge thermal drift for simple magnet assembly in Zeiss Prismo CMM 5.1.7 at CERN Metrology laboratory 5.1.3**

permanently glued to the surface of the quadruple magnet, alignment arms, granite cube and granite mount base. Each sphere was measured and her centre defined by the CMM used for the drift evaluation. The spheres used were 6 mm diameter stainless steel ball bearings of Class 3 (ISO-3290) with a maximum out of roundness error of 1 µm. They were permanently glued compressing them toward the metal face with a thin layer of Araldite® epoxy glue with CTE of 0.09µm/mm/K (Huntsman, 2007).

Following the initial location measurements, the thermal loads on the assembly were varied via a combination of water chiller thermal control system **5.1.6** and air fan as shown in **Figure 44.** The temperature of the assembly was stabilised at various thermal gradients close to 10°C above and below the state at which the initial alignment measurements were taken. The new deformed location of the alignment arms and assembly was measured via WPS system within the tunnel laboratory and with the CMM and WPS systems within the metrology laboratory. The data from the tunnel experiment was used for the creation of Empirical (**5.2.5**), PFEM (**5.2.6**) and Meta-model based on PFEM (**5.2.7**). The experiments were then repeated within the metrology laboratory and models predictions were gain validated against the WPS and the independent CMM measurements.

### 5.1.4 Single component test bench

The thermal drift test performed for the magnet assembly in **5.1.3** were repeated for a 'single component'. This component was one of the disassembled alignment aluminium arms. This was done with the purpose of simplifying further the problem by reducing the possible variables and influencing factors due to the complexity of studying an assembly instead of single component. This set of experiment campaigns were done to see how results of modelling single component would vary in precision concerning the more complex magnet assembly.

The aluminium alignment arm was glued permanently with a thin layer of Araldite® epoxy (Huntsman, 2007) for the Granite mount cube. Resistive heaters were permanently glued to the inner mounting faces of the component by deposing thin drops of Araldite® at the four corners of each heater. High thermal conductivity silicon paste (Electrolube, 2013) was distributed among the heater faces to ensure minimal thermal gradient between the heater temperature and the aluminium component face temperature. Thermal Load Sensors (TLS) were installed on all component surface directions (Top, Front, Back, Bottom), resistive heaters, Granite cube bottom and Granite CMM base (see **Figure 45**).

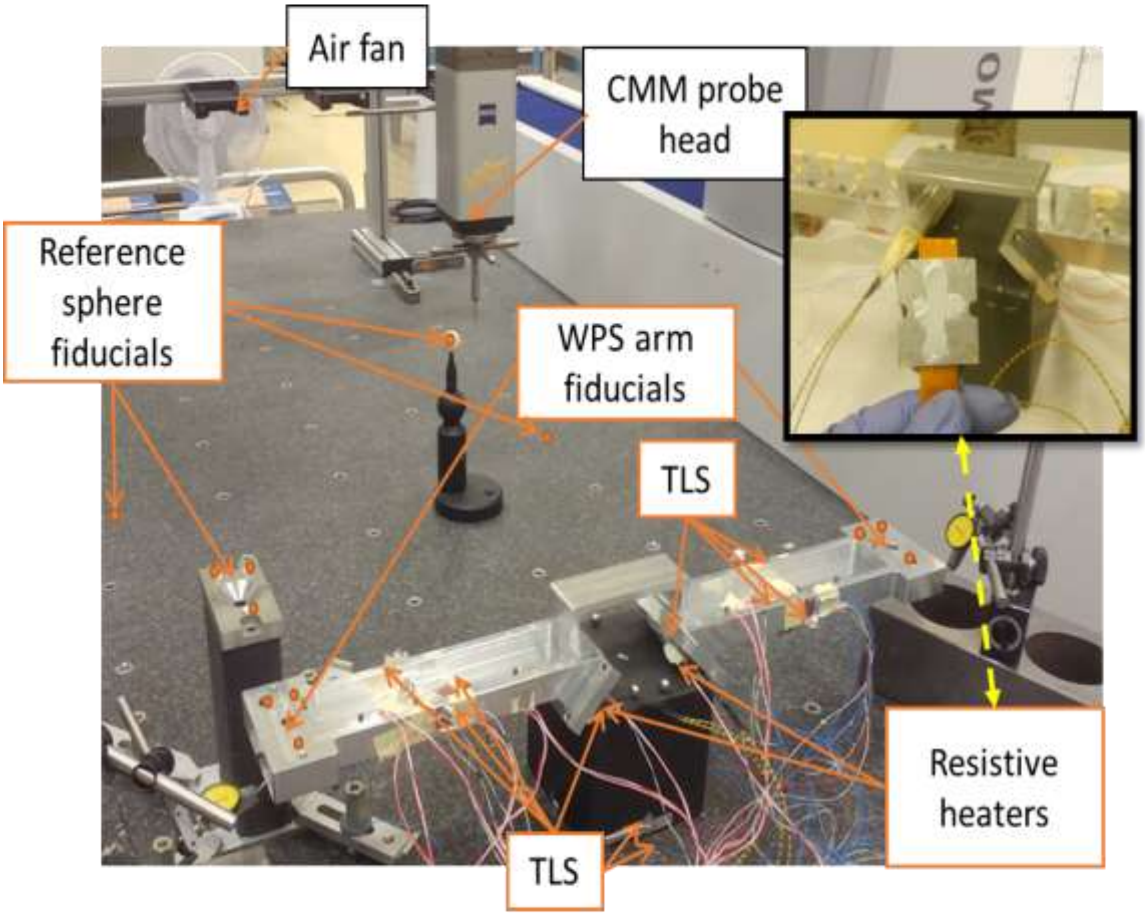


**Figure 45: Single component test bench**

## 5.1.5 Thermal loads measurements

Three types of thermal load measuring sensors were used: temperature, heat-flux and infra-red radiation camera measurements. In this subchapter, the sensors types, their calibration and uncertainty qualifications can be seen. In **5.2.4** one can further see the procedures and philosophy applied during the thermal load's measurement experiments.

### 5.1.5.1 Temperature measurements

Temperature sensors used for measurement and application material can be seen in **Figure 46**.

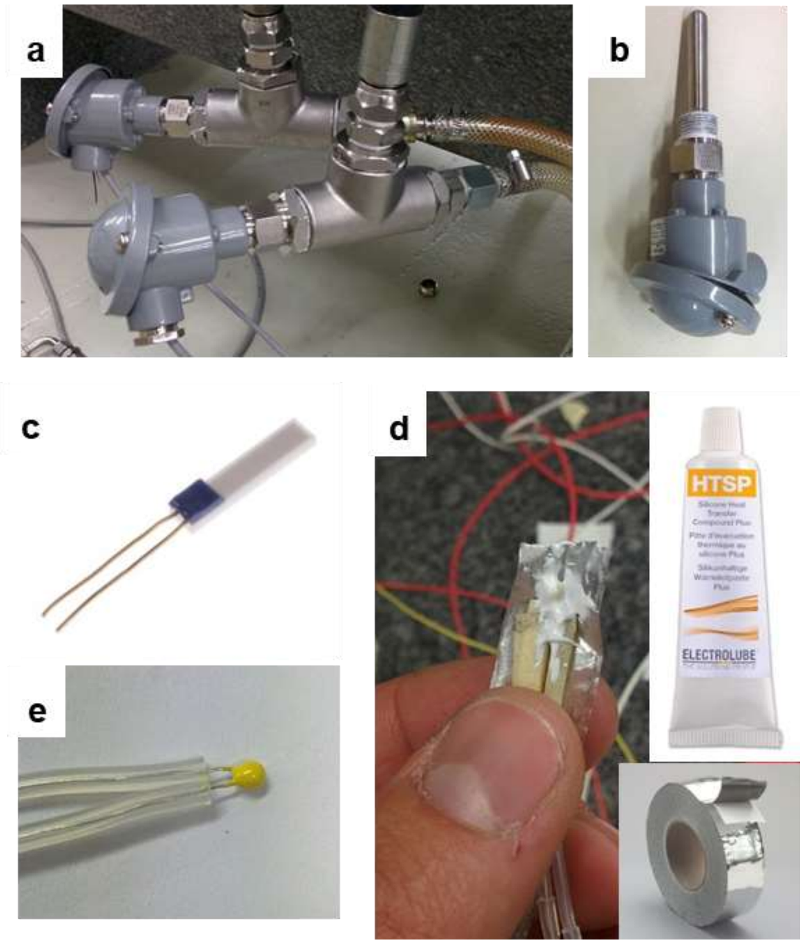


**Figure 46: a) T-junction for magnet coils water IN/OUT flow temperature sensors; b) Water flow thermometers Krone®** (KROHNE Group, 2017a, 2017b) **; c) PT-1000 temperature sensors** (Farnell, 2017; RS components, 2017) **;c) NTC-10K thermistors** (Digi Key Electronics, 2017)**; d) PT-100 and NTC-10K thermistors surface grounding** (Laird technologies, 2003; Electrolube, 2013)

The same figure a) and b) shows water flow thermometer by Krone® (KROHNE Group, 2017a, 2017b) that were installed in a hydraulic T-junction as part of the IN/OUT magnet cooling water flow. Description of the water chiller thermal control of the magnet can be seen in **5.1.6**. In **Figure 46 – c), e)** one can see the two types of thermal sensors used for the measurement of components surface temperature – Platinum Resistance Thermometers (PRT) (National Physical Laboratory, 2010; Farnell, 2017; RS components, 2017) and Negative Temperature Coefficient (NTC) thermistors (Ametherm Circuit Protection Thermistors, 2017; Digi Key Electronics, 2017). Those two types of thermal sensors based on different technologies were used to capture any possible bias error in measurements based on the measurement method. Those two type of thermal sensorial types were chosen as proven as most sensitive (0.3 % to 0.4 % $K^{-1}$ for RTD and NTC – with calibration), accurate ( ±0.01 K to ±0.2 K for PRT and ±0.005 °K for NTC - with calibration) and common in the field of precision engineering (Moffat, 1988; Childs, Greenwood and Long, 2000) and thermal measurement. The thermal sensors were covered by a layer of high thermal conductivity (2.0 W/m.K) silicon paste (Electrolube, 2013) which is frequently used in the microprocessor industry In **Figure 46 – d)**. This was done to ensure best thermal contact and minimum difference between the surface measured, and sensor used temperature. Heat shield aluminium foil with integrated adhesive (Laird technologies, 2003) was used to glue the thermal probes to the surfaces studied. This type of adhesive tape was used to make sure minimum influence (radiation, convection) from external heat sources to the thermal probeThe thermal probes were interfaced to Data Acquisition system (DAQ) **Figure 47, a)** via digital Multiplexer **Figure 47, b)** controlled via calibrated software **Figure 47, c)**

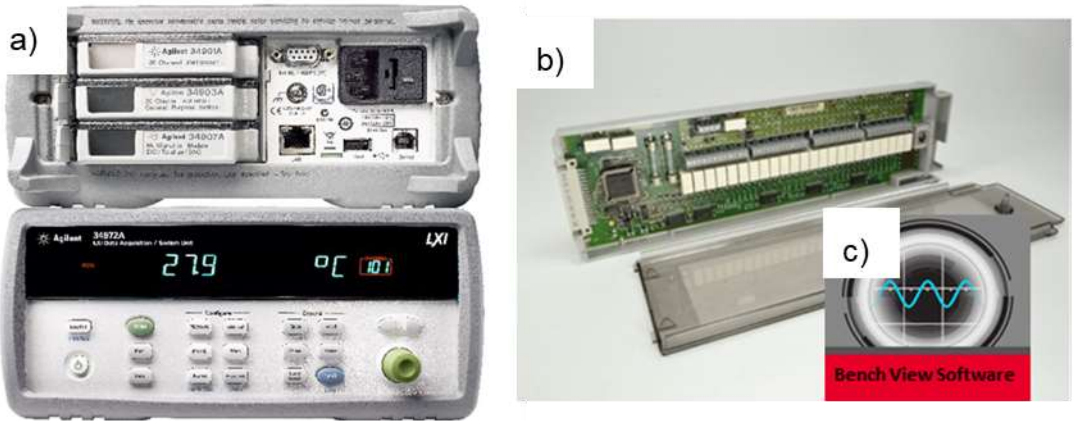


**Figure 47: a) Data acquisition system Agilent** (Keysight (formerly Agilent's Electronic Measurement), 2017b) **with b) multiplexer cards** (Keysight (formerly Agilent's Electronic Measurement), 2017a) **used for thermal sensors measurements via Agilent 'Bench View' software – c)** (Keysight, 2017)

Once received from the manufacturer, all the used sensors were tested in series of experimental campaigns within CERN metrology laboratory which has 20°C ± 0.5 °C stability over 24 hour period. This was done to evaluate their measurement performance as bought from the manufacturer without additional calibration. The various surface and air temperature probes were mounted on and next to large thermal soaked steel piece (High thermal inertia). Continuous temperature measurements were performed over several nights **Figure 49**. In **Figure 48** the results over 8-hour measurement camping for PRT and NTC sensors are shown. There is an obvious systematic shift between the two types of sensors.

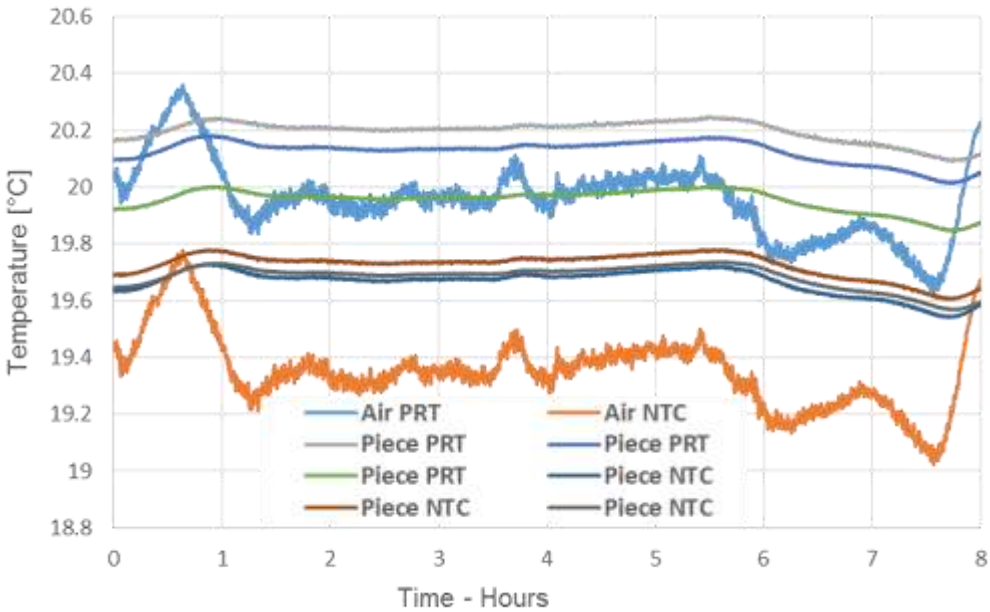


**Figure 48: Variation of temperature measurements of the same object and air by different NTC and PT-1000 sensors before calibration at NPL**

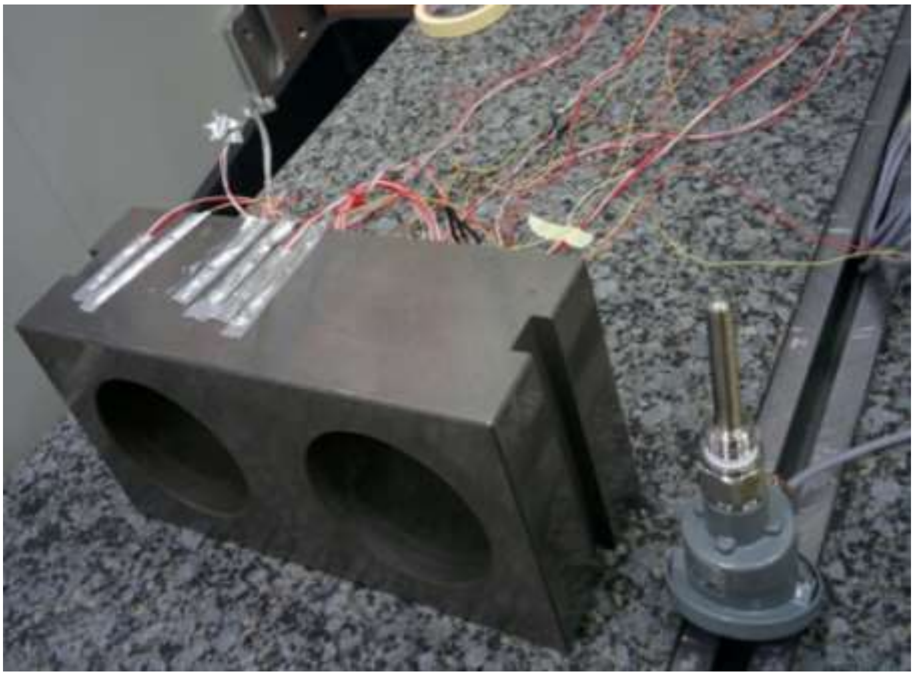

**Figure 49: Different thermal sensors performance variation tested overnight in CERN metrology laboratory**

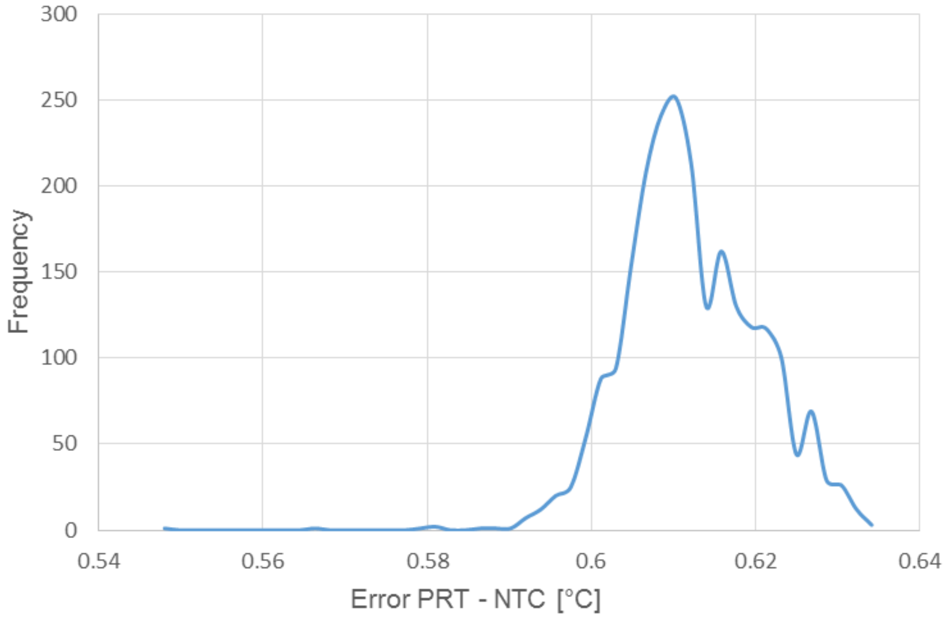


**Figure 50: Histogram of difference between NTC and PT-100 sensors measurements of air before calibration at NPL**

In **Figure 50** one can see the measured error between PRT and NTC factory calibrated sensors shown in a frequency plot. Mean error is 0.61°C with a standard deviation around the mean error of 0.008 °C.

Following this initial campaign, all the thermal sensors and DAQ system were sent to the National Physics Laboratory (NPL), UK. There first, an initial calibration of the probe was performed with respect to the triple point of water reference as defined in International temperature scale standard of 1990 (ITS-90) (BIPM, 1997, 2015) (see – Appendix **9.2A.7**). Consequently, a complete temperature system uncertainty analysis was performed at NPL to estimate the total system temperature measurement uncertainty with respect to (ITS-90) calibrated equipment (see – Appendix **9.2A.8**). The largest bias errors of the calibrated sensors with the Agilent DAQ was used as the side of a square shape uncertainty for the determination of the thermal measurement uncertainty in the later studies **Table 3** on next page.

**Table 3: NPL Uncertainty quantification after calibration for NTC and PRT sensors used**

| **DAQ + Sensor Type** | **Uncertainty (1 σ – Square shape)** [°C] |
|---|---|
| PRT | 0.031; a = 0.054 |
| NTC | 0.027; a = 0.047 |

Following the calibration at NPL, the correction factors were added to all thermal measurements **Figure 51**.

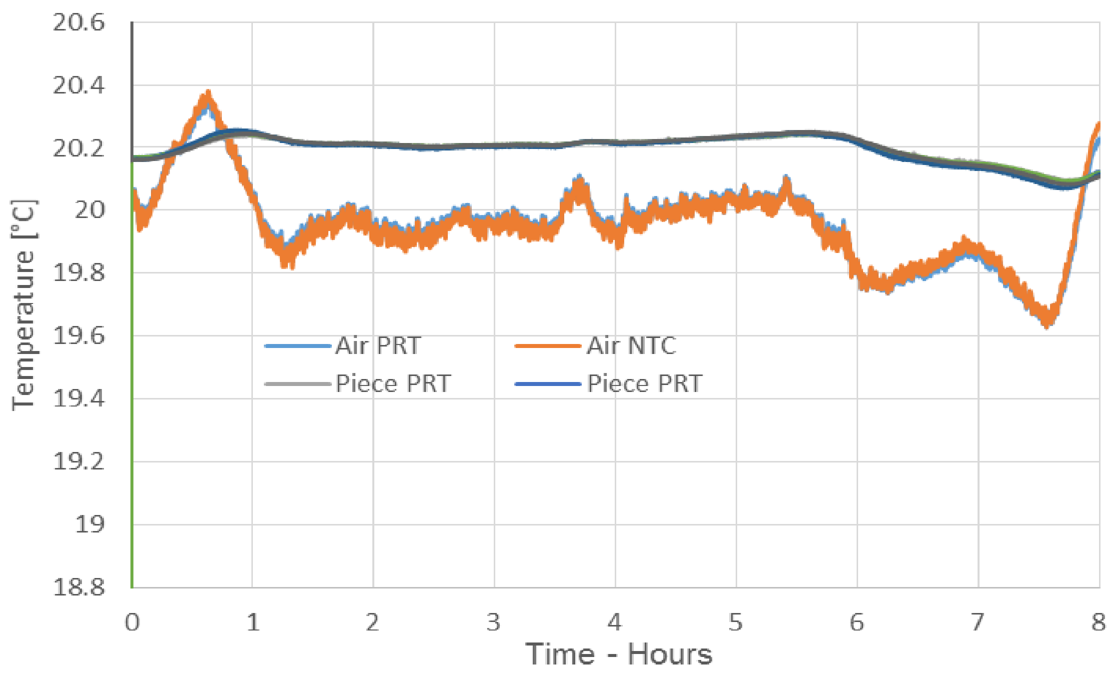


**Figure 51: Variation of temperature measurements of the same object and air by different NTC and PT-1000 sensors after calibration at NPL**

#### 5.1.5.2 Heat-flux measurements

Heat flux measurements were performed in combination with thermal measurements for the help of determining heat flow and thus convection coefficients through surfaces. The procedure is explained further in **5.2.4**. The heat flux sensors used was based on integrated circuit technology can be seen best described in (Thery and Raucoules, 2006) **Figure 52**.

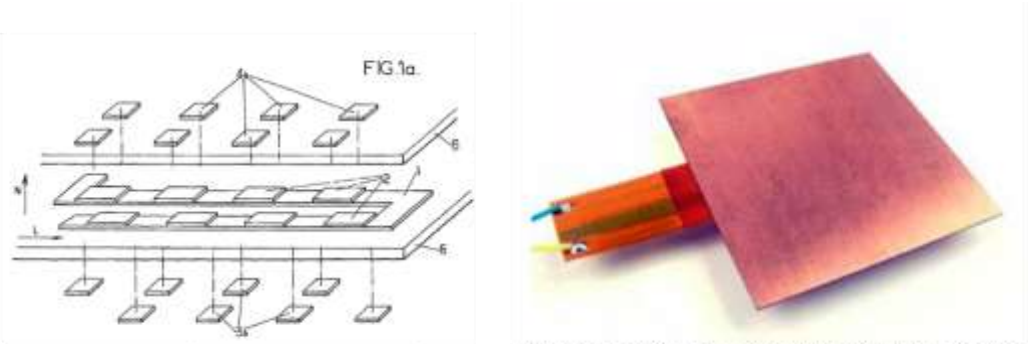


1 = constantan metal strip 2 = Copper pads on constantan strip 3a, 4a = Copper pads 5, 6 = Kapton film

**Figure 52: Thin integrated circuit heat flux sensor** (Thery and Raucoules, 2006)**.**

They use two arrays of thermocouples: One measuring heat flux entering the sensor from one surface and one measuring the exit heat flux at the opposite surface. The difference is the heat flux passing through the sensor. It is claimed (Thery and Raucoules, 2006) that such arrangement eliminates temperature dependency of the sensor to detect heat flux. The voltage output produced is directly proportional to the heat flux, is linear, and passes exactly through zero. Voltage polarity determines heat flux direction. The calibration procedure gives the slope and offset of each sensor voltage to heat-flux linear transfer function. The sensors were purchased from external supplier (Thery and Raucoules, 2006) which claimed ‘accuracy concerning confidential internal test procedures’ to ± 3 %. ISO Standards and methods for the calibration and uncertainty sensors of such type of sensors do exist (Tsai *et al.*, 2004; ISO, 2010) however no confirmation or certificate was received from the manufacturer. The heat-flux sensors were not sent to a national institute for traceable uncertainty statement and calibration. Their uncertainty analysis was based on a combination of the quoted performance from the manufacturer and internal tests at CERN metrology laboratory. Test of the sensor to sensor variance of readings was performed as the one done for the thermal probes. The heat flux sensors were all thermally insulated from each other and positioned in a stack within a closed box with a precision calibrated thermal sensor at CERN thermally controlled laboratory 20°C ± 0.5 °C.

The thermal isolation and the closed box were used to stabilise the air current and the influence of radiative and convective external heat inputs. All sensors were expected to experiencing minimal and similar to each other heat flux at these conditions if calibrated by the manufacturer. In **Figure 53** seven hours of test data of both heat-flux sensors and a thermal probe available within the text box.

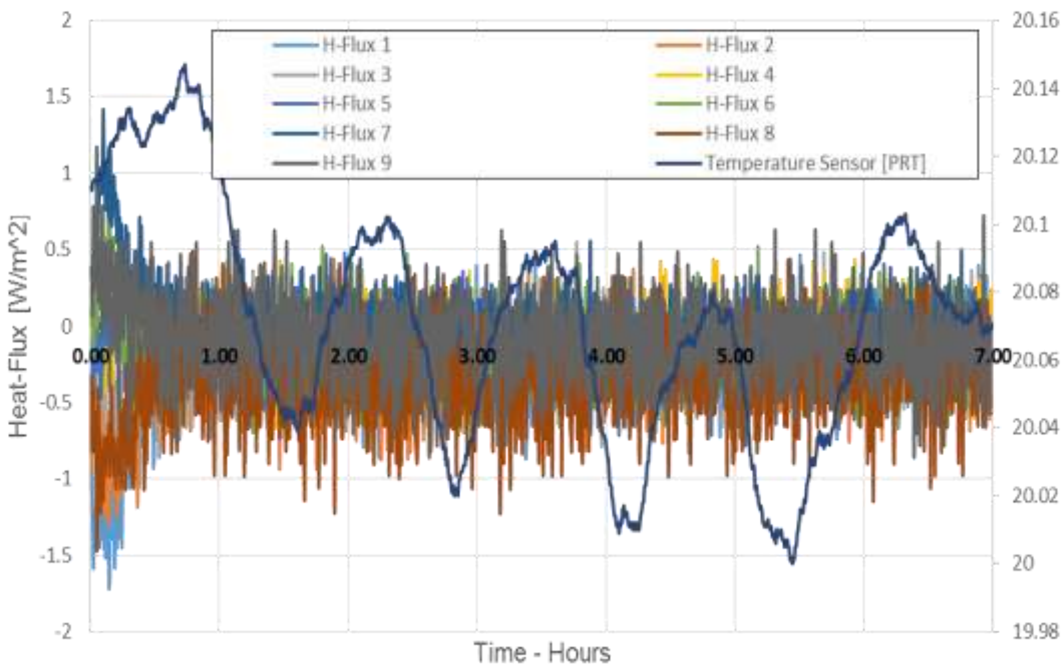


**Figure 53: Heat-Flux and temperature readings for overnight measurements at test box inside CERN metrology laboratory**

At the current arrangement with minimum heat transfer between the sensors, an assumption is made that the measured heat-flux would be zero with a signal function to the electronics White Noise signature. The measured within the test box temperature (In **Figure 53**) can be seen following the room thermal controller sinusoidal behaviour. The heat-flux sensors as expected can be seen uninfluenced by the air temperature variation (due to the thermal isolation applied). All sensors stabilise to similar steady-state noise signature close to zero. The noise signature was used as a quantification of the sensors uncertainty as for the area 2a of square distribution **Table 4**.

**Table 4: Uncertainty of heat-flux sensors**

| DAQ + Heat Flux sensor | Uncertainty (1 σ – Square shape) $[\frac{w}{m^2}]$ |
|---|---|
| Thin integrated circuit design (Thery and Raucoules, 2006) | 0.59; a = 1.025 |

The heat flux sensors were later installed on each of the components studied. One sensor was mounted in the middle of each component surface face **Figure 54**.

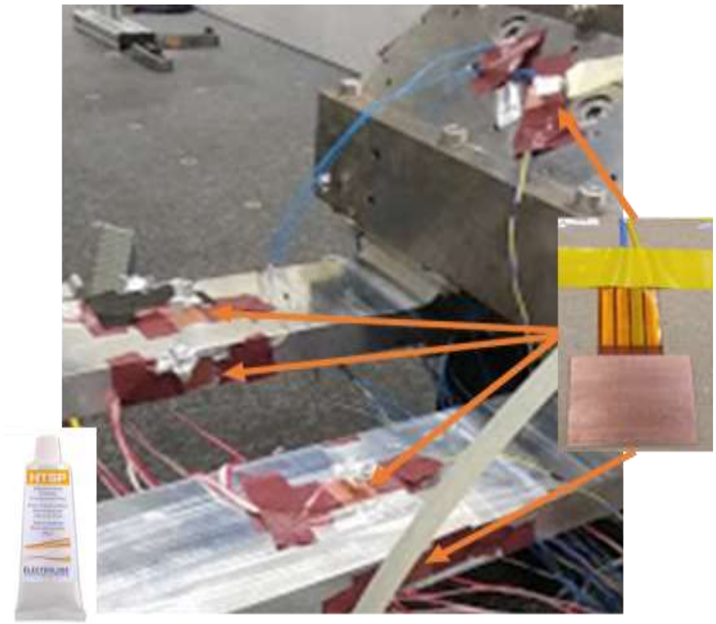

**Figure 54: Heat flux sensor installation**

Each sensor was installed with the use of a thin layer of thermally conductive paste (Electrolube, 2013). The opposite side was left to air exposure. Next, to each heat flux sensor, there was precision surface temperature probe and precision air measurement thermal probe installed. The combination of heat flux and thermal sensors was used to evaluate the convection coefficients for each of the assembly faces. Further procedure details can be seen in **5.2.4**.

### 5.1.5.3 Thermal radiation measurements

Thermal heat radiation was included in the FEM models as a possible heat load. Thus it was important to ensure correct emissivity coefficients were used for the materials studied. For this purpose, literature was reviewed, and simple experiment were performed. Thermal camera (FLIR, 2013) was used to make an experimental estimate (FLIR, 2015; Keysight, 2015) of the emissivity of the assembly aluminium and steel components. Black marker (Scotch® black Vinyl electrical tape Ɛ = 0.96 (Scotch, 2017)) of known emissivity and temperature sensors underneath was used to calibrate the emissivity of the infrared camera **Figure 55**.

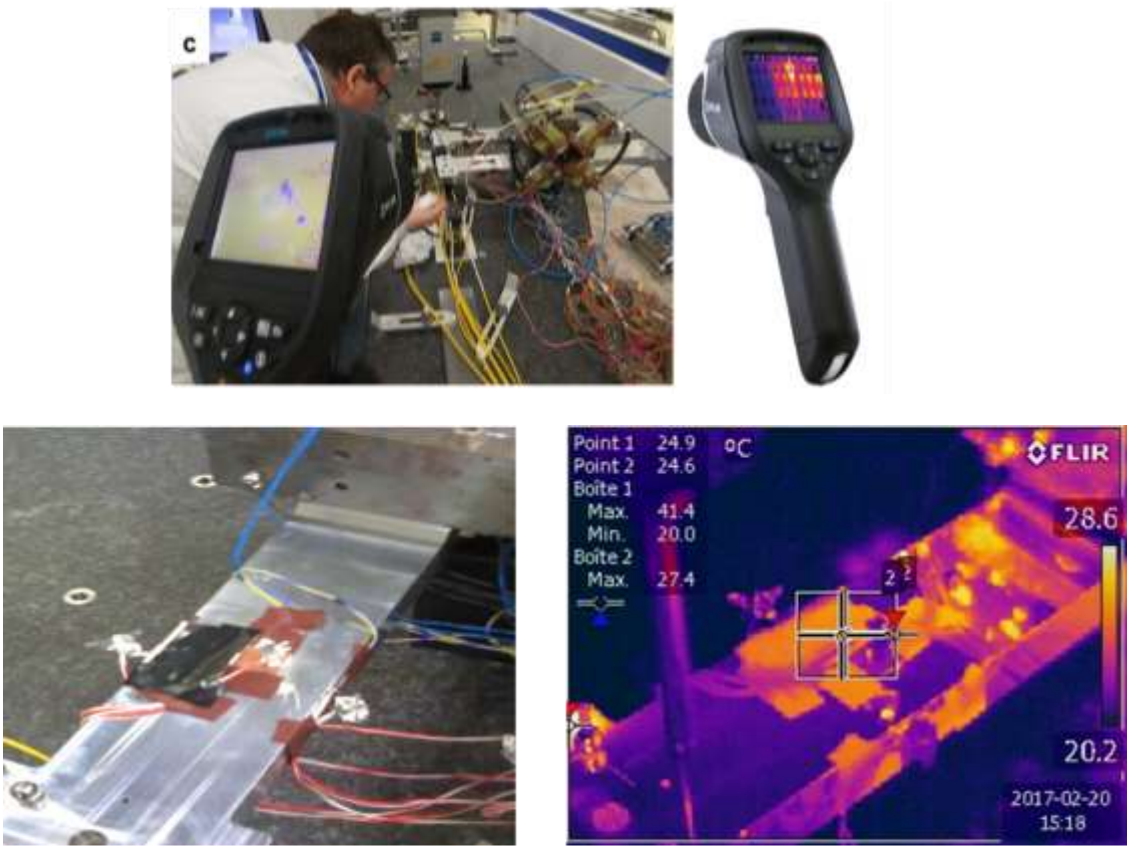


**Figure 55: Dark marker emissivity evaluation experiment** (Tsai *et al.*, 2004; ISO, 2010; FLIR, 2015)

The emissivity of the infrared camera was manually corrected until the shown temperature of the shining material surface matched the known temperature (of the black marker with thermal probe underneath). The measured values matched results seen in emissivity tables for the materials. Uncertainty was set as the range of the largest and smallest emissivity recorded, and it can be seen in **Table 5**.

**Table 5: Mean emissivity coefficient and associated uncertainty estimated**

| **Material** | **Mean Emissivity coefficient Ɛ** | **Uncertainty (1 σ – Square shape)** |
|---|---|---|
| Steel AFNOR XC 10 (Magnet Yoke) | 0.275 | 0.078; a = 0.135 |
| Aluminium 6082 (WPS alignment arms) | 0.172 | 0.070; a = 0.122 |

### 5.1.6 Thermal loads control

Both the single component and magnet assembly campaigns required thermal controls for setting steady state thermal states with internal gradients different than 20°C. The MBQ magnet has hollow magnet coils which are available for water cooling during operation (Vorozhtsov and Modena, 2012). Thermal gradients within magnet assemblies arise due to the differential heat load of the magnet coils (caused by the water flow temperature inside them), mounting link to the base (acting as a heat bridge) and surrounding environment convection. Controlling the water flow temperature within magnet coils and forcing convection coefficients to rise with surrounding air reproduces extreme case thermal load changes. Those will be experienced if alignment metrology is performed at room 20 °C temperature and used for alignment at nominal operational CLIC tunnel

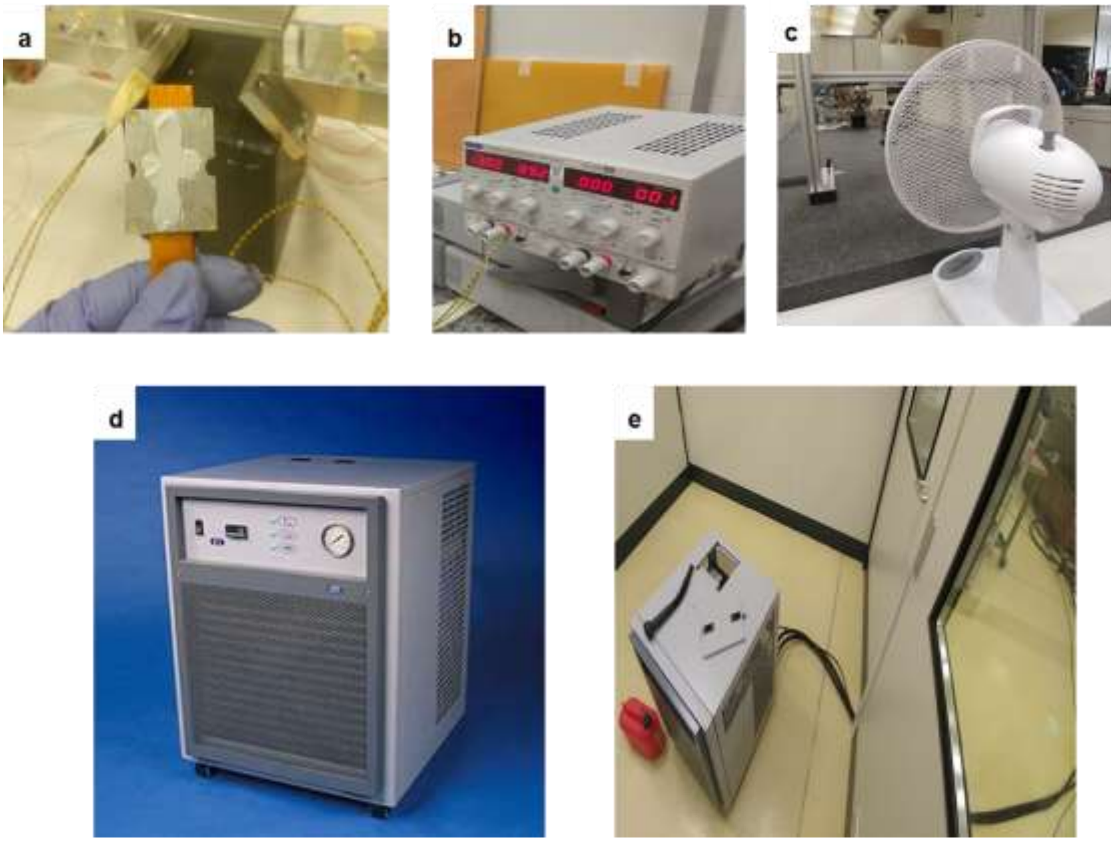


**Figure 56: a) Resistive heater (HP05** (Farnell, 2017)**) for single piece experiments; b) Power Supply for heaters (PL303 QMD-P** (TTi, 2017a, 2017b)**); c) Electric fan; d) Water chiller (ATC 3K** (ATC, 2017a, 2017b)**); e) K3 chiller installed in separate room in CMM laboratory**

conditions (CLIC CDR, page 675 (CLIC (Collaboration), 2012)). For the ‘magnet assembly’, this was done via ATC K3 water chiller thermal unit system (ATC, 2017a, 2017b) and air fan **Figure 56 c),d),e)**. The ATC K3 unit had 3.2 kW of cooling capacity and capability of varying outlet temperature between + 4 °C up to + 35 °C with the stability of ± 0.1 °C (ATC, 2017a). In this campaign the water control unit was positioned in the separate isolated room thus not influencing the air environment within the CMM laboratory **Figure 56, e).** The air temperature was controlled by the metrology air conditioning unit with a set desired temperature of 20 °C. The unit has a specification of controlling the outlet air temperature to ± 0.5°C. For the ‘single piece’ **Figure 45**, main thermal load change was due to heat conduction loads set at the mounting faces used for MBQ interface and forced air convection. This was done via resistive thermal heaters powered by Power Supply Unit (PSU) unit **Figure 56 a),b)**. They were bonded via small of Araldite® (Huntsman, 2007) epoxy by the heater four corners (**Figure 56 a)**) to the single pieces MBQ mounts faces. High conductivity heat transfer silicon paste (Electrolube, 2013) was used to equalise the heater surface temperature to its mounting base surface temperature.

### 5.1.7 CMM systems

Two CMM systems were used for the results obtained in this thesis: Leitz INFINITY and Zeiss PRISMO **Figure 57**; their standard test performance can be seen in **Table 7**.

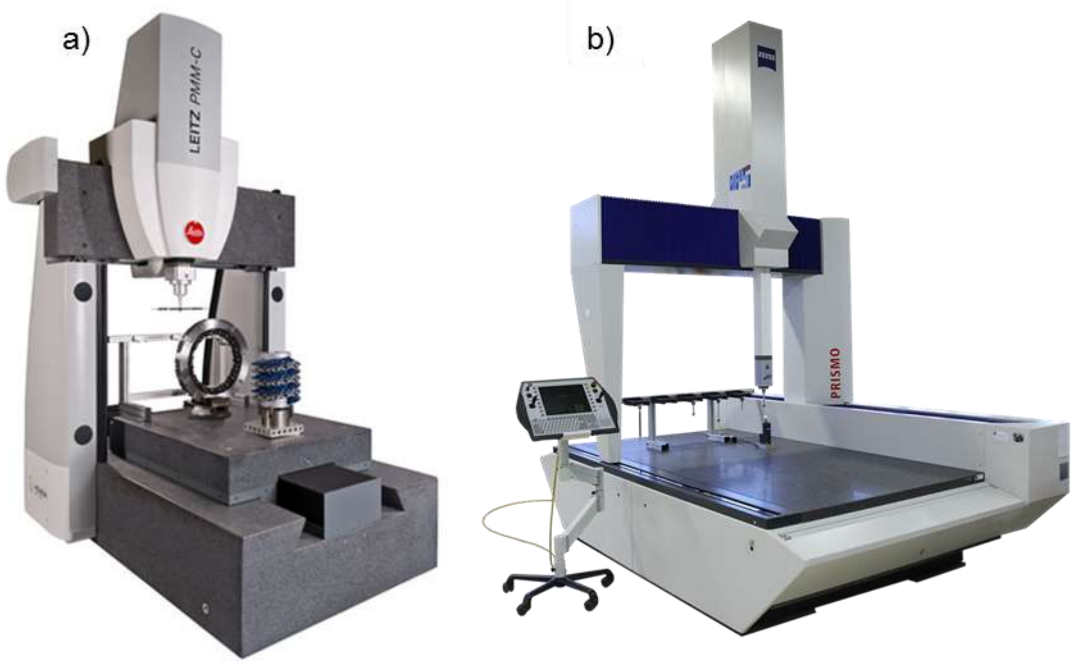


**Figure 57: CMMs used in studies: a) Leitz INFINITY**(HexagonAB, 2017)**; b) Zeiss PRISMO** (Carl Zeiss AG, 2017)

The Leitz INFINITY was used for the alignment measurement of CLIC T1 module and further for its thermal drift evaluations. It was also used for the measurements of the tetrahedron artefact (see **5.1.2**)**,** and thus the CMM Uncertainty model was validated on it. The Zeiss PRISMO CMM was used for the thermal drift studies of the Simple Component **5.1.4** and Magnet Assembly **5.1.3.**

First, the uncertainty of defining the location of the furthest fiducial in the assembly Dimensional Reference Frame (DRF) was studied. Then, the final alignment measurement uncertainty of the magnetic axis, which included magnetic measurement, non-contact measurement of the wire and tactile measurement of the sphere fiducials, was carried out. A commercially available software PUNDITCMM™ (METROSAGE, 2009), which implements the Simulation By Constraints (SBC) method, was calibrated from measurements and used (Phillips *et al.*, 1997; Summerhays *et al.*, 2004) as detailed procedures subchapter in **5.2.1**. The evaluated shape errors of the targets measured (spheres and stretched wire) is summarised in **Table 6**.

**Table 6: Evaluated shape errors of measurement targets for determination of $\mathbf{U_{sh}}$ contributor to the task specific uncertainty**

| | **Best Measured** [μm] | **Worst Measured** [μm] | **Sphericity** [μm] |
|---|---|---|---|
| **Fiducials used (PACMAN experiment)** | N/A | N/A | 1 |
| **100 μm diameter CuBe stretched wire** | 1.76 | 2.93 | N/A |

The data concerning the Leitz Infinity CMM (HexagonAB, 2017) was taken from the verification standard tests performed by the manufacturer on site during the yearly checks. The ISO test were performed with Zerodour artefact with CTE =0.1 μm/m/K ± 0.05 μm/m/K. Thus for the Class 1 room environment the $U_{tu}$ was estimated to be less than 0.02 μm.

The data for the Zeiss PRISMO CMM was taken from the manufacturers' quoted performance of their Zeiss PRISMO ULTRA 16/30/10 (capable of taking up to 3 meter long objects in its measurement volume) (Carl Zeiss AG, 2017). It is expected that on-site measurements after calibrations can show better results than those quoted by the manufacturer. This is the case as the one quoted by the manufacturer usually refers to worst-case scenario based on their experiments of multiple CMM systems. The performance of a particular CMM can be better (due to the better controlled environment or lower to the machine geometrical errors). Thus the quoted data for the Zeiss PRISMO can be considered as conservative. The non-contact measurement probe head was estimated internally at CERN's metrology lab. Its repeatability measurement was performed by measuring the wire surface in two small areas and fitting a circle on these results. It was used as a repeatability measurement of the non-contact sensor, equivalent to MPEml results of the tactile sensors. The MPS/MPE is the maximum offset error between measurement of the centre of a sphere with non-contact and tactile sensors defined as $L_{\mathrm{Dia.nx25::MPS}}$ in ISO 10360 – 9 (ISO, 2013a).

**Table 7: CMM and probe heads used for uncertainty study based on ISO 10360-5 and ISO 10360-9 qualification and specification(room environment - Class 1 +/- 0.1)**

| | Leitz Infinity | Zeiss PRISMO |
|---|---|---|
| **MPEE [µm]** | 0.3+L/1000 | 1.9+L/400 |
| **MPEml [µm]** | 0.62 | 1.7 |
| **MPEms [µm]** | 0.13 | 1.1 |
| **MPEmf [µm]** | 1.02 | 2.3 |
| **Non-Contact wire probe head repeatability on cylinder location [µm]** | 0.7 | 0.7 |
| **Non-Contact wire probe head MPS/ MPE [µm]** | 3 | 3 |
| **Largest distance sphere to sphere [m]** | 0.63 | 2.1 |
| **Stylus length [m]** | 0.08 | 0.08 |

Where:

**MPEE** = Maximum Permissible Size Error**; MPEml** = Largest range of centre coordinates for the 5 25-point spheres fit; **MPEms** = Deviation of the 125-point sphere fit diameter from calibrated diameter; **MPEmf** = Range of residuals of the 125-point sphere fit; **MPS/ MPE** = maximum permissible multiple probing system location errors for 5 25 point sphere fit

### 5.1.8 Wire positioning system

The Wire Positioning System (WPS) sensor was developed for CERN alignment applications. It is 2 D capacitive based precision sensor (**Figure 58**, **Left**).

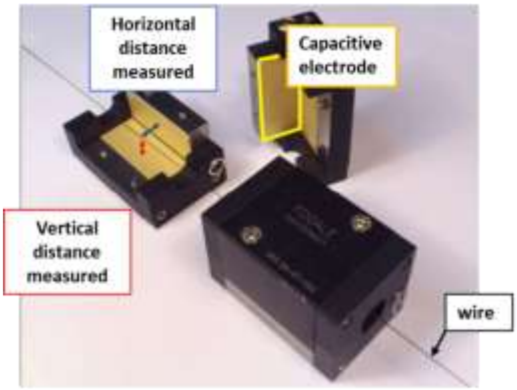


**Figure 58 Left: the WPS capacitive sensor, Right: Kinematic base on which it can be precisely mounted** (PERRIER, 2015)**.**

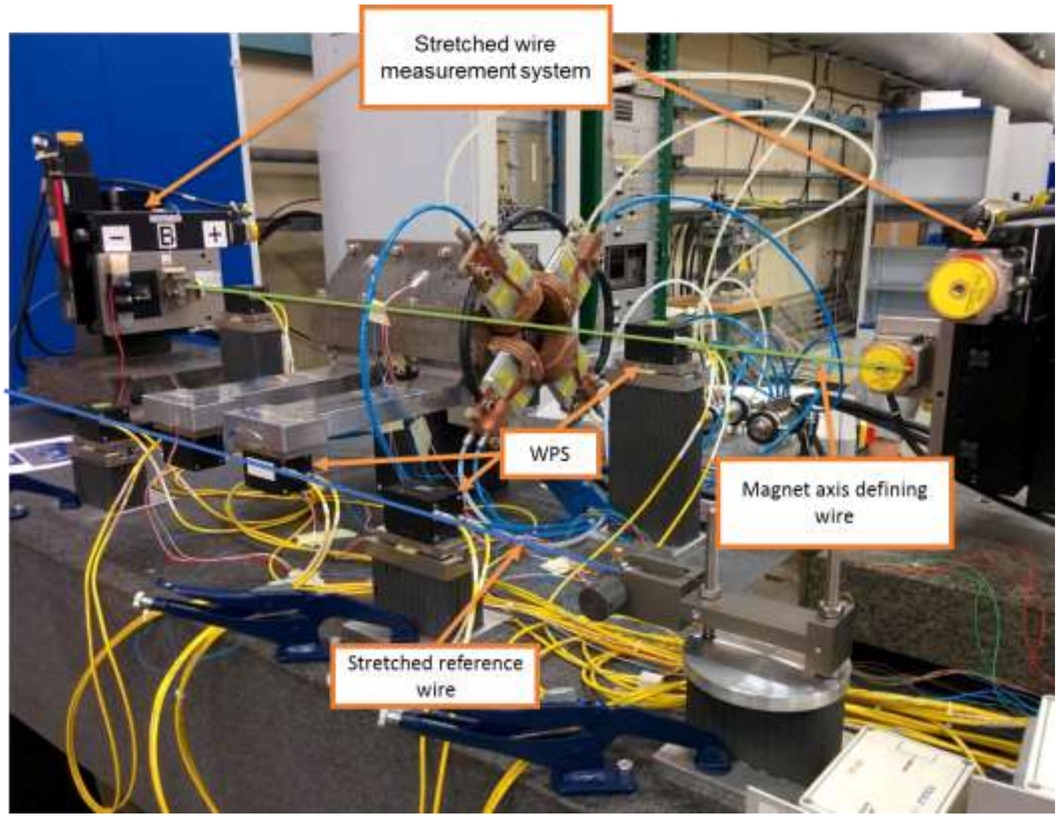


**Figure 59: WPS system setup as used for stretched wires drift and location measurement**

It is assembled around thin steadily stretched carbon fibre wire. The capacitor sensors produce a voltage proportional to the exact distance in X and Y. The system can be seen as best described in:(Herty, 2004; CLIC (Collaboration), 2012; Durand *et al.*, 2012; PERRIER, 2015; '*Wire Position Sensor*', 2017).

This system was installed on the magnet assembly as seen in **Figure 59** was used to measure the drift of the WPS alignment arm with respect to stable stretched wire reference. To ensure that the reference is stable, further WPS sensors were mounted directly on the Granite base to monitor the stretched wire stability during measurement. The mounting bases were manufactured by carbon fibre towers (for maximum thermal stability) with aluminium kinematic clamps as seen in **Figure 58-right**.

The WPS sensors were as well installed on higher towers to monitor the location of a stretched wire magnetic measurement system used for the definition of the magnetic axis **5.1.9**. The WPS sensors uncertainty is estimated in-house as the uncorrelated sum of $U_{WPS}$, $U_{wire}$ **Eq.(5-1)** on next page.

$$U_{WPSsys} = \sqrt{{U_{WPS}}^2+{U_{wire}}^2} \tag{5-1}$$

Where $U_{WPS}$ is the uncertainty of the WPS sensor traceable calibration performed at CERN **Figure 60**. The $U_{wire}$ is the uncertainty due to the wires (magnetic measurement and reference stretched wire) stability's used as reference for the drift experiments. $U_{wire}$ was evaluated experimentally by separate drift experiments **Figure 62**, **Figure 61** where the largest measured drift of the wires location was used as the 2a of square shaped uncertainty.

The stability of the WPS systems used for the wire drift determination was as well estimated using the measured CTE coefficients (of Aluminium and Carbon fibre) for the supporting towers and added to the $U_{wire}$ (**Table 8**) as the uncorrelated uncertainty of the reference wire dimensional drift $U_{wire\ drift}$ and the Carbon fibre WPS supports dimensional stability used for the evaluation $U_{towers}$ **Eq.(5-2)** on next page.

$$U_{wire} = \sqrt{U_{towers}{}^2 + U_{wire\ drift}{}^2} \qquad \textbf{(5-2)}$$

**Table 8: Uncertainties of WPS system**

| | $U_{WPS}$ | $U_{wire}$ (magnetic axis wire) See Figure 61 | $U_{wire}$ (alignment reference wire) *See Figure 62* | $U_{WPSsys}$ (magnetic axis wire) | $U_{WPSsys}$ (alignment reference wire) |
|---|---|---|---|---|---|
| **Uncertainty [µm] 1 σ – Square shape** | 0.29; a=0.5 | 0.64; a=1.1 | 1.15; a=2 | 0.70; a=1.21 | 1.18; a=2.04 |

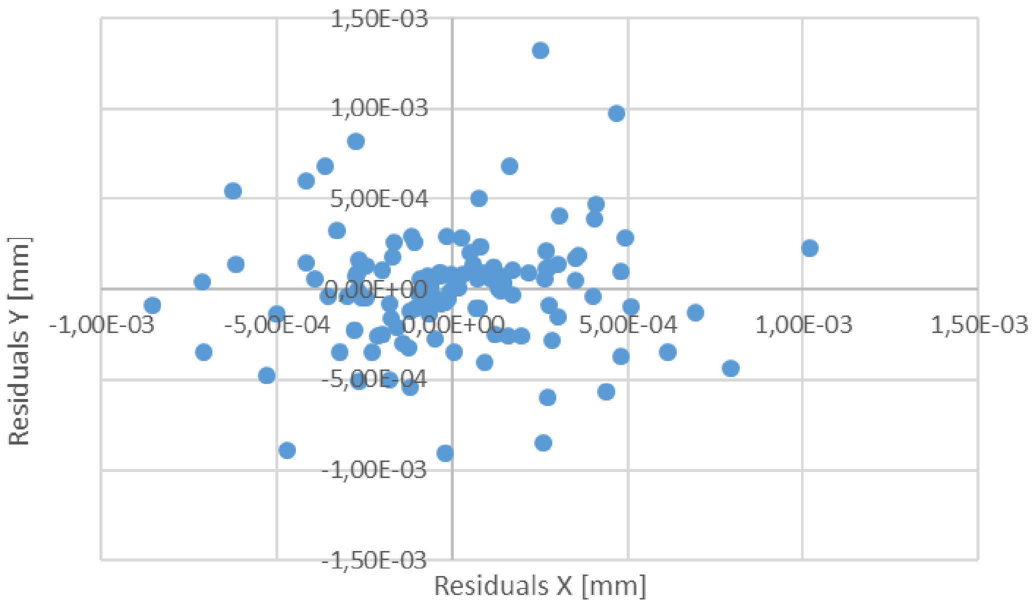


**Figure 60: Residuals of WPS sensor at calibration**

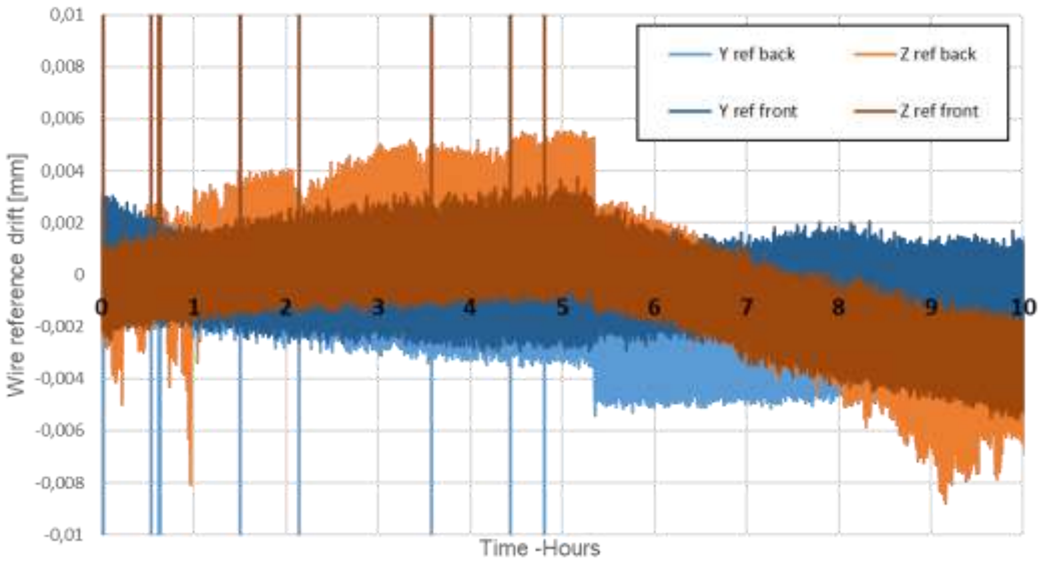


**Figure 62: Stability of alignment in tunnel reference stretched wire and carbon fibre towers at magnetic measurement laboratory (ISR8 – CERN)**

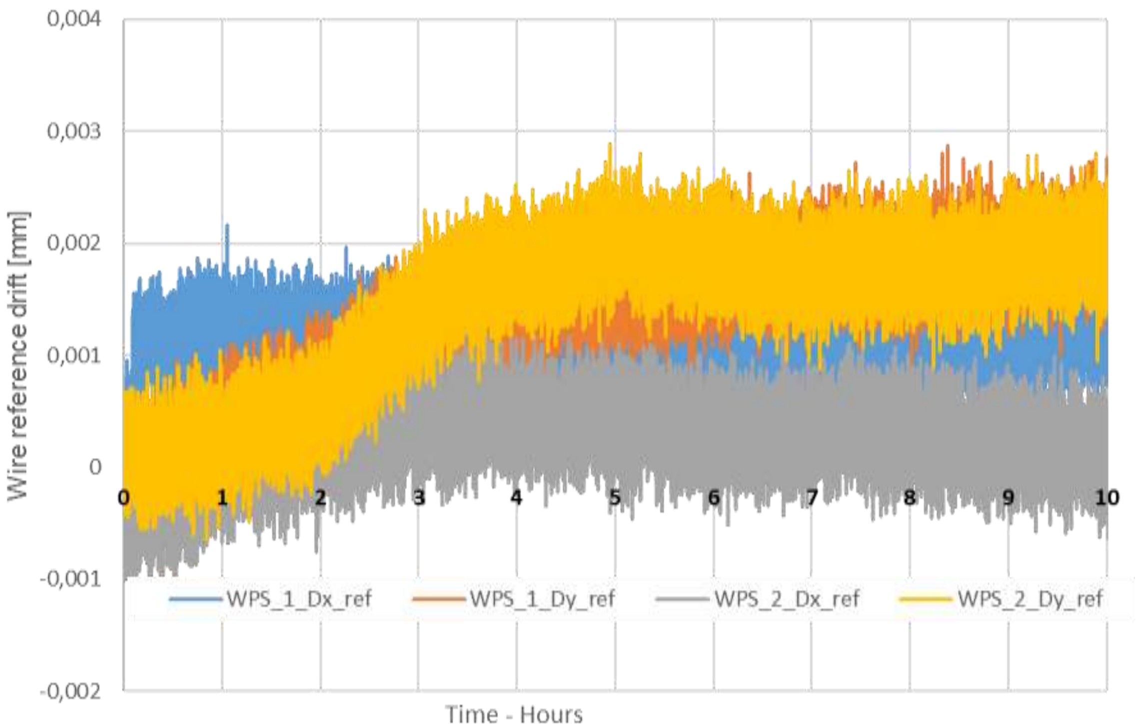


**Figure 61: Stability of magnetic measurement axis defying stretched wire and carbon fibre towers at magnetic measurement laboratory (ISR8 – CERN)**

### 5.1.9 Magnetic measurement system

A magnetic measurement system (Arpaia *et al.*, 2015; Caiazza, 2015) developed as part of US collaboration for the test of the LHC quadrupoles and dipoles magnets. It was Designed and built at Fermilab (Fermilab, 2017) by Joe DiMarco (DiMarco, Krzywinski and Fermilab MTF, 1996; DiMarco *et al.*, 2000). The system was re-designed to utilise the vibrating wire method (Petrone, 2013; Arpaia *et al.*, 2015; Severino and Caiazza, 2017) by a PACMAN team member D.Caiazza. Following those two methods, the system best fits thin conductive wire with the to the magnetic axis of a magnet with the help of high-precision linear stages **Figure 63**.

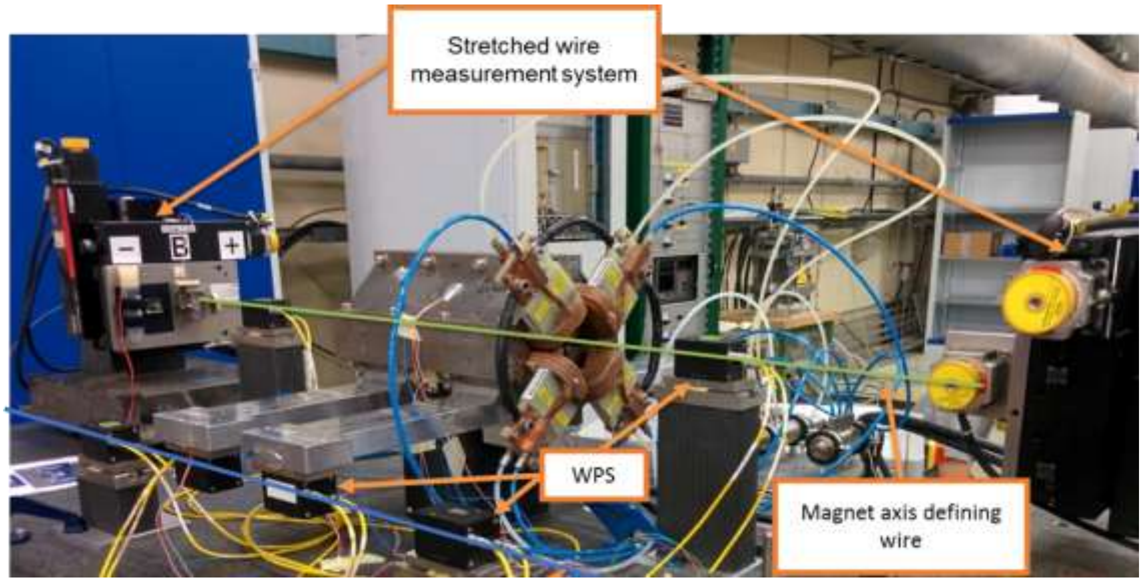


**Figure 63: Magnetic Measurement system used for magnet drift monitoring**

The setup shown in **Figure 63** was used to evaluate the drift of the magnetic axis as a function of the magnet assembly thermal condition. Thermal conditions were varied by creating steady state thermal loads by controlling the coils temperature via water chiller (**Figure 64**). The magnet assembly was left to establish a full thermal steady state at each new temperature with a time constant for each gradient ≈ 4.5 hours. At each steady state, the magnetic measurement system was used to best fit the thin stretched wire to the magnet axis. The X, Y coordinates were recorded with the WPS system. The uncertainty of the Magnetic

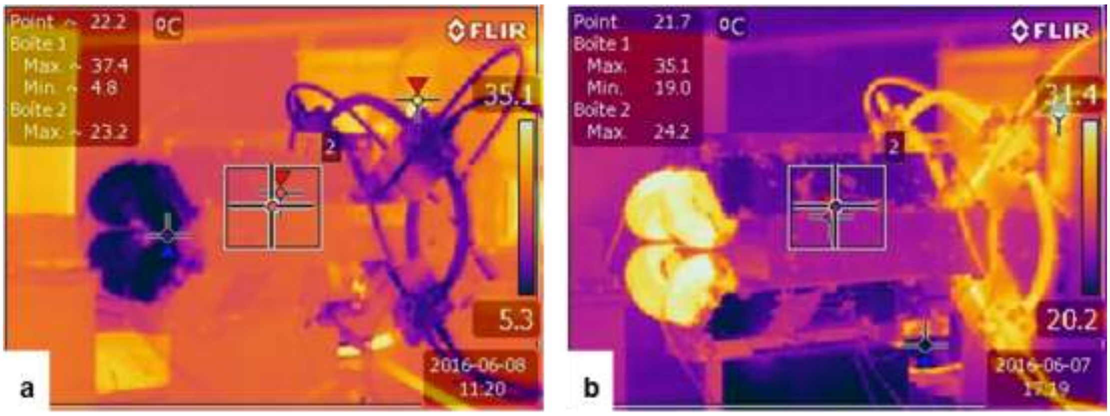


**Figure 64: Coils thermal loading infra-red: a) Low temperature loading; b) High temperature**

measurement system according to the two methods was studied by D. Caiazza. There is currently no SI unit standard or reference for a magnetic axis. The traceability and uncertainty analysis is currently done only by the experts developing and studying the system performance. It is a function of the magnet type, length, power, gradient and many more factors. The studies performed for the PACMAN project provided comparative results for both methods as summarised in (Arpaia *et al.*, 2015) and shown below in **Table 9**.

**Table 9: Uncertainty of stretched wire system for axis best fit according to measurement method applied** (Arpaia *et al.*, 2015)

| Studies on 1 meter stretched wire length for CLIC T1 Magnet | Vibrating wire method | Stretched wire method |
|---|---|---|
| Uncertainty [µm] 1 σ – Gaussian | X=2.2; Y=3 | X=62.2; Y=64.7 |

The stretched wire method is based on Lorentz law of electromagnetic induction. Series of movements of the wire are performed through the magnetic field measuring the induced current. The magnetic null is defined as the location at which the induced current is minimum or null. The vibrating wire method works on a different principle. AC currents of specific amplitude are put through the wire. The AC and the magnetic field interact causing the wire to vibrate. The AC currents and the wire are calibrated at their resonant frequency and the vibration of the wire measured via high accuracy optical sensors. The magnetic axis is defined as the location where the stretched wire vibration is minimum or null.

### 5.1.10 CTE coefficients evaluation

All Coefficients of Thermal Expansions (CTEs) of the materials part of the assemblies and alignment apparatus were experimentally studied. This was the case as accurate knowledge of CTE parameters are fundamental for the accurate predictions of the FEM for thermal deformation. As seen in (Doiron, 2001, 2006) text book tabled references for CTE coefficients can have large uncertainties from the actual performance of real materials. As shown in **Figure 65,** CTE coefficients even of different steel grades can vary by 50% and even among same steel grades; they can vary up to 5 ppm.

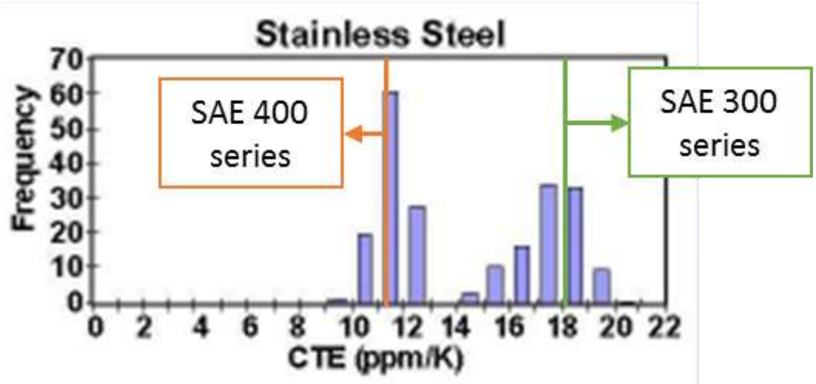


**Figure 65: CTE samples SAE 400 and SAE 300 Stainless Steel grades** (Doiron, 2006; John Bringas, 2016)

Thus for precision application is critical to measure the exact used material CTE with known uncertainty of this calibration measurement.

Probes from the same material slabs used for the machine of the magnet steel yoke and the alignment aluminium arms were cut via Electrical Discharge Machining (EDM) process. The numerous samples (three samples per material) were measured three times per sample with high precision dilatometer available at CERN materials laboratory (Netzsch, 2017) **Figure 66**.

**Figure 66: Top - Material samples EDM cut for CTE measurement at Bottom - Dilatometer DIL 402 E** (Netzsch, 2017)

The same process was used for cutting samples from the Carbon Fibre material used for the WPS support sensors. The specification of the instrument can be seen summarised in **Table 10**.

**Table 10: Dilatometry Specification**

| Standard | Atmosphere | Temperature program | Correction measurement | Expected Error [µm] |
|---|---|---|---|---|
| ASTM E 228 | Inert gas: He Flow rate: 100 ml/min | Range of T: RT50 ° Heating rate: 1.5 K/min | Reference material: Graphite Length: 24.995 mm | 4% (International Atomic Energy Agency., 2008; Perret, 2014) |

The experimental campaign gave measurements of the Secant CTE (Nayfeh and Verdirame, 2017) **Figure 67**.

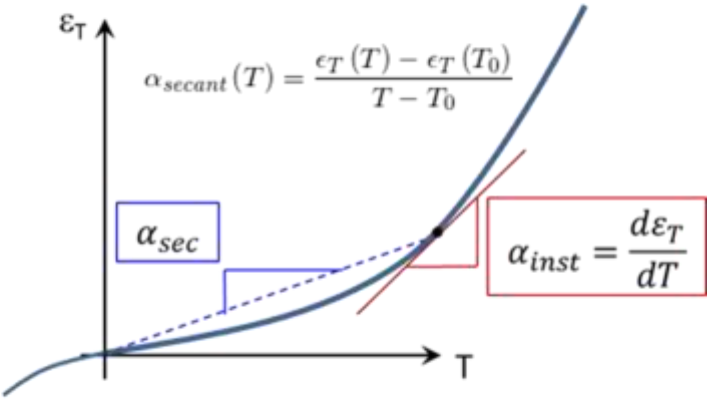


**Figure 67: Graphic representation of secant CTE ($\alpha_{sec}$) and instantaneous CTE ($\alpha_{inst}$)** (Nayfeh and Verdirame, 2017)

This is the average CTE for a specified thermal range (20°C to 50°C in the current studies). Such secant CTE was estimated for each sample three or more times for both cooling phases **Figure 68** and heating **Figure 69**.

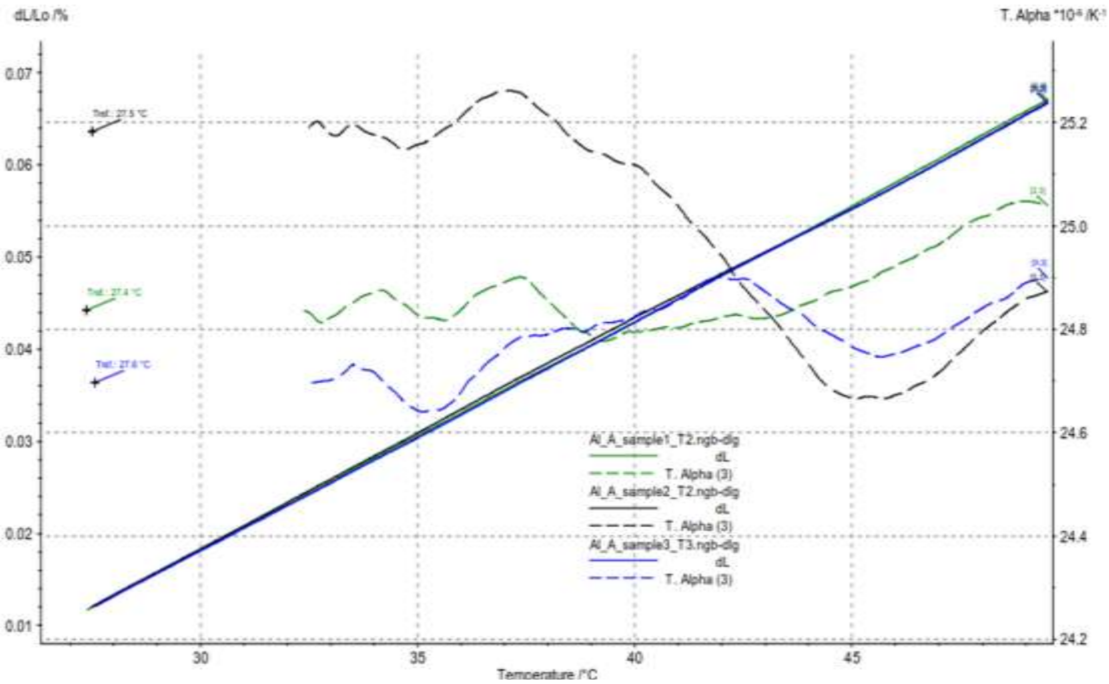


**Figure 68: Comparison between three different samples of Aluminium batch A CTE (dashed line) evaluated in the cooling phase.**

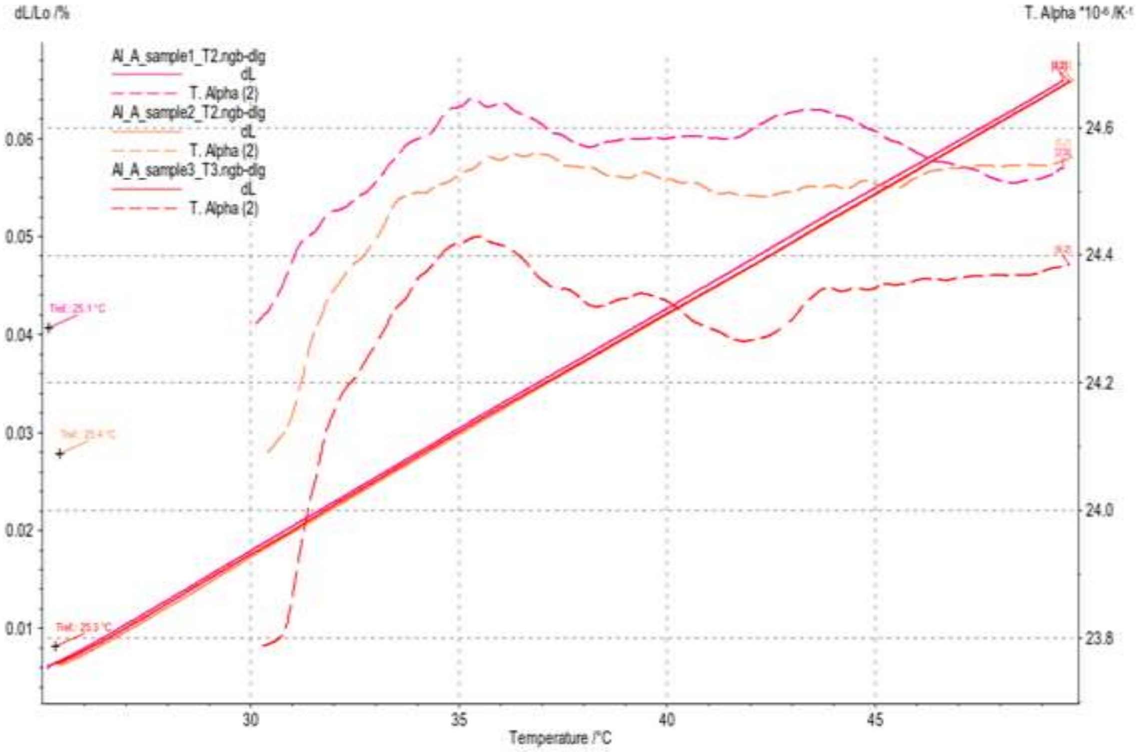


**Figure 69: Comparison between three different samples of Aluminium batch A CTE (dashed line) evaluated in the heating phase.**

The uncertainty of the experimental evaluating of the CTE coefficient for the material used was evaluated as the uncorrelated sum from the previous estimation of the dilatometer accuracy as a % of the CTE measured $U_{CTE\ error}$ and the experimental variance taken as a square shaped uncertainty between the lowest and highest CTE measured among all the samples studied for each material $U_{CTE\ error}$ - **Eq.(5-3)**. Summary of the findings can be seen in **Table 11**.

$$U_{CTEtotal} = \sqrt{U_{CTE\ error}{}^2 + U_{CTE\ variance}{}^2} \tag{5-3}$$

**Table 11: Evaluated CTE (secant) coefficients for materials part of assembly and associated variance, errors and total uncertainty**

| | Aluminium EN AW-6082 batch A | Aluminium EN AW-6082 batch B | Steel AFNOR XC10 | Carbon fibre rod 90° to fibre direction |
|---|---|---|---|---|
| **Average CTE (Secant) [µm/m/°C] taken for 20 - 50 [°C]** | 24.2 | 23.7 | 12.8 | 3.25 |
| **Experimental variance** $U_{CTE\ variance}$ **(3 material samples x 3 measurement repetitions on each) [µm/m/°C]** | 0.65 | 0.8 | 0.44 | 0.67 |
| **4% Error [µm] ; calibration** $U_{CTE\ error}$ **[µm/m/°C] 1 σ – Square** | 0.56 | 0.55 | 0.29 | 0.07 |
| **Uncertainty total** $U_{CTEtotal}$ **[µm/m/°C] 1 σ – Square** | U=0.86; a=1.49 | U=0.97; a=1.68 | U=0.53; a=0.92 | U=0.67; a=1.17 |

### 5.1.11 Pundit CMM software

PUNDITCMM™ (Phillips *et al.*, 2003; Summerhays *et al.*, 2004; METROSAGE, 2009) is a commercial CMM Uncertainty modelling software developed as a spinoff on NIST research based on the Simulation By Constraints (SBC) Monte Carlo method. The software was calibrated and used as a tool for the uncertainty prediction of the CMM used for alignment measurements. User interface illustrations can be seen in **Figure 70**.

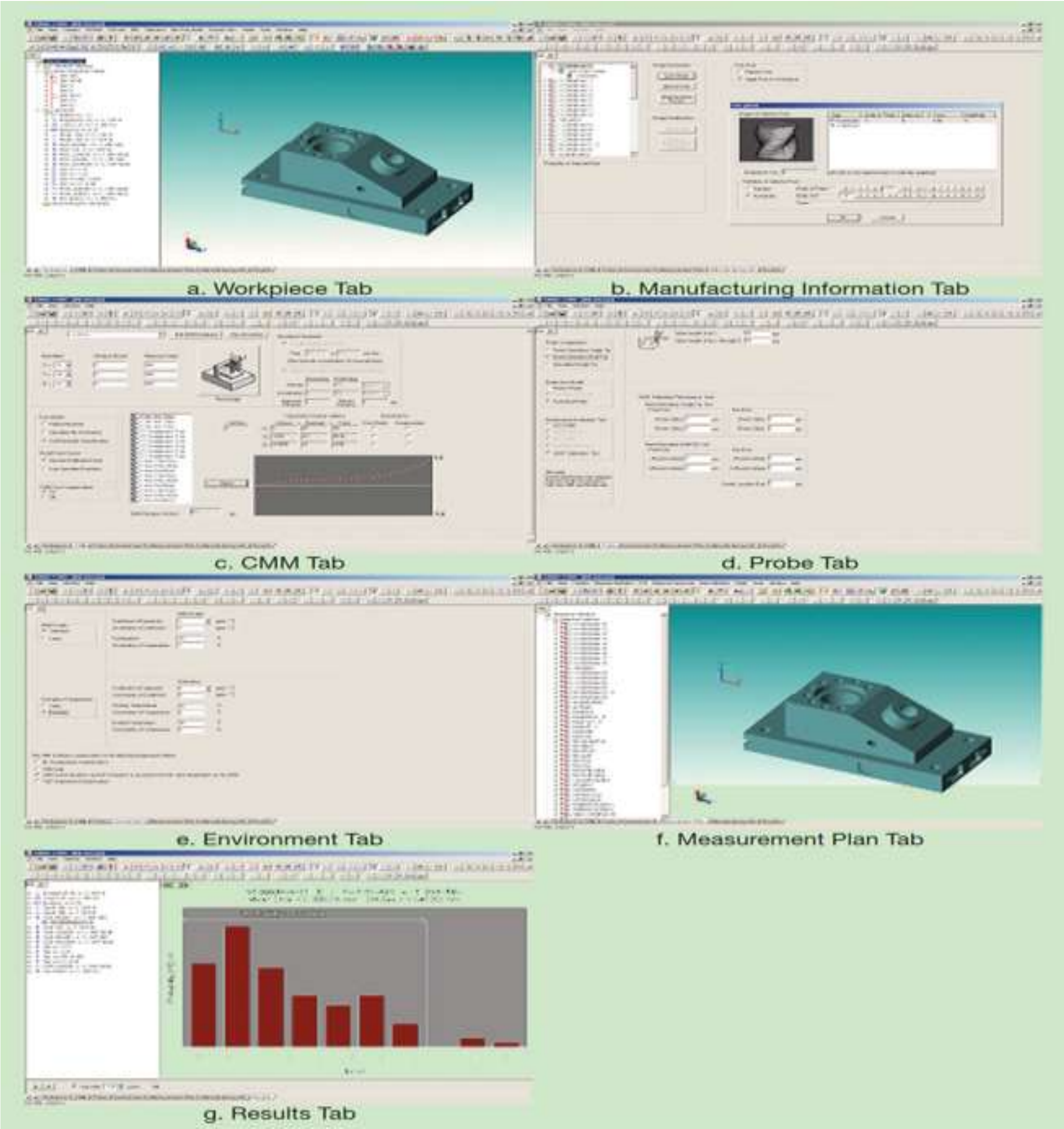


**Figure 70: User Interface illustrations** (Summerhays *et al.*, 2004)

The software was used as a variance estimation tool together with additional uncertainty estimation procedures as detailed further in **5.2.1, 5.2.2, 5.2.3.**

### 5.1.12 Dynardo Opti-Slang software

Opti-Slang is a statistical and optimisation software property of the German-based company Dynardo (Most and Dynardo GmbH, 2010) which specialised in Probabilistic and Stochastic modelling and analysis (Most and Dynardo GmbH, 2010). This software can be interfaced with a large variety of solvers and use them to perform statistical Monte-Carlo like analysis, meta-modelling and optimisation studies. It has a specialised interface for ANSYS in which any FEM model can be used as a solver for the statistical studies. The software was calibrated and used for the performance of Probabilistic FEM detailed in **5.2.6, 5.2.7**.

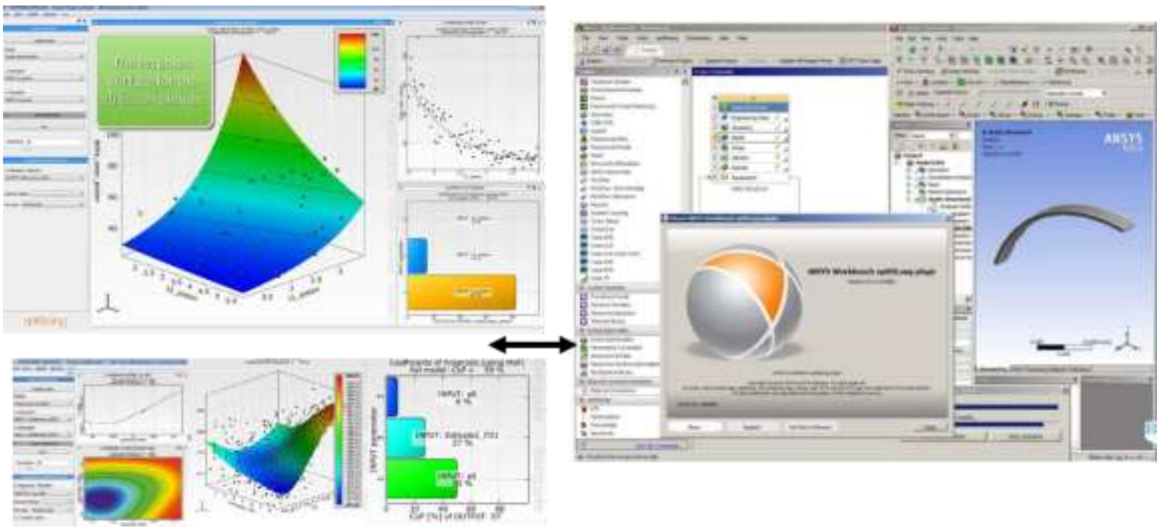

**Figure 71: ANSYS Opti-Slang plug in and stand-alone software user interface examples**

## 5.2 PROCEDURES

In the following sub-chapter specifics on the various modelling and experimental procedures are detailed. Part of the modelling sub-procedures were integral part of the commercial software's (**5.1.11**, **5.1.12**) and other were developed specifically as part of this PhD thesis work. This is clarified at each occasion.

### 5.2.1 CMM measurement uncertainty modelling procedure

The CMM measurement uncertainty was modelled as function of three general factors. The first is the difference (variance and bias combined) between the "**Virtual CMM measurement**" probabilistic model and the "**Real CMM measurement**". This was done by experimentally calibrating a PUNDITCMM (see **5.1.11**) software (see **Figure 72**).

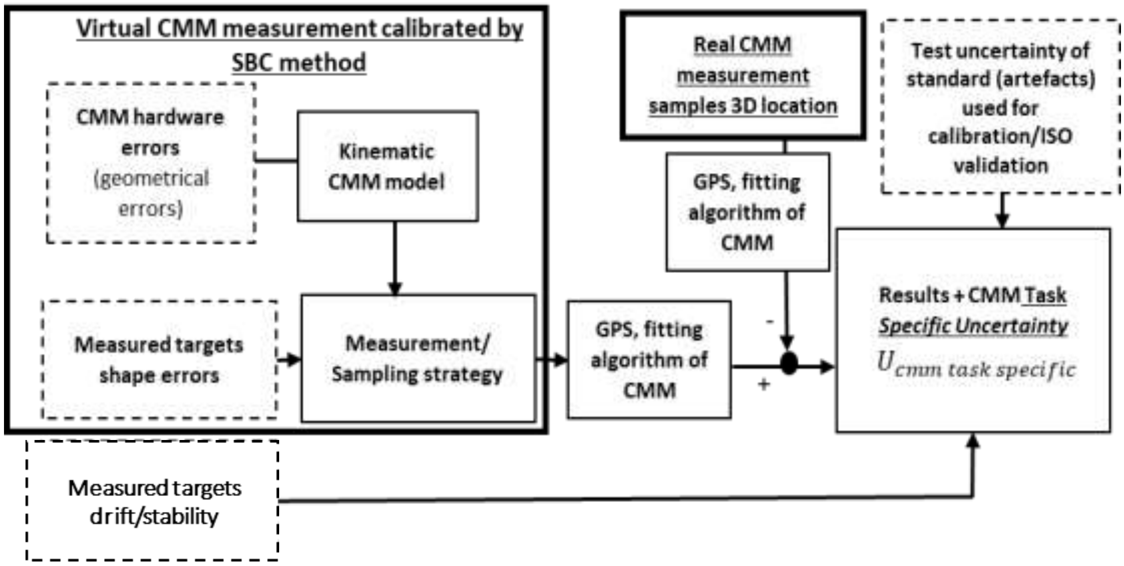


**Figure 72: Monte Carlo model for CMM measurement specific uncertainty propagation**

The other two uncertainty contributors propagated were the **Test uncertainty of the standard (artefacts)** used to calibrate the virtual CMM model and the **Measured targets drift/stability**. Those were evaluated by vendor supplier laboratories or measured experimentally at CERN as explained later in the sub-chapter.

The '**Virtual CMM measurement**' probabilistic model used (**5.1.11**), was a function of the **CMM hardware errors** (which include the 21 geometrical error parameters for Cartesian type CMM (J . Soon et al., 1992; Schwenke *et al.*, 2008) and the repeatability of the sampling probe head) and **Measured targets shape errors**. Both **CMM hardware errors** and **Measured targets shape errors** were defined in the model as Probability Density Functions (PDFs) calibrated by the Simulation By Constraitns (SBC) method. Those were propagated trough the virtual CMM model to define a PDF for the possible location of each sample coordinate of the measurement plan. s

#### 5.2.1.1 Virtual CMM model calibration

The '**Virtual CMM measurement'** calibration required experimental evaluation for the **CMM hardware errors** and **Measured targets shape errors**. The **CMM hardware errors** were mapped using Simulation By Constrains (SBC) method. Following this method, ISO 10360 standard measured parameters for the CMM volumetric performance (MPE), and the touch probe characteristics (MPEml, MPEms, MPEmf **Table 7**) were used to calibrate the model control parameters. This was done by PUNDITCMM via optimisation state space search using the machine kinematics and touch probe model as propagation function. In this way, the possible error sources for CMM hardware geometric errors and probe head repeatability (see **Figure 73**) Probability Density Functions (PDFs) were mapped. Once those determined, the '**Virtual CMM measurement'** was calibrated for forward uncertainties propagation (see **Figure 72, Figure 73**).

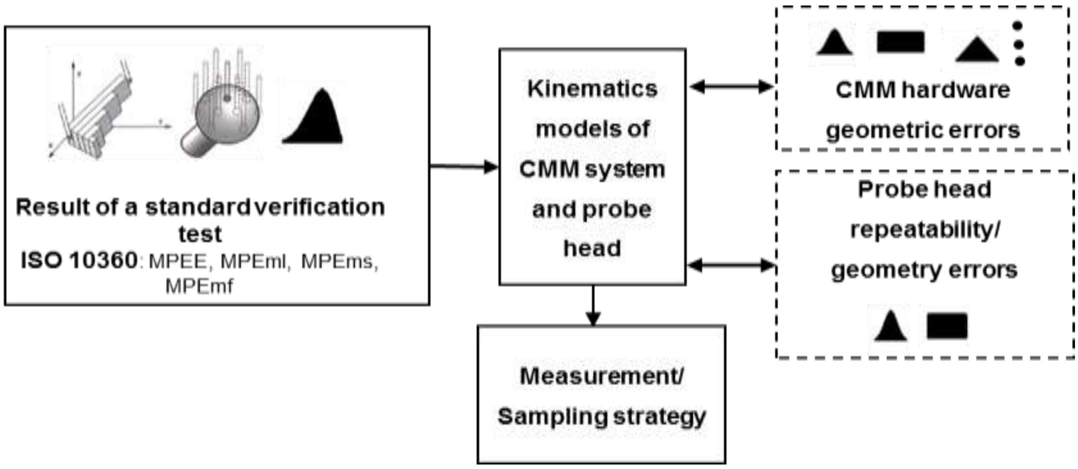


**Figure 73: Using standard tests results in order to map CMM and probe head errors using the Kinematic models of the CMM system and probe head. SBC method**

**Measured targets shape errors** (**Figure 72**) The uncertainty value of the fiducials shape was estimated as the maximum form error estimated by the manufacturer and documented in their calibration certificates. This value was used as the side $a_s$ of square shaped uncertainty quantifying the uncertainty due Measured targets shape errors - $U_{sh}$ **Eq.(5-4)**.

$$U_{sh} = \frac{a_s}{\sqrt{3}} \qquad \textbf{(5-4)}$$

#### 5.2.1.2 Test uncertainty of standard evaluation

**Test uncertainty of standard (artefact)** (see **Figure 72**) was evaluated as the uncorrelated sum of several uncertainty contributors **Eq.(5-5)** following suggestions defined in (ISO/TS, 2006; ISO, 2013b).

$$U_{tu} = \sqrt{U^2(art.calib.) + U^2(art.\alpha) + U^2(art.T) + U^2(art.Fix)} \qquad \textbf{(5-5)}$$

Where, $U_{(art.calib.)}$ was the estimated uncertainties due to the sole calibration of the artefacts (tetrahedron (**5.1.2**) or precision reference sphere for probe head qualification) used for system qualification; $U(art.\alpha)$ was the unawareness of the exact thermal expansion coefficient of the artefacts used; $U(art.T)$ was the uncertainty in the artefact temperature during the tests performance and $U(art.Fix)$ was the uncertainty caused by the stability of the fixture and orientation of the artefact.

#### 5.2.1.3 Propagation of the CMM uncertainties

Once the error sources were calibrated, the CMM virtual model (PUNDITCMM) was used to sample intterativly (Monte Carlo method) from the PDFs of the **CMM Hardware** and **Measured targets shape errors**. In this way they were propagated trough the CMM software fitting algorithum according to the GPS task (see **Figure 40**, chapter **5.1.1**) defined for the alignment measurments procedure. The real measured point coordinates are propagated through the same GPS task and fitting algorithm and from them random virtual measurements from the software are iteratively subtracted (Monte Carlo Method) (see **Figure 72**). The output is PDF (**Figure 74**).

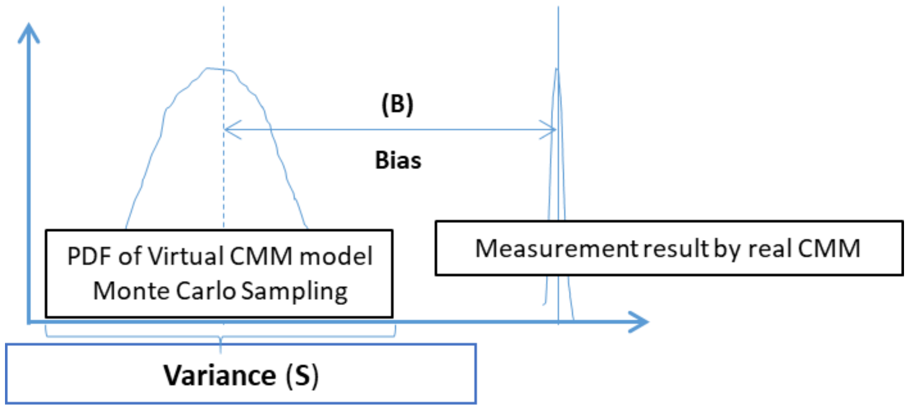


**Figure 74: Variance and Bias of Virtual CMM model**

The PDF one σ standard deviation represents the CMM system measurement variance (**S**) due to its **CMM Hardware** and **Measured targets shape errors** uncertainties (defined as PDFs). The error between the output PDF mean value (of the virtual CMM) and the real measured by the CMM system value would be its bias (**B**) due to the Virtual CMM model imperfect representation of the real world CMM system and measurement procedure **Figure 74**. The Virtual CMM model variance (**S**), bias (**B**) and test uncertainty **Utu** were used as quantification for the CMM specific uncertainty **Eq.(5-6)** as following recommendations of (NIST, 2014).

$$\boldsymbol{U}_{cmm\,specific} = \boldsymbol{S} * \boldsymbol{k} + \boldsymbol{B} + \boldsymbol{U}_{\boldsymbol{tu}} \qquad \textbf{(5-6)}$$

where **k** is the expansion coefficient for the significance level σ (i.e. 1σ, 2σ or 3σ).

In measurements where multisensorial CMM's measurements were used (measuring several features with one type of probe and several with other, i.e. tactile, non-contact in the same reference frame) two sets of parameter errors were calibrated (one for each particular sensor). Thus sampling points uncertainty was propagated according to the type of sensors/measurement head used. Measurement offset for measuring the same feature (***O***) between different probes exist due to the nature of their working method of how they "see/sample" a measurand (Morse and Bhamidi, 2003; Bhamidi and Morse, 2004). This offset was evaluated experimentally as the $L_{\text{Dia.nx25::MPS}}$ in ISO 10360 – 9 (maximum permissible multiple probing system location error for 5x25 point sphere fit) (ISO, 2013a). The experimental result was added as fully correlated additional bias to the $\boldsymbol{U}_{cmm\ specific}$ uncertainty budget **Eq.(5-7)**. The $L_{\text{Dia.nx25::MPS}}$ evaluation is function not only of the offset (***O***) between two different working principle common bridge probes but also includes errors due the CMM geometry. Thus addition of (***O***) as fully correlated bias to the other uncertainty contributors would provide small overestimation of the total uncertainty. This assumption was accepted to be correct, following guidance of ISO PUMA method (ISO, 2011c), where such statement is correct as long as $\boldsymbol{U}_{cmm\ specific} < \boldsymbol{U}_{\boldsymbol{targeted}}$. If this was not the case and $L_{\text{Dia.nx25::MPS}}$ contributed to a significant amount of $\boldsymbol{U}_{cmm\ specific}$, a more thorough investigation for the exact value of (***O***) would have been performed and added to $\boldsymbol{U}_{cmm\ specific}$ **Eq.(5-7)**.

$$\boldsymbol{U}_{cmm\ specific} = \boldsymbol{S} * \boldsymbol{k} + \boldsymbol{B} + \boldsymbol{U}_{\boldsymbol{tu}} + \boldsymbol{O} \qquad \textbf{(5-7)}$$

### 5.2.2 Measured targets drift during metrology evaluation procedure

Metrologist should quantify the measured targets stability/drift in space during the measurement procedure. One of the most influential factors in metrology and precision engineering are the thermal effects (California *et al.*, 1965; Bryan, 1967; Weck *et al.*, 1995; Doiron, 2001; Bryan and Doiron, 2011). Those could create a dimensional drift in both the CMM machine and the measurand with a peak when biases are in opposite phases (California *et al.*, 1965; Trapet, 2010). As modern high-end CMM have integrated thermal error compensation and thermally stable reference scales, the stability of the measurand can be accepted as a main influencing factor (Trapet, 2010; Bryan and Doiron, 2011; Gestel, 2011).

In this work the CMMs (**5.1.7**) were be used as a comparators by evaluating the location of assembly fiducials with respect to stable reference during different time periods. Measurement were done initially with thermal sources 'off' with assembly thermally 'soaked' to at 20 °C reference temperature **Figure 75, a)**.

Following thermal sources were switched on and at their peak influence fiducials were measured again with respect to the stable reference targets on the grainite base **Figure 75, b)**.

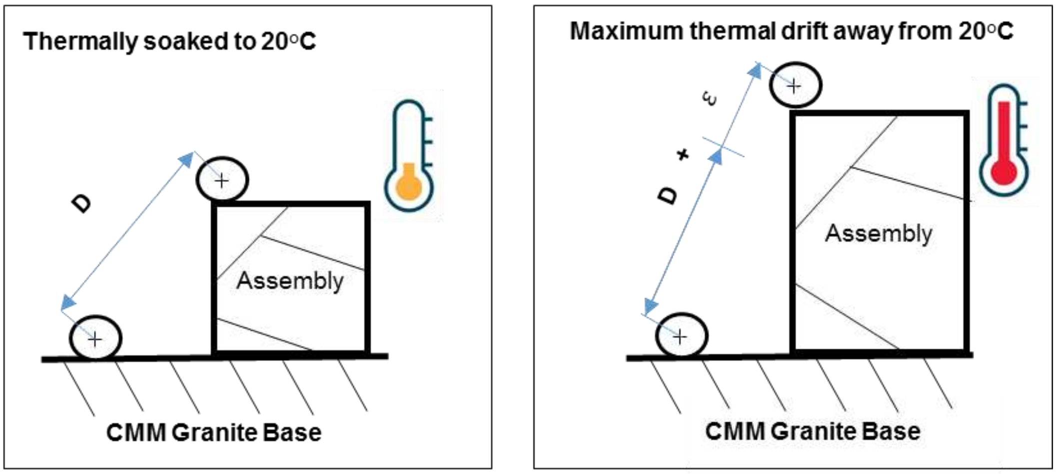


**Figure 75: Change in distance between reference target mounted on granite and drifting one mounted on thermally drifting assembly**

Measured coordinates of fiducials were found dependent on the coordinate reference frame assumed/set by metrologies. Different CMM operators and measurement strategies produced varying results for the coordinates locations. Thus it was found that direct, coordinate comparison of fiducials in time could hold false information. As an alternative direct comparison of fixed distances (between reference fiducials and the assembly fiducials) was used. The 3D distance of a rigid body is independent of the coordinate frame assumed and must stay constant as long as the body dimensions are constant. Thus any measured 3D distance drift between the references Granite targets and the assembly was used as quantification for the drift in space of the assembly **Figure 75**. The uncertainty due to any thermally or other induced drift to the alignment measurements was defined as a square shape uncertainty **Eq.(5-8)** with square half side $a_t$equal to the maximum evaluated 3D drift (between granite reference and assembly targets) **Eq.(5-9);**

$$U_{ex} = \frac{a_t}{\sqrt{3}} \quad \textbf{(5-8)}$$

and

$$a_t = \max_{n=r-i}(D_{thermally\ soaked\ \mathbf{20°C}} - D_{Maximum\ thermal\ drift\ from\ 20°C}) \quad \textbf{(5-9)}$$

### 5.2.3 CMM measurment uncertainty model validation procedure

The final stage was to validate the task specific measurement uncertainty predictions. A calibrated dimensionally stable artefact (**5.1.2**), with targets (fiducials) of similar shape/size to the one used on the assembly and distributed at similar distances, was measured **Figure 76**, **b)**. The maximum 3D location errors calculated between the calibration certificate of the artefact and the measurements by the studied CMM were compared. If the measured location errors are within the modelled uncertainty of the CMM then the method is validated successfully **Figure 76, a)** this was checked as suggested by **Eq.(5-10)** as defined in (ISO/TS and ISO, 2008).

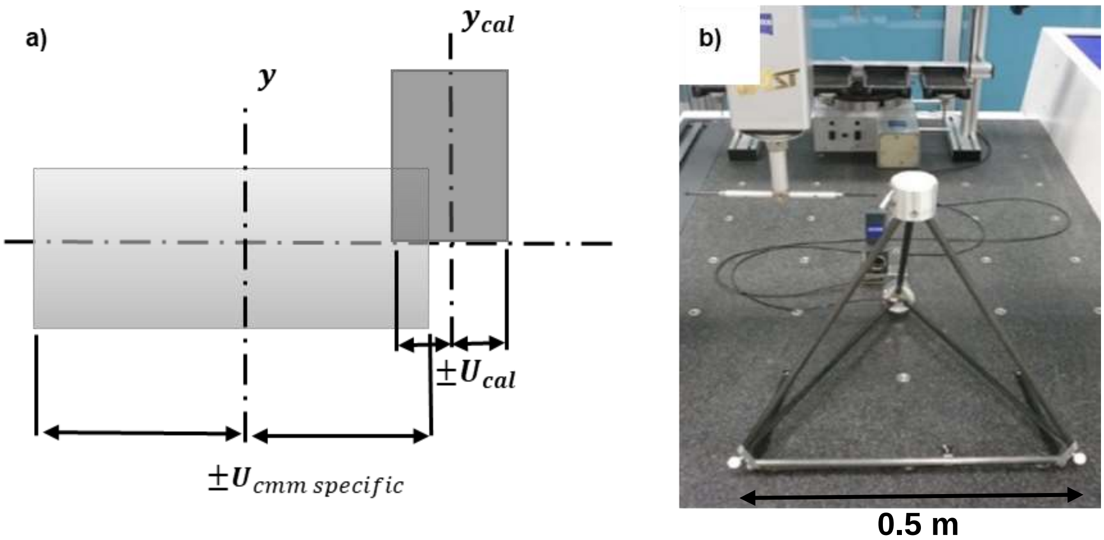


**Figure 76: Left a): Combining uncertainty regions. Right b): Carbon-Fibre tetrahedron artefact (5.1.2) with ceramic sphere ends used for validation**

$$\frac{|y - y_{cal}|}{\sqrt{U_{cal}^2 + \boldsymbol{U}_{cmm\,specific}{}^2}} \leq 1 \qquad \textbf{(5-10)}$$

Where in **Eq.(5-10)** and **Figure 76** $\boldsymbol{y}$ was the measurement result, $\boldsymbol{y_{cal}}$ was the artefact calibrated value, $\boldsymbol{U_{cal}}$ was the expanded uncertainty of the calibrated artefact and $U_{cmm\,specific}$ was the modelled expanded task specific uncertainty for the CMM measurements.

### 5.2.4 Change in thermal loads evaluation

If alignment measurements need to be carried out within an accelerator tunnel under real thermal operational conditions of the machine (i.e. full magnet power of ~ 120 Amperes +, water cooling, air ventilation), accurate corrections to the systematic offsets will need to be applied. Systematic offsets are expected in the order of hundreds of μm, due to large thermal gradients between alignment measurements and operational conditions (i.e. gradients of +20 $^{o}$C). These effects were studied by using the following procedures:

The change of the thermal field within the assembly components was quantified either by direct measurement or by modelling or by both. Critical for the evaluation process were valid statements of uncertainty. A thermal 3D field within solid components part of the assembly might not be possible to be evaluated by direct measurements. However, change in the thermal field within components assemblies is dictated by the change in heat transfer state conditions (Conduction, Convection, and Radiation). Thus an alternative aproach was devised by which the thermal state of the assembly was quantified by misture of heat loads mesurments and moddeling applying the equations of heat transfer. Simplified schematic of the assumed heat transfer analysis mechanism of the solid assemblies can be seen in **Figure 77** and the approach applied can be summarised in the following manner:

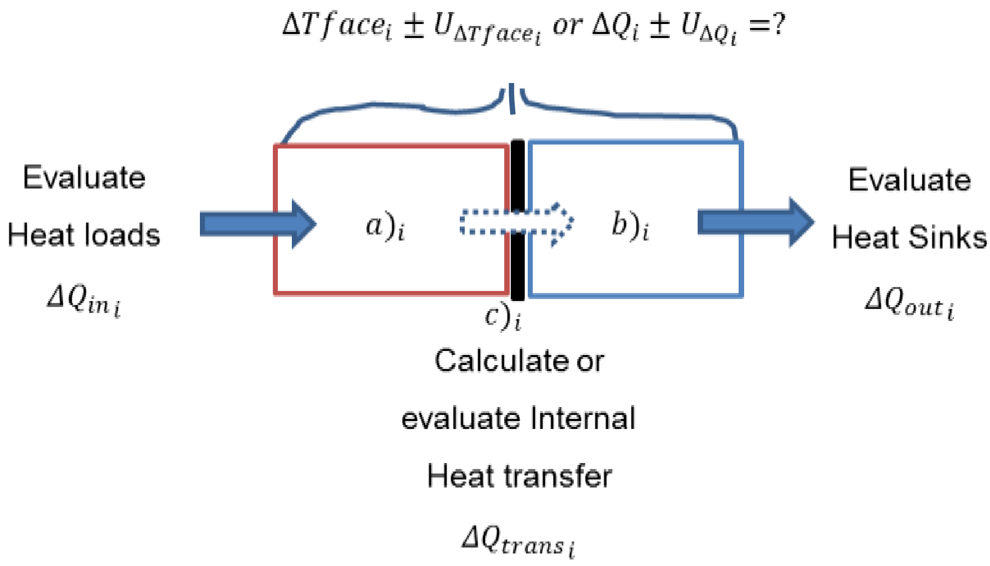


**Figure 77: Thermal loads boundary and internal conditions of assembly**

There would be $a)_i$ number of components that would in total experience positive change of increase of heat loads/Inputs ($\Delta Q_{in_i}$) and thus surface area temperature ($\Delta T_{face\ in_i}$). There would be $b)_i$ number of components that would experience a general decrease of heat flow ($\Delta Q_{out_i}$) and thus surface temperature ($\Delta T_{face\ out_i}$). There would be $c)_i$ number of inter-component interfaces for which there will be internal heat transfer ($\Delta Q_{trans_i}$) and thus internal assembly faces change in temperature ($\Delta T_{face\ trans_i}$). variation **Figure 77.** If all boundary changes (internal and external) of heat transfer are measured or calculated (with a statement of uncertainty), the knowledge can be used to calculate the change in the assembly components thermal field. This in consequence can be used to calculate any change in internal stresses and thus dimensions of the assembly as function of the current mechanical constraints. The thermo-mechanical models can be used to propagate their control parameters ($\Delta T_i, \Delta Q_i$) uncertainty to their output prediction variance as further detailed in **5.2.5**, **5.2.6** and **5.2.7** chapters.

In the current work assembly boundary surfaces which were practically accessible and were considered equipotential across the surface were measured with high precision thermal probes providing a set of boundary surfaces temperatures **Eq.(5-11)**.

$$T_{measured_i} \pm U_{T_{measured}} \quad \textbf{(5-11)}$$

Where $U_{T_{measured}}$ was the estimated uncertainty of the surface area of interest.

Temperature changes of assembly boundary or internal faces that could not be measured directly with thermal sensors were estimated with the help of heat transfer equations for Conduction, Convection and Radiation based on measured heat loads.

For example: Heat flow $Q_i$through a specific assembly component area $A_{surface\ i}$ is direct function of heat-flux. Itself defined as the heat flow per unit area ($HF_i[\frac{W}{m^2}]$) and is dependent on the temperature gradient ($\Delta T_i[K] = T_{high} - T_{low}$ between heat source higher temperature $T_{high}$ and heat sink with lower temperature $T_{low}$) times the heat transfer coefficient ($HTC_i$ [$\frac{W}{m^2K}$]) **Eq.(5-12)**.

$$\Delta Q_i = HF_i * A_{surface\ i} \text{ where,}$$

**(5-12)**

$$HF_i = HTC_i * \Delta T_i$$

Thus Heat-Flux was measured directly for each surface area via heat flux sensors. Such sensors produce a voltage signal proportional to the heat flux flowing through it **Figure 78, Eq.(5-13)**.

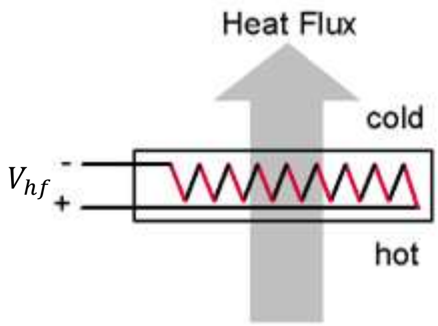


**Figure 78: Heat Flux sensor simplified diagram**

$$HF_i = V_{hf_i} * c_i$$

**(5-13)**

Where $(\boldsymbol{c_i})$ were the calibration coefficients for each heat flux probe used provided by their manufacturer. The uncertainty associated with a heat-flux measurement was evaluated and shown in **Table 4** in chapter **5.1.5.**

If a heat flux sensor covers completly an area of interest, it can be used to quantify the complete $\Delta Q_i$ through the surface **Figure 79**, **a)**.

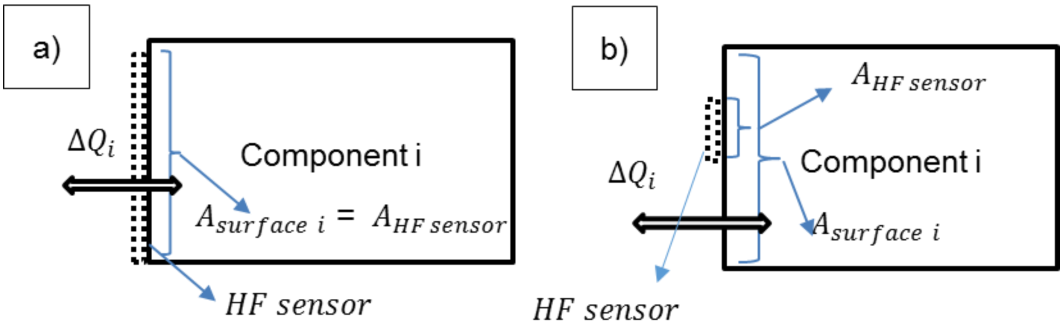


**Figure 79: a) Thin Heat-Flux sensor covering completely the area of interest b) Thin Heat-Flux sensor measuring heat flux through a local area**

Any such area heat flux sensor should be able to measure the heat flux as two dimensional field thus knowing the exact heat flux at each location of the component face/wall. Knowing any existing heat flux gradients on surface areas can be an important factor for the accurate calculation of the internal to the structure thermal fields and thus accurate prediction of the structure deformations. Available hardware on the marked did not had such capabilities thus an alternative approach was devised.

A thin heat flux sensors of smaller area were used to estimate expected for the surfaces heat transfer coefficients $HTC_i$ **Figure 79**, **b)**. It was assumed to be a function of the local $HF_i$ (measured by the Heat Flux sensor) and the thermal gradient between the thermally loaded surface and thermally loading source $\Delta T_i$ **Eq.(5-14).** This approach was assumed valid as the local measured heat flux $(\widehat{HF_i})$ for the sensor area ( $A_{HF\ sensor}$) was estimated equipotential to the total heat flux $HF_i$ of the studied surface $(A_{surface\ i})$ **Figure 79**, **b)**. Thus the heat transfer coefficients estimated via the local heat flux sensor( $\widehat{HTC_i}$ ) were assumed similar across the complete surface $A_{surface\ i}$ of interest: $\widehat{HTC_i} \approx\ HTC_i$.

$$\widehat{HTC_i} = \frac{HF_i}{\Delta T_i} where,$$

**(5-14)**

$$U_{\widehat{HTC_i}} = F(U_{T_{measured}}, U_{\widehat{HF}})$$

Additional heat loads such as radiative were experimentally estimated as shown in **5.1.5**. Internal heat transfer was calculated via FEM based on classic laws of heat transfer. Internal conduction heat transfer coefficients for the bolted metal to metal contact joints were taken from state of the art studied (Thompson, 2007; Hasselström, 2012). The values used in the modelling was the mean of the full experimental range findings (dependent on bolted joints pressure) 20 000 [$\frac{W}{m^2K}$] to 200 000 [$\frac{W}{m^2K}$] for contact pressures of 7 [Mpa] to 25 [Mpa]. The full experimental range from literature was accepted as square shaped uncertainty with $a_t$=90 000 [$\frac{W}{m^2K}$].

$$U_{hc} = \frac{a_t}{\sqrt{3}} \qquad \textbf{(5-15)}$$

### 5.2.5 Probabilistic empirical modelling

From the evaluated change in thermal conditions $(\Delta Tface_i\ and\ \Delta Q_i)$ and metrology frame nominal expansion $NE_{A-B_i}$, a direct empirical model linking the cause and effect was created and it's uncertainty evaluated. The model was used as "digital twin" (as suggested in Glaessgen and Stargel, 2012; Schluse and Rossmann, 2016) of the assembly representing its nominal expansion behaviour at various alignment temperatures and thus its results used for thermal error corrections. This was done following a three step procedure. First: *Selection of control parameters;* Second: *Fitting the empirical model* and Third: *Uncertainty evaluation of fitted model.* Once this model was created, real time measured thermal loads during alignment were used as input to the model which provided expected compensation value - $\widehat{NE_{A-B_i}}$ (for the metrology) associated with uncertainty statement $U_{\widehat{U_{NE_{A-B_i}}}}$. This work was performed with MATLAB and Dynardo software the statistical analysis tools **5.1.12**.

### 5.2.5.1 Selection of control parameters

As demonstrated in (Most and Will, 2008) the prediction quality of the empirical model may be optimal when parameters of 'high influence' to the model output are used. Having more parameters with lower influence toward the model output could include unnecessary noise within the model. Thus once thermal loads and structure responses are measured, the most significant or correlated to the structure response thermal loads have to be defined for the empirical model creation.

This was done by evaluating the correlation coefficient of each separate Thermal Load ($TL_i = Tface_i \; or \; \Delta Q_i$) with respect to the measured nominal expansion $NE_{A-B_i}$of the feature of interest. This was the standardized covariance between the $NE_{A-B_i}$and $TL_i$ as shown in **Eq.(5-17)** where the nominal expansion is accepted to be a function of the evaluated thermal loads **Eq.(5-16)**

$$NE_{A-B_i} = f(TL_1, TL_2, , \dots TL_n) \quad \textbf{(5-16)}$$

and

$$\rho(TL_i, NE_{A-B_i}) = \frac{cov(TL_i, NE_{A-B_i})}{\sigma(TL_i)\,\sigma(NE_{A-B_i})} \quad \textbf{(5-17)}$$

Where $\boldsymbol{cov}$ is the covariance and $\boldsymbol{\sigma}$ is the variance. Thus $\rho(TL_i, NE_{A-B_i})$ was estimated from the given measurement sampling sets as follows:

$$\rho(TL_i, NE_{A-B_i}) \approx$$

$$\frac{1}{N-1}\frac{\sum_{i=1}^{N}(TL_i - \mu_{Tface_i})(TL_i - \mu_{NE_{A-B_i}})}{\sigma_s(TL_i)\,\sigma_s(NE_{A-B_i})} \in \{1; -1\} \quad \textbf{(5-18)}$$

Where $\mu$ and $\boldsymbol{\sigma_s}$ are the mean and standard deviation. A correlation coefficient $\rho(TL_i, NE_{A-B_i})$ closer to 1 or – 1 will reflex higher positive or negative correlation between the thermal and drift measurements and a higher amount of influence to the model output. With this quantification, it was decided which of the evaluated thermal loads on the studied assemblies are best for use in the empirical regression model for the thermal drift prediction. At this stage, engineering judgment was applied and it was concluded if the sensors are mounted at the optimum places-components and if which represent best the thermal loads that cause the studied thermal drift.

#### 5.2.5.2 Fitting the empirical model

Once the most representative thermal loads have been identified, they were fitted into a model representing the drift. This was done via a commonly used approximation method the polynomial regression. This method accepts that any response can be approximated by a polynomial basis function of linear or quadratic order with or without coupling terms. Thus the model output $NE_i$ (Drift at fiducial) for a given set $TL_i$ was formulated as the sum of the approximated value $\widehat{NE}_i$ and error term $\varepsilon_i$

$$NE_{A-B_i}(TL_i) = \widehat{NE_{A-B_i}}(TL_i) + \varepsilon_i = P^T(TL_i)\beta + \varepsilon_i \qquad \textbf{(5-19)}$$

Where $P^T(TL_i)$ is the polynomial basis,

$$P^T(TL_i) = [1\ TL_1 TL_2\ TL_3 \ldots TL_1^2 TL_2^2 TL_3^2 \ldots\ TL_1 TL_2\ \ TL_1 TL_3 \ldots\ TL_2 TL_3 \ldots] \qquad \textbf{(5-20)}$$

And $\beta$ is a vector containing the unknown regression coefficients. These coefficients were estimated from the measured sample set of $NE_{A-B_i}$(drifts) and $TL_i$ (thermal loads). By using matrix notation, the resulting vector of estimated regression coefficient was as defined in **Eq.(5-21)**:

$$\hat{\vec{\beta}} = (P^T P)^{-1} P^T\, NE_{A-B_i} \qquad \textbf{(5-21)}$$

Where $P$ is the matrix containing the polynomial of the basis for the evaluated thermal samples/measurements $TL_i$ and $NE_{A-B_i}$ is a vector of the measured/evaluated experimentally drifts.

### 5.2.5.3 Estimation of empirical model uncertainty

The uncertainty of any empirical model prediction was assumed to be related to the extrinsic uncertainty of the measurements used for its creation $U_{NE_{A-B_i}}$, $U_{TL_i}$ and the *bias (difference)* between a known value/validation measurement ($NE_{A-B_i}$) and the model prediction($\widehat{NE_{A-B}}_i$) The complete process can be seen visually represented in **Figure 80**. Thus the prediction uncertainty of the empirical model was quoted as function of the empirical model variance directly summed to its uncorrected bias **Eq.(5-22)**. This concept was first defined as the 'SUMU method' for summation of uncorrected bias by (Phillips, Eberhardt and Parry, 1997) and now for first time applied in the field of uncertainty propagation for empirical models.

$$U_{NE_{\widehat{A-B_i}}(TL_i)} = f(P^T(TL_i)\beta, \varepsilon_i) = f(P^T(TL_i)\beta) + \varepsilon_i \qquad \textbf{(5-22)}$$

Where $\varepsilon_i$ can be re-defined as the bias between the true value and predicted one the model created. The true value can be determined with indipendent high precision reference measurment. As the measurement used to define the drift would have a related uncertainty $U_{NE_{A-B_i}}$. Thus the bias error was estimated with respect to the worst possible case ($NE_{A-B_i} + U_{NE_{A-B_i}}$). The bias was defined as in **Eq.(5-23).**

$$\varepsilon_\mathrm{i} = (NE_{A-B_i} + U_{NE_{A-B_i}}) - \widehat{NE_{A-B}}_i \qquad \textbf{(5-23)}$$

To evaluate the uncertainty of an Empirical model the uncertainty of $P^T(TL_i)$ and $\beta$ where evaluated as function of the measurement uncertainties used for their definition:

$$U_{P^T(TL_i)} = f(U_{TL_i}) \text{ and } U_\beta = f(U_{TL_i}, U_{NE_{A-B_i}}) \qquad \textbf{(5-24)}$$

The measurment uncertainties used for the empirical model creations were propagated by applying the Monte Carlo method. By this $U_{TL_i}, U_{NE_{A-B_i}}$ were represented by probability density functions of the evaluated experimentally uncertainties. From those, random sampling was performed and the sampled values were propagated through the complete regression model for the evaluation of $P^T(TL_i), \beta$ iteratively. Thus each output prediction of the regression model for nominal expansion was defined by output PDF with mean - $\mu_{\{\widehat{NE_{A-B_i}}\}_{PDF}}$ representing the most likely value and a variance- $S_{\{\widehat{NE_{A-B_i}}\}_{PDF}}$ represented by the 1 sigma standard deviation of the prediction. The nominal drift prediction variance (scaled by the expansion coefficient $k$ for 1,2 or 3 σ) summed with the measured during model validation bias $\varepsilon_i$ provided the statement of uncertainty for the Empirical model for this particular assembly and thermal load ranges **Eq.(5-25)**.

$$U_{\widehat{NE_{A-B_i}}} = (k * S_{\{\widehat{NE_{A-B_i}}\}_{PDF}}) + \varepsilon_i \qquad \textbf{(5-25)}$$

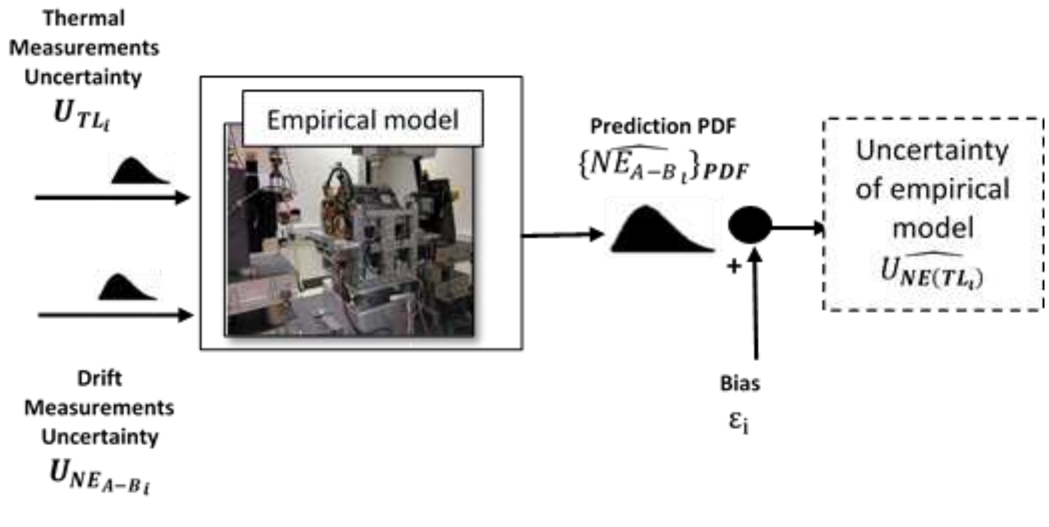


**Figure 80: Flowchart expressing the uncertainty of empirical model prediction as sum of its prediction variance and bias flowchart**

### 5.2.6 Probabilistic FEM

In this chapter the procedure designed for evaluation of FEM predictions ($\widehat{NE_{A-B_i}}$) uncertainty ($U_{\widehat{NE_{A-B_i}}}$) is defined and detailed. The approach mixes Probabilistic FEM and reference measurements that combined quantify the prediction uncertainty ($U_{\widehat{NE_{A-B_i}}}$). The approach is more flexible than the Empirical modelling one as once validated it can be used to predict nominal expansion with associated uncertainty for condition ranges outside the one performed experimentally. A visual summary of the method can be seen in **Figure 81.**

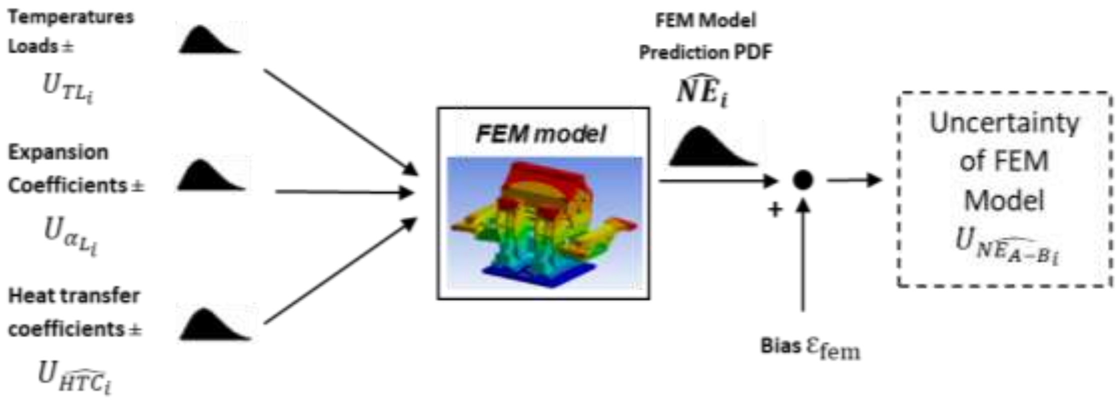


**Figure 81: Uncertainty propagation of a FEM model as sum of its prediction variance and bias flowchart**

The initial step was the creation of thermo-mechanical FEM model. The model was created in ANSYS FEM software using the 3D manufacturing drawings of the components. Mechanical constraints were set exact as the one for the real assembly. The boundary conditions – thermal loads ($TL_i$), material expansion coefficients ($\alpha_{L_{i_i}}$), internal and external for the assembly heat transfer coefficients ($\widehat{HTC_i}$) were set to the one measured during alignments. Next step was to parametrise the FEM model and to link ANSYS and Dynardo statistical software (**5.1.12**) thus enabling probabilistic FEM modelling. In this way the input parameters were defined by PDFs from which iteratively was sampled applying Latin Hyper Cube smart sampling technique (**Figure 81**, as techniques applied explained in **2.1.1**, **2.3.3**). Only a few hundred (~ 250) FEM model iterations were required for achieving a probabilistically significant result for the $\{\widehat{NE_{A-B_i}}\}_{\boldsymbol{PDF}}$ (**2.1.1**). High Performance Cluster (HPC) cluster computing was used performing the iterations in parallel on separate cores, processors and servers as suggested by (Microconsult Engineering GmbH and Mai, 2010). Thus samples were propagated through the FEM model acting as a 'virtual experiment' thus applying design of experiment methodology for FEM as suggested in the work of (Fong, Filliben and Heckert, 2008) and (Borror, Montgomery and Myers, 2002). The output from the numerous iterative FEM simulations ('virtual experiments') formed an PDF with associated mean ($\mu_{\{\widehat{NE_{A-B_i}}\}_{PDF}}$) and variance ($S_{\{\widehat{NE_{A-B_i}}\}_{PDF}}$). The mean of the output PDF was accepted as the most likely nominal expansion according to the model. Following this the bias of the Probabilistic FEM model was estimated by comparing it to traceable to the meter calibration measurement (with uncertainty $U_{NE_{A-B_i}}$). This acting as the standard of best knowledge for the real Nominal Expansion. The bias error was estimated with respect to the worst possible case which is direct sum of the Nominal Expansion measured and its measurment uncertainty $(NE_{A-B_i} + U_{NE_{A-B_i}})$ **Eq.(5-26)**.

$$\varepsilon_{\text{FEM}} = (NE_{A-B_i} + U_{NE_{A-B_i}}) - \widehat{NE_{A-B_i}} \qquad \textbf{(5-26)}$$

The final prediction uncertainty of the Probabilistic FEM was evaluated following the 'SUMU method' for summation of uncorrected bias (as suggested by Phillips, Eberhardt and Parry, 1997) **Eq.(5-27),** and **Figure 81**.

$$U_{\widehat{NE_{A-B_i}}} = (k * S_{\{\widehat{NE_{A-B_i}}\}_{PDF}}) + \varepsilon_{\text{fem}} \qquad \textbf{(5-27)}$$

With the current procedure predictions with associated uncertainty can be performed however in non-real-time. Even a highly optimised High Performance Computing (HPC) system might fail to provide near-real time computing for the several hundred FEM iteration of a computationally intensive model. Thus if near or real time compensation results with uncertainty statements (based on Probabilistic FEM) are required additional sub modelling procedure (meta-modelling) should be performed in advance. This procedure is detailed in next chapter (**5.2.7**).

### 5.2.7 Probabilistic FEM meta-models

The concept behind meta-modelling is to use the FEM instead the real assembly as transfer function for propagation of input parameters (thermal conditions) to output responses (Nominal Expansions). Thus the measured thermal loads ($TL_i$) and the output results ($\widehat{NE}_i$) of the Probabilistic FEM were used to create analytical 'meta-model' (**2.3.4)** applying regression analysis. This provided a linear equation that can link measured ($TL_i$) and provide predicted by the meta-model Nominal-Expansion ($\widehat{\widehat{NE}}_i$). The uncertainty of the meta-model was propagated following the same procedure (**5.2.5.3**) designed for the empirical models uncertainty analysis. Thus the meta-model uncertainty was devised to be a function of the thermal loads measurements uncertainty's ($U_{TL_i}$) and the PFEM model prediction uncertainty ($U_{\widehat{NE}_i}$) as shown in **Figure 82**. Those were propagated via the Monte-Carlo method thought the regression analysis procedure in the same way as for the empirical measurement models (**5.2.5.3**). The output of the probabilistic propagation being an output PDF of the meta-model with associated mean ($\mu_{\{N\widehat{\widehat{E_{A-B_i}}}\}_{PDF}}$) and variance ($S_{\{N\widehat{\widehat{E_{A-B_i}}}\}_{PDF}}$). The mean of the PDF prediction of the meta model was then validated against calibration prediction made by the PFEM (with uncertainty $U_{N\widehat{E_{A-B_i}}}$ **5.2.6**). This was used as a virtual standard defining the best knowledge of the assembly expansion. The bias error was estimated with respect to the worst possible case which is the direct sum of the validation PFEM prediction and it's evaluated uncertaity ($\widehat{NE_{A-B}}_i + U_{\widehat{NE_{A-B_i}}}$), **Eq.(5-28)**.

$$\varepsilon_{\text{meta model}} = \max_{NE}[(\widehat{NE_{A-B}}_i + U_{\widehat{NE_{A-B_i}}}) - N\widehat{\widehat{E_{A-B_i}}}] \tag{5-28}$$

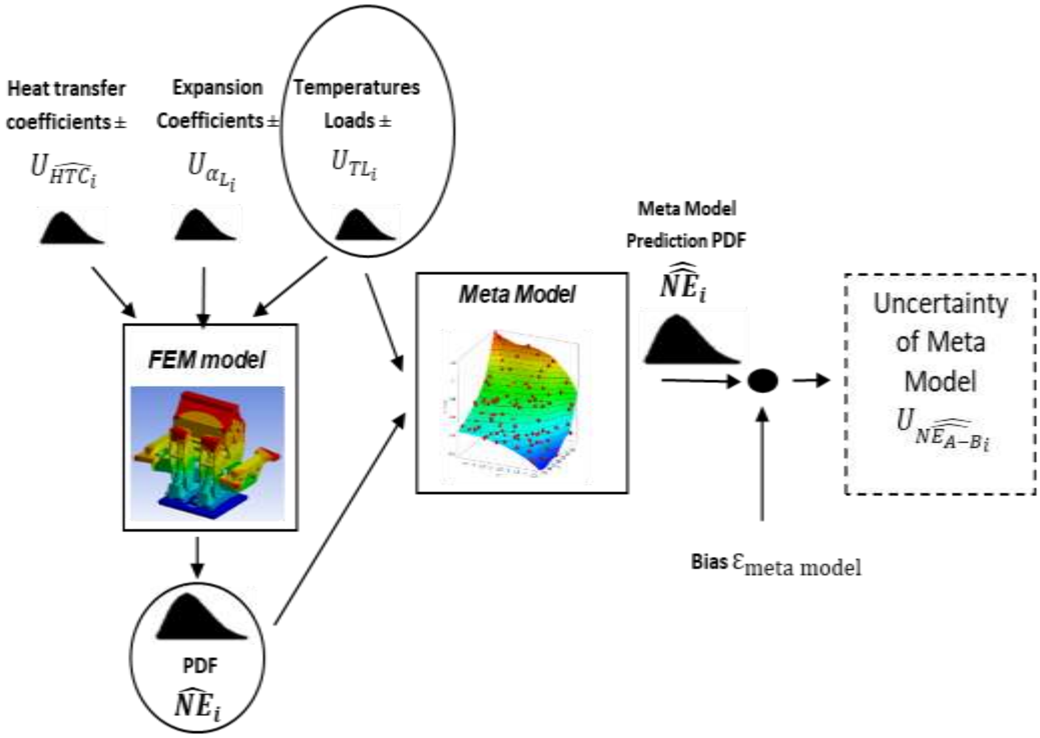


**Figure 82: Uncertainty propagation of a Meta-Model being a sum of its prediction variance and the validated bias flowchart**

The final prediction uncertainty of the meta-model was finaly estimated as function of its propagated variance ($S_{\{\widehat{NE_{A-B}}_i\}_{PDF}}$) and evaluated bias ($\varepsilon_{\text{meta model}}$) **Eq.(5-29)** and **Figure 82**.

$$U_{\widehat{NE_{A-B}}_i} = S_{\{\widehat{NE_{A-B}}_i\}_{PDF}} + \varepsilon_{\text{meta model}} \quad \textbf{(5-29)}$$

### 5.2.8 Thermal drift uncertainty models validation procedure

The final step for Empirical, FEM and meta models was validation of their predictions and statements of uncertainty against traceable to the meter standard measurment references. This was done following suggestions from (ISO/TS and ISO, 2008). The final check was performed by comparison of the overlap of the uncertainty intervals of the validation measurement $\boldsymbol{U_{val}}$ and the uncertainty predicted by the models $\boldsymbol{U}_{model\ applied}$ as shown in **Eq.(5-30)**

$$\frac{Ymodel\ applied - Yval}{\sqrt{Uval^2 + Umodel\ applied^2}} \leq \ 1 \text{ Y or N?} \tag{5-30}$$

Where $Ymodel\ applied$ is the prediction of a model (PFEM, empirical or meta-model). $Yval$ is high precision reference measurment of the drift (via CMM or stretched wire measurment system). By this equation If the result is less than 1, it can be considered that the validation measurement was within the predicted uncertainty region and thus the uncertainty region of the model is being predicted correctly **Figure 83**.

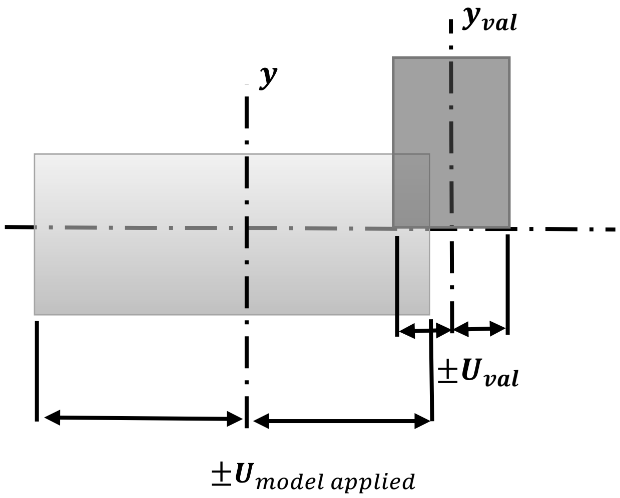


**Figure 83: Combining Uncertainty regions of the model applied and of the validation measurement**

If the ISO test **Eq.(5-30)** is not passed, then the method fails to predicts accurately the uncertainty region.

# 6 RESULTS

In **6.1** the task-specific uncertainties for the alignment measurements performed for CLIC magnet assemblies are reported. In there the method proposed for alignment measurements uncertainties in **4.2** is applied via a mixture of CMM uncertainty modelling and reference drift measurements. This was done following procedures documented in **5.2.1** and **5.2.2**. A visual diagram showing references to the input parameters for the analysis and the output uncertainty results can be seen in Appendix (**A.2**)**.** In **6.2**, the evaluated uncertainties for thermal drift prediction via empirical, FEM and meta-modelling are reported. This was done applying the method proposed in **4.3** by applying a mixture of probabilistic modelling and precise and traceable reference measurements. This was done following procedures defined in **5.2.5**, **5.2.6** and **5.2.7.** A visual diagrams showing references to the input parameters for the analysis and the output uncertainty results can be seen in Appendix (**A.3**, **A.4**, **A.5**)

## 6.1 Task-specific uncertainty for CLIC CMM measurements

First, the CMM uncertainty model validation results are reported in **6.1.1**. Following are the results for applying the validated model in mixture with reference measurements for prediction of CLIC T1 assembly series alignment measurements uncertainties **6.1.2** and CLIC T4 **6.1.3**. The discussion of this section results can be seen in chapter **7.2**.

### 6.1.1 Validation of CMM simulation by constraints uncertainty model

The CMM uncertainty prediction model was validated against the traceable tetrahedron artefact described in **5.2.3**. Results (see **Figure 84**) show that the maximum measured error (Er max) was within the prediction of the CMM uncertainty model (**Figure 84**).

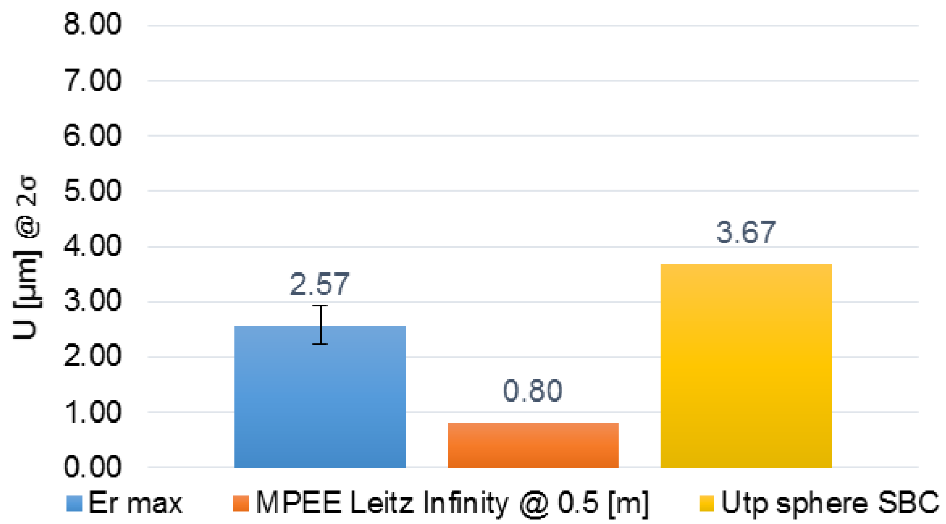


**Figure 84: Comparison of measured errors versus the predicted by model uncertainty and MPEE of Leitz Infinity CMM for 0.5 m**

The Er max value has the artefact calibration test uncertainty as an error band shown in the same figure. The calculated validation ratio as described in **5.2.3** is lower than 1 being equal to 0.18 (dimensionless), thus passing the validation test **Eq.(5-10)** for this particular CMM and measurement task.

### 6.1.2 Alignment measurements uncertainty prediction of 0.6 m T1 assembly

#### 6.1.2.1 Assembly thermal drift

The alignment set up of the PACMAN T1 magnet assembly prototype (as shown in **Figure 41, 5.1.1.**) temperature and fiducials location in 3D were monitored continuously within CERN metrology laboratory with Leitz CMM system (**5.1.7**).

Each experiment cycle took several days. Results for the temperature and associated dimensional drift can be seen in **Figure 85** and **Figure 86**.

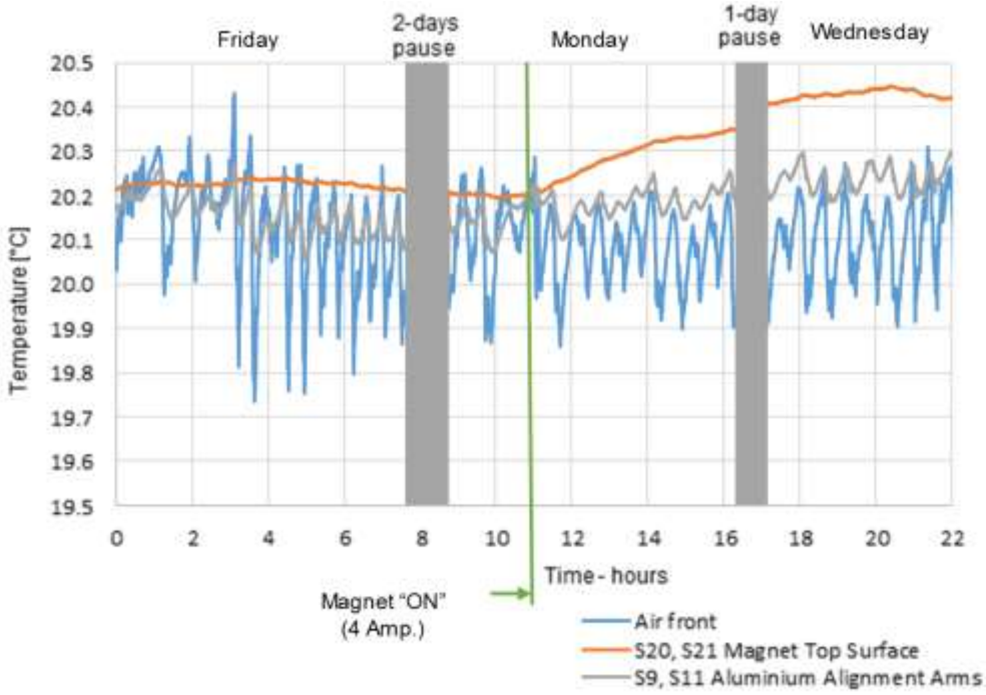


**Figure 85: Thermal variation of air, magnet, and alignment arm part of the assembly T1**

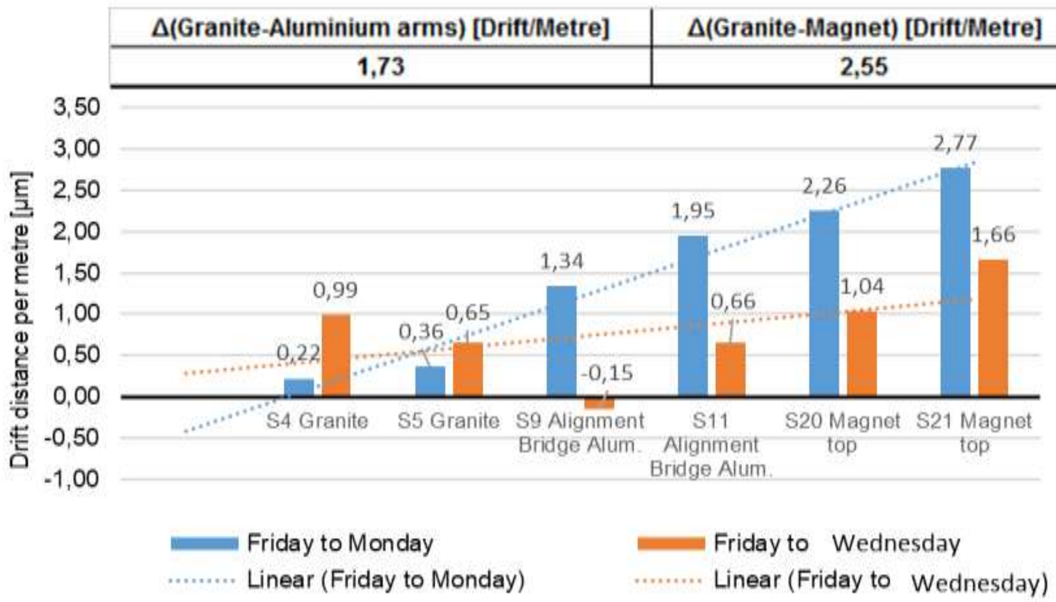


**Figure 86: Spheres normalised to the metre 3D drift for various locations on the assembly**

Where the dimensional drift in **Figure 86** is evaluated following procedure defined in **5.2.2** performed during each of the measurement days. All drift results in the figure are normalised to microns per metre. As seen in (**Figure 86**) the drift between the granite base, aluminium arms and the granite magnet has a maximum value of 2.55 μm/metre. This value was used for the estimation of the thermal drift (environment) uncertainty, accepted as the side of a uniform uncertainty distribution $a_t = 2.55\ \mu\text{m} * 0.63\ \text{m} = 1.6\ \mu\text{m}$ thus from **Eq.(5-8)**, $\text{U}_{\text{ex}} = \frac{a_t}{\sqrt{3}} = 0.92\ \mu\text{m}$. This was added as an uncorrelated uncertainty to the task specific uncertainty budget further shown in **Figure 89**.

#### 6.1.2.2 CMM model uncertainty prediction

In **Figure 87** the calculated MPE of the Leitz Infinity machine, for the furthest measured distance on the T1 assembly (0.95 μm), is compared to the modelled tactile measurement uncertainties of a fiducial sphere location with respect to a three-sphere dimensional reference frame.

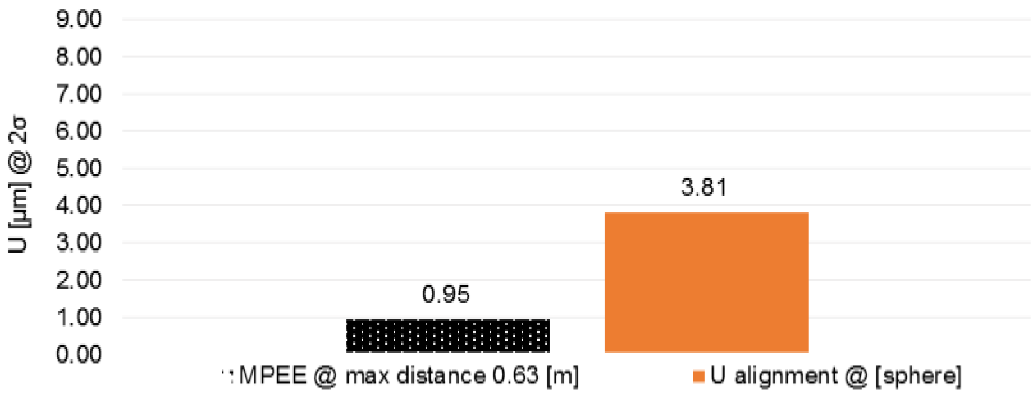


**Figure 87: MPEE of Leitz Infinity for the furthest distance on the assembly VS alignment measurements uncertainty of sphere in three sphere reference datum**

The effect of fiducial grade (shape form error), on the tactile measurement uncertainties, was studied in more detail and is shown in **Figure 88**. The same model from the previous study was ran for fiducials with varying form errors/specification. Results are highlighted in **Figure 88**.

It was observed that uncertainty significantly increases as a function of fiducials spheres shape quality. For example, using the highest commercially available grade spheres (ISO-3290) with 0.13 µm form error can lower the alignment measurement uncertainty by 0.5 µm to a total of 3.36 µm. However, using spheres of poorer quality (5 µm), sphericity can rise by 3.87 µm to a total of 7.23 µm (**Figure 88**).

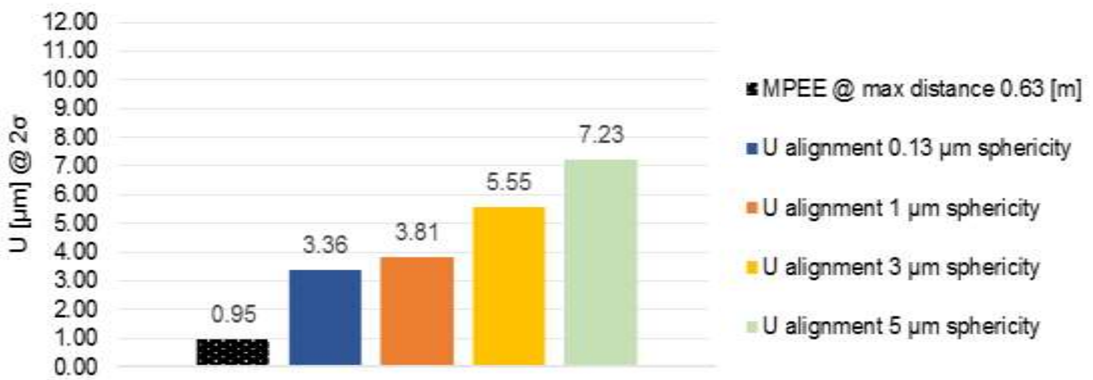


**Figure 88: Variation of alignment uncertainty as a function of fiducials form errors**

As a final study, the task-specific alignment uncertainty of defining the location of the magnetic axis in the three-sphere assembly datum c was studied (blue 6.91 µm @ 1σ). This was compared to the MPEE (black pattern furthest right in the same figure) and all other major uncertainty contributors.

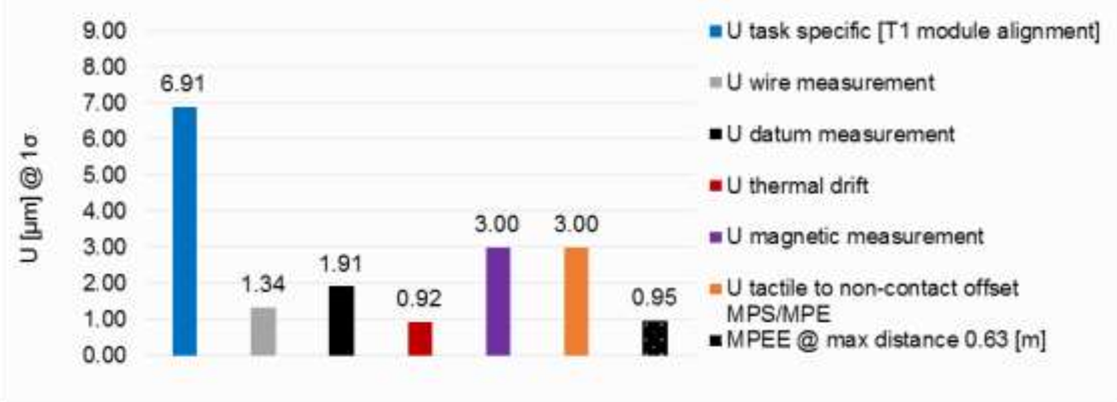


**Figure 89: Final alignment uncertainty of magnetic axis alignment measurements using the three spheres datum of CLIC T1 assembly and respective quadratic contributors**

### 6.1.3 Alignment measurements uncertainty prediction of 2 m T4 assembly

An SBC stochastic model was calibrated using the ISO 10360-5 data of a Zeiss PRISMO CMM (**5.1.7**) capable of holding an assembly up to 3m **Table 7**. The MPEE of this machine for the furthest distance on the assembly and the modelled tactile measurement location uncertainty of a sphere defined in another three spheres dimensional reference frame can be seen compared in **Figure 90**.

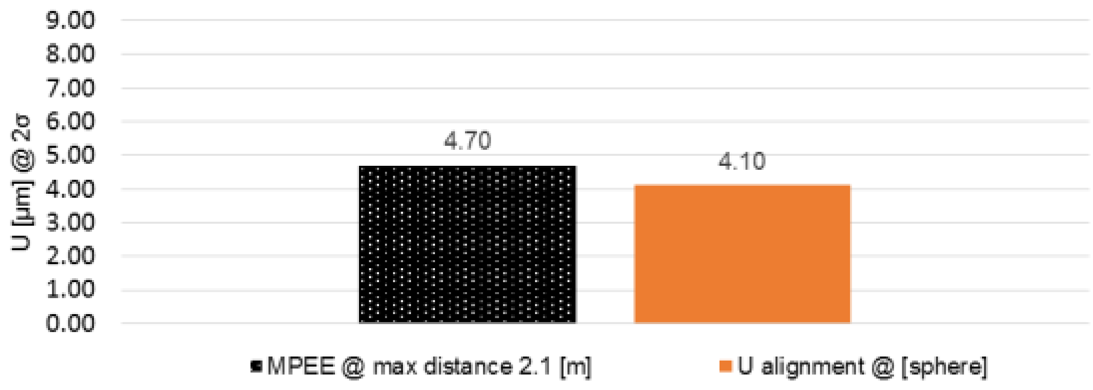


**Figure 90: MPEE of Zeiss PRISMO CMM for the furthest distance on the assembly VS predicted by model alignment measurements uncertainty of sphere in three sphere datum**

The location uncertainty of the sphere (4.10 µm) is lower than the MPEE given by the manufacturer. The predicted task-specific alignment measurement uncertainty is shown in **Figure 91**.

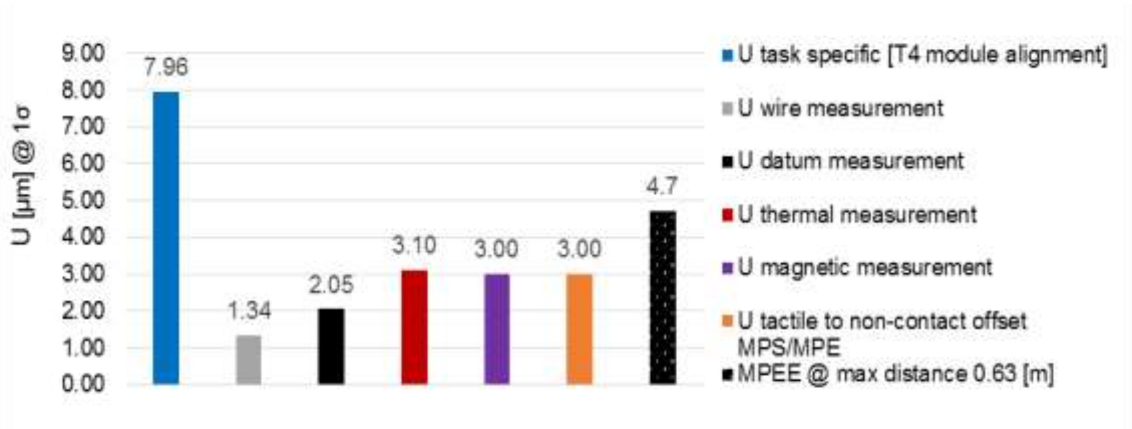


**Figure 91: Final alignment uncertainty of magnetic axis of CLIC T4 assembly and respective quadratic contributors**

### 6.1.4 CLIC alignment uncertainty budget left over

The remaining uncertainty budget from CLIC alignment target of 12 μm can be seen in **Figure 92,** calculated as the uncorrelated remaining quadratic contributors.

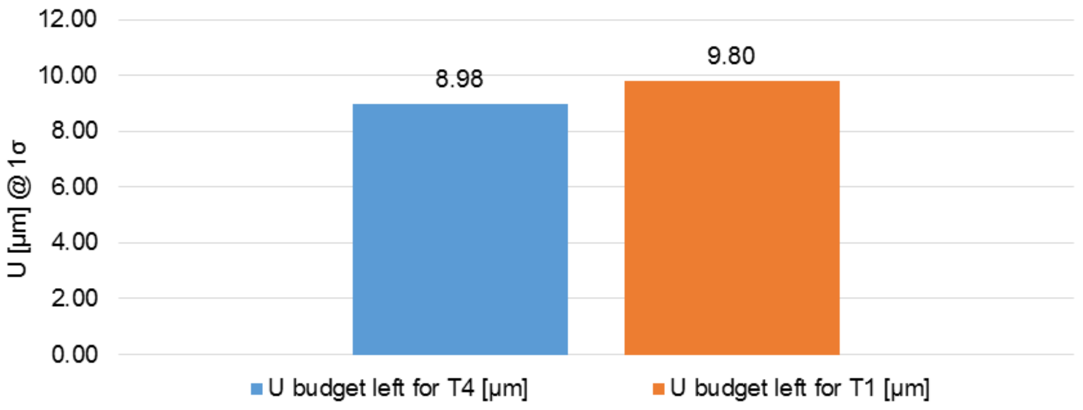


**Figure 92: Uncertainty tolerance left over for any additional uncorrelated error sources from targeted alignment uncertainty**

The leftover from the targeted tolerance (**Figure 92**) was accepted as targeted uncertainty budget for systematic thermal drift error compensation applied. This was the thermal drift due to variance in assemblies operational thermal conditions from one at metrology (results shown in **6.2**).

## 6.2 Uncertainty of magnet assembly alignment due to variable thermal conditions

Thermal deformations cause drift in the location of both the magnet axis and the alignment WPS arms used to find the tunnel reference. In this chapter results of compensation models for both are shown. First, the uncertainties of compensating the magnet axis drift using empirical method are outlined (**6.2.1**). Following the uncertainties of the WPS, arms drift by the use of Empirical (**6.2.1**), Probabilistic FEM (**6.2.1**) and Meta-model based on Probabilistic FEM (**6.2.1**) results are shown. The discussion of this section results can be further seen in chapter **7.2**.

### 6.2.1 Uncertainty for empirical model correction of magnet axis thermal drift

In several experimental campaigns, the drift of the magnetic axis as a function of the changes in the assembly temperatures was studied. An example of magnetic measurement wire location and assembly temperatures can be seen for a single such measurement cycle in **Figure 93.** In the same figure a) one can see the data from the WPS system used to measure the location of the magnetic axis stretched wire sensor. In **Figure 93,** b) one can see a summary of various thermal sensors readings for the same period. "*Sense*" in the same figure is a reference for sensor. The two noisy signatures (**Figure 93,** b)) are the temperature of the water flowing in and out of the circuit, commanded by the water chiller (noisy signature) control system. Following are the temperature readings from various locations on the magnet surface, support structures, and air sensors around the assembly.

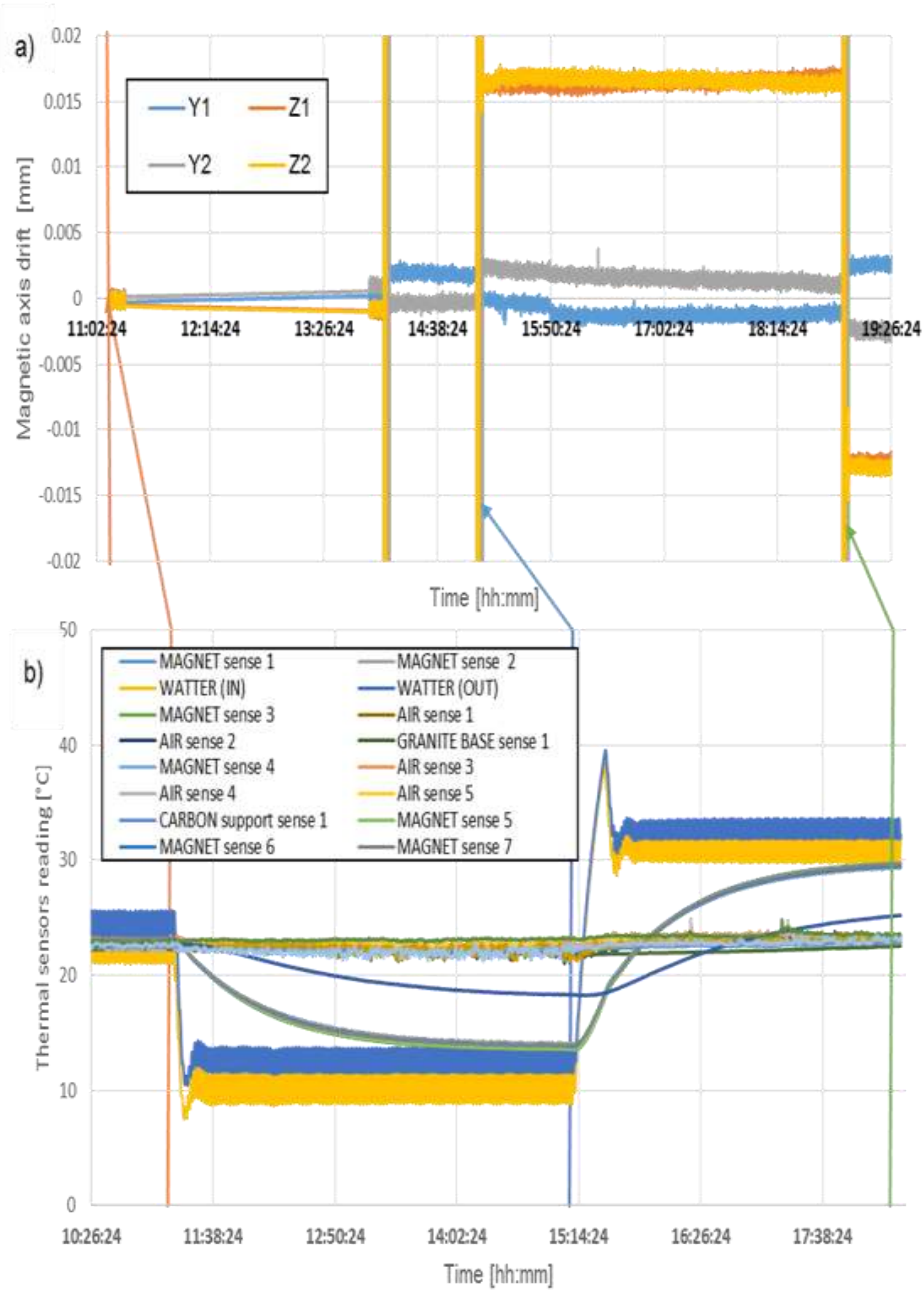


**Figure 93: Single thermal cycle: a) Magnetic axis location; b) Temperatures recorded**

Linear correlation analysis between the various thermal probes and the measured drift in Y and Z was performed to evaluate the most representative for the behaviour responses **Figure 94** and **Figure 95**.

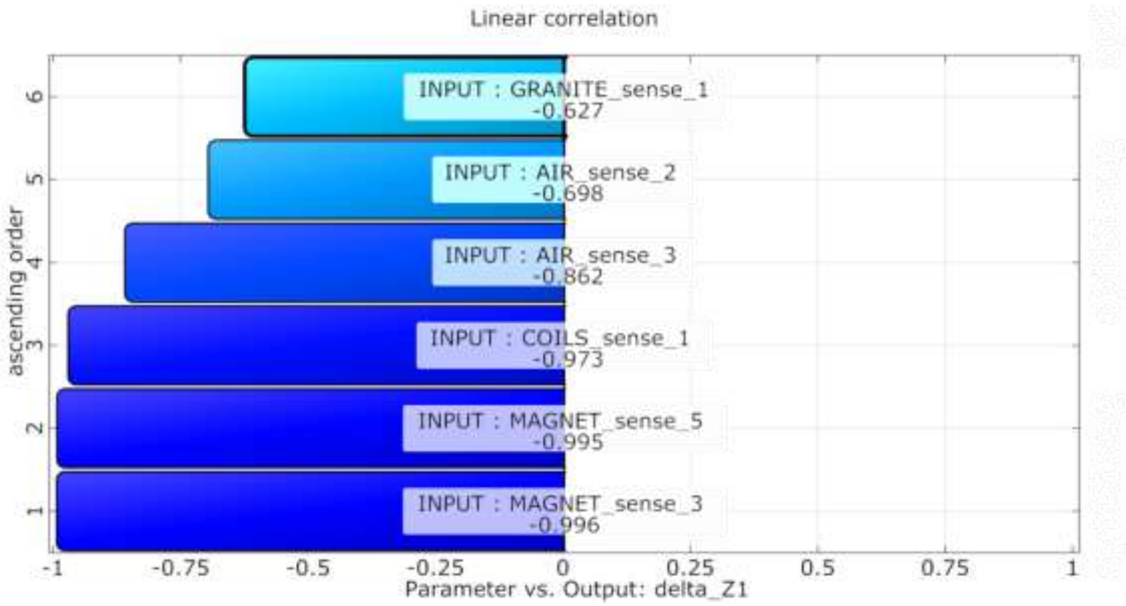


**Figure 94: Thermal sensors data VS Magnet axis drift in Z direction – correlation coefficients (via Opti Slang software 5.1.12)**

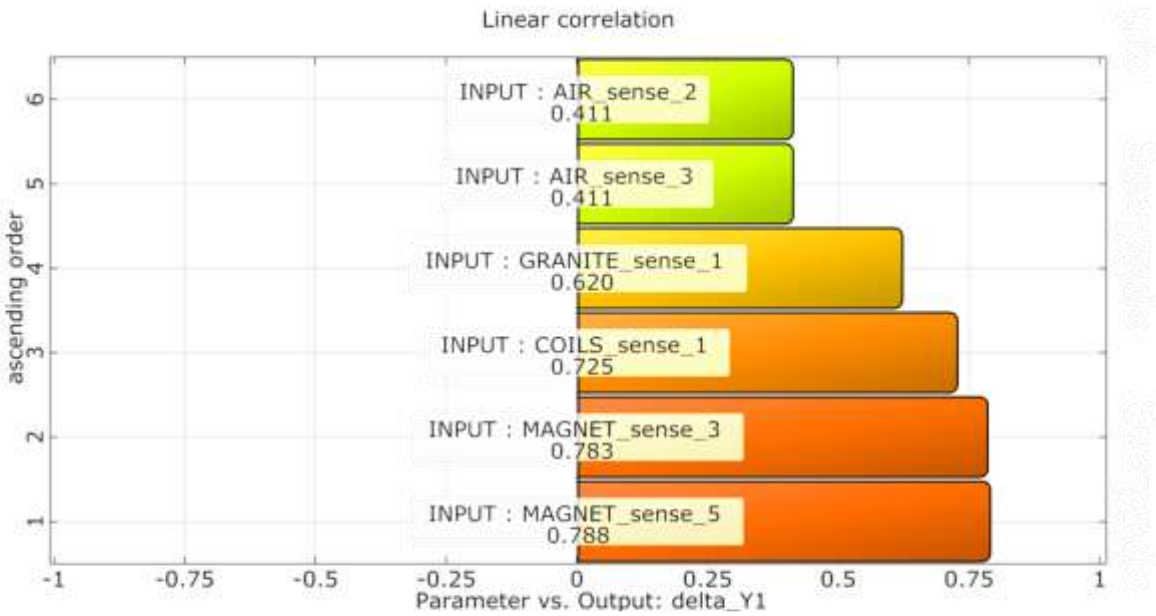


**Figure 95: Thermal sensors data VS Magnet axis drift in Y direction – correlation coefficients (via Opti Slang software 5.1.12)**

In **Figure 96** a spread of temperature readings for sensors distributed across the magnet yokes. The spread of the temperature readings contributed to the uncertainty (**Eq.(6 2)**) in the definition of a mean magnet temperature (mean of magnet yoke readings as shown in **Figure 96**) which was used for the magnet axis empirical models definition as described in **7.2.1.**

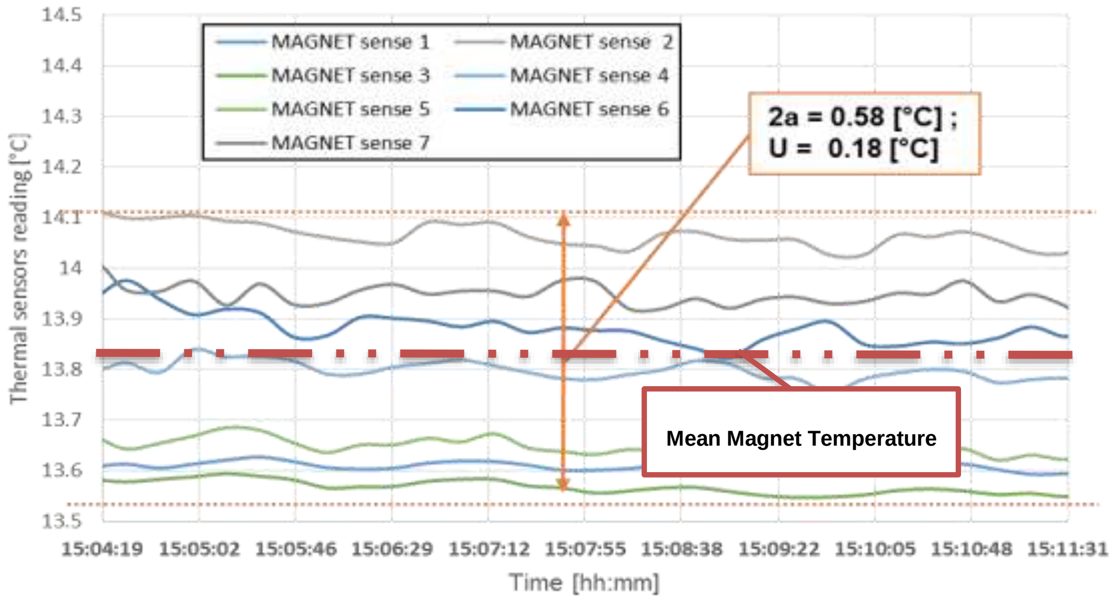


**Figure 96: Magnet temperature readings from various sensors and associated**

In **Figure 97** one can see the measured magnet axis location as a function of the mean magnet temperature.

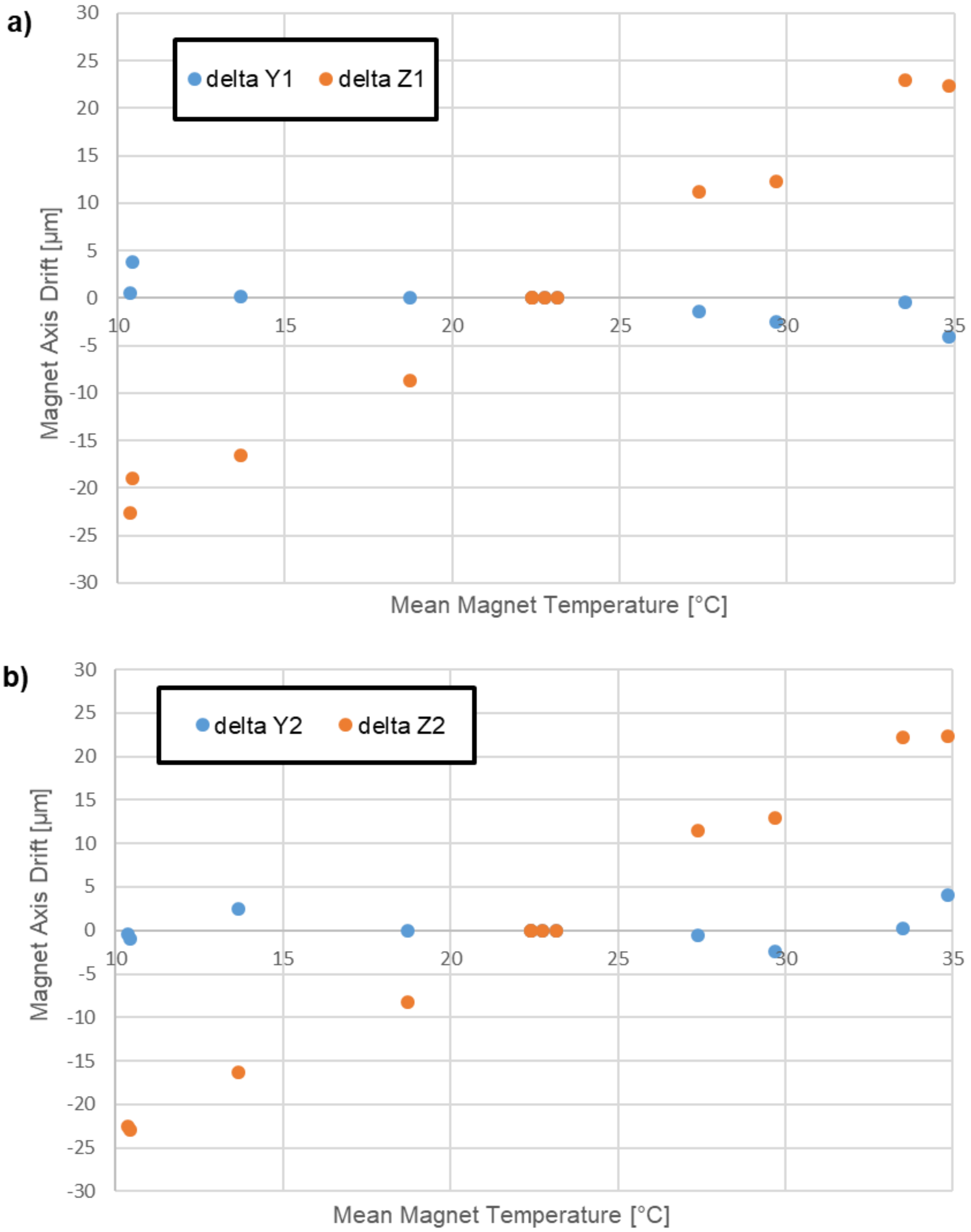


**Figure 97: Axis location VS temperature: a) “front” magnet measurements; b) “Behind” magnet measurements**

The mean magnet temperature and magnetic axis measurement variances are required for the empirical model prediction variance estimation. Those were calculated as shown in **Eq.(6-1),** and **Eq.(6-2)**.

$$U_{magnetic\ axis\ drift\ measure} = \sqrt{U^2_{WPSsys} + U^2_{magnetic\ measurment}} \quad \textbf{(6-1)}$$

Where $U_{magnetic\ measurment}$ is the uncertainty on the magnetic measurement system for vibrating wire method as defined in **5.1.9** and $U_{WPSsys}$is the uncertainty of the wire positioning system as defined in **5.1.8.**

$$U_{mean\ magnet\ temperature} = \sqrt{U^2_{temp\ measure} + U^2_{temp\ spread}} \quad \textbf{(6-2)}$$

Where $U_{temp\ measure}$ is the uncertainty of the temperature measurement for RTS sensor as is defined in **5.2.4,** and $U_{temp\ spread}$ is the uncertainty in knowing the complete thermal state of the magnet using a mean value defined as a square shaped uncertainty (see **Figure 96**)**.** Thus the two inputs propagated trough an empirical Monte Carlo study (following procedure outlined in **5.2.5, Figure 80** for the magnet axis drift can be seen in **Table 12**

**Table 12: Monte Carlo uncertainty input parameters for compensation law**

| $U_{magnetic\ axis\ drift\ measure}$ @ 1σ [μm]; Square shape | $U_{mean\ magnet\ temperature}$ @ 1σ [°C]; Square shape |
|---|---|
| 3.08; a=5.33 | 0.32 a=0.64 |

Following the procedure in **5.2.5,** regression analysis was applied to obtain equations representing the drift in Y1 **Eq.(6-3)** and Z1 **Eq.(6-4)**.

$$\widehat{Z1} = \mathrm{b1} - \mathrm{a1} * (\mathrm{Mean\ Magnet\ Temperature}) \quad \textbf{(6-3)}$$

Where b1 = 3.71626 and a1 = 0.180655

$$\widehat{Y1} = \mathrm{b2} - \mathrm{a2} * (\text{Mean Magnet Temperature}) \qquad \textbf{(6-4)}$$

Where b2 = -41.2232 and a2 = 1.84305

A Monte Carlo model of the regression analysis was first ran **5.2.5** to estimate the variances of the empirical model coefficients ($S_{a1}$, $S_{b1}$, $S_{a2}$, $S_{b2}$). Coefficients PDFs can be seen In **Figure 98**. Their associated variances in **Table 13**.

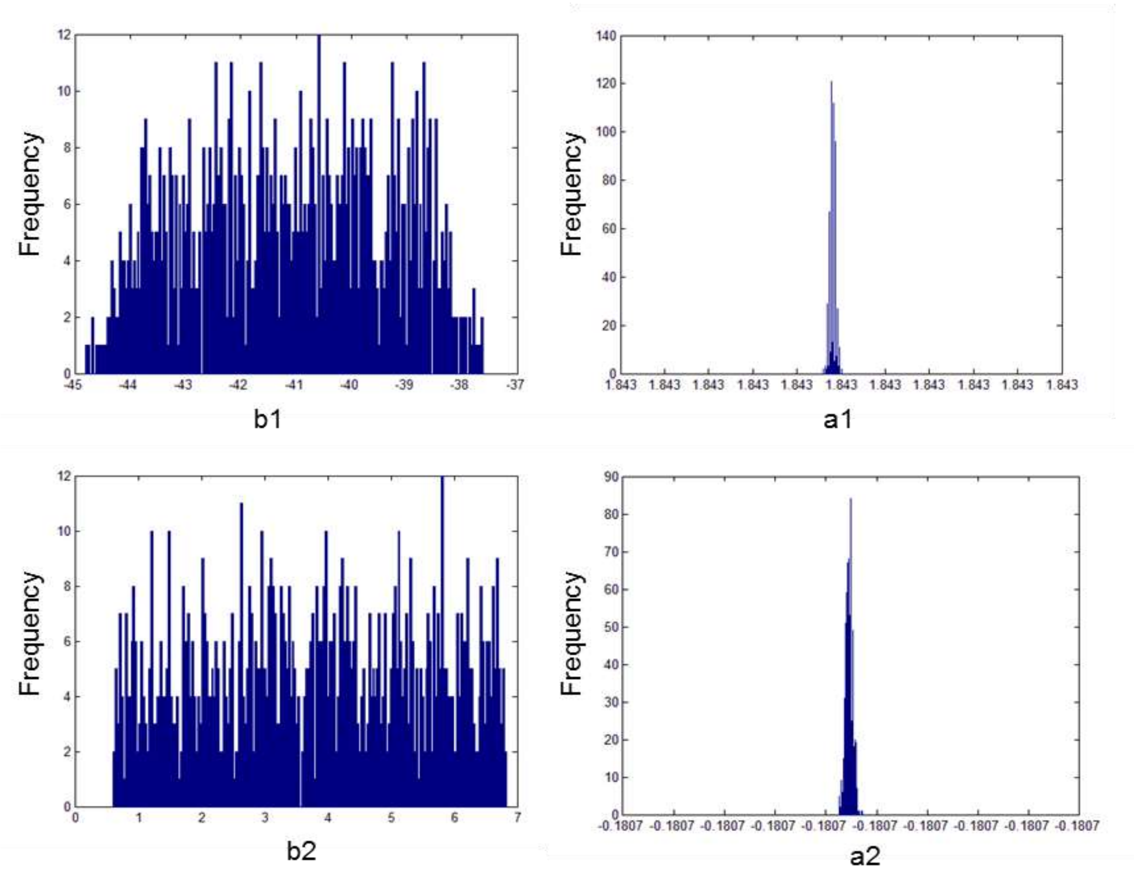


**Figure 98: Monte Carlo samplings defining PDFs for a1,b1; a2,b2 parameters of $\widehat{Z1}$, $\widehat{Y1}$ empirical models for Z1, and Y1 drift (MATLAB)**

**Table 13: Magnet axis empirical drift model coefficients variance as function of measurement uncertainties**

| $S_{a1}$ (1 σ) | $S_{b1}$ (1 σ) | $S_{a2}$ (1 σ) | $S_{b2}$ (1 σ) |
|---|---|---|---|
| 4.66 e-15 | 3.05 | 4.99e-16 | 3.05 |

The evaluated parameter variances and measurement uncertainties were used further in the Monte Carlo model to define a PDFs and variances for $\widehat{Z1}$ and $\widehat{Y1}$ as seen below in **Figure 99** and in **Table 14** on next page.

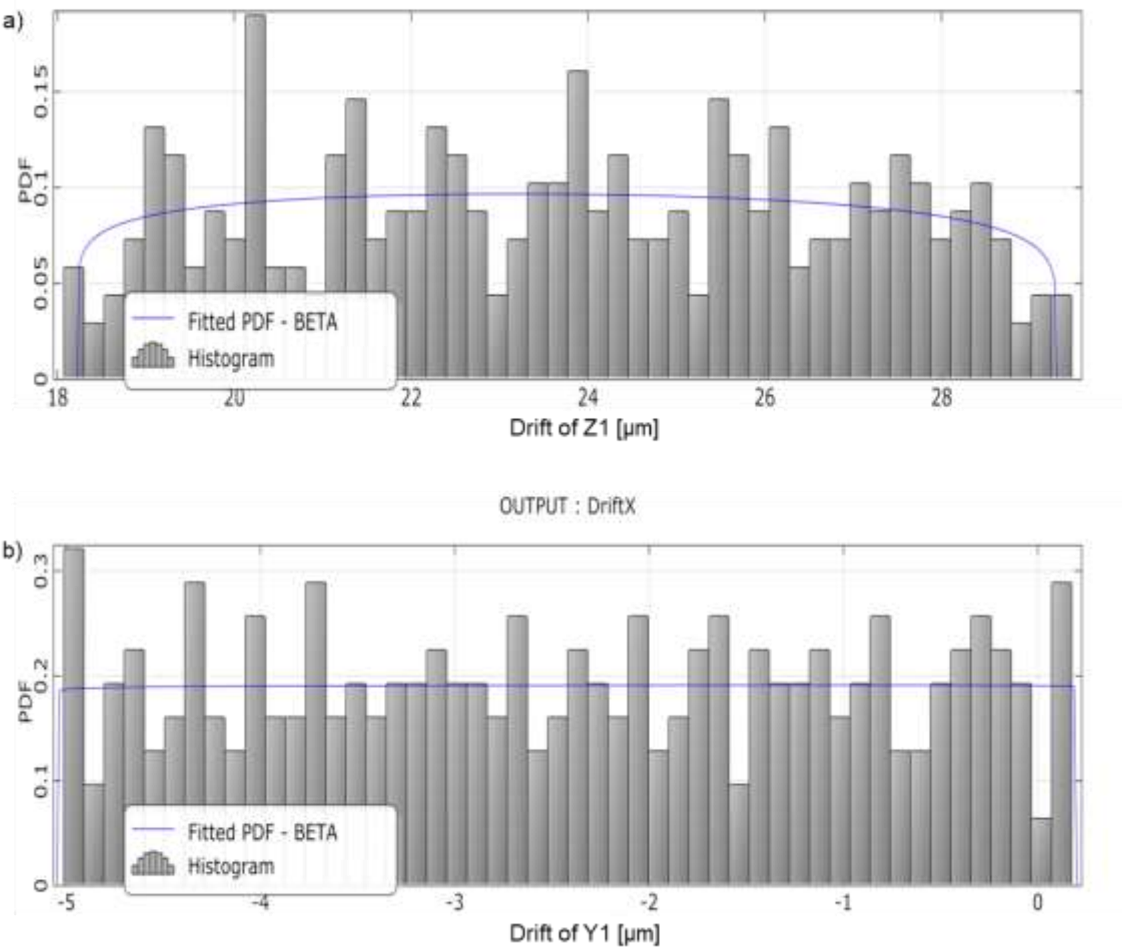


**Figure 99: PDFs of Z1 and X1 drift prediction of magnetic axis for 35 °C operating temperature (alignment measurement at 22.4°C)**

**Table 14: Variances of magnetic axis drift empirical models function of measurement uncertainties**

| $S_{\widehat{Z1}}$ (1 σ) [μm] | $S_{\widehat{Y1}}$ (1 σ) [μm] |
|---|---|
| 3.08 | 1.51 |

The bias error of the model was evaluated as defined in chapter **5.2.5**, **Eq.(5-23)** as a function of the error between the model prediction and the measurement combined with the one σ of the measurement uncertainty (**Figure 100** and values summarized in **Table 15**).

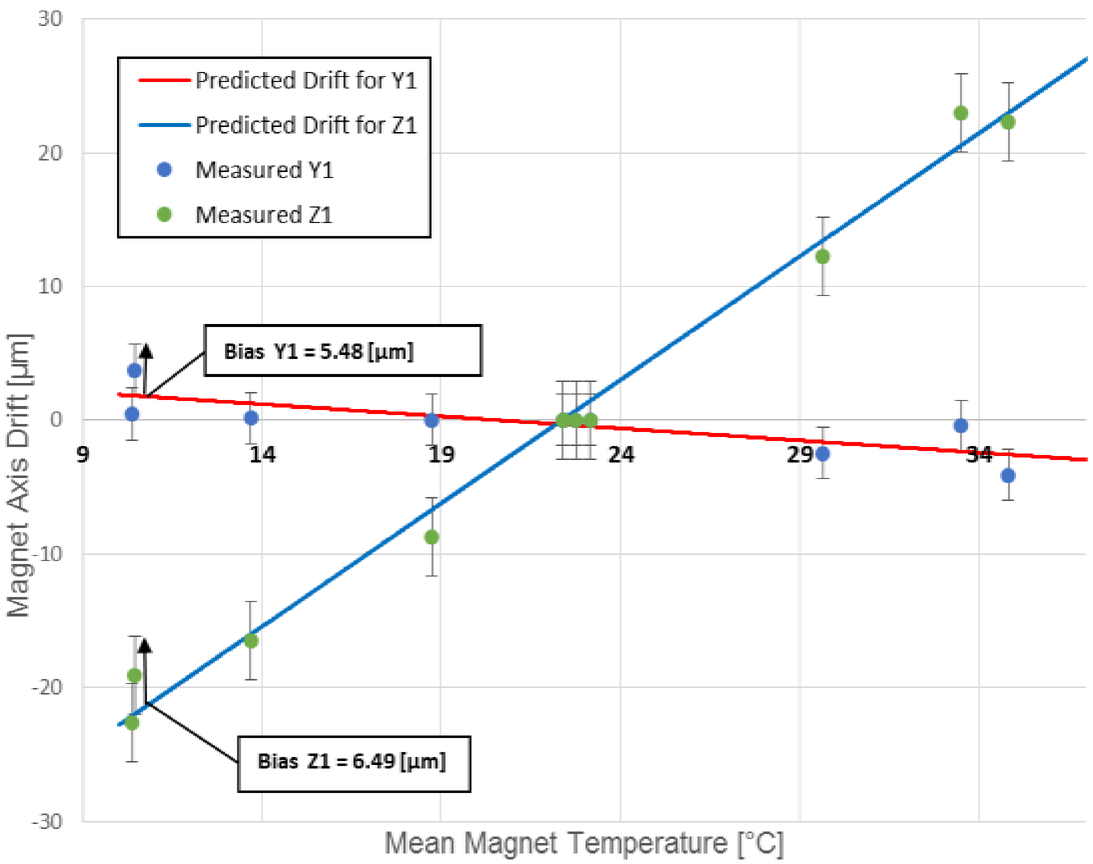


**Figure 100: Bias errors between empirical models and measurements for Z1 and Y1**

**Table 15: Bias error ε between model and prediction (including measurement uncertainty) and error between measurement and prediction $\Delta\,(\mathbf{Z1}-\widehat{\mathbf{Z1}})$**

| $\Delta\,(\mathrm{Z1}-\widehat{\mathrm{Y1}})$ [μm] | $\Delta\,(\mathrm{Y1}-\widehat{\mathrm{Y1}})$ [μm] | $\varepsilon_{Y1}$ [μm] | $\varepsilon_{Z1}$ [μm] |
|---|---|---|---|
| 1.92 | 2.93 | 5.48 | 6.49 |

Finally, the uncertainty of the empirical model at one σ (being a function of the evaluated model variance and bias (**Eq.(5-25)**)) can be seen shown as tolerance band (*U(Y1) 1sigma* and *U(Z1) 1sigma*) bellow at **Figure 101**. A summary of the measurement uncertainties, bias, variance and predicted model uncertainty at one σ can be seen in **Table 16**.

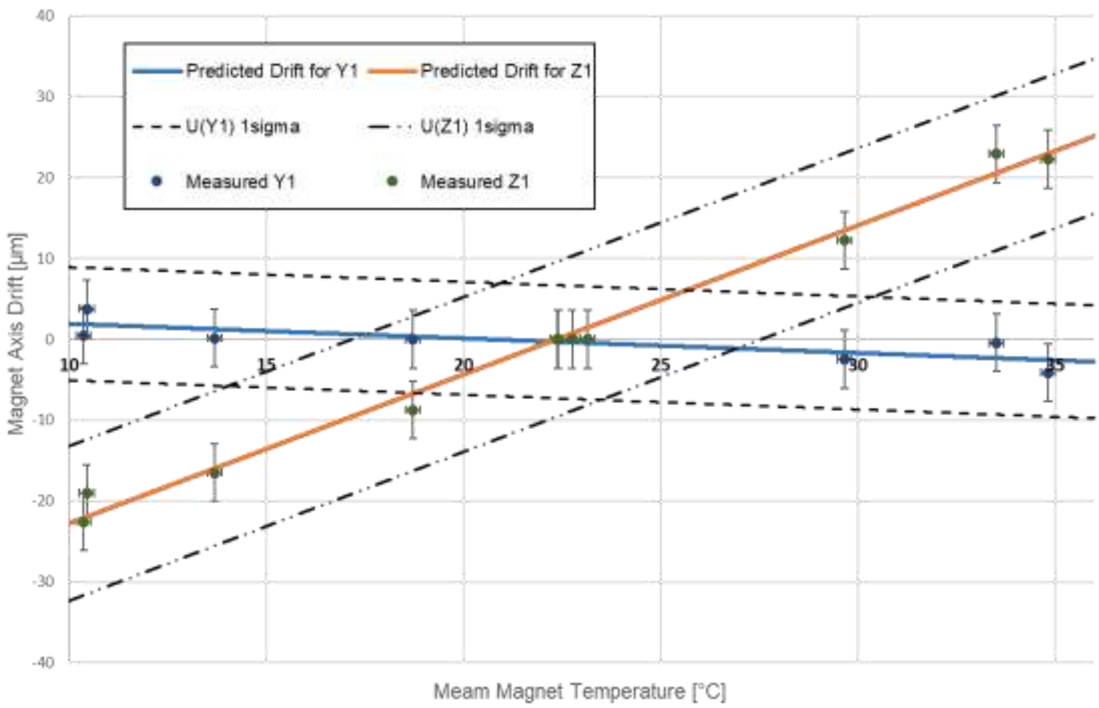


**Figure 101: Magnet axis drift prediction, associated prediction uncertainty and measurement samples**

**Table 16: Total uncertainty of magnetic axis empirical prediction model in Z1 direction as function of measurement uncertainties**

| Measurement uncertainties 1σ [μm]; Square shape | | Empirical model prediction | | | |
|---|---|---|---|---|---|
| U $_{magnet\ axis\ drift}$ | U $_{mean\ magnet\ temperature}$ | $S_{\widehat{Z1}}$(1σ) [μm] | $\varepsilon_{Z1}$ [μm] | a) $U_{\widehat{Z1}}$ (1 σ) [μm] | b) $U_{\widehat{Z1}}$ (1 σ) [μm] |
| 3.56; a=6.17 | 0.182; a=0.32 | 3.08 | 6.49 | 9.57 | 7.18 |

Where the uncertainty was calculated via two different methods: (a) the SUM*U* method (summing the variance and bias arithmetically) as both defined in (Phillips, Eberhardt and Parry, 1997) and b) the RSS*U* method (considering the bias and variance as uncorrelated entities summed by the Route Sum of the Squares law). Only Z1 direction results are shown as most representative for the largest uncertainty at one σ for the empirical model.

### 6.2.2 Uncertainty for empirical model corrections of WPS arms thermal drift

Thermal data from single calibration cycle in from CERN tunnel laboratory (see chapter **5.1.3**, **Figure 44 a)**) can be seen in **Figure 102, b)**. In the same figure**,** **a)** one can see the continuous reading of the WPS sensors mounted at the end

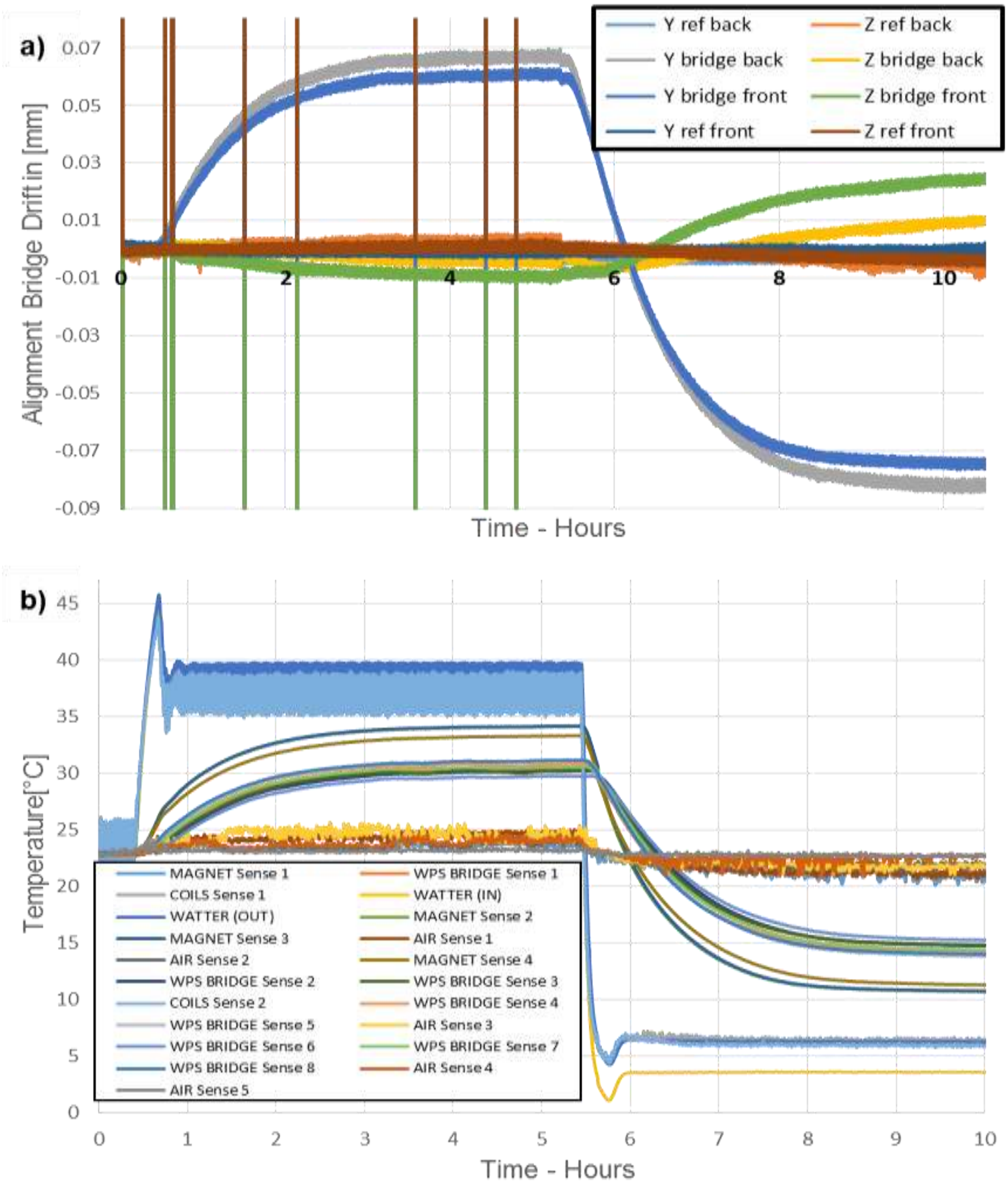


**Figure 102: Single thermal cycle at accelerator tunnel: a) WPS bridges location drift; b) Temperatures recorded**

of each the alignment arm (**Figure 44**). Error! Reference source not found. **shows** the thermal readings taken during the validation cycle in the metrology laboratory CMM system (**Figure** 44 **a)**).

Correlation analysis performed for the various groups of thermal sensors (**Figure 102, b)**) during model mapping stage (**Figure 44**) is shown in Error! Reference source not found. in **Figure 103**.

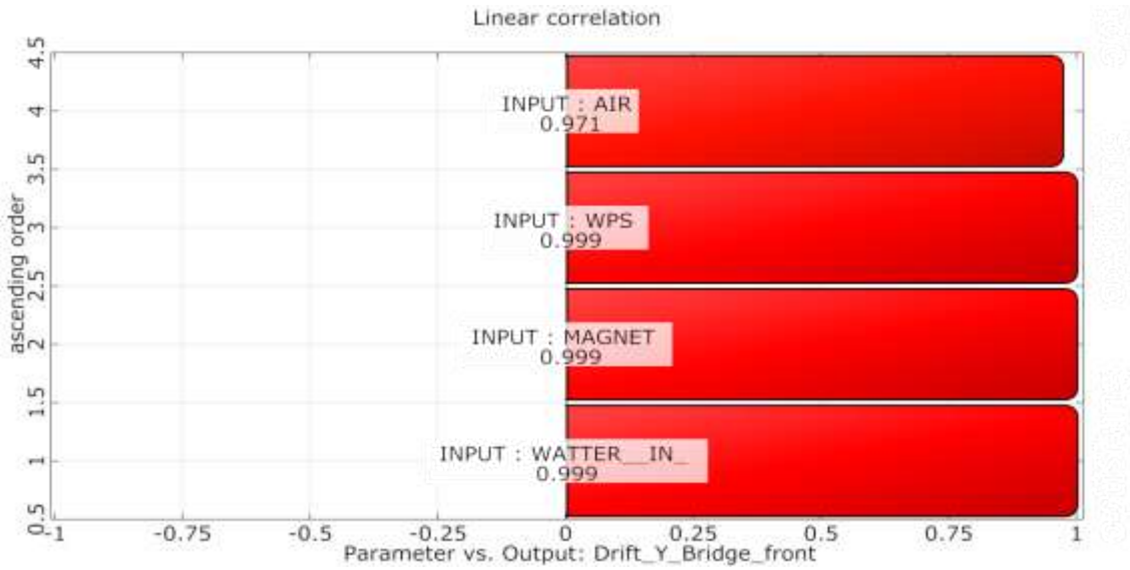


**Figure 103: Average of several thermal sensors data VS WPS bridges drift in Y direction – correlation coefficients (via Opti Slang software 5.1.12)**

Drift in Y and Z as a function of mean magnet temperature and mean WPS bridges temperature as shown in **Figure 104**.

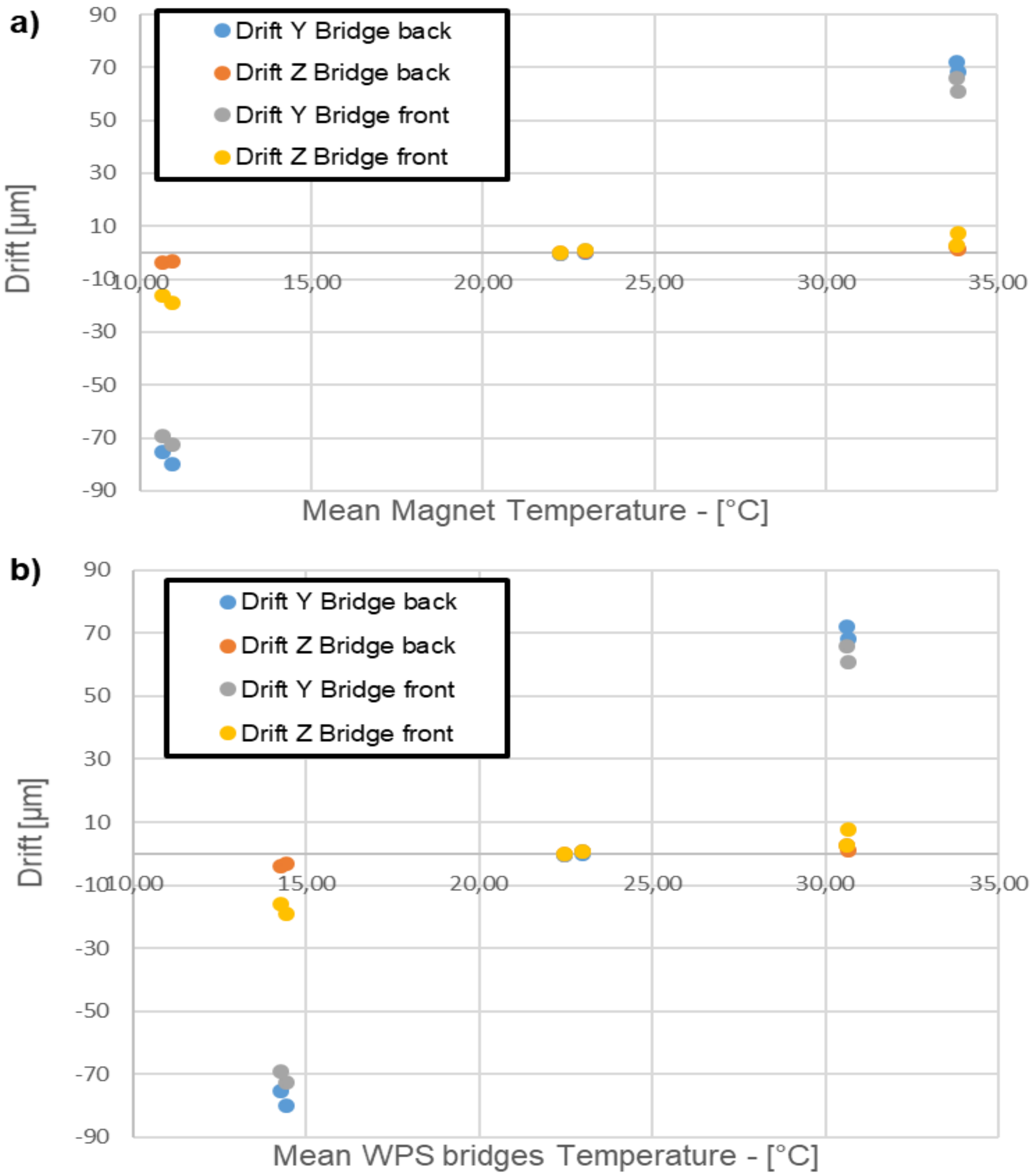


**Figure 104: WPS bridges location VS temperature: a) Mean Magnet ; b) Mean WPS**

The input for the Monte Carlo method $U_{WPSsys}$, $U_{Temp\ Magnet\ sense}$ and $U_{Temp\ WPS\ sense}$ uncertainties and the uncertainty of the CMM used later for traceable validation are summarised below in **Table 17**

**Table 17: Uncertainties of drift and temperature measurements**

| $U_{CMM\_Zeiss}$ @ 1σ [μm]; Gaussian | $U_{WPSsys}$ @ 1σ [μm]; Square shape | $U_{Temp\ Magnet\ sense}$ @ 1σ [°C]; Square shape | $U_{Temp\ WPS\ sense}$ @ 1σ [°C]; Square shape |
|---|---|---|---|
| 2.05 | 1.18; a=2.04 | 0.26;a=0.445 | 0.43;a=0.74 |

Regression analysis was applied, and polynomial equations for the drift in X and Z evaluated. Monte Carlo method was applied to propagate the variances of the polynomial equation parameters and their prediction as summarised in **Table 18**. The PDF of the empirical model's predictions in Z and Y can be seen in **Figure 105 a)** and **b)**.

**Table 18: Empirical model of WPS bridge coefficients their variance and expected output variances for mean Magnet Temperature of 27.9 [°C]**

| **For Y** | | | **For Z** | | |
|---|---|---|---|---|---|
| Parameter | Mean value | Variance S 1σ | Parameter | Mean Value | Variance S 1σ |
| a 1 | 6.40 | 1.15e-14 | a 2 | 0.23 | 4.72e-16 |
| b 1 | -146.00 | 3.00 | b 2 | -5.66 | 2.02 |
| **Y** | F(a1,b1,T) | 3.69 | **Z** | F(a2,b2,T) | 2.04 |

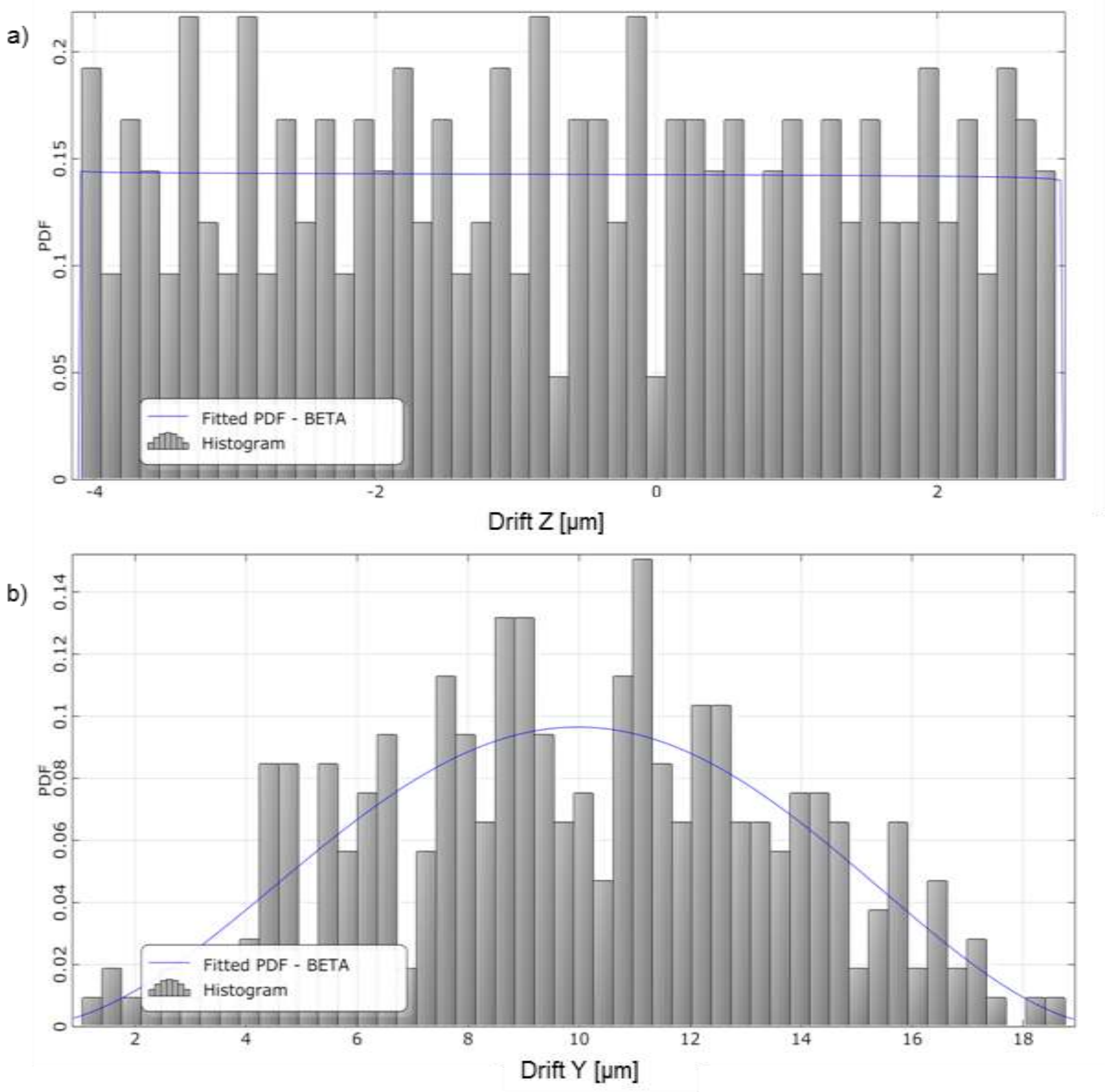


**Figure 105: PDFs of Z1 and X1 drift prediction of magnetic axis for 35 °C operating temperature (alignment measurement at 27.9 [°C]**

The bias error of the empirical models based on the date in ISR 8 tunnel was estimated with respect to readings made by WPS system within the Zeiss Prismo CMM at CERN metrology laboratory. Bias again being the sum of the model error (mode to WPS reading) and of the measurement uncertainty ($U_{WPSdrift}$) **Figure 106**.

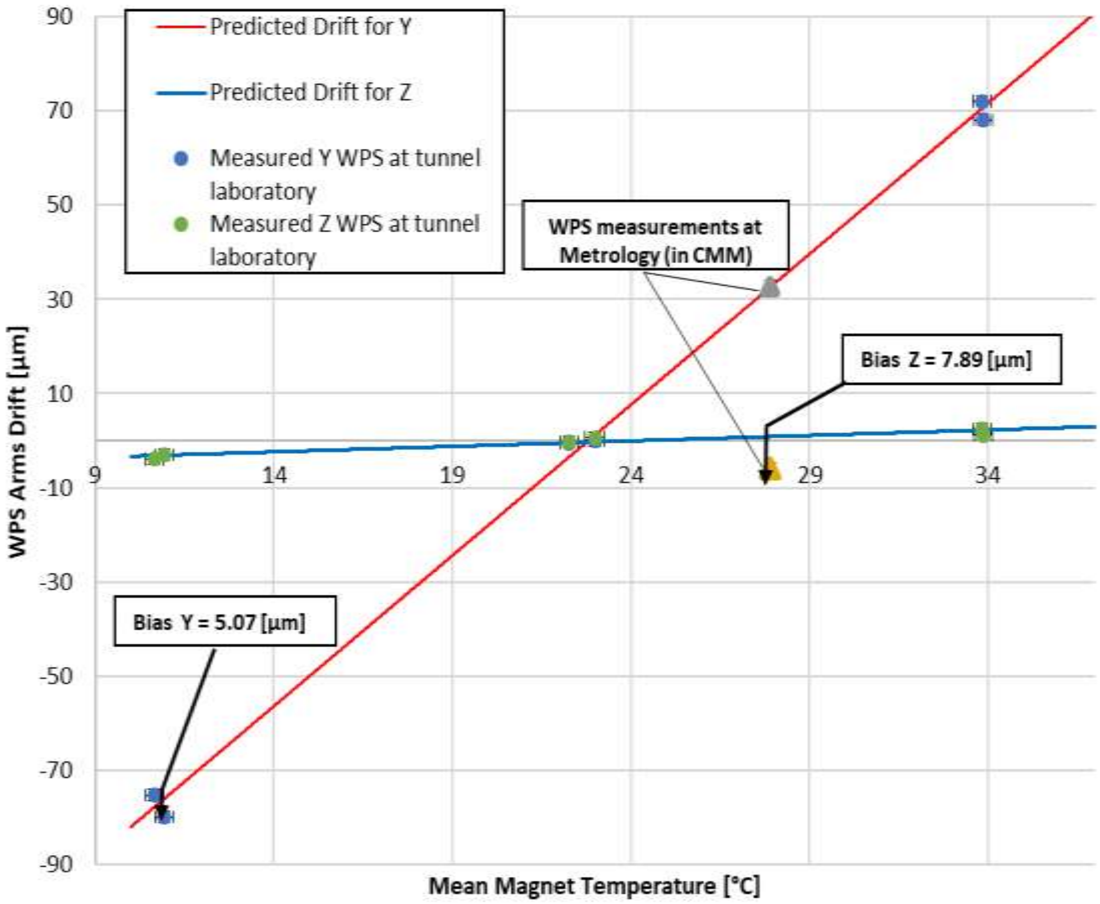


**Figure 106: Bias errors between empirical models and WPS measurements for Z and Y performed both at tunnel laboratory**

The largest bias errors for Z and Y models are summarised below in **Table 19**.

**Table 19: Bias error ε between model and prediction including measurement uncertainty**

| $\varepsilon_Y$ [µm] | $\varepsilon_Z$ [µm] |
|---|---|
| 5.07 | 7.89 |

Finally, the empirical models and their associated uncertainties (as one sigma tolerance around the model – dotted line) function of the model's variance and bias are in summarised in **Table 20** and **Figure 107**.

**Table 20: WPS arms empirical model of drift uncertainty and validation**

| Direction | $S(1\sigma)$ [μm] | $\varepsilon$ [μm] | a) $U$ (1 σ) [μm] | b) $U$ (1 σ) [μm] | ISO test w.r.t.(CMM) **5.2.8** |
|---|---|---|---|---|---|
| $\hat{Y}$ | 3.69 | 5.07 | 8.76 | 6.27 | 0.32 |
| $\hat{Z}$ | 2.04 | 7.89 | 9.93 | 8.14 | 0.58 |

In **Figure 107** the interpolation of the CMM validation measurement next to the WPS validation measurements with respect to the model, and it's one σ uncertainty region is represented.

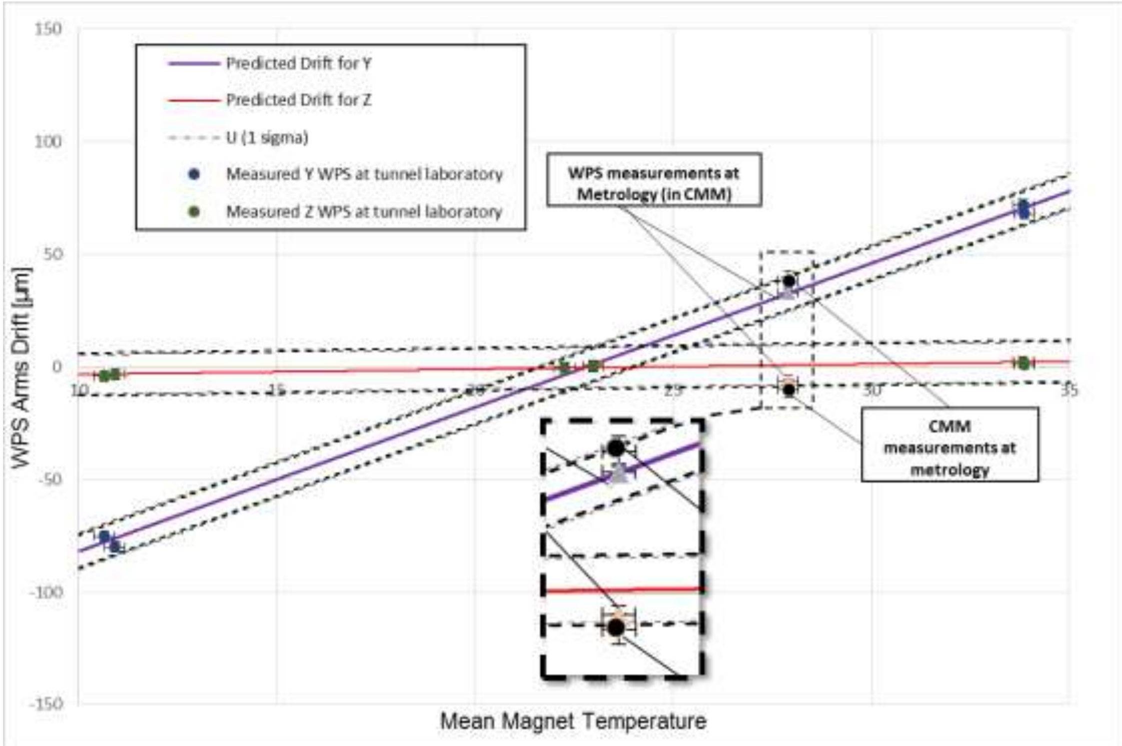


**Figure 107: WPS arms drift prediction, associated prediction uncertainty and measurement samples**

### 6.2.3 Uncertainty of FEM and FEM-based Metamodels for WPS arms drift

Bellow in **Table 21** a summary of the FEM models control parameters and their uncertainties can be seen for ("single component" **5.1.4**) and magnet assembly (**5.1.3**). Single FEM visual results for the single component and magnet assembly thermal fields and related deformation can be seen outlined in **Figure 107** and **Figure 108**.

**Table 21: Models Input parameters and their associated uncertainty**

| **Input Parameter Class** | **Mean Values ranges for class** | $\mathit{Uncertainty}$ **1 σ** | **PDF shape** |
|---|---|---|---|
| **CTE coefficients of materials** **[μm/M/°C]** | From **6.9** (Granite base) to **24.2** (Aluminium WPS arm) | From **1.05** (Granite) to **0.44** (Steel of MBQ magnet) | Square shape |
| **Convection coefficients *hc*** (forced convection) **[W/m^2/K]** | **10.67** (furthest away from air flow facing wall on WPS arms) to **35.33** (closest to air flow facing directly face of WPS arms) | From **0.65** to **2.11** (calibration certificate accuracy = 6% of Heat – Flux sensors reading value) | Square shape |
| **Emissivity coefficients** $\boldsymbol{\varepsilon}$ | **0.172** (Aluminium WPS arms) to **0.275** (Steel of Magnet) | **0.0078** to **0.07** (experimentally) | Square shape |
| **Thermal loads** **[°C]** | **21.23** (Granite Base); **33.16** (Magnet inner faces at coils) | **0.031** (direct measurement at granite base) to **1.62** (extrapolation between magnet outer faces and coils measured temperatures) | Square shape and Triangular biased |

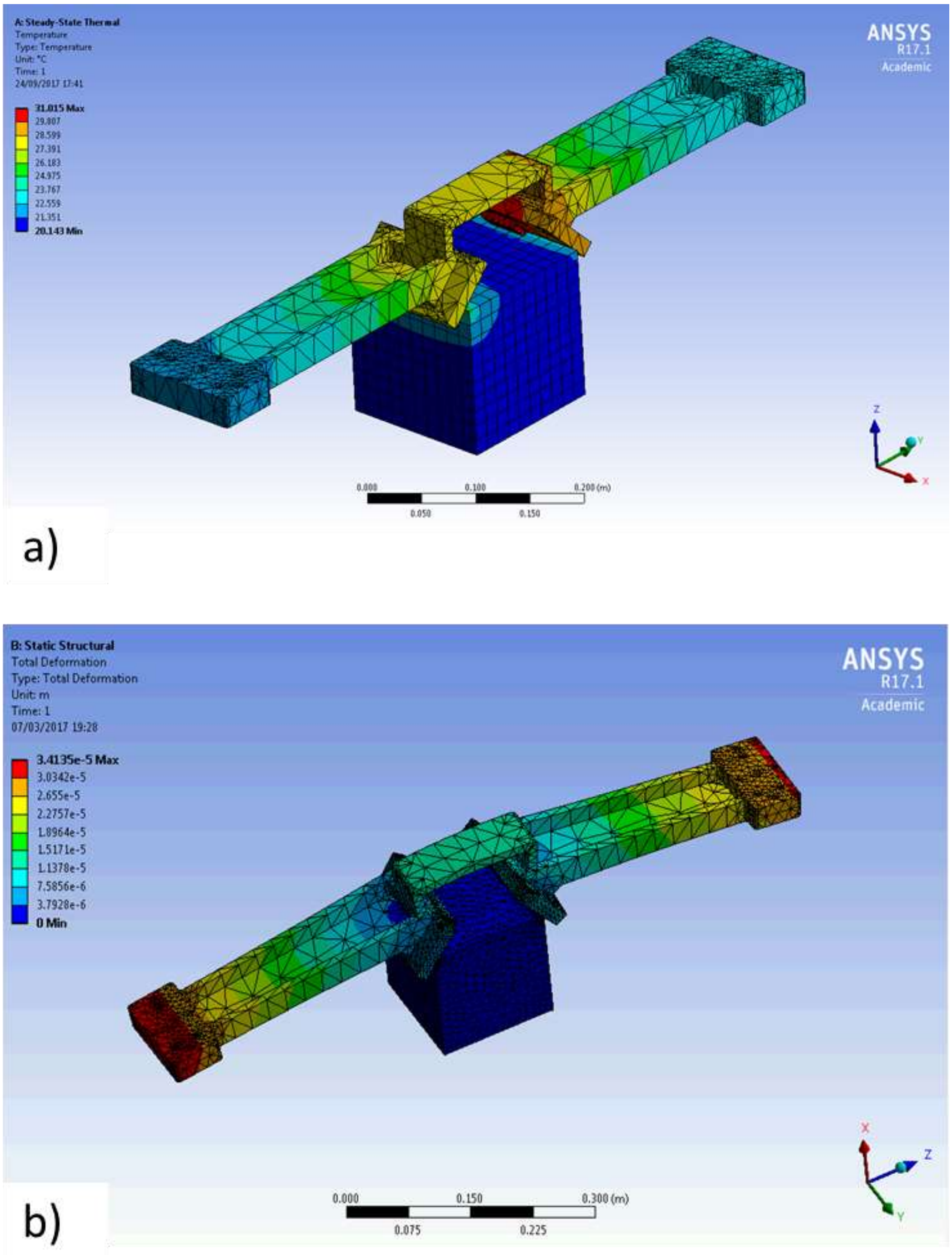


**Figure 108: Single Iteration FEM Single piece results visualisation: a) Thermal field; b) Total structural deformation**

**Table 22: Single-Component Probabilistic FEM results**

| Single Component (WPS arm only) FEM | | | | |
|---|---|---|---|---|
| DoF | Variance **S** 1σ [µm] | **Bias** [µm] | Uncertainty $U_{NE\widehat{single}}$ 1σ [µm] | ISO Test < 1 = PASS (Validation of Uncertainty prediction) |
| **Y (Left)** | 1.10 | 10.16 | **11.17** | **0.35** |
| **Z (Left)** | 1.48 | 7.38 | **8.86** | **0.31** |
| **Y (Right)** | 1.10 | 6.16 | **7.26** | **0.27** |
| **Z (Right)** | 1.48 | 6.10 | **7.58** | **0.26** |

**Table 23: Magnet Assembly Probabilistic FEM results**

| Magnet Assembly FEM | | | | | |
|---|---|---|---|---|---|
| DoF | Variance S 1σ [µm] | Bias [µm] | Error (w.r.t CMM validation reading) [µm] | Uncertainty $U_{NE\widehat{assembly}}$ 1σ [µm] | ISO Test < 1 = PASS |
| **Y (back)** | 6.29 | 3.36 | 3.47 | **9.65** | **0.18** |
| **Z (back)** | 1.12 | 1.22 | 3.8 | **2.34** | **0.62** |
| **Y (front)** | 6.29 | 4.84 | 3.46 | **11.13** | **0.15** |
| **Z (front)** | 1.12 | 10.16 | 11.04 | **11.28** | **0.48** |

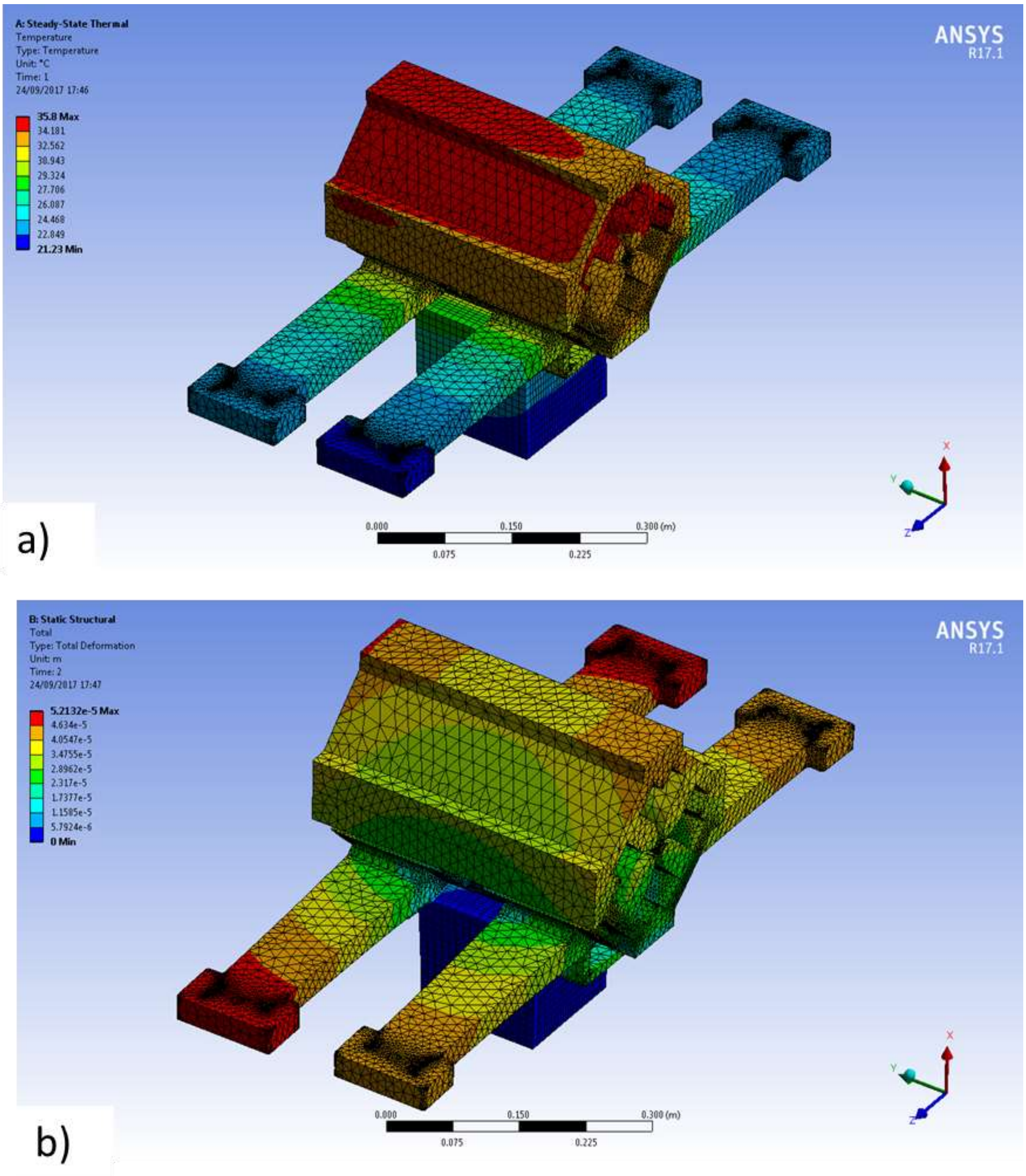


**Figure 109: Single Iteration FEM Simple Assembly results visualisation: a) Thermal field; b) Total structural deformation**

Analytical metamodels based on FEM prediction was created and it's uncertainty studied following the procedure suggested in **5.2.7.** Results can be seen summarised bellow in **Table 24**

**Table 24: Magnet Assembly Meta model analysis results**

| **Magnet Assembly Meta Model FEM** | | | | |
|---|---|---|---|---|
| **Drift direction** | **Variance S 1σ [μm]** | **Bias [μm]** | **Uncertainty $U_{NE\widehat{\widehat{assembly}}}$ 1σ** | **Validation Test < 1 = PASS** |
| **Y (back)** | 0.7 | 11.54 | 12.24 | 0.42 |

# 7 DISCUSSION

In the first section (**7.1**) a discussion of the CMM alignment measurements uncertainty's results (**6.1**) is made. In the second section (**7.2**) the results of from thermal drift models prediction uncertainty (**6.2**) are discussed. In (**7.2**) a general analysis of the results meaning and findings with respect to the hypothesis (**3**), aim and objectives of the thesis are given.

## 7.1 CMM alignment measurement uncertainties

### 7.1.1 Validation of probabilistic CMM measurement uncertainty model

The validation experiment performed for the CMM uncertainty model (**5.2.1**) based on SBC calibration method (**2.2.2**, **5.2.1.1**) has shown results (see **6.1.1, Figure 84**) that prove the capability of the model predicting the measurement errors for the CMM studied (Leitz Infinity - **5.1.7**). The results confirm for the applied case the previous successful validation of the method as seen in (Phillips *et al.*, 2003; Zhang, 2013). In previously published validations (Phillips *et al.*, 2003; Zhang, 2013) the SBC calibration method for CMM probabilistic modelling tended to overestimate between 1.3 and 5 times the uncertainty. The ratio depended on the type/shape of feature/fiducial measured and the type of GPS (ISO, 2011b) task selected. This overestimation is due to the nature of the method that uses ambiguous information from the standard verification tests (**5.2.1.1**) used for the errors mapping. The ambiguity of the tests lead to a larger possible state space of errors than the actual one associated with the particular CMM studied. In the current case, a tight ratio between the predicted uncertainty and the measured error was observed (**Figure 84**). This behaviour can be explained with the physical similarity of the tetrahedron spheres, magnet fiducials (high precision spheres) with the standard verification tests used for the ISO qualification and calibration of the model (high precision spheres). The CMM model, as validated, was employed to study the expected task specific measurement uncertainty of both smallest and largest assemblies of CLIC T1 **(**7.1.2**)** and T4 **(**7.1.3**)** respectively.

### 7.1.2 CLIC T1 alignment measurements uncertainties

The experimental study for the T1 module alignment measurement uncertainty was performed with Leitz Infinity CMM system (**5.1.7**) within CERN metrology laboratory as shown in (**Figure 41**). First, the CMM measurements were taken with no power input into the system as a reference day (Friday) with thermal signature as shown for such thermal cycle in **Figure 85**. Following days' magnet was switched on and thermal, CMM and magnetic measurements were performed and repeated overall several day cycles. Example of such cycle can be seen in (**Figure 85**). As expected, due to the switching (on) the magnet to minimum current (**Figure 85** – green line, Friday), an internal small concentrated heat source was created. This caused, the magnet temperature to start rising during Monday (**Figure 85** - orange) from 20.2 °C to 20.45 °C peak on Wednesday. The aluminium arms thermal field was slightly influenced (seen drifting toward the magnet temperature) by this source as well as seen from the thermal sensor reading on the same figure. However, their temperature followed more closely the peak-to-peak air conditioning bias due to aluminium's lower thermal inertia. The peak drift was recorded between Friday and Monday measurement results as shown in **Figure 86** being at maximum of 2.77 μm/m for the magnet top. Friday to Wednesday results showed a reduction of relative 3D distance drift between the measurement and reference targets of maximum drift of 1.66 μm/m for the magnet top. This is believed to be due to the room AC system managing actively compensating for the additional heat source (the switched magnet) by that day. The aluminium alignment arms reduced their dimensional expansion from 1.34 μm/m to -0.15 μm/m (contraction) for Friday to Wednesday too. This is believed to be due to the lower thermal inertia of the aluminium component and further distance from the concentrated heat source (magnet coils). Magnet targets, closest to the heat source (magnet coils), had the highest recorded drift (**Figure 86**). These results further contributed to the task specific uncertainty estimation.

This study was performed for the calibration data of Leitz Infinity CMM (**Table 7**) measuring available and mounted spheres on T1 assembly with shape tolerance of 1 μm (**Table 6**). This study only accounts for the CMM geometric machine errors, contact probe heads repeatability and features form errors. It is important to note that this particular study does neither include the magnetic measurement nor the thermal errors nor the non-contact sensor repeatability and offset error contributors. Those are later shown in **Figure 89**. Thus the result showed that the modelled CMM tactile uncertainty being one of several contributors for the task specific uncertainty for a sphere location is significantly larger than the MPEE given by the manufacturer. Being 3.81 µm at 2 sigma VS the MPEE = 0.95 µm for the Leitz infinity for the maximum point to point distance on the T1 assembly – 0.63 m. The results in **Figure 87** are represented in 2σ (95%) coverage interval, as suggested as standard in (BSI ISO/TS, 2013). This is believed to be due to the MPEE qualification given by the manufacturer is based on a single specific test rather than complete task specific uncertainty propagation. The MPEE does not include all the possible errors due to the multiple measurements required for the Dimensional Frame of Reference and defining the location of a fiducial within it.

The CMM uncertainty model for the Leitz Infinity was ran for fiducials with varying form errors/specification as a separate study. Results are highlighted in **Figure 88**. It was observed that uncertainty significantly increases as a function of fiducials spheres shape quality. For example, using the highest commercially available grade spheres (ISO-3290) with 0.13 µm form error can lower the CMM measurement uncertainty by 0.5 µm to a total of 3.36 µm. However, using spheres of poorer quality (5 µm), CMM uncertainty can rise by 3.87 µm to a total of 7.23 µm (**Figure 88**). In all cases the CMM modelled uncertainty was seen significantly higher than the MPEE reported by the manufacturer.

The task-specific alignment measurement uncertainty for T1 assembly was reported as the sum of all correlated and uncorrelated sources as shown in blue, **Figure 89** - 6.91 µm @ 1σ). The uncorrelated error sources were the magnetic measurement, the thermal drift wire measurement and the datum measurement. The offset between tactile and non-contact sensor was conservatively accepted as a bias value equal to the worst value of the MPS/MPE tests (3 µm **Table 7**, Orange in **Figure 89**). Wire measurement standard uncertainty was modelled

(1.34 µm grey in **Figure 89**) using the same CMM model based on SBC as with the spheres. However, the SBC calibration was done for the non-contact sensor, mounted and tested on Leitz CMM with measured repeatability of finding the centre of cylinder = 0.7 µm (**Table 7**). The datum reference uncertainty was estimated as the location tactile measurement uncertainty of a sphere part of a three-sphere defined datum for the same CMM and tactile probe studied in **Figure 87**. The thermal drift uncertainty was the one estimated experimentally for the assembly (**Figure 86**). The magnetic measurement uncertainty was found by the magnetic measurement expert studies and quoted in (Mainaud Durand *et al.*, 2017). Results are given in 1σ in relation to the targeted alignment uncertainty defined as well in 1 σ and can be seen in **Figure 89**.

From this study, it can be deduced that the MPEE given by the manufacturer not a correct reference for alignment measurement uncertainty. In the current experiments it was shown that it underestimates the assembly alignment measurement uncertainty by a factor of nearly 15, if task-specific uncertainty is presented as expanded to k=2 or 2σ (13.81 µm).

### 7.1.3 CLIC T4 alignment measurements uncertainties

The results for the CMM uncertainty for T4 assembly were, as expected, higher du the larger assembly size and lower performance CMM used (Zeiss Prizmo instead of Leitz infinity) than the T1 results but not by large amount as shown in **Figure 90**. The MPEE, in this case, covered the sphere alignment uncertainty. From this It can be concluded that the CMM measurement uncertainty is not directly proportional to the assembly size as the MPEE. On this occasion the, MPEE could however cover the tactile location measurement uncertainty in contrast to the case with T1 assembly. In this case the MPEE overestimates the CMM uncertainty. It is important to note that the CMM uncertainty was modelled without the inclusion of all other uncertainty contributors including the thermal drift errors.

The T4 full length assembly module prototype is not yet produced and the non-contact sensor used has never been integrated with the Zeiss machine before. Thus two assumptions were made for the further part of the alignment task specific uncertainty analysis: Firstly, the tactile to non-contact offset was assumed to be the same as the one measured on the Leitz Infinity (3 μm at 1 σ). Secondly, the thermal effects for the T4 assembly were considered linearly increasing with size from the one measured for T1 due to the longer size of the assembly. This was accepted viable due to the exact similarity of the two assemblies different only in their length dimension **Figure 7**. Both assumptions can be validated by future work once the T4 assembly is available for experimentation.

The spread of the various uncertainty contributors and the grand summation to the task specific alignment uncertainties can be seen in **Figure 91**. The main variation of T4 assembly results with respect to the T1 is related to the expected increased thermal drift (3.1 μm extrapolated from the 2.55 μm/m experimental results for T1). Tactile location measurement uncertainty has a minimal variation from 1.91 μm **Figure 89** for T1 to 2.05 μm for T4 **Figure 91**. In this study, the MPE covered the 1σ of each of the separate uncertainty contributors. However, it failed again to cover the complete task specific alignment uncertainty of 15.92 μm @ 2σ with a factor of three.

### 7.1.1 Summary of CMM alignment measurement uncertainty's

The CMM probabilistic modelling implemented via calibrated by SBC method PUNDITCMM™ software was successfully validated via traceable artefact. The measured errors of the Leitz Infinity CMM fitted closely with the predicted by the model uncertainty. This is believed to be due to the similarity of the reference spheres used for the calibration of the model and the studied artefact and fiducials on the magnet. The method combined with reference thermal drift measurements was applied for the estimation of the T1 and T4 alignment measurement uncertainty. Important findings were the confirmation that the MPEE of CMM system cannot be considered as an accurate input for the alignment uncertainty budgets. A complete task-specific uncertainty evaluation is required. Critical for lowering the alignment uncertainty was the use of high-quality sphere fiducials and the minimisation of any thermal drift effects during metrology. The task-specific alignment measurement uncertainty was found to be within the 12 μm @

1σ targeted for CLIC budget and provided figures for a left-over of the consumed budget of 8.89 μm and 9.80 μm at 1σ for T1 and T4 type modules. This was calculated as the uncorrelated leftover (square root of the of the subtraction of the squares) with respect to the targeted uncertainty.

## 7.2 Thermal compensation models uncertainty

### 7.2.1 Magnet axis drift compensation uncertainty

As seen in **Figure 93,** a) and b) the magnetic axis drifts dominantly in vertical Z direction with minimal drift in Y as function of the assembly temperature variations. This is believed to be due to the general expansion or contraction of the magnet assembly being constrained only vertically for this experimental setup. Further in the analysis performed (**Figure 94**, **Figure 95**) It can be seen that drift in both Y and Z are mostly correlated to the thermal variation of the magnet yokes steel body part of the assembly. This is expected, as the magnetic axis location is dictated by the location and shape of the magnet assembly yokes. Thus any change in the thermal field would cause a change in the yokes dimensions that affect the magnetic axis location. From this correlation analysis, it can be concluded that the drift of the magnetic axis can be best represented as a function of a temperature measured on the steel magnet part of the assembly. As the magnetic axis location is the sum of the total thermal state of the magnet, then an assumption was made that it would be best to define the axis drift as a function of a mean magnet temperature measured by multiple probes distributed around the steel magnet and its yokes. This being the average temperature form the distributed sensors around the magnet yokes. Example of such temperature distribution can be seen in **Figure 96** where the uncertainty on the mean is taken as square uncertainty which 2a is equal to the total range for the thermal readings. Further in **Figure 97** the relationship between magnet axis drift measured at the front and back in X and Y can be seen as relationship to the mean magnet temperature. In there again clearly linear relationship between the magnet axis vertical drift and the mean magnet temperature can be observed. The experimental data was used to fit linear empirical model for the magnet axis drift for Z and Y (as shown by **Eq.(6-3)** and **Eq.(6-4)**). Following the procedure proposed in **5.2.5.3,** the empirical model bias and variance were estimated. The Monte Carlo modelling showed a larger variance (see **Table 13**) in the **b1** and **b2** equation parameters responsible for the linear model intercept. Propagating the coefficients variance and measured mean magnet temperature uncertainty through the model provided estimates for the empirical model prediction variance as shown in **Table 15** is between 3.08 μm for Z and 1.51 μm for Y which is less than the uncertainty in a single magnet axis measurement 3.56 μm at 1 σ. The empirical model was best fitted using multiple experimental measurements thus relying on more correlated information for its definition with respect to a single measurement. According to GUM (JCGM, 2008a) if all systematic errors are compensated a model uncertainty can be represented by Bayesian theorem and thus probabilistic propagation of its parameters. Thus a model uncertainty would be a function of its control parameters variance. This shows that if a model can represent perfect or near perfect the real behaviour of a measurand it is uncertainty can be lower than the uncertainty of the single measurements used for its creation. This behaviour is one of the foundations for the Simultaneous Localisation and Mapping (SLAM) algorithms widely applied in the field of robotics and automation (Durrant-Whyte and Bailey, 2006). In the current case, however, the model is not a perfect representation of reality and bias errors were measured as shown in **Figure 100** and **Table 15**. The bias of the current model is significantly larger from both the measurements uncertainties and the model variances (5.48 μm for Y1 model bias to 6.49 μm for Z1 model bias). This bias is due to the imperfect representation of the linear model to the real behaviour of the magnet axis drift.

As seen in **Figure 101,** the one σ predicted uncertainty being a function of the measured bias and modelled variance covered the entire measures sample set with their associated uncertainties. No alternative and more accurate method than the vibrating wire (**5.1.9**) to cross check the results is currently known. No international standard of magnetic axis does exist. However, the magnetic axis is defined as the location of the lowest magnetic field strength in a focusing magnet. Magnetic field strength, however, is defined as a function of two other SI units H=[Amper/Meter]. Currently, in the magnetic measurement of focusing magnets axis, no traceability chain has been established to national institute and SI unit standard. Thus it is not possible to ultimately validate the uncertainty of the magnetic axis measurement systems. The uncertainty region is based and trusted to the available for the accelerator laboratory magnet metrology expert's evaluation and intellectual honesty. This can be a limiting factor in further validating the magnetic measurement systems uncertainties. Thus a creation of traceable, portable and stable magnetic axis standard for the purpose is recommended. Such has standards have previously been created for inter-comparison and study of the national institute's magnetic measurements uncertainties (Garrett and Pissanetzky, 1971; Weyand *et al.*, 2001). Dialog and common research program between accelerator institutes and national laboratories for the creation and validation of such magnet field transferable artefact is suggested as possible future work.

### 7.2.1 Uncertainty for empirical model correction of WPS arms thermal drift

In parallel to magnetic axis measurements in the accelerator tunnel laboratory, thermal drift of WPS alignment arms, part of the magnet assembly (**5.1.3**), was mapped with the WPS alignment system (**5.1.8**). The results for temperature and WPS sensors reading for component location from a single thermal cycle can be seen in **Figure 102.** The drift the WPS alignment arms was observed predominantly in the Y direction (main direction of arms expansion). Drift in the Z direction was as well present due to structural deformation from magnet assembly constraints which was later validated from the FEM modelling results (**6.2.3**).

The same experiment was repeated within the body of Leitz Infinity CMM (**5.1.7**) at CERN metrology laboratory for validation. In there however the thermal loads were variated away from the one during the mapping process (in the accelerator laboratory) by introducing forced convection with an air fan. This caused larger thermal gradient between the temperature forced by the hydraulic control system of the magnet coils and the temperature of the WPS arms as shown in Error! Reference source not found.. This was done in order to simulate expected variance in actual alignment conditions with respect to metrology conditions.

Correlation analysis between the various thermal probes and drift measurements was performed. The analysis reviewed strongest correlation between the water input temperature and Z and Y deformation. This was however disregarded as useful sensorial data for any model due to the nature of the chiller controller system behaviour. The mean water temperature has a large sinusoidal variance (as seen in **Figure 102, b)**) thus having a large error on the mean from an instantaneous reading. Additional to that water temperature although highly correlated to the X and Y drift does not poses any information on the any external thermal loads such as the one imposed by convection. Next and with really close to correlation for Z direction was the mean WPS temperature Error! Reference source not found. and for Y the mean magnet temperature **Figure 103**. Both were used to define the drift in Y and Z as shown in **Figure 104**.

The uncertainties of the WPS alignment measurement system and thermal measurements were propagated (following **5.2.5.3**) through the regression analysis and thus empirical models best fitting the data. This provided variance in the order of 3.69 μm @ 1σ for Y and 2.04 μm @ 1σ for Z. Bias was evaluated with respect to the WPS measurements performed at the CMM being between 5.07 μm for Y and 7.89 μm for Z. The final prediction uncertainty of the model was estimated between 6.27 μm and 8.76 μm in Y direction and 8.14 μm and 9.93 μm in Z depending on which summation rule was used (**Table 20**)**.** The prediction uncertainty can be seen plotted in **Figure 107** as tolerance bad around the empirical model prediction. In the same figure the validation measurements made by the CMM can be observe plotted with their evaluated 1 sigma uncertainty. Both WPS and CMM measurements methods can be seen producing results with uncertainties within the 1 sigma predicted uncertainty interval for the empirical model. Final ISO validation tests were performed according to **5.2.8** with results shown in **Table 20.** The test was successfully passed (<1) proving the validity of the predicted model uncertainty region by an independent experiment and measurement system.

Thus the uncertainty prediction methodology suggested in **5.2.5.3** was successfully validated.

### 7.2.2 Uncertainty of FEM and FEM-based Metamodels for WPS arms drift

FEM models for both the single WPS arm component ("single component" **5.1.4**) and magnet assembly (**5.1.3**) were created. The FEM models were continually improved and their accuracy with respect to experimental measurements increased. This was done by first evaluating the most influential parameters to the final prediction parameters using Correlation and other statistical analysis performed in Opti Slang Software (**5.1.12**). Then, the model itself was corrected iteratively (thermal loads, physical constraints and other) until its bias errors were minimised optimally in the time available. The most influential parameters used as input for the models were experimentally derived with associated uncertainty defined by a PDF function with associated variance. Those can be seen summarised in **Table 21.** The calculated results for both thermal field and related structural deformation for the single component (**5.1.4**) and magnet assembly (**5.1.3**) are shown in **Figure 107** and **Figure 108**. Those are the results of a single deterministic simulation performed. The same deterministic ANSYS model was used as a solver for probabilistic study as described in (**5.2.6**). In this study, 300 samples (distributed efficiently via the application of Latin Hyper Cube technique **2.1.1**.) of the input parameters were propagated through the FEM models as solvers. This created PDFs are describing the variance of the FEM models as a function of the variance of the measured input parameters (**Table 22** and **Table 23**). The final bias of the FEM and their metamodels were evaluated by WPS measurements in CERN metrology laboratory for the magnet assembly and CMM for the single component. For the magnet assembly, and single piece the CMM measurement with Zeiss Infinity CMM was used uncertainty model validation. A summary of the results including visual representation can be seen for both in **Table 22, Figure 111** (single piece) and Error! Reference source not found. and **Figure 109** (magnet assembly). In both figures, the mean of the PFEM and its predicted uncertainty ( a function of the variance and bias) can be seen compared to the validation measurements in the CMM laboratory. All measurements for both single component and magnet assembly passed the validation test with a result <1 as shown in **Table 22,** (single piece) and **Table 23** (magnet assembly).

Those results validated the suggested methodology **4.3**, and procedure **5.2.6** showing that it is possible to evaluate the exact prediction uncertainty of an FEM model.

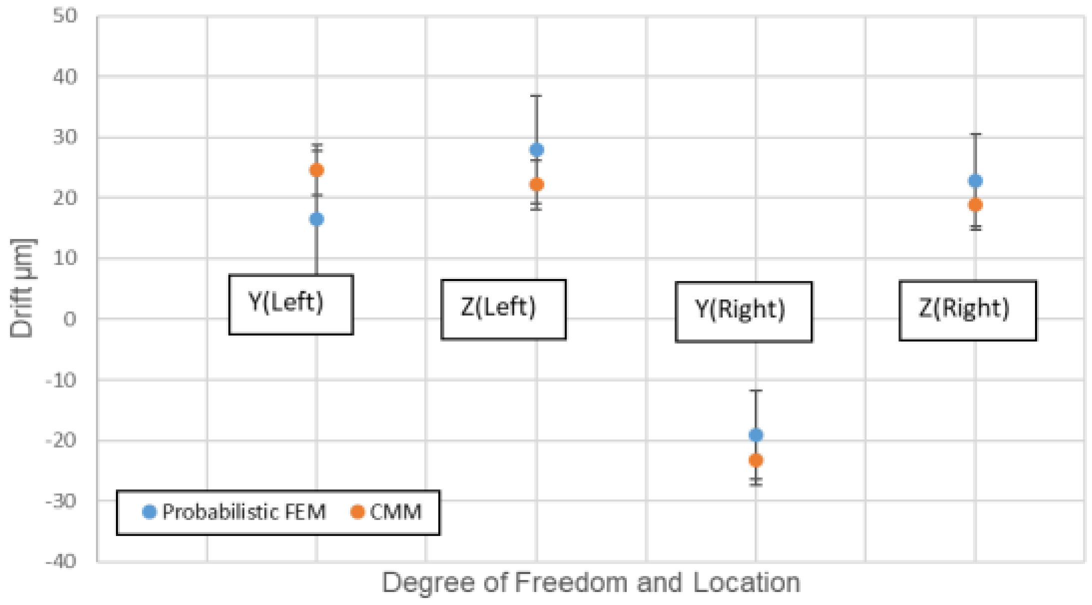


**Figure 111: Predicted vs measured during validation stage drift and associated 1 sigma uncertainties visualisation for WPS arms as single component (5.1.4)**

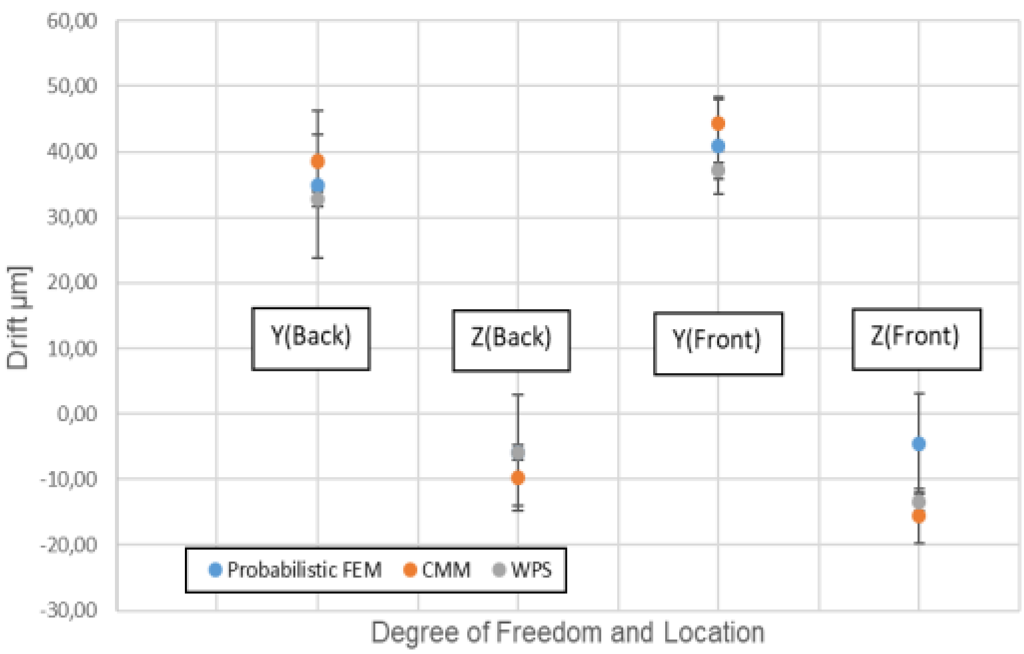


**Figure 110: Predicted vs measured drift and associated 1 sigma uncertainties visualisation for the magnet assembly (5.1.3)**

Using the statistical data available from the Probabilistic FEM, a Metamodel was created. The Metamodel represented a polynomial analytical best fit to the Probabilistic FEM samplings, regarding them as a form of 'virtual measurements' (**5.2.7**). The correlation analysis defined the output deformation best described by a mean magnet temperature measurement similar as with the empirical analysis.

A probabilistic analysis (using MATLAB and Dynardo software **5.1.12**) was performed on the Metamodel polynomial function thus establishing its variance as a function of the FEM prediction uncertainty and measured temperature. Due to the high number of samples (300 samples) the final variance of the metamodel function was estimated significantly lower (0.7 μm **Table 24**) than the input uncertainties (11.13 μm for FEM prediction of drift in Y direction **Table 23**). This lowering of the meta model variance as function of the increase of the number of samples again can be explained due to the same reasons as with the empirical models (chapter **7.2.1**) founding its origins in the cross correlation of the sample data (Durrant-Whyte and Bailey, 2006). This results showed that with the capability of numerous virtual FEM samples the variance of the metamodel used can be significantly decreased.

The bias of the Metamodel was evaluated as the sum of the largest error between the Metamodel polynomial and the FEM samples combined with the one σ of the FEM uncertainty (determined by the previous analysis). The results together with the final predicted uncertainty for the Metamodel can be seen summarised in **Table 24**.

### 7.2.3 Summary of CMM alignment measurement uncertainty's

In the current chapter, the results of the uncertainty evaluation of three different types of thermal compensation models (Empirical, Probabilistic FEM and Metamodel based on Probabilistic FEM) following, the method suggested in **4.3** were outlined. The model prediction uncertainty was defined as the direct sum of the model's variance evaluated by Probabilistic based model which parameters were calibrated by precision experiments and bias to reference value by a precision drift measurement combined with its one σ uncertainty. For both

Empirical, PFEM and Meta-model, a validation experiment was performed within a traceable CMM system. Thus the drift was determined by a precision measurement system working on a principle independent to the one used for its calibration or bias error detection. All validation measurements with their uncertainties were captured successfully by the predicted for the model's uncertainty passing the validation ISO test **5.2.8** thus proving the hypothesis suggested in chapter **3.1**. The combined uncorrelated uncertainty for compensating the magnetic axis and alignment arms was evaluated to be between 13.79 μm and 15.54 μm as shown in **Figure 112**

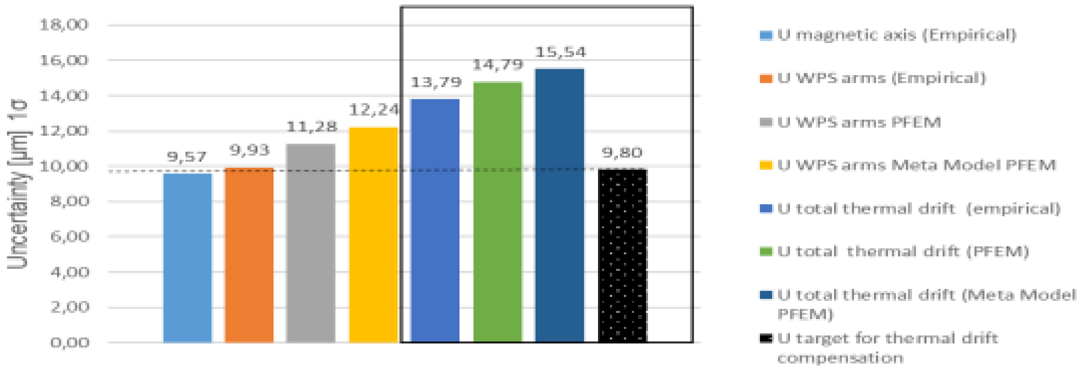


**Figure 112: Thermal compensation uncertainties for various approaches vs targeted drift uncertainty**

It was shown that the current thermal compensation models could not reach the desired uncertainty target if 9.8 μm for imposed on the assembly thermal conditions variations.

## 7.3 Results contribution to knowledge

The results for CMM measurement (**6.1**) and thermal drift compensation uncertainties (**6.2**) have confirmed the suggested in **3.1** hypothesis. Notably that probabilistic modelling combined with traceable to the meter, high precision reference measurements can accurate predict measurement or compensation models uncertainty. Moreover, the results showed that accurate knowledge of alignment measurement uncertainties is critical in tight alignment and assembly budgets.

The results for CMM measurements showed that it could be erroneous and misleading to use a metrology machine qualification such as the MPE for any high precision alignment uncertainty and error budgets. It is important to perform a full and specific uncertainty analysis of the system used as previously discussed in literature (Bottura *et al.*, 2006; Leãoa, 2017). The probabilistic CMM uncertainty modelling calibrated by SBC method proved to be capable of evaluating the task-specific uncertainty of a fully calibrated CMM. The validation was done with the help of traceable to national institute reference artefact. However, when performing measurements of an assembly where known and unknown bias errors exist (drift due to internal heat sources) such statistical model might not be entirely sufficient. Following the suggested hypothesis (**3.1**) in the current PhD thesis, the additional bias errors were estimated with the help of reference measurement of the 3D distance drift. In this way, both the CMM system variance the additional bias error was estimated in an absolute manner (traceable to the metre standard) and was specific for measurement case. The most important conclusion would be that, by the use of Probabilistic based CMM uncertainty model, the metrologist can know which error parameters are critical for their alignment measurement performance. In the case of magnet alignment with sphere fiducials, that was the precision of the sphere fiducials shape tolerance and the minimisation of the thermal drift during metrology.

The studies and application of the hypothesis on thermal drift validated the importance of addressing thermal error and drift problems in a detailed manner. Frequently missed in alignment measurement budget, a posteriori of measurements thermal drift can be critical for successful alignment. Previously uncompensated in accelerators alignment, the results showed that thermal effects could drift the magnetic axis location by dozens of μm and alignment features locations by as much as hundreds of μm and more. Thus for tight precision applications, not only accurate alignment metrology is important but precision compensation for the a posterior of metrology and during alignment thermal effects. Although thermal compensation by the use of models has been performed on many occasions in state of the art (Weck *et al.*, 1995; Ramesh, Mannan and Poo, 2000; Ni and Wu, 2003; Schwenke *et al.*, 2008; Morishima *et* *al.*, 2015; Ross-Pinnock and Bingru Yang Glen Mullineux, 2016), no statements of uncertainty validated and traceable to the meter standard were found. In the current work the method (**4.2**) and procedures (**5.2.5** to **5.2.8**) proposed were applied. Thus the thermal compensation models were regarded as a form of virtual measurements and validated against traceable artefacts being the high precision measurements of the real drift. The input parameters for the various compensation models were evaluated themselves with valid uncertainty statements and propagated through the models. The evaluated variance by the probabilistic methods was combined with the measured models bias in predicting real drift of components and assemblies. An outline of the evaluated variances, biases and uncertainty for the different thermal error compensation models can be seen below in **Figure 113**.

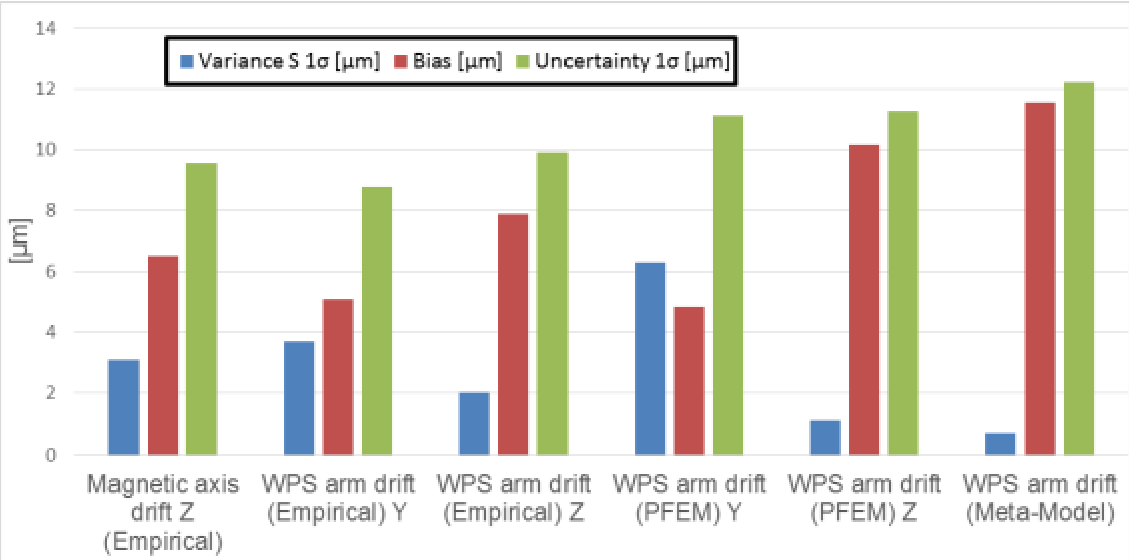


**Figure 113: Thermal error compensation models variance, bias and combined uncertainty**

It is important to outline that measured bias is a predominant component of the prediction models uncertainties, exception makes the PFEM model for Y direction of alignment bridge drift **Figure 113**. The larger bias errors can be explained by the not perfect representation of the models to reality. In this particular occasion modelling the drift in Z direction had large systematic bias error (**Figure 110**). For Empirical models, large bias errors can occur due to the difference between the thermal conditions at calibration and the one when the model is applied. The further thermal conditions operation drift from the one in the calibration of the model, the larger would be the bias error of such model. Alternative would be to use accurately calibrated FEM. Applying Probabilistic FEM, one can not only learn the variance of his predictions but as well locate via correlation based analysis which are the most influential parameters to the output variance. For example, uncertainty of 10 % in the CTE coefficients of the materials could have large impact on the uncertainty of drift prediction. Thus use of more precise measurements on the CTE of the materials can lower the variance of the FEM model prediction.

It is important to note that without actual physical reference measurements the bias error of a model cannot be determined and thus the true FEM prediction uncertainty. Performing calibration measurements however in a manner traceable to the meter can help calibrate a Probabilistic FEM and FEM Meta-models to values close to the empirical one. This would mean that, if once a numerical model is calibrated with minimised and known bias errors it can be applied for any desired conditions with known uncertainty statement. Thus with minimum number of experimental measurements the designers can use it to predict and compensate deformation behaviour for a wide band of conditions that might not be economically viable to be tested and represented by empirical measures. To do this with a known and valid statement of uncertainty.

Unique for this strategy would be the capability to perform number of 'virtual experiments' limited only by the computational power available to the researcher without the extensive experimental costs. This as previously discussed in **7.2.1** and **7.2.2** can further lower the variance of the prediction models considerably with respect to the uncertainty of the measurements used for its calibration (as seen In the metamodel results in **Figure 113**).

Additional property linked empirical and meta models fitted to measurements or virtual measurements (FEM) is the 'variance bias trade-off error' (Hero, Fessler and Usman, 1996; Friedman, 1997; Yu *et al.*, 2006). The more complex function fitting closely to the data (with more parameters) is best fitted, the larger would be the prediction variance. The simpler a model is (two parameters polynomial), the less would be the variance error, but it would fit poorer to the data and thus having a larger bias. This property can be used to make decisions on how complex representative model should be with respect to the measured bias errors. For the Probabilistic FEM, the bias errors are largely a limit and would be a function mainly of how accurately are represented the physics, initial conditions, mechanical constraints represented by the model. Thus finding a way of virtually 'mimicking' those is crucial. If all known and unknown biases errors are corrected, then the GUM scheme would hold completely (zero variance and bias of the mean), and the probabilistic model output variances would represent their ultimate uncertainties (a function of their calibration measurements uncertainties).

This, however, might not always be economically or technically possible. Thus it is critical and important as shown in the current work to evaluate and understand the bias errors of the models and include them in the uncertainty statement.

## 7.4 Results interpretation for CLIC

The results have shown that the combined alignment uncertainty of task-specific CMM measurements and the thermal error compensation (for any large variation of thermal conditions of the assembly from metrology) is above the target of 12 μm (for fiducialisation measurements) at one σ.

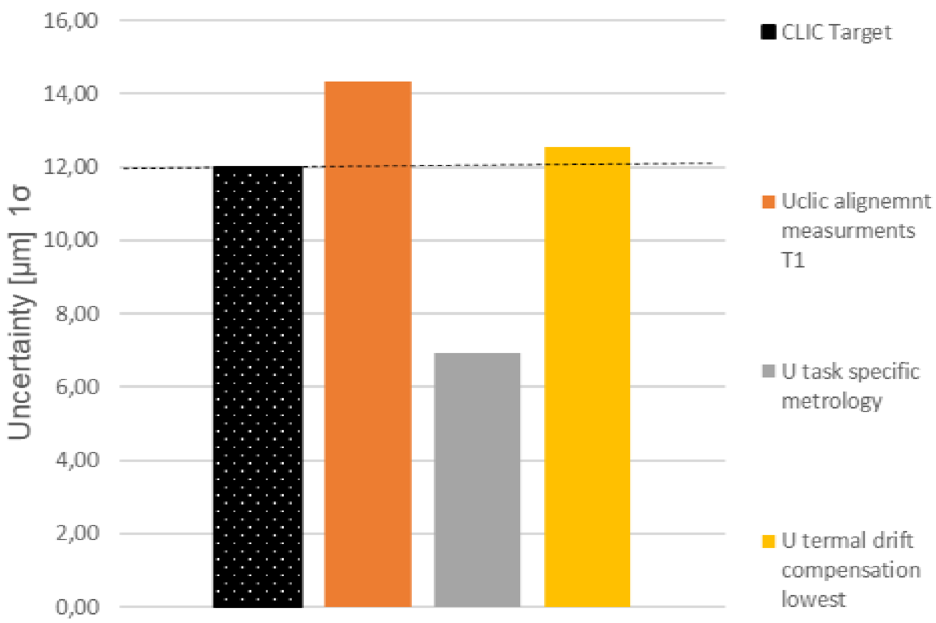


**Figure 114: CLIC Magnet axis alignment targeted budget (up to WPS reference sensors) VS Total estimated; Metrology; Drift compensation**

The largest contributor is due to the thermal error compensation for the variable thermal conditions. If an alignment strategy is adopted such that the measurements are performed at the same thermal load conditions as the one experienced during operation, the alignment measurements budget would be maintained and CLIC alignment targets be achivable. This however might not be economically viable due to the large cost associated with active thermal control of km range accelerator machine. Thus a detailed study on the economic viability of such strategy can be conducted in future.

# 8 CONCLUSIONS

The work presented studied a general challenge in the field of high precision alignment of large objects - the accurate knowledge of alignment measurement uncertainties. Those are proven to be critical in situations where the alignment tolerance is at the limit of the metrology performance. The literature has shown a general lack of understanding of uncertainties and application of state of the art uncertainty analysis and propagation methods in this field of engineering. Cause for that was the rare occasions at which alignment measurement uncertainties are tightly matching the uncertainty of the metrology applied. An additional challenge was the absence of uncertainty quantification for the compensation of systematic errors such as the thermal effects (one of the largest contributors to alignment and measurement uncertainty). In this PhD work motivated by the challenges in the CLIC project, a hypothesis and methodology were proposed as an answer. An accurate and traceable alignment metrology is possible by the mixture of application of GUM Supplement 1 method (Probabilistic modelling) for the evaluation of model variance and traceable measurements for the evaluation of model biases. The hypothesis and methodology were proven by answering the two set objectives as stated in **3.2.** This was done experimental and modelling work is done for both metrology and thermal error compensation.

The first objective was to accurately be able to state the task-specific CMM uncertainty of magnet axis alignment. This was achieved by predicting the uncertainty of alignment measurements of the T4 magnet assembly to 6.91 μm (1σ) and 7.96 μm (1σ). The method was validated by traceable tetrahedron artefact (**5.1.2**) on which measured errors with respect to calibration of 2.57 μm were successfully captured by modelled uncertainty of 3.67 μm (1 σ).

The second objective was to prove that following the hypothesis thermal deformation and drift can be predicted with an accurate statement of uncertainty. This was achieved by applying the defined methods following the hypothesis to Empirical, FEM and Metamodels. The Empirical models proven as one with the lowest uncertainty for prediction of fiducials drift of maximum 8.7 μm (1 σ). This was validated with independent test by two separate metrology systems with ISO test (**5.2.8**) bellow 1 (0.32 to 0.58). The methodology was successfully validated for the Probabilistic FEM with ISO test (**5.2.8**) bellow 1 (0.15 to 0.48) with uncertainties varying between 2.34 μm (1 σ) to 11.28 μm (1 σ). Finally, the methodology was validated on Metamodels based on the FEM with largest uncertainties in the range of 12.24 μm (1 σ). with ISO test (**5.2.8**) bellow 1 (0.42).

In general, this method and PhD work contribute to knowledge by:

1. Correcting erroneous assumptions about the use of MPE qualifications of metrology equipment for propagation in error and uncertainty budges. Suggesting as an alternative a mixture of probabilistic CMM modelling calibrated by SBC method and reference drift measurements.
2. Defining the methodology by which Empirical, Probabilistic FEM and Metamodels prediction uncertainty can be accurately (traceable to an SI unit) be evaluated predicted and studied.
3. Proving that large thermally active assemblies of up to 2 meters can be aligned under 15 μm uncertainty at one σ at variable (from alignment) thermal conditions by dozens or more °C. This is done with statement trustworthy and traceable to an SI unit and via a method that can be applied to large-scale projects and manufacturing.

# 9 FUTURE WORK

## 9.1 CLIC challenges

Tree alternatives can be suggested as part of CLIC future work. First to apply active metrology such as FSI or Micro Triangulation to compensate any drifts in real time. Similar techniques have been applied for the drift corrections at other large structures such as telescopes (Dale *et al.*, 2014; Rakich *et al.*, 2016) or accelerator detectors [198,199]. This however might be cost challenging to be implemented on the large and industrial scale. Second would be to reduce the uncertainty of any thermal compensation models applied which is already close to the desired values. This can be done by investing in further work on compensating the model's bias and variance errors. Third, the alignment tolerances can be investigated further, and possible release of the tolerance could be negotiated with the physicist.

## 9.2 Further methodology validations and applications

Future work can be suggested in applying the so far validated methodology on more complex assemblies. The time constraints did not allow the full development, calibration and testing of uncertainty models applied for alignment measurements and compensations on largest T4 type two-meter assembly.

Once such large assembly prototype exists the predicted CMM alignment uncertainty results (**6.1.3**) can be verified. This can be done by the manufacture and calibration of two meters bespoke thermally stable artefact. Such artefact should be manufactured from carbon fibre or other low or zero CTE material. It should have fiducials of the same shape and size and locations as the two meter T4 magnet assembly. The important addition would be the addition of two thin cylinders' fiducials (representing the stretched wire) within the artefact volume of stable location and geometry. Such artefact should be made traceable and calibrated and verified by a national metrology institute to possess the lowest measurement uncertainty with traceability to the SI unit of meter.

The uncertainty evaluation for the magnetic measurement system was out of the scope of the current thesis. However, a gap of knowledge in this field was found as well. Currently, the only way uncertainty statements for this metrology routine are only done via the "*expert judgement*" method (**2.2.2, page 37**). If further need in decrease and traceability of magnetic measurement uncertainty's is required a working group with the national institute on the topic has to be established. Such group can research the possible ways to establish possible and practical for application magnetic axis artefacts and method by which traceability to SI units can be established among international laboratories.

The methodology defined in this PhD thesis (**4.3**) can be further applied to more complex assembly such as the T1 or T4 type assemblies having more mechanical interfaces. It could be tested on more and various thermal conditions. During such campaign, further tests on techniques for direct measurement of thermal loads with various sensors can be made. The Heat flux sensors used in the thesis (**5.1.5**) were used were providing single heat flux value for a surface and no reading for heat flux field. Such knowledge is useful in the models as long as assumptions for heat-flux equipotential across measured surfaces holds. In a more complex situation with existent surface area gradients in heat flux strength a study and development of pixelated-heat flux sensors is suggested. Studies for development of such sensors in the state of art can be already seen in the are of robotic sensors development so-called "artificial skin" (Zhao and Zhu, 2017). If such sensors are proven accurate and, traceable (to the SI realisation of the unit meter) measurement and accurate model predictions of more complex cases of heat loadings can be established.

The methodology for traceable prediction of models (**4.3**) (Empirical, FEM and Meta-models) uncertainty was validated in the current work with respect to thermo-mechanical drift prediction. However, the idea could be seen well applicable in other fields of engineering and science where having accurate uncertainty statement of the predictions is important. This could be directly seen as a need in industries such as the aerospace where uncertainty on predictions can have high legal and financial impact. A direct example is a trend in state of the art of having ''digital twins'' (Sch, Schluse and Rossmann, 2016) models of critical systems (assemblies engines). In parallel to system exploitation, a digital representative model is kept and feed in real time with data from the conditions under which the critical systems (assembly's engines) are subjected. Such models can be used to predict possible future behaviour (failure modes) or used as feedback to next-generation system design. Having an accurate uncertainty statements of such predictions could help engineers in the taking of critical decisions. Thus it is recommended for this methodology to be studied and validated further in the wide band of possible cases of applications.

# REFERENCES

Ametherm Circuit Protection Thermistors (2017) ‘*What Is An NTC Thermistor*’. Available at: https://www.ametherm.com/thermistor/what-is-an-ntc-thermistor (Accessed: 9 September 2017).

Arpaia, P., Caiazza, D., Petrone, C. and Russenschuck, S. (2015) ‘*Performance of the stretched and vibrating wire techniques and correction of backgroung fields in locating quadrupole magnetic axes*’, *IMEKO World Congress*. Available at: https://cds.cern.ch/record/2037071/files/CERN-ACC-2015-0074.pdf (Accessed: 12 September 2017).

ATC (2017a) ‘*ATC-K3 Chiller specifications*’. Available at: http://app-therm.com/wp-content/uploads/2016/02/k3-brochure.pdf (Accessed: 16 August 2017).

ATC (2017b) ‘*K3 Chiller - Applied Thermal Control*’. Available at: http://app-therm.com/product/k3/ (Accessed: 16 August 2017).

Bhamidi, K. and Morse, E. P. (2004) ‘*Performance testing of multisensor CMMs based on single artifact measurement*’, in *American Society of Precision Engineers (ASPE) Anual Publications*. Orlando. Available at: http://www.aspe.net/publications/Annual_2004/POSTERS/3METRO/5MEASU/1588.PDF (Accessed: 30 June 2017).

BIPM (1997) ‘*Supplementary Information for the international temperature scale of 1990 (1997 reprinting of the 1990 first edition)*’. Paris.

BIPM (2006) ‘*International System of Units (SI)*’. doi: 10.1007/BF00594162.

BIPM (2008) ‘*JCGM 101 : Evaluation of measurement data - Supplement 1 to the “ Guide to the expression of uncertainty in measurement ” - Propagation of distributions using a Monte Carlo method*’. Paris.

BIPM (2015) ‘*BIPM - ITS-90*’. Available at: http://www.bipm.org/en/committees/cc/cct/guide-its90.html (Accessed: 11 September 2017).

BIPM (2017) ‘*Boreau International des Poids et Mesures*’. Available at: http://www.bipm.org/en/about-us/ (Accessed: 31 August 2017).

Borror, C. M., Montgomery, D. C. and Myers, R. H. (2002) ‘*Evaluation of Statistical Designs for Experiments Involving Noise Variables*’, *Journal of Quality Technology*, 34(1), pp. 54–70.

Bottura, L., Buzio, M., Pauletta, S. and Smirnov, N. (2006) ‘*Measurement of magnetic axis in accelerator magnets: critical comparison of methods and instruments*’, in *IEEE Instrumentation and Measurement Technology Conference Proceedings*. Sorrento: IEEE, pp. 765–770. Available at:

http://ieeexplore.ieee.org/document/4124432/ (Accessed: 27 October 2017).

Box, G. E. P. and Wilson, K. B. (1992) '*On the Experimental Attainment of Optimum Conditions*', in. Springer, New York, NY, pp. 270–310. doi: 10.1007/978-1-4612-4380-9_23.

Bryan, J. B. (1967) '*International Status of Thermal Error research*', *Mechanical Engineering CIRP*, (September), pp. 25–50.

Bryan, J. B. and Doiron, T. (2011) '*Temperature Fundamentals*', in *Coordinate Measuring Machines and Systems, Second Edition*. CRC Press, pp. 273–303. doi: 10.1201/b11022-11.

BSI ISO/TS (2013) '*ISO 15530-1 Technique for determining the uncertainty of measurement Part 1: Overview and metrological characteristics*'.

Bueno, R.; Arzamendi, J; Almandoz, J. (1997) '*Thermal modal analysis of machine-tools*', *Integrated Design and Manufacturing in Mechanical Engineering*, pp. 307–315.

Caiazza, D. (2015) '*Measuring the magnetic axis of quadrupoles by a stretched wire [Power point presentation]*'. Available at: https://indico.cern.ch/event/332431/contributions/775855/attachments/648173/891487/pacman_workshop15_dcaiazza_PA.pdf (Accessed: 8 August 2017).

Caiazza, D. (2017) '*Metrological performance enhancement of wire methods for magnetic field measurement in particle accelerators [PhD Thesis]*'. University of Sannio.

California, L., Brewer James Bryan Eldon R McClure J W Pearson, W. B., Bryan, J., Pearson, J., Brewer, W. and McClure, E. (1965) '*Thermal effects in dimensional metrology*', *Mechanical Engineering*. Available at: http://emtoolbox.nist.gov/Publications/UCRL-1965-12409-ThermalEffectsinDimensionalMetrology.pdf (Accessed: 3 July 2017).

Carl Zeiss AG (2017) '*ZEISS PRISMO CMM - Manufacturers website*'. Available at: https://www.zeiss.com/metrology/products/systems/bridge-type-cmms/prismo-navigator.html (Accessed: 20 June 2017).

CERN (2017a) '*Future Circular Collider Study*'. Available at: https://fcc.web.cern.ch/Pages/default.aspx (Accessed: 6 September 2017).

CERN (2017b) '*PACMAN Innovative Doctoral Program*'. Available at: https://pacman.web.cern.ch/ (Accessed: 31 July 2017).

Chida, Y., Ohnishi, J. and Matsui, S. (1995) '*Laser and CCD camera system for magnet alignment on girder in the SPring-8 storage ring*', *eConf*, C951114, pp. 194–200. Available at: http://inspirehep.net/record/413572 (Accessed: 31 July 2017).

Childs, P. R. N., Greenwood, J. R. and Long, C. A. (2000) '*Review of temperature measurement*', *Review of Scientific Instruments*. American Institute of Physics, 71(8), pp. 2959–2978. doi: 10.1063/1.1305516.

CLIC (Collaboration) (2012) '*A Multi-TEV linear collider based on CLIC technology conceptual design report*'. Geneva. doi: 10.5170/CERN-2012-007.

Coe, P. A. (2001) '*An Investigation of Frequency Scanning Interferometry for the alignment of the ATLAS semiconductor tracker [PhD Thesis]*'. Oxford. Available at: http://cds.cern.ch/record/1074719/files/thesis-2007-082.pdf (Accessed: 13 October 2017).

Committee for Guides in Metrology, J. (2008) '*Evaluation of measurement data - Guide to uncertainty in measurement*'. Available at: http://www.bipm.org/utils/common/documents/jcgm/JCGM_100_2008_E.pdf.

Couto, P. R. G., Damasceno, J. C. and Oliveira, S. P. (2013) '*Monte Carlo simulations applied to uncertainty in measurement*', *Theory and Applications of Monte Carlo Simulations*, pp. 27–51. doi: 10.5772/53014.

Dale, J., Hughes, B., Lancaster, A. J., Lewis, A. J., Reichold, A. J. H. and Warden, M. S. (2014) '*Multi-channel absolute distance measurement system with sub ppm-accuracy and 20 m range using frequency scanning interferometry and gas absorption cells.*', *Optics express*, 22(20), pp. 24869–93. Available at: http://www.ncbi.nlm.nih.gov/pubmed/25322060 (Accessed: 13 October 2017).

Digi Key Electronics (2017) '*DC95 - Amphenol Advanced Sensors - Thermistors NTC (Negative Temperature Coefficient)* | *Online Catalog* | *DigiKey Electronics*'. Available at: https://www.digikey.com/catalog/en/partgroup/dc95/23406 (Accessed: 9 September 2017).

DiMarco, J., Glass, H., Lamm, M. J., Schlabach, P., Sylvester, C., Tompkins, J. C. and Krzywinski, I. (2000) '*Field alignment of quadrupole magnets for the LHC interaction regions*', *IEEE Transactions on Appiled Superconductivity*, 10(1), pp. 127–130. doi: 10.1109/77.828192.

DiMarco, J., Krzywinski, J. and Fermilab MTF (1996) '*MTF Single Stretched Wire System*', *Fermilab MTF*. Available at: http://inspirehep.net/record/438616?ln=en.

Doiron, T. (2006) '*Uncertainties Related to Thermal Expansion in Dimensional Metrology*'. Available at: http://emtoolbox.nist.gov/Publications/NCSLIMeasure011-2006.pdf (Accessed: 3 July 2017).

Doiron, T. D. (2001) '*Temperature and Dimensional Measurement*'. Available at: http://emtoolbox.nist.gov/Temperature/Temperature and Dimensional Measurement.pdf (Accessed: 13 June 2017).

Dornfeld, D. and Lee, D.-E. (2008) '*Precision Manufacturing*'. Boston, MA: Springer US. doi: 10.1007/978-0-387-68208-2.

Doytchinov, I. (2017) '*Alignment measurement uncertainties for large assemblies via probabilistic modeling techniques [PhD Thesis]*'. Cranfield University.

Dupont, M., Missiaen, D. and Winkes, P. (2004) '*The laser tracker: A major tool for the metrology of the LHC*', *International Workshop on Accelerator Alignment*. Available at: http://www.slac.stanford.edu/econf/C04100411/papers/045.PDF (Accessed: 31 July 2017).

Durand, H. M., Anastasopoulos, M., Griffet, S., Kemppinen, J., Rude, V. and Sosin, M. (2012) '*Validation of the CLIC alignment strategy on short range*'. Available at: https://cds.cern.ch/record/1483223/files/CERN-ATS-2012-272.pdf (Accessed: 14 August 2017).

Durrant-Whyte, H. and Bailey, T. (2006) '*Simultaneous localization and mapping: part II*', *IEEE Robotics & Automation Magazine*, 13(2), pp. 99–110. doi: 10.1109/MRA.2006.1638022.

Egawa, K., Masuzawa, M., Kek and Ibaraki, J. (1998) '*PRELIMINARY RESULTS OF THE KEKB QUADRUPOLE MAGNET MEASUREMENTS*', *EPAC*. Available at: http://accelconf.web.cern.ch/AccelConf/e98/PAPERS/TUP17G.PDF (Accessed: 31 July 2017).

Electrolube (2013) '*HTSP Silicone Heat Transfer Compound Plus*'. Available at: http://www.farnell.com/datasheets/2335156.pdf?_ga=2.8943157.1815871589.1502890150-608970073.1502890150 (Accessed: 16 August 2017).

Fan, K., Yang, J. and Yang, L. (2013) '*Orthogonal polynomials-based thermally induced spindle and geometric error modeling and compensation*', *The International Journal of Advanced Manufacturing Technology*. Springer-Verlag, 65(9–12), pp. 1791–1800. doi: 10.1007/s00170-012-4301-2.

Farkhondeh, M., Holmberg, S. P., Sapp, W. W. and Zumbro, J. D. (1991) '*Fiducialization of Magnets for the MIT-Bates SHR*', in *Particle Accelerator Conference*. IEEE, pp. 634–636. doi: 10.1109/PAC.1991.164387.

Farnell (2017) '*HP Series of PTC Heaters*'. Available at: http://www.farnell.com/datasheets/477436.pdf?_ga=2.203020049.1815871589.1502890150-608970073.1502890150 (Accessed: 16 August 2017).

Fermilab (2017) '*Fermilab | Home*'. Available at: http://www.fnal.gov/ (Accessed: 12 September 2017).

Fines, J. M. and Agah, A. (2008) '*Machine tool positioning error compensation using artificial neural networks*', *Engineering Applications of Artificial Intelligence*, 21(7), pp. 1013–1026. doi: 10.1016/j.engappai.2007.10.001.

Fischer, G. E., Bressler, V. E., Cobb, J. K., Jensen, D. R., Ruland, R. E., Walz, H. V. and Williams, S. H. (1992) '*Precision fiducialization of transport components*'. Available at: https://inis.iaea.org/search/search.aspx?orig_q=RN:23058946 (Accessed: 31

July 2017).

Fisher, R. A. (1992) '*The Arrangement of Field Experiments*', in *Rothansted Experimental Station*, pp. 82–91. doi: 10.1007/978-1-4612-4380-9_8.

Flack, D. (2011) '*Good Practice Guide No. 42 - CMM Verification*', (42). Available at: http://publications.npl.co.uk/npl_web/pdf/mgpg42.pdf (Accessed: 4 September 2017).

FLIR (2013) '*FLIR E50BX Infrared Camera*'. Available at: https://www.flir-direct.com/product/flir-e50bx-infrared-camera (Accessed: 11 September 2017).

FLIR (2015) '*Use low-cost materials to increase target emissivity*'. Available at: http://www.flir.com/science/blog/details/?ID=71556 (Accessed: 11 September 2017).

Florian, A. (1992) '*An efficient sampling scheme: Updated Latin Hypercube Sampling*', *Probabilistic Engineering Mechanics*, 7(2), pp. 123–130. doi: 10.1016/0266-8920(92)90015-A.

Fong, J., Filliben, J. and Heckert, A. (2008) '*Design of experiments approach to verification and uncertainty estimation of simulations based on Finite Elements Modeling*', in *The American Society of Engineering Education*. Pittsburgh, PA. Available at: https://www.nist.gov/publications/design-experiments-approach-verification-and-uncertainty-estimation-simulations-based.

Fong, J. T., Filliben, J. J., DeWit, R., Fields, R. J., Bernstein, B. and Marcal, P. V (2006) '*Uncertainty in finite element modeling and failure analysis: A metrology-based approach*', *Journal of pressure vessel technology-transactions of the ASME*, 128(1), pp. 140–147. doi: 10.1115/1.2150843.

Fransen, S., Doyle, D. and Catanzaro, B. (2011) '*Opto-mechanical modeling of the Herschel Space Telescope at ESA/ESTEC*', in *Integrated Modeling of Complex Optomechanical Systems. Vol. 8336. International Society for Optics and Photonics*. doi: 10.1117/12.915669.

Friedman, J. H. (1997) '*On Bias, Variance, 0/1—Loss, and the Curse-of-Dimensionality*', *Data Mining and Knowledge Discovery*. Kluwer Academic Publishers, 1(1), pp. 55–77. doi: 10.1023/A:1009778005914.

Fukami, K., Azumi, N., Kai, T., Kimura, H., Kiuchi, J., Matsui, S., Watanabe, T. and Zhang, C. (2016) '*Estimation of magnet alignment accuracy for Spring-8 upgrade using resonance-frequency tracked vibrating wire*', in *IWAA*. Available at: https://indico.cern.ch/event/489498/contributions/2217459/attachments/1355009/2047391/TUO_fukami.pdf (Accessed: 29 October 2017).

Garrett, M. W. and Pissanetzky, S. (1971) '*Polygonal Coil Systems for Magnetic Fields with Homogeneity of the Fourth to the Eighth Order*', *Review of Scientific Instruments*, 42(6), pp. 840–857. doi: 10.1063/1.1685243.

Gestel, N. Van (2011) '*Determining measurement uncertainties of feature measurements on CMMs*', *Thesis*. Available at: https://lirias.kuleuven.be/bitstream/123456789/312758/1/phd-nickvangestel-lowres.pdf (Accessed: 2 May 2017).

Gibson, S. M., Coe, P. A., Dehchar, M., Fopma, J., Howell, D. F., Nickerson, R. B. and Viehhauser, G. (2008) '*First Data From the ATLAS inner detector FSI alignment system*', in *The 10th International Workshop on Accelerator Alignment*. Tsukuba. Available at: http://citeseerx.ist.psu.edu/viewdoc/download;jsessionid=8BB880734196D5AFA9EC0819B759387D?doi=10.1.1.559.3875&rep=rep1&type=pdf (Accessed: 13 October 2017).

Glaessgen, E. and Stargel, D. (2012) '*The Digital Twin Paradigm for Future NASA and U.S. Air Force Vehicles*', in *53rd Struct. Dyn. Mater. Conf. Special Session: Digital Twin*. doi: 10.2514/6.2012-1818.

Glassman, T., Levi, J., Liepmann, T., Hahn, W., Bisson, G., Porpora, D. and Hadjimichael, T. (2016) '*Alignment of the James Webb Space Telescope optical telescope element*', in MacEwen, H. A., Fazio, G. G., Lystrup, M., Batalha, N., Siegler, N., and Tong, E. C. (eds) *SPIE Astronomical Telescopes - Instrumentation. International Society for Optics and Photonics*. International Society for Optics and Photonics. doi: 10.1117/12.2233792.

Habib, H. (2016) '*Uncertainty of Coordinate Measuring Machines*'. Available at: https://www.slideshare.net/hassang66/uncertainty-of-coordinate-measuring-machines (Accessed: 5 September 2017).

Hasselström, A. (2012) '*Thermal Contact Conductance in Bolted Joints [Master Thesis]*'. Chalmers university of technology. Available at: http://publications.lib.chalmers.se/records/fulltext/159027.pdf.

Hero, A. O., Fessler, J. A. and Usman, M. (1996) '*Exploring estimator bias-variance tradeoffs using the uniform CR bound*', *IEEE Transactions on Signal Processing*, 44(8), pp. 2026–2041. doi: 10.1109/78.533723.

Herty, A. (2004) '*Test and calibration facility for HLS and WPS sensors*', pp. 4–7. Available at: https://iwaa2004.web.cern.ch/iwaa2004/subsite/PDF/20041006_TS08-2_Andreas-Herty.pdf (Accessed: 12 September 2017).

HexagonAB (2017) '*Leitz PMM-C manufacturer website and descriptions*'. Available at: http://hexagonmi.com/products/coordinate-measuring-machines/bridge-cmms/leitz-pmmc Last accessed on 09.2016.

Hexagon metrology (2009) '*LEICA absolute tracker AT402 product brochure*', pp. 4–5. Available at: http://metrology.leica-geosystems.com/downloads123/m1/metrology/general/brochures/Leica Absolute Tracker AT402_brochure_en.pdf.

Hocken, R. J. and Pereira, P. H. (2016) '*Coordinate measuring machines and systems*'. Second Edi. CRC Press. Available at: https://www.taylorfrancis.com/books/9781420017533 (Accessed: 7 August 2017).

Homann, B. and Thornton, A. (1998) '*Precision machine design assistant: A constraint-based tool for the design and evaluation of precision machine tool concepts*', *AI EDAM*. Cambridge University Press, pp. 419–429.

Huntsman (2007) '*Araldite-2011 adhesive properties*'. Available at: http://www.dawex.cz/userFiles/technicke-listy/huntsman/araldite-2011.pdf (Accessed: 15 August 2017).

Huo, D., Maropoulos, P. G. and Cheng, C. H. (2010) '*The Framework of the Virtual Laser Tracker – A Systematic Approach to the Assessment of Error sources and Uncertainty in Laser Tracker Measurement*', in. Springer, Berlin, Heidelberg, pp. 507–523. doi: 10.1007/978-3-642-10430-5_39.

Iman, R. L. and Conover, W. J. (1980) '*Small sample sensitivity analysis techniques for computer models.with an application to risk assessment*', *Communications in Statistics - Theory and Methods*. Marcel Dekker, Inc. , 9(17), pp. 1749–1842. doi: 10.1080/03610928008827996.

International Atomic Energy Agency. (2008) '*Thermophysical properties of materials for nuclear engineering : a tutorial and collection of data.*' International Atomic Energy Agency. Available at: http://www-pub.iaea.org/books/IAEABooks/7965/Thermophysical-Properties-of-Materials-for-Nuclear-Engineering-A-Tutorial-and-Collection-of-Data (Accessed: 18 September 2017).

ISO (2009) '*ISO 10360-2 Geometrical product specifications (GPS) - Acceptance and reverification tests for coordinate measuring machines (CMM) - Part 2: CMMs used for measuring linear dimensions*'.

ISO (2010) '*Fire tests - Calibration and use of heat flux meters - Part 1: General principles*'. Available at: https://www.iso.org/standard/55659.html (Accessed: 11 September 2017).

ISO (2011a) '*ISO 15530-3 Geometrical product specifications (GPS) — Coordinate measuring machines (CMM): Technique for determining the uncertainty of measurement — Part 3: Use of calibrated workpieces or measurement standards*'. Available at: https://www.iso.org/obp/ui/#iso:std:iso:15530:-3:ed-1:v1:en (Accessed: 5 September 2017).

ISO (2011b) '*ISO 8015, Geometrical product specifications (GPS) — Fundamentals - Concepts, principles and rules*'. Available at: https://www.iso.org/obp/ui/#iso:std:iso:8015:ed-2:v1:en (Accessed: 14 August 2017).

ISO (2011c) ‘*ISO 14253-2 Geometrical product specifications (GPS)- Inspectionby measurement of workpieces and measuring equipment- Part 2: Guidancefor the estimation of uncertainty in GPS measurement in calibration of mea-suring equipment*’, *Geneva, CH: International Organisation for Standardisation*. Available at: https://www.iso.org/standard/53631.html (Accessed: 21 June 2017).

ISO (2012) ‘*ISO 230-1 - Test code for machine tools - Part 1: Geometric accuracy of machines operating under no-load or quasi-static conditions*’. Available at: https://www.iso.org/standard/46449.html (Accessed: 1 September 2017).

ISO (2013a) ‘*ISO 10360-9 Geometrical product specifications (GPS) — Acceptance and reverification tests for coordinate measuring systems (CMS) — Part 9: CMMs with multiple probing systems*’. Available at: https://www.iso.org/obp/ui/#iso:std:iso:10360:-9:ed-1:v1:en.

ISO (2013b) ‘*ISO 14253-1 - Geometrical product specifications (GPS) -- Inspection by measurement of workpieces and measuring equipment -- Part 1: Decision rules for proving conformity or nonconformity with specifications*’. Available at: https://www.iso.org/standard/63638.html (Accessed: 6 July 2017).

ISO (2015) ‘*ISO 14644-1:2015 - Cleanrooms and associated controlled environments -- Part 1: Classification of air cleanliness by particle concentration*’. Available at: https://www.iso.org/standard/53394.html (Accessed: 26 October 2017).

ISO (2017) ‘*ISO 1101 - Geometrical product specifications (GPS) - Geometrical tolerancing - Tolerances of form, orientation, location and run-out*’. Available at: https://www.iso.org/standard/66777.html (Accessed: 3 July 2017).

ISO/TR (2003) ‘*ISO/TR 16015 Geometrical product specifications (GPS) - Systematic errors and contributions to measurement uncertainty of length measurement due to thermal influences*’, *Building*.

ISO/TS (2006) ‘*ISO/TS 23165 - Geometrical product specifications (GPS) - Guidelines for the evaluation of coordinate measuring machine (CMM) test uncertainty*’. Available at: https://www.iso.org/standard/24236.html (Accessed: 6 July 2017).

ISO/TS and ISO (2008) ‘*ISO 15530-4 Geometrical product specifications (GPS) - Coordinate measuring machines (CMM): Technique for determining the uncertainty of measurement - Part 4: Evaluating task-specific measurement uncertainty using simulation*’. Available at: https://www.iso.org/standard/38696.html (Accessed: 5 September 2017).

ISO 14253-2 (2011) ‘*Geometrical product specifications (GPS) -- Inspection by measurement of workpieces and measuring equipment -- Part 2: Guidance for the estimation of uncertainty in GPS measurement, in calibration of measuring equipment and in product verification*’.

ISO draft/FDIS (2010) '*Geometrical Product Specifications (GPS) - Acceptance and reverification tests for coordinate measuring machines (CMM) - Part 5*'.

J.W. Li, W.J. Zhang. G.S. Yang S.D. Tu, X. B. C. (2008) '*Thermal-error moddeling for complex physical systems: the-state-of-arts review*', *International journal of advanced manufacturing technologyes*, (42(1-2)), p. p.168. Available at: https://link.springer.com/article/10.1007/s00170-008-1570-x.

J . Soon et al. (1992) '*Modelling the error of multi-axis machines*', *Precision Engineering*, 14(1), pp. 5–19.

JCGM (2008a) '*JCGM 100: Evaluation of measurement data - Guide to the expression of uncertainty in measurement (GUM 1995 with minior corrections)*', (September).

JCGM (2008b) '*JCGM 100 201X CD: Evaluation of Measurement Data - Guide to the Expression of Uncertainty in Measurement*'. Available at: http://www.affidabilita.eu/pdfeventi/JCGM_100_201X_CD.pdf (Accessed: 22 August 2017).

JCGM (2012) '*JCGM 200: International vocabulary of metrology - Basic and general concepts and associated terms ( VIM ) 3rd edition Vocabulaire international de métrologie – Concepts fondamentaux et généraux et termes associés ( VIM ) 3 e édition*'.

John Bringas (2016) '*Handbook of Comparative World Steel Standards: 5th Edition*'. ASTM inter. Available at: https://www.astm.org/DIGITAL_LIBRARY/MNL/SOURCE_PAGES/DS67D.htm (Accessed: 14 September 2017).

Keysight (2015) '*Keysight Technologies How to Measure the Unknown Thermal Emissivity of Objects/Materials Using the U5855A TrueIR Thermal Imager*'. Available at: http://literature.cdn.keysight.com/litweb/pdf/5992-0222EN.pdf (Accessed: 12 September 2017).

Keysight (2017) '*BenchVue Software*'. Available at: https://www.keysight.com/zz/en/software/application-sw/benchvue-software.html (Accessed: 16 August 2017).

Keysight (formerly Agilent's Electronic Measurement) (2017a) '*34902A 16 Channel Multiplexer (2/4-wire) Module for 34970A/34972A DAQ of Agilent*'. Available at: http://www.keysight.com (Accessed: 9 September 2017).

Keysight (formerly Agilent's Electronic Measurement) (2017b) '*34970A Data Acquisition / Data Logger Switch Unit*'. Available at: http://www.keysight.com/ (Accessed: 16 August 2017).

Khuri, A. I. and Mukhopadhyay, S. (2010) '*Response surface methodology*', *Wiley Interdisciplinary Reviews: Computational Statistics*. John Wiley & Sons, Inc., 2(2), pp. 128–149. doi: 10.1002/wics.73.

Knapp, W. (2001) '*Tolerance And Uncertainty*', *WIT Transactions on Engineering Sciences*. WIT Press, 34. doi: 10.2495/LAMDAMAP010321.

KROHNE Group (2017a) '*Industrial Temperature Assemblies – OPTITEMP TRA/TCA-S11*'. Available at: http://krohne.com/en/products/temperature-measurement/industrial-temperature-assemblies/tratca-s11-assembly-for-screw-in/ (Accessed: 16 August 2017).

KROHNE Group (2017b) '*Technical Datasheet*'. Available at: http://cdn.krohne.com/dlc/TD_OPTITEMP_TRA_TCA_en_120727_4001819303_R03.pdf (Accessed: 9 September 2017).

Kucuk, S. and Bingul, Z. (2006) '*Robot Kinematics: Forward and Inverse Kinematics*', in *Industrial Robotics: Theory, Modelling and Control*. doi: 10.5772/5015.

Laird technologies (2003) '*Aluminium thermal shield tape*'. Available at: http://www.farnell.com/datasheets/63665.pdf?_ga=2.269079409.1815871589.1502890150-608970073.1502890150 (Accessed: 16 August 2017).

Leãoa, R. (2017) '*Uncertainty evaluation for the alignment of particle accelerators [PhD Thesis]*'. Instituto Technologico de Aeronautica.

Leãoa, R., Baldob, C., Reisc, M., Trabancod, J. L. A., Rodriguesa, F. and Neuenschwandera, R. (2016) '*Magnet alignment on a common girder: Development of a length artefact for measurement accuracy improvement*', *Journal of the International Societies for Precision Engineering and Nanotechnology*. doi: https://doi.org/10.1016/j.precisioneng.2017.04.013.

Leito, I., Jalukse, L. and Helm, I. (2017) '*Estimation of measurement uncertainty in chemical analysis ( analytical chemistry ) course*'. Available at: https://sisu.ut.ee/measurement/35-other-distribution-functions-student-distribution (Accessed: 30 August 2017).

Loulergue, A. (2005) '*Status of the SOLEIL booster synchrotron*', *Proceedings of the IEEE Particle Accelerator Conference*. IEEE, 2005(figure 1), pp. 2155–2157. doi: 10.1109/PAC.2005.1591041.

Luhmann, T., Robson, S., Kyle, S. and Boehm, J. (2013) '*Close-Range Photogrammetry and 3D Imaging*', *Close-Range Photogrammetry and 3D Imaging*. doi: 10.1515/9783110302783.

Mainaud Durand, H. (2016) '*Fiducialisation and initial alignment of the CLIC components within a micrometric accuracy*', in *14th International Workshop on Accelerator Alignment*.

Mainaud Durand, H., Artoos, K., Buzio, M., Caiazza, D., Catalan Lasheras, N., Cherif, A., Doytchinov, I., Faus-Golfe, A., Fuchs, J., Gaddi, A., Galindo Munoz, N., Gayde, J., Kamugasa, S. W., Modena, M., Novotny, P., Russenschuck, S., Sanz, C., Severino, G., Tshilumba, D., Vlachakis, V. and Zorzetti, S. (2017) '*Main* *achievements of the PACMAN project for the alignment at micrometric scale of accelerator components*', *IPAC 2017*. Available at: http://vrws.de/ipac2017/papers/tupik077.pdf (Accessed: 1 June 2017).

Mainaud Durand, H., Artoos, K., Buzio, M., Caiazza, D., Catalán Lasheras, N., Cherif, A., Doytchinov, I., Fuchs, J.-F., Gaddi, A., Galindo Munoz, N., Gayde, J.-C., Kamugasa, S., Modena, M., Novotny, P., Russenschuck, S., Sanz, C., Severino, G., Tshilumba, D., Vlachakis, V., Wendt, M. and Zorzetti, S. (2016) '*PACMAN Project: A New Solution for the High-accuracy Alignment of Accelerator Components*', p. MOOCB01. doi: 10.18429/JACOW-IPAC2016-MOOCB01.

Mainaud Durand, H., Duquenne, M., Rude, V., Sosin, M., Durand, H. M., Duquenne, M., Rude, V. and Sosin, M. (2014) '*Alignment methods developed for the validation of the thermal and mechanical behaviour of the two beam test modules for the CLIC project*', *International Workshop on Accelerator Alignment*. Available at: http://www.slac.stanford.edu/econf/C1410132/papers/103.pdf (Accessed: 14 August 2017).

Mainaud Durand, H. and T.Touze (2006) '*The active pre-alignment of the CLIC components*', in 9th International Workshop on Accelerator Alignment (ed.) *9th international workshop on accelerator alignment, stanford, USA,*. Stanford, USA.

Manteufel, R. (2000) '*Evaluating the convergence of Latin Hypercube Sampling*', *41st Structures, Structural Dynamics, and Materials Conference and Exhibit American Institute of Aeronautics & Astronautics*, (41). Available at: https://arc.aiaa.org/doi/pdf/10.2514/6.2000-1636.

Di Marco, J. (2005) '*LHC IR Quadrupole Alignment Experience at Fermilab*', in *14th International Magnetic Measurement Workshop, CERN*. Available at: https://indico.cern.ch/event/408147/contributions/980924/contribution.pdf.

Matsuo, M., Yasui, T., Inamura, T. and Matsumura, M. (1986) '*High-speed test of thermal effects for a machine-tool structure based on modal analysis*', *Precision Engineering*, 8(2), pp. 72–78. doi: 10.1016/0141-6359(86)90089-9.

Merlin, P. (2009) '*Design and Development of the Blackbird: Challenges and Lessons Learned*', in *47th AIAA Aerospace Sciences Meeting including The New Horizons Forum and Aerospace Exposition*. Reston, Virigina: American Institute of Aeronautics and Astronautics. doi: 10.2514/6.2009-1522.

Metropolis, N. and Ulam, S. (1949) '*The Monte Carlo Method*', *Journal of the American Statistical Association*, 44(247), pp. 335–341. doi: 10.1080/01621459.1949.10483310.

METROSAGE (2009) '*PUNDITCMM:: Metrosage*'. Available at: http://www.metrosage.com/punditcmm.html (Accessed: 12 June 2017).

Microconsult Engineering GmbH and Mai, H. (2010) '*ANSYS & OptiSLang on a*

*HPC-Cluster*'. Weimarer: Dynardo. Available at: https://www.dynardo.de/fileadmin/Material_Dynardo/bibliothek/WOST_7.0/Presentation_Mai.pdf (Accessed: 10 August 2017).

Microplan-gorup (2017) '*Microplan granite cubes specification*'. Available at: https://www.microplan-group.com/images/pdf/cu.pdf (Accessed: 16 August 2017).

Microplan-group (2017) '*Granite cubes - Microplan*'. Available at: https://www.microplan-group.com/en/products/standard-granite-products/108-granite-cubes-cu.html (Accessed: 16 August 2017).

MIT (2003) '*The Central Limit Theorem - Lecture MIT School of managment*'. Available at: https://ocw.mit.edu/courses/sloan-school-of-management/15-063-communicating-with-data-summer-2003/lecture-notes/lecture10.pdf (Accessed: 30 August 2017).

Moffat, R. J. (1988) '*Describing the uncertainties in experimental results*', *Experimental Thermal and Fluid Science*, 1(1), pp. 3–17. doi: 10.1016/0894-1777(88)90043-X.

Morishima, T., Van Ostayen, R., Van Eijk, J. and Schmidt, R. H. M. (2015) '*Thermal displacement error compensation in temperature domain*', *Precision Engineering*. doi: 10.1016/j.precisioneng.2015.03.012.

Morse, E. and Bhamidi, K. (2003) '*Uncertainty of measurments using multisensor CMMs*', in *ASPE Anual Publications*. Available at: http://www.aspe.net/publications/Annual_2003/PDF/3metro/5measu/1317.PDF (Accessed: 30 June 2017).

Most, T. and Dynardo GmbH (2010) '*Variance-based sensitivity analysis in the presence of correlated input variables*'.

Most, T. and Will, J. (2008) '*Meta-model of Optimal Prognosis - An automatic approach for variable reduction and optimal meta-model selection*', *Weimarer Optimierungs-und Stochastiktage*. Available at: http://citeseerx.ist.psu.edu/viewdoc/download;jsessionid=56BFA6867DBA96D6C200BCACD14EA530?doi=10.1.1.411.1767&rep=rep1&type=pdf (Accessed: 11 July 2017).

Musk, E. (2013) '*Hyperloop Alpha*', *SpaceX/Tesla Motors*. doi: 10.1002/9781119171386.

Myers, R. H., Montgomery, D. C. and Anderson-Cook, C. M. (2011) '*Response Surface Methodology : Process and Product Optimization Using Designed Experiments.*' John Wiley & Sons.

National Physical Laboratory (2010) '*What is a platinum resistance thermometer? (FAQ - Thermal)*'. Available at: http://www.npl.co.uk/reference/faqs/what-is-a-platinum-resistance-thermometer-(faq-thermal) (Accessed: 9 September 2017).

‘*National Physical Laboratory*’ (2017). Available at: http://www.npl.co.uk/ (Accessed: 31 August 2017).

Nayfeh, S. and Verdirame, J. (2017) ‘*Thermal Expansion: CTE Definitions and Thermal Strain | Mechanics and Machines*’. Available at: http://www.mechanicsandmachines.com/?p=219 (Accessed: 13 September 2017).

Nelson, J. and Sanders, G. H. (2008) ‘*The status of the Thirty Meter Telescope project*’, *Proc. SPIE 7012, Ground-based and Airborne Telescopes II, 70121A*, 7012, p. 70121A. doi: 10.1117/12.788238.

Netzsch (2017) ‘*DIL 402 Expedis Classic - NETZSCH Analyzing & Testing*’. Available at: https://www.netzsch-thermal-analysis.com/en/products-solutions/dilatometer/dil-402-expedis-classic/ (Accessed: 2 November 2017).

Ni, J. and Wu, S. M. (2003) ‘*Dynamic modeling for machine tool thermal error compensation*’, *Transactions-American Society of Mechanical Engineers Journal of Manufacturing Science and Engineering*, 125(2), p. pp.245-254.

NIST (2014) ‘*Standard Operational Procedures No. 29 Standard Operating Procedure for the Assignment of Uncertainty*’. Available at: https://www.nist.gov/pml/weights-and-measures/laboratory-metrology/standard-operating-procedures.

Okafor, A. C. and Ertekin, Y. M. (2000) ‘*Derivation of machine tool error models and error compensation procedure for three axes vertical machining center using rigid body kinematics*’, *International Journal of Machine Tools and Manufacture*, 40(8), pp. 1199–1213. doi: 10.1016/S0890-6955(99)00105-4.

Ostrowska, K., Gąska, A. and Sładek, J. (2014) ‘*Determining the uncertainty of measurement with the use of a Virtual Coordinate Measuring Arm*’, *The International Journal of Advanced Manufacturing Technology*. Springer London, 71(1–4), pp. 529–537. doi: 10.1007/s00170-013-5486-8.

Pagano, O., Rohmig, P., Walckiers, L. and Wyss, C. (1984) ‘*A highly automated measuring system for the LEP magnetic lenses*’, *Le Journal de Physique Colloques*. EDP Sciences, 45(C1), pp. C1-949-C1-952. doi: 10.1051/jphyscol:19841193.

Pérez, J. G., Galbraith, P., Buzio, M., Charrondiere, C., Coccoli, M., Laface, E., Pauletta, S. and Ruccio, A. (2005) ‘*Axis measurement with AC mole: Geometric and Magnetic calibration*’, 2709. Available at: https://pauletta.web.cern.ch/pauletta/Pubblicazioni Ufficiali/Special_devices_Garcia-Perez.pdf (Accessed: 31 July 2017).

Perret, N. (2014) ‘*Dilatometry | Document 1371432 (v.1) EDMS - CERN*’. Available at: https://edms.cern.ch/ui/#!master/navigator/document?D:1237080807:12370808

07:subDocs (Accessed: 18 September 2017).

PERRIER, É. (2015) ‘*Mise en place d’un nouveau banc d’étalonnage des capteurs WPS (Wire Positionning System) Présenté*’.

Petrone, C. (2013) ‘*Wire methods for measuring field harmonics, gradients and magnetic axes in accelerator magnets*’. Available at: https://cds.cern.ch/record/1601973/files/CERN-THESIS-2013-130_2.pdf (Accessed: 12 September 2017).

Phillips, S., Borchardt, B., Abackerli, A. J., Shakarji, C. and Sawyer, D. (2003) ‘*The Validation of CMM Task Specific Measurement Uncertainty Software*’, *In Proc. of the ASPE 2003 summer topical meeting ‘Coordinate Measuring Machines’*. Available at: http://www.aspe.net/publications/Summer_2003/03SU Extended Abstracts/Phillips.PDF (Accessed: 27 June 2017).

Phillips, S. D., Borchardt, B., Estler, W. . and Buttress, J. (1998) ‘*The estimation of measurement uncertainty of small circular features measured by coordinate measuring machines*’, *Precision Engineering*, 22(2), pp. 87–97. doi: 10.1016/S0141-6359(98)00006-3.

Phillips, S. D., Borchardt, B. R., Sawyer, D., Estler, W. T., Ward, D., Eberhardt, K., Levenson, M. S., McClain, M., Melvin, B., Hopp, T. and Shen, Y. (1997) ‘*The Calculation of CMM Measurement Uncertainty via The Method of Simulation by Constraints*’, in *Proceedings of the 12th Annual Meeting of the American Society for Precision Engineering*, pp. 443–446.

Phillips, S. D., Eberhardt, K. R. and Parry, B. (1997) ‘*Guidelines for expressing the uncertainty of measurement results containing uncorrected bias*’, *Journal of Research of the National Institute of Standards and Technology*, 102(5), p. 577. doi: 10.6028/jres.102.039.

‘*Physikalisch-Technische Bundesanstalt*’ (2017). Available at: https://www.ptb.de/cms/en.html (Accessed: 31 August 2017).

Rakich, A., Dettmann, L., Leveque, S. and Guisard, S. (2016) ‘*A 3D metrology system for the GMT*’, in, p. 990614. doi: 10.1117/12.2234301.

Ramesh, R., Mannan, M. . and Poo, A. (2000) ‘*Error compensation in machine tools - a review*’, *International Journal of Machine Tools and Manufacture*, 40(9), pp. 1257–1284. doi: 10.1016/S0890-6955(00)00010-9.

Ramesh, R., Mannan, M. A., Poo, A. N. and Keerthi, S. S. (2003) ‘*Thermal error measurement and modelling in machine tools. Part II. Hybrid Bayesian Network—support vector machine model*’, *International Journal of Machine Tools and Manufacture*. Elsevier, 43(4), pp. 405–419. doi: 10.1016/S0890-6955(02)00264-X.

Redaelli, S. (2004) ‘*Alignment and Stabilization Issues in the Compact LInear Collider (CLIC)*’. Available at: https://cds.cern.ch/record/1350206?ln=en

(Accessed: 31 July 2017).

Rogers, W., Armstrong, N. A., Feynman, R., Acheson, D., Covert, E., Kutyna, D., Ride, S., Rummel, R., Sutter, J., Walker, A., Wheelon, A. and Yeager, C. (1986) '*Report to the President by the Presidential Commission on the Space Shuttle Challenger Accident*'. Available at: https://spaceflight.nasa.gov/outreach/SignificantIncidents/assets/rogers_commission_report.pdf (Accessed: 9 June 2017).

Ross-Pinnock, D. and Bingru Yang Glen Mullineux, B. (2016) '*Point-based models for compensation of thermal effects in dimentional metrology*', *Tools and Methods of Competitive Engineering*. Available at: http://opus.bath.ac.uk/.

Ross-Pinnock, D., Yang, B. and Maropoulos, P. G. (2015) '*Integration of thermal and dimensional measurement – a hybrid computational and physical measurement method*', in *38th MATADOR Conference*. Available at: http://opus.bath.ac.uk/.

RS components (2017) '*RS - Pt1000 Class A technical specification*'. Available at: http://docs-europe.electrocomponents.com/webdocs/15bb/0900766b815bbe5d.pdf (Accessed: 16 August 2017).

Ruland, R., Arnett, D., Bowden, G., Carr, R., Dix, B., Fuss, B., Cocq, C. Le and Wolf, Z. (1999) '*VISA Undulator Fiducialization and Alignment ♦*'. Available at: http://www.slac.stanford.edu/econf/C9910183/papers/017.PDF (Accessed: 30 September 2017).

Saadat, M. and Cretin, C. (2002) '*Dimensional variations during Airbus wing assembly*', *Assembly Automation*. MCB UP Ltd, 22(3), pp. 270–276. doi: 10.1108/01445150210436482.

Salsbury, J. G., Corporation, M. A. and Boulevard, C. (2003) '*Calibrating and Testing CMMs in a World of Uncertainty and Accreditation*', *ASPE Anual Publications*, pp. 1–6. Available at: http://www.aspe.net/publications/Summer_2003/03SU Extended Abstracts/SALSBURY.PDF (Accessed: 5 July 2017).

Sanz, C. (2018) '*Non contact sensor for high precision Coordinate Measurement Machine [PhD Thesis]*'. Cranfield University.

Satterthwaite, F. E. (1946) '*An Approximate Distribution of Estimates of Variance Components*', *Biometrics Bulletin*, 2(6), p. 110. doi: 10.2307/3002019.

Sch, Schluse, M. and Rossmann, J. (2016) '*From simulation to experimentable digital twins: Simulation-based development and operation of complex technical systems*', *2016 IEEE International Symposium on Systems Engineering (ISSE)*. IEEE, pp. 1–6. doi: 10.1109/SysEng.2016.7753162.

Schöck, M., Do, T., Ellerbroek, B., Herriot, G., Meyer, L., Suzuki, R., Wang, L.

and Yelda, S. (2013) '*Developing performance estimates for high precision astrometry with TMT*', in *Third AO4ELT Conference*. Firenze. Available at: https://ao4elt3.sciencesconf.org/13356/document (Accessed: 31 August 2017).

Schöck, M., Ellerbroek, B., Do, T., Gilles, L., Herriot, G., Meyer, L., Suzuki, R., Wang, L. and Yelda, S. (2014) '*TMT Top Down Astrometry Error Budget*'.

SCHOTT AG (2017) '*ZERODUR® Extremely Low Expansion Glass Ceramic: SCHOTT Advanced Optics | SCHOTT AG*'. Available at: http://www.schott.com/advanced_optics/english/syn/advanced_optics/products/optical-materials/zerodur-extremely-low-expansion-glass-ceramic/zerodur/index.html (Accessed: 2 August 2017).

Schwenke, H., Knapp, W., Haitjema, H., Weckenmann, A., Schmitt, R. and Delbressine, F. (2008) '*Geometric error measurement and compensation of machines-An update*', *CIRP Annals - Manufacturing Technology*, 57(2), pp. 660–675. doi: 10.1016/j.cirp.2008.09.008.

Scotch (2017) '*Scotch® Professional Grade Vinyl Electrical Tape Super 88*'. Available at: https://www.3m.com/3M/en_US/company-us/all-3m-products/~/Scotch-Professional-Grade-Vinyl-Electrical-Tape-Super-88?N=5002385+3294355634&rt=rud (Accessed: 12 September 2017).

Severino, G. and Caiazza, D. (2017) '*PACMAN Meeting (Domenico's and Giordana's presentations)*'. Available at: https://indico.cern.ch/event/601972/contributions/2429506/ (Accessed: 12 September 2017).

Siciliano, B., Sciavicco, L., Villani, L. and Oriolo, G. (2010) '*Kinematics*', in. Springer, London, pp. 39–103. doi: 10.1007/978-1-84628-642-1_2.

Slac, Z. W. (2005) '*A Vibrating wire system for quadrupole fiducialization*'. Available at: http://www.slac.stanford.edu/cgi-wrap/getdoc/slac-tn-10-087.pdf (Accessed: 31 July 2017).

Slocum, A. (1992) '*Precision machine design*'. Society of Manufacturing Engineers.

Slocum, A. H. and Donmez, A. (1988) '*Kinematic couplings for precision fixturing*', *Precision Engineering*, 10(3), pp. 115–122. doi: 10.1016/0141-6359(88)90029-3.

Stahl, H. P. (2013) '*Metrology of Large Parts*', in *Handbook of Optical Dimensional Metrology*, pp. 239–262. Available at: https://ntrs.nasa.gov/archive/nasa/casi.ntrs.nasa.gov/20120015323.pdf (Accessed: 28 July 2017).

Summerhays, K., Baldwin, J., Campbell, D., Henke, R. and Jon M. Baldwin, Kim D. Summerhays, Daniel A. Campbell, R. P. H. (2004) '*Application of simulation software to coordinate measurement uncertainty evaluation*', in *Aspe "Uncertainty Analysis in Measurement and Design (2004).* Available at:

http://www.aspe.net/publications/Summer_2004/04SU Extended Abstracts/Summerhays-1605.PDF (Accessed: 2 May 2017).

Taylor, C. L., Hyde, D. J. and Barr, L. C. (2016) ‘*Hyperloop Commercial Feasibility Analysis: High Level Overview*’. Available at: https://ntl.bts.gov/lib/59000/59300/59393/DOT-VNTSC-NASA-16-01.pdf (Accessed: 31 July 2017).

Ted Doiron (2007) ‘*20 °C—A Short History of the Standard Reference Temperature for Industrial Dimensional Measurements*’, *Journal of Research of the National Institute of Standards and Technology*, 112(1). Available at: http://nvlpubs.nist.gov/nistpubs/jres/112/1/V112.N01.A01.pdf (Accessed: 8 June 2017).

Temnyjh, A. (2005) ‘*Magnetic Survey of the CESR interaction region quadrupole magnets using vibrating wire technique*’, in *14th International Magnetic Measurement Workshop, CERN*. CERN.

Temnykh, A. (2005) ‘*Application of the vibrating wire technique for solenoid magnetic center finding*’, in *14th International Magnetic Measurement Workshop, CERN*. CERN.

Thery, P. and Raucoules, F. (2006) ‘*Heat flux comparator*’. Available at: http://www.google.sr/patents/US6994468?hl=nl&cl=nl (Accessed: 11 September 2017).

Thompson, D. C. and Fix, B. L. (1995) ‘*Comparison Between Predicted and Actual Accuracies for an Ultra-Precision CNC Measuring Machine*’, *8th International Precision Engineering Seminar*. Compiègne. Available at: https://static1.squarespace.com/static/55d2a0e2e4b0cb42737278a2/t/55df7992e4b0e7e8a5f9aaf8/1440709010327/copgagefollowup+copy.pdf (Accessed: 31 August 2017).

Thompson, D. C., Youden, D. H. and Hampshire, N. (2013) ‘*Error budgeting as applied to the design of the international x-ray observatory mandrel measuring machine*’, *ASPE*. doi: 10.1117/12.974873.

Thompson, M. K. (2007) ‘*A Multi Scale Iterative Approach for Finite Element Modeling of Thermal Contact Resistance [PhD Thesis]*’, p. 100.

Thompson and D.C. (1988) ‘*COP Gage error budget*’. Available at: https://www.osti.gov/scitech/biblio/6733443 (Accessed: 31 August 2017).

Trapet, E. (2010) ‘*Temperature effects in dimensional metrology. influences of temperature on the accuracy and how to cope with them.*’, in *CIMI*. Gijon, pp. 1–5.

Trapet, E. (2012) ‘*Verification of large CMMs -Artefacts and Methods*’, in *NACMA Annual Workshop and Conference In Conjunction with Simposio Metrologia*. Qro, Mexico. Available at: http://www.cenam.mx/ammc/eventos/Evento2012/Dr.

Eugen Trapet - Verification of Large CMMs by Means of Artifacts.pdf (Accessed: 7 August 2017).

Trapet, E. (2015a) '*Inter-laboratory tetrahedron comparison and artifact study*', *Zenodo DOI: 10.5281/ZENODO.842757*. doi: 10.5281/ZENODO.842757.

Trapet, E. (2015b) '*Inter-laboratory tetrahedron comparison and artifact study sponsored by Entidade Nacional de Acreditação (ENAC) Spain*'. doi: 10.5281/ZENODO.842757.

Trapet, E. (2017) '*Trapet Precision Engineering*'. Available at: http://www.trapet.de/ (Accessed: 12 June 2017).

Trapet, E. and Wäldele, F. (1991) '*A reference object based method to determine the parametric error components of coordinate measuring machines and machine tools*', *Measurement*, 9(1), pp. 17–22. doi: http://dx.doi.org/10.1016/0263-2241(91)90022-I.

Trbojevic, D., Cameron, P., Ganetis, G. L., Goldman, M. A., Gupta, R., Harrison, M., Hemmer, M. F., Karl, F. X., Jain, A., Louie, W., Mulhall, S., Peggs, S., Tepikian, S., Thomas, R. and Wanderer, P. (1996) '*Alignment and Survey of the Elements in RHIC*', in *Particle Accelerator Conference, IEEE*, pp. 2099–2101. Available at: http://accelconf.web.cern.ch/Accelconf/p95/ARTICLES/TAA/TAA09.PDF (Accessed: 7 September 2017).

Trbojevic, D., Jain, A., Tepikian, S., Grandinetti, R., Ganetis, G., Wei, J. and Karl, F. (1998) '*Alignment of the high beta magnets in the RHIC interaction regions*'. Institute of Electrical and Electronics Engineers Inc. Available at: https://scholars.opb.msu.edu/en/publications/alignment-of-the-high-beta-magnets-in-the-rhic-interaction-region-3 (Accessed: 31 July 2017).

Trenk, M., Franke, M. and Schwenke, H. (2004) '*The "Virtual CMM" a software tool for uncertainty evaluation – practical application in an accredited calibration lab*', *ASPE Proc., Uncertainty Analysis in Measurement and Design*, p. 6.

Tsai, B. K., Gibson, C. E., Murthy, A. V, Early, E. A., Dewitt, D. P. and D., S. R. (2004) '*NIST MEASUREMENT SERVICES: Heat-Flux Sensor Calibration*'. Available at: https://www.nist.gov/sites/default/files/documents/calibrations/sp250-65.pdf (Accessed: 11 September 2017).

TTi (2017a) '*PL Series DC Power Supplies | Aim-TTi International*'. Available at: https://www.aimtti.com/product-category/dc-power-supplies/aim-plseries (Accessed: 16 August 2017).

TTi (2017b) '*TTi PSU product sheet*'. Available at: http://resources.aimtti.com/datasheets/psu-npl-series-8p.pdf (Accessed: 16 August 2017).

Turner, S. and CAS-CERN Accelerator School (1998) '*Measurement and Alignment of Accelerator and Detector Magnets*'. CERN. doi: 10.5170/cern-1998-005.

Vasserman, I. (2000) '*Quadrupole Magnetic Center Definition Using the Hall Probe Measurement Technique*'. Available at: https://www1.aps.anl.gov/icms_files/lsnotes/files/APS_1418216.pdf (Accessed: 31 July 2017).

Vollard, A. (2005) '*Global confidence from identifiability in the SI sistem*', *Measurement Techniques*, 4805(7), pp. 3–4. Available at: https://link.springer.com/content/pdf/10.1007%2Fs11018-005-0194-x.pdf (Accessed: 24 October 2017).

Vorozhtsov, A. and Modena, M. (2012) '*Design and Manufacture of a Main Beam Quadrupole Model for CLIC*', *IEEE Transactions on applied superconductivity*. Available at: http://ieeexplore.ieee.org/stamp/stamp.jsp?arnumber=6081904.

Walter and M (2002) '*Error budget as a design tool for ultra-precision diamond turning machines*', *Proceedings of the ASPE's 17th Annual Meeting. 2002*. Available at: http://ci.nii.ac.jp/naid/10018659546/ (Accessed: 31 August 2017).

Weck, M., McKeown, P., Bonse, R. and Herbst, U. (1995) '*Reduction and Compensation of Thermal Errors in Machine Tools*', *CIRP Annals - Manufacturing Technology*. doi: 10.1016/S0007-8506(07)60506-X.

Weckenmann, A., Knauer, M. and Kunzmann, H. (1998) '*The influence of measurement strategy on the uncertainty of CMM-measurements*', *CIRP Annals - Manufacturing Technology*, 47(1), pp. 451–454. doi: 10.1016/S0007-8506(07)62872-8.

Welch, B. L. (1947) '*The Generalization of `Student's' Problem when Several Different Population Variances are Involved*', *Biometrika*, 34(1/2), p. 28. doi: 10.2307/2332510.

Wenninger, J. (2007) '*Operational challenges of the LHC*'. Available at: https://indico.lal.in2p3.fr/event/330/attachments/7695/9066/Dapnia-Nov07-partA.pdf (Accessed: 6 September 2017).

Weyand, K., Simon, E., Henderson, L., Bartholomew, J., Teunisse, G. M., Blanc, I., Crotti, G., Kupec, J., Jeglic, A., Gersak, G., Humar, J. and Puranen, L. (2001) '*Final report (draft B) on EUROMET Project No. 446: International comparison of magnetic flux density by means of field coil transfer standards*', *Metrologia*. IOP Publishing, 38(2), pp. 187–191. doi: 10.1088/0026-1394/38/2/11.

Wilhelm, R. G., Hocken, R. and Schwenke, H. (2001) '*Task specific uncertainty in coordinate measurement*', *CIRP Annals - Manufacturing Technology*, 50, pp. 553–563. doi: 10.1016/S0007-8506(07)62995-3.

'*Wire Position Sensor*' (2017). Available at:

http://www.opensourceinstruments.com/WPS/ (Accessed: 14 August 2017).

Wolf, Z., Ruland, R., Dix, B. and Arnett, D. (2005) '*Alignment Tools Used To Locate A Wire And A Laser Beam In The VISA Undulator Project*', in *IWAA*. Available at: http://www.iaea.org/inis/collection/NCLCollectionStore/_Public/32/068/32068852.pdf (Accessed: 31 July 2017).

Youssef, S. A. M., Paik, J. K., Kim, Y. S., Kim, M. S. and Cheng, F. (2013) '*Probabilistic Selection of Ship-Ship Collision Scenarios*', *Volume 2A: Structures, Safety and Reliability*, (June 2013), p. V02AT02A027. doi: 10.1115/OMAE2013-10316.

Yu, L., Lai, K. K., Wang, S. and Huang, W. (2006) '*A Bias-Variance-Complexity Trade-Off Framework for Complex System Modeling*', in. Springer, Berlin, Heidelberg, pp. 518–527. doi: 10.1007/11751540_55.

Zachary Wolf, Vsevolod Kaplunenko, Yurii Levashov and Achim Weidemann (2007) '*LCLS undulator tuning and fiducialization*', in *2007 IEEE Particle Accelerator Conference (PAC)*. IEEE, pp. 1320–1322. doi: 10.1109/PAC.2007.4441069.

Zangrando, D. and Walker, R. P. (1993) '*Magnetic measurement and alignment of the ELETTRA storage ring quadrupole, sextupole and steerer magnets*', *Conf.Proc.*, C930517, pp. 2844–2846. Available at: http://inspirehep.net/record/356884 (Accessed: 31 July 2017).

Zhang, C., Mitsuda, C. and Kajimoto, K. (2016) '*Eigenfrequency wire alignment system for magnet fiducialization*', in *IWAA*. Available at: https://indico.cern.ch/event/489498/contributions/2217498/attachments/1352850/2066525/Chao_ZHANG_iwaa2016.pdf (Accessed: 29 October 2017).

Zhang, L. W., Zhu, P. and Liew, K. M. (2014) '*Thermal buckling of functionally graded plates using a local Kriging meshless method*', *Composite Structures*, 108, pp. 472–492. doi: 10.1016/j.compstruct.2013.09.043.

Zhang, X. (2013) '*Metrology-Based Process Modelling Framework for Digital and Physical Measurement Environments Integration*', *University of Bath*. Available at: http://opus.bath.ac.uk/44918/1/Thesis_Xi_Zhang.pdf (Accessed: 3 July 2017).

Zhao, S. and Zhu, R. (2017) '*Electronic Skin with Multifunction Sensors Based on Thermosensation*', *Advanced Materials*, 29(15), p. 1606151. doi: 10.1002/adma.201606151.

Zorzetti, S. (2017) '*Radio frequency characterization and alignment to the nanometer scale of a beam position monitor for particle accelerators [PhD Thesis]*'. University of Pisa.

## A.1 Error Budgets literature review analysis summary

| **RSS = sqrt(Σui^2) = Root Sum of the Squares = Combined Uncorrelated Uncertainty with gaussian or t Distribution** | | | | | |
|---|---|---|---|---|---|
| **Error Budget Case** | **Final function to be verified** | **System Degrees of Freedom** | **Error sources top level split** | **Total Error propagation rule** | **Remarks** |
| Error Budgeting in Precision Machine Design [B.W.Moren, R.M.Miler] | **The combined uncertainty for the machine centre** A detail spread on how geometrical errors (one of the top level contributors to the combined uncertainty - Carriage Position) in X,Y,Z of carrige position propagate to the X,Y,Z of the machine tool. | **X, Y, Z** of machine tool given by carriages DoF | ***Carriage Position(*** Sub budget a function of X,Y,Z carrige: *Pitch, Yaw, Roll, Straightnes X,Y,Z* **)** ***Artefact Calibration, Orthogonality, Coolant temperature*** | **Arithmetic Sum**, **RSS** as final | Introductory paper to Error Budgeting |
| Error Budget as a Design Tool For Ultra-Precision Diamond Turning Machines Mark Walter, Bruce Norlund, Robert Koning, Jeff Roblee, Preciteh, inc | **The combined uncertainty for the UPC machine centre** | **X** and **Z** movable axes with **Z** rotational DoF | **Stability errors; Length Based errors; Time Based Errors; Other Errors** Each of this categories contains sub-error budgets containing numerous contributors. | **Type B** Assumptions for the different types of errors were made on adding correction factor to the **Maximum** error estimations. **The RSS** rule is used for the Total Combined Uncertainty | Biggest sources of error were the **Length based** and the **Thermal based** one. For the former one it was mentiond a routine error correction tecniques and compensation procedures could be used. The budget showed it was vital to concentrate effort in those domains. |
| COP Gage Error Budget & Comparison Between Predicted and Actual Accuracies for an Ultra-Precision CNC Measuring Machine [D.C. Thompson] | **Total Combined Radial Figure Uncertainty Calculated as vector sum of X and Z components** | **X** and **Z** movable axes | **Probe Path associated Errors; Probe accuracy associated Errors; Measurment Provess associated Errors.** Each of this categories contains sub-error budgets containing numerous contributors. | Half's of the most pessimistic (shear arithmetic sum of the worst case scenario) and most optimistic (the Rout Sum of the Squares - uncertainty combinatorial rule ):"The Hocken's rule" **Utotal = (Aritmetic Sum + RSS)/2** | The paper shows remarkably good correlation between predicted and measured results. Biggest contributor to the error budget was identified as **Thermal related issues** among the various categories. |
| Developing Performance Estimates for High Precision Astrometry with TMT [Schock M. ; Do T. et all] | **Total uncertainty with the asociated de-centring errors at various astrometric experiments evaluated in parametric form.** Investigating uncertainty from the source (star) to the end - the telescope oprics and reciver. | Complex measurement system made of other systems. The error budget degree of freedom are related to the type of astrometry being done (absolute or differential) and the type and number of experiment related measurement 'fiuducials' (N reference sources, N science objects). Separate Total uncertainty for each case. | **Reference Source and Catalog errors, Atmospheric refraction correction errors, Other residual atmospheric effects, Opto-mechanical errors and Focal plane measurement errors** Each of this categories contains sub-error budgets containing numerous contributors. All of the error contributors are described in parametric manner depending on the magnitude of their related uncertainty | As the total system error budget was presented in parametrised form, no discussion on specific error propagation roule was made. The authors however mention that in future such table would be created. | The type of experiment: Absolute or Differential greatly influences the total asociated experiment uncertainty. The bigger the number of celestial measurement 'fuducials' and refference sources, the better the error compensation and the less is the uncertainty |
| Error budgeting as applied to the design of the International X-Ray Observatory Mandrel Measuring Machine D.C. Thompson et all | **The total uncertainty of each of the critical shape paramers of the measured components - the observatory mandrels** | The measurement machine DoF: **X,Y,Z** Translational and **C** (rotational degree of freedom) ; **Y'** and **Y''** passive (translational DoF for the sensors) | **Radius(Average radius, Radius Variation); Cone Angle(Average Cone Angle, Cone Angle Variation); Axial Sag(Average Sag, Sag Variation); Axial Figure(Low Frequency, Mid Frequency, High Frequency)** Each of this categories contains sub-error budgets containing numerous contributors. The contributors errors are spread among the DoF of the machine | Type B Assumptions for the different types of errors were made , on adding correction factor to the P-V error estimations. For the estimation of the combined uncertainty a Gaussian distribution is being accepted. The "Hocken's rule" applied **Utotal = (Aritmetic Sum + RSS)/2** | The use of error budgeting and other precision engineering principles as a guide helped to meet the very stringent accuracy requirements. |

## A.2 Input-output schematic CMM uncertainty evaluation

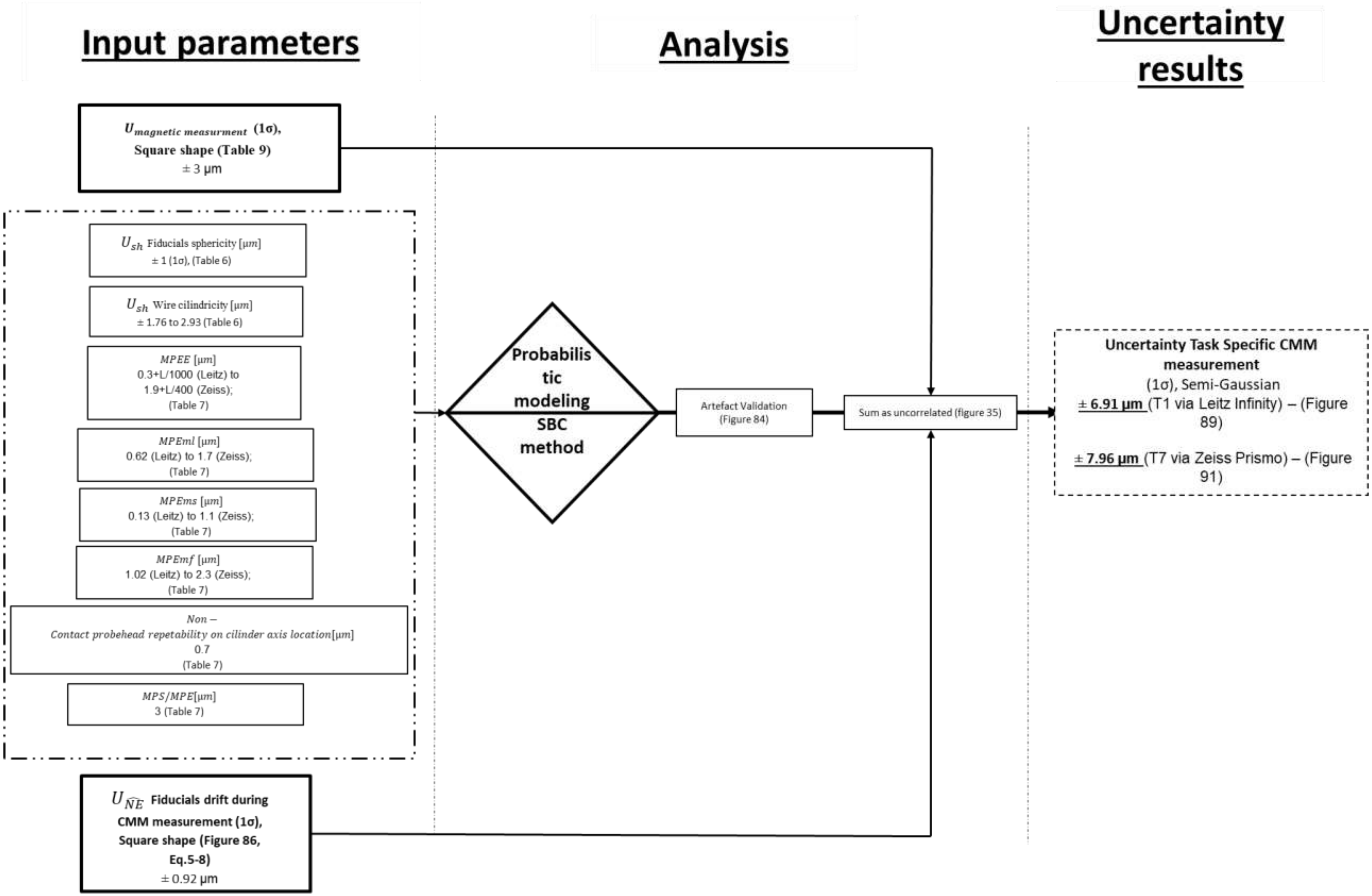

**A.3 Input-output schematic empirical modelling]**

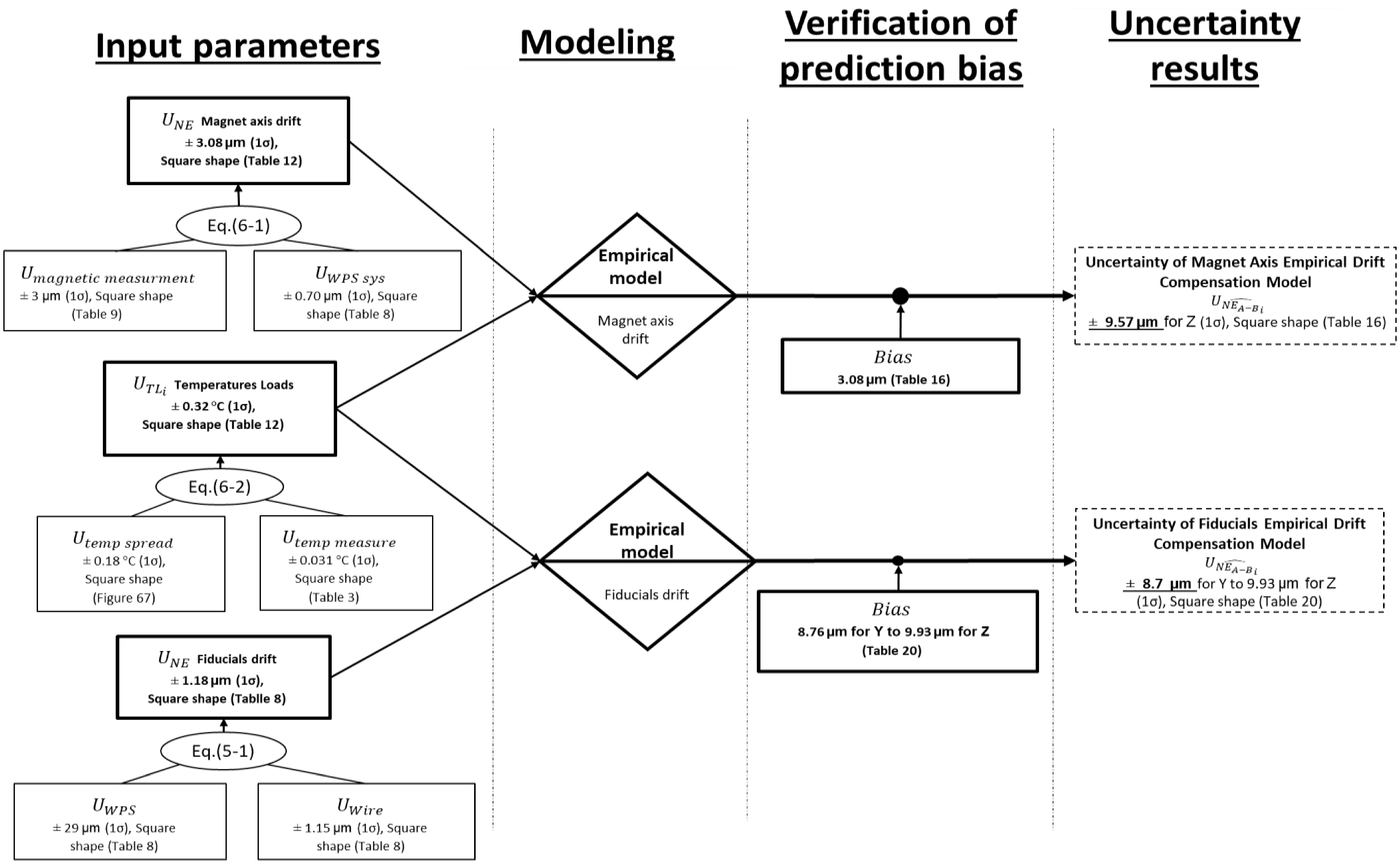

### A.4 Input-output schematic Probabilistic FEM

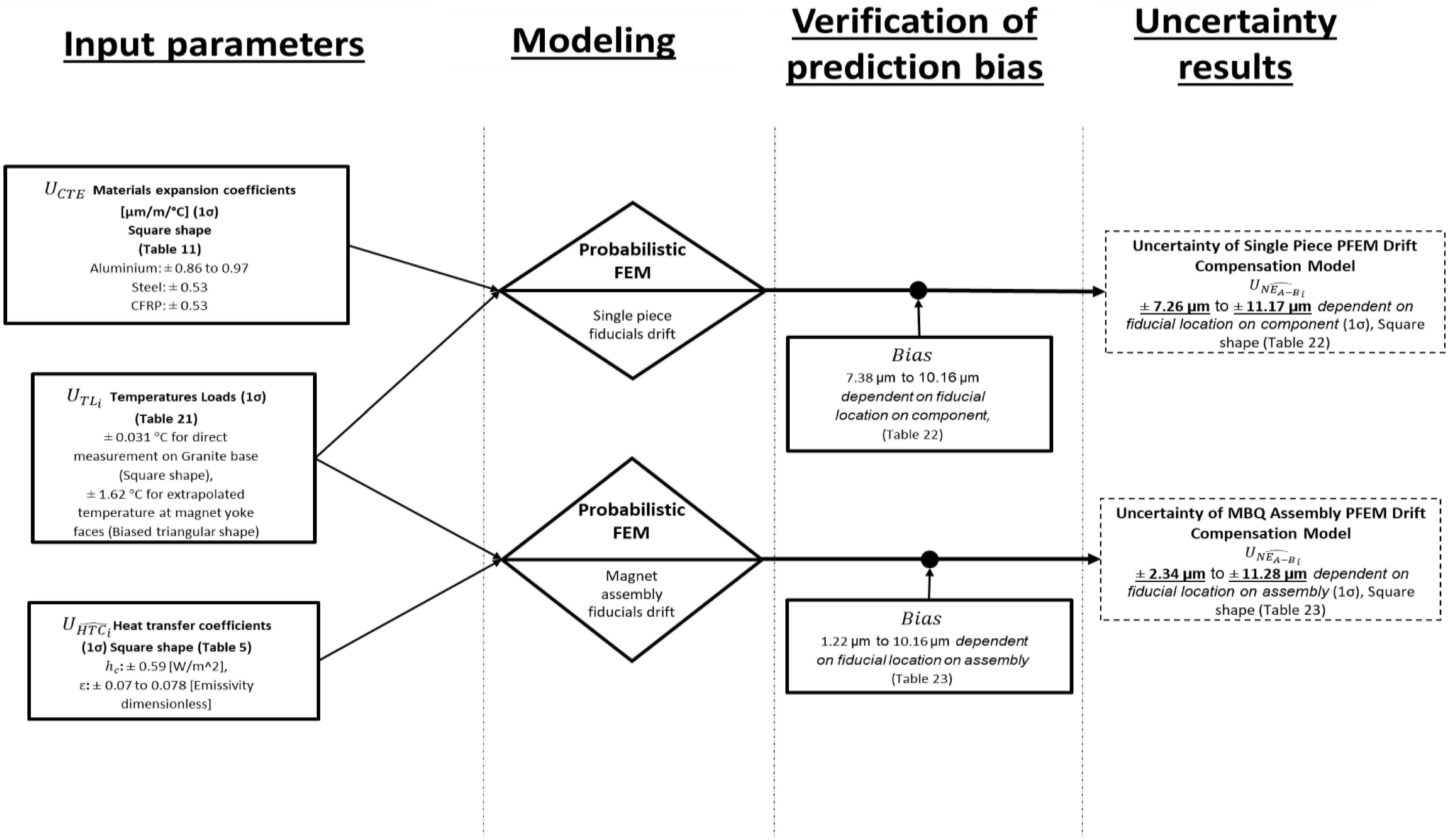

A.5 Input-output analysis Meta-models

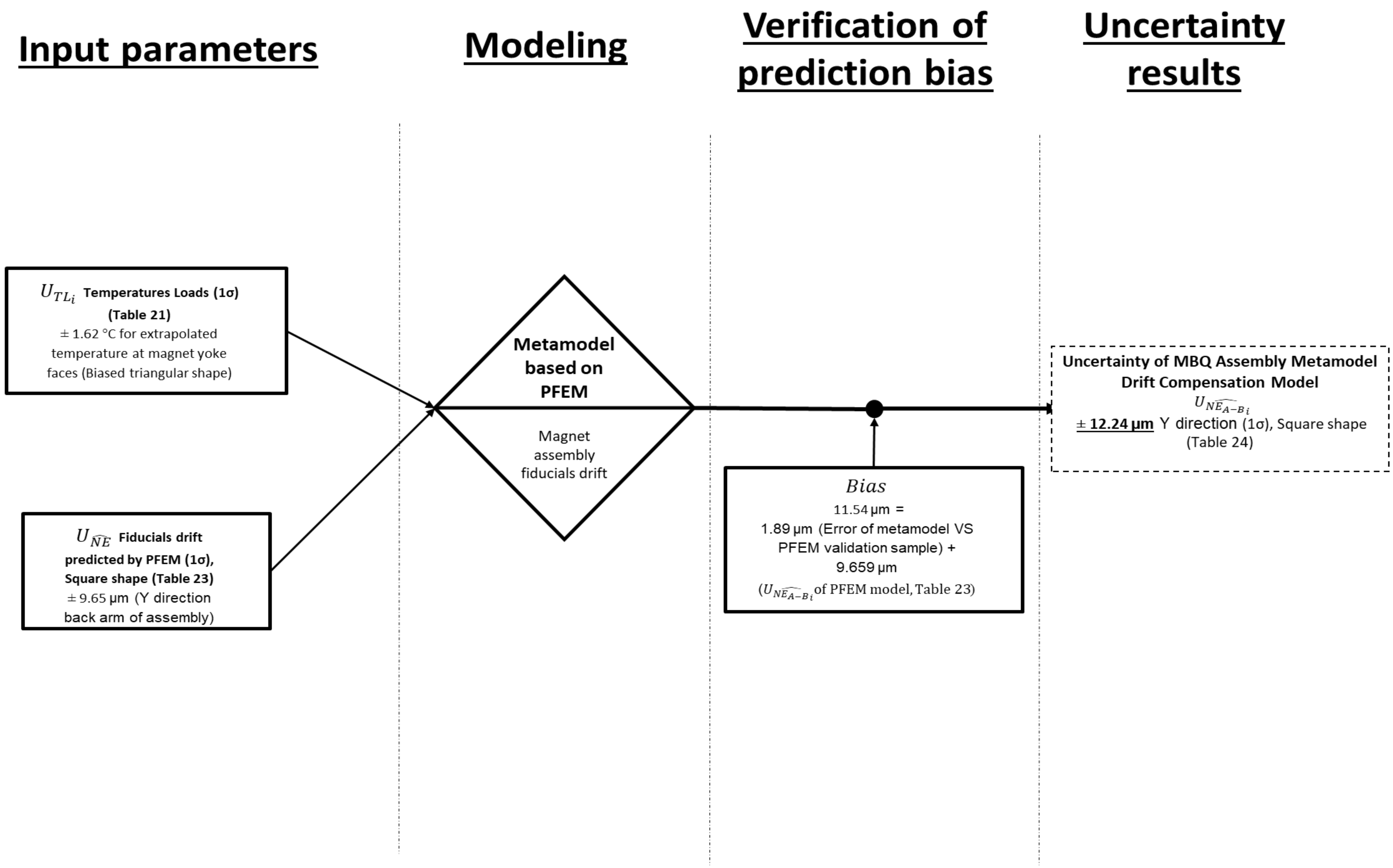

## A.6 Accelerator alignment state of art errors as quoted in [8]

| Accelerator | | | Magnet | | | | | | | | | Instrumentation | | Uncertainty | | |
|---|---|---|---|---|---|---|---|---|---|---|---|---|---|---|---|---|
| Institute | Machine | L [m] | Type | Technology | Lm [m] | Aperture [mm] | I [A] | dB/dr [T/m] | $B_{max}$ [T] | T [K] | Moves | Magnetic | Survey | Axis to sensor [um] | Sensor to ref. [um] | Total [um] |
| BNL | RHIC | 3862 | quad | superconducting | 1.13 | 80 | 5000 | 71.00 | 5.7 | 4.5 | no | Colloidal Cell | Theodolite | 40 | 25 | 47 |
| BNL | RHIC | 3862 | quad | superconducting | 1.13 | 80 | 10 | 0.14 | 0.01 | 300 | no | Harmonic Coil | Theodolite | 25 | 25 | 35 |
| BNL | SASE | - | undulator | permanent | 4.00 | 6 | - | - | 0.8 | 300 | no | Pulsed Wire | Interferometer | 10 | 8 | 13 |
| KEK | B-factory | 3016 | quad | resistive | 0.40 | 110 | 500 | 10.20 | 1.12 | 300 | yes | Harmonic Coil | Laser Tracker | 15 | 5 | 16 |
| SLAC | LCLS | 3000 | quad | resistive | 0.05 | 12 | n.a. | 15.00 | 0.18 | 300 | no | Hall Sensor | CMM | 8 | 1 | 8 |
| SLAC | LCLS | 3000 | undulator | permanent | 3.40 | 12 | - | - | 1.3 | 300 | no | Hall Sensor | CMM | 8 | 15 | 17 |
| SLAC | LCLS | 3000 | quad | resistive | 0.15 | 12 | n.a. | 12.00 | 0.14 | 300 | yes | Vibrating Wire | CMM | 18 | 10 | 21 |
| JASRI | SPring-8 | 1436 | quad | resistive | 0.64 | 85 | n.a. | 17.40 | 1.48 | 300 | yes | Harmonic Coil | Laser + CCD | 2 | 15 | 15 |
| SLAC | FFTB | 3200 | quad | resistive | 0.46 | 23 | 220 | 83.00 | 1.91 | 300 | no | Vibrating Wire | CMM + Micrometer | 4 | 15 | 15 |
| MIT-Bates | SHR | 190 | quad | resistive | 0.28 | 35 | | 0.50 | 0.02 | 300 | no | Harmonic Coil | Theodolite | *26* | *43* | 51 |
| FNAL | LHC | 26660 | quad | superconducting | 8.00 | 63 | 11850 | 215.00 | 13.55 | 4.5 | no | Stretched Wire | Laser Tracker | 33 | 50 | 60 |
| FNAL | LHC | 26660 | quad | superconducting | 8.00 | 63 | 2 | 0.04 | 0.00 | 300 | no | Stretched Wire | Laser Tracker | 33 | 50 | 60 |
| CERN | LHC | 26660 | quad | superconducting | 8.00 | 40 | 11850 | 223.00 | 8.92 | 1.9 | no | SSW | Laser Tracker | 5 | 80 | 80 |
| CERN | LHC | 26660 | quad | superconducting | 8.00 | 50 | 2 | 0.04 | 0.00 | 300 | no | SSW | Laser Tracker | 20 | 80 | 82 |
| CERN | LHC | 26660 | quad | superconducting | 8.00 | 50 | 0.5 | 0.01 | 0.00 | 300 | no | AC Harmonic Coil | Laser Tracker | 51 | 80 | 95 |
| Cornell | CESR | 768 | quad | superconducting | 7.50 | 67 | n.a. | 13.00 | 0.87 | n.a. | no | Vibrating Wire | Laser Tracker | 10 | 51 | 52 |
| Cornell | CESR | 768 | solenoid | superconducting | 0.30 | 200 | n.a. | - | 0.008 | 300 | no | Vibrating Wire | Laser Tracker | 10 | 25 | 27 |
| CNRS/CEA | SOLEIL | 354 | quad | resistive | 0.46 | 66 | n.a. | 23.00 | 1.52 | 300 | yes | Harmonic Coil | (mech. tol.) | *5* | *30* | 30 |
| ELETTRA | SR | 259 | quad | resistive | 0.49 | 75 | n.a. | 20.60 | 1.55 | 300 | yes | Harmonic Coil | Telescope | *5* | *25* | 25 |
| CERN | LEP | 26660 | quad | resistive | 1.55 | 59 | n.a. | 9.70 | 0.57 | 300 | yes | Harmonic Coil | Laser + PSD | 20 | 50 | 54 |

## A.7 Thermal Probes calibration NPL Certificates

NATIONAL PHYSICAL LABORATORY

Teddington Middlesex UK TW11 0LW Telephone +44 20 8977 3222

# Certificate of Calibration

UKAS CALIBRATION 0478

PLATINUM RESISTANCE THERMOMETERS

*This certificate is issued in accordance with the laboratory accreditation requirements of the United Kingdom Accreditation Service. It provides traceability of measurement to the SI system of units and/or to units of measurement realised at the National Physical Laboratory or other recognised national metrology institutes. This certificate may not be reproduced other than in full, except with the prior written approval of the issuing laboratory.*

| | |
|---|---|
| FOR: | PACMAN – an EU project<br>c/o CERN build 156-R003<br>CH-1211 Geneva 23<br>Switzerland |
| FOR THE ATTENTION OF: | Mr Iordan Doytchinov |
| DESCRIPTION: | Resistance thermometers, type PT 100 |
| IDENTIFICATION: | 01/11, 02/12, 03/13, 04/14, 05/15, 06/16, 07/17, 08/18, 09/19, 10/20, 01/11-2, 02/12-2, 03/13-2 |
| DATE OF CALIBRATION: | 6 April 2016 to 8 April 2016 |
| BASIS OF TEST: | Calibration in terms of the ITS-90 |

**Reference:** 2016030103/1/PM04 **Page 1 of 4**

**Date of issue:** 19 April 2016 **Signed:** (Authorised Signatory)

**Checked by:** RW BWS **Name: Mr Bruce Duncan** **on behalf of NPLML**

# NATIONAL PHYSICAL LABORATORY

Continuation Sheet

## MEASUREMENTS

The platinum resistance thermometers were submitted for calibration over the temperature range from 0 °C to 30 °C in terms of the International Temperature Scale of 1990. For calibration purposes the thermometers were placed in close-fitting glass tubes. The resistance was measured at the triple point of water and in a well stirred liquid bath controlled at about 15 °C and 30 °C.

## RESULTS

The results of the calibration are given in terms of the resistance ratio $W(t_{90})$ defined by

$$W(t_{90}) = R(t_{90}) \ / \ R(0.01\ °C)$$

where $R(t_{90})$ is the resistance at temperature $t_{90}$ and $R(0.01\ °C)$ is the resistance at the triple point of water, 0.01 °C.

The value of $R(0.01\ °C)$ was measured before and after calibration. The measurements were made with a current of 1 mA. The initial and final resistance values at TPW and the self heating effect of the above current are listed in the tables below.

The values of resistance and $W(t_{90})$ given on this certificate were obtained directly from the measurements without adjustment to zero current.

| | 01/11 | 02/12 | 03/13 | 04/14 |
|---|---|---|---|---|
| TPW initial, Ω | 100.01724 | 100.00214 | 100.03484 | 99.98014 |
| TPW final , Ω | 100.01704 | 100.00044 | 100.03334 | 99.98084 |
| Self-heating, Ω | 0.00843 | 0.00768 | 0.00818 | 0.00963 |

| | 05/15 | 06/16 | 07/17 | 08/18 |
|---|---|---|---|---|
| TPW initial, Ω | 99.99414 | 100.01844 | 99.97994 | 100.01474 |
| TPW final , Ω | 99.99414 | 100.01814 | 99.98004 | 100.01464 |
| Self-heating, Ω | 0.00793 | 0.00833 | 0.00848 | 0.00973 |

| | 09/19 | 10/20 | 01/11-2 | 02/12-2 | 03/13-2 |
|---|---|---|---|---|---|
| TPW initial, Ω | 100.01254 | 100.01864 | 100.00894 | 100.01774 | 99.98494 |
| TPW final , Ω | 100.01254 | 100.01854 | 100.00884 | 100.01774 | 99.98504 |
| Self-heating, Ω | 0.00888 | 0.00928 | 0.00883 | 0.00883 | 0.00673 |



**Checked by:** RIV bmr

**RESULTS (Continued)**

The resistance ratios which were measured at the calibration points, the calibration coefficients, as defined in ITS-90 and the estimated uncertainties are listed in the following table.

| Serial No | $t_{90}$ / °C | $W(t_{90})$ | Coefficient a | Uncertainty/ °C |
|---|---|---|---|---|
| 01/11 | 15.1259 | 1.0589608 | | ±0.010 |
| | 29.9786 | 1.1166060 | -0.0203990 | ±0.010 |
| 02/12 | 15.1259 | 1.0590420 | | ±0.010 |
| | 29.9786 | 1.1167300 | -0.0193152 | ±0.010 |
| 03/13 | 15.1259 | 1.0591346 | | ±0.010 |
| | 29.9786 | 1.1169262 | -0.0176052 | ±0.010 |
| 04/14 | 15.1259 | 1.0590004 | | ±0.010 |
| | 29.9786 | 1.1166774 | -0.0197750 | ±0.010 |
| 05/15 | 15.1259 | 1.0589890 | | ±0.010 |
| | 29.9784 | 1.1166550 | -0.0199640 | ±0.010 |
| 06/16 | 15.1259 | 1.0589332 | | ±0.010 |
| | 29.9784 | 1.1165380 | -0.0209877 | ±0.010 |
| 07/17 | 15.1259 | 1.0590244 | | ±0.010 |
| | 29.9784 | 1.1167318 | -0.0192926 | ±0.010 |
| 08/18 | 15.1259 | 1.0590200 | | ±0.010 |
| | 29.9784 | 1.1167122 | -0.0194641 | ±0.010 |
| 09/19 | 15.1257 | 1.0590417 | | ±0.010 |
| | 29.9782 | 1.1167663 | -0.0189852 | ±0.010 |
| 10/20 | 15.1257 | 1.0590028 | | ±0.010 |
| | 29.9782 | 1.1166879 | -0.0196696 | ±0.010 |
| 01/11-2 | 15.1257 | 1.0589509 | | ±0.010 |
| | 29.9782 | 1.1165845 | -0.0205741 | ±0.010 |
| 02/12-2 | 15.1257 | 1.0589386 | | ±0.010 |
| | 29.9782 | 1.1165604 | -0.0207853 | ±0.010 |
| 03/13-2 | 15.1259 | 1.0590363 | | ±0.010 |
| | 29.9786 | 1.1167523 | -0.0191211 | ±0.010 |

The alpha coefficient for the Pt-wires has been calculated and it is found to be 0.00385.

**Reference:** 2016030103/1/PM04 

**Checked by:** RW Run

## A.8 Thermal Probes with Agilent DAQ calibration NPL Certificates

NATIONAL PHYSICAL LABORATORY

Teddington Middlesex UK TW11 0LW Telephone +44 20 8977 3222

# Certificate of Calibration

UKAS CALIBRATION 0478

**DIGITAL THERMOMETER AGILENT 34970A**
**WITH TWENTY FOUR PROBES**

*This certificate is issued in accordance with the laboratory accreditation requirements of the United Kingdom Accreditation Service. It provides traceability of measurement to the SI system of units and/or to units of measurement realised at the National Physical Laboratory or other recognised national metrology institutes. This certificate may not be reproduced other than in full, except with the prior written approval of the issuing laboratory.*

FOR: PACMAN – an EU project
c/o CERN build 156-R003
CH-1211 Geneva 23
Switzerland

For the attention of: Mr Iordan Doytchinov

DESCRIPTION: Agilent 34970A Digital Thermometer with associated 13 PT100 resistor and 11 thermistor probes

IDENTIFICATION: Agilent 34970A s/n MY41018958 with probes 01/11, 02/12, 03/13, 4/14, 5/15, 6/16, 7/17, 8/18, 9/19, 10/20, 1/11-2, 2/12-2, 3/13-2, 04-2, 05-2, 06-2, 07-2, 08-2, 09-2, 14-2, 15-2, 16-2, 17-2, 18-2

DATE OF CALIBRATION: 14 April 2016

**Reference:** 2016030103/2/PM04
**Date of issue:** 19 April 2016
**Checked by:** RW

**Signed:**
**Name:** Mr Bruce Duncan

**Page 1 of 4**
**(Authorised Signatory)**
**On behalf of NPLML**

## RESULTS

The results of the test are set out in the following table, where the corrections to obtain the ITS-90 temperature are stated to the nearest 0.001 °C and represent the means of the observations. To obtain the correct temperature the appropriate correction from the calibration should be added to the reading, with due regard to the sign.

| T / °C | PRT Channels | | | | | | |
|---|---|---|---|---|---|---|---|
| | 101 | 102 | 103 | 104 | 105 | 106 | 107 |
| | serial numbers | | | | | | |
| | 01/11 | 02/12 | 03/13 | 04/14 | 05/15 | 06/16 | 07/17 |
| 15.127 | 0.000 | -0.004 | -0.025 | 0.005 | 0.010 | 0.024 | -0.002 |
| 17.596 | 0.003 | -0.003 | -0.028 | 0.006 | 0.012 | 0.029 | -0.001 |
| 20.051 | 0.002 | -0.007 | -0.037 | 0.003 | 0.011 | 0.030 | -0.004 |
| 22.488 | 0.000 | -0.012 | -0.045 | 0.002 | 0.008 | 0.029 | -0.009 |
| 25.061 | 0.000 | -0.015 | -0.054 | -0.001 | 0.007 | 0.030 | -0.011 |

| T / °C | PRT Channels | | | | | |
|---|---|---|---|---|---|---|
| | 108 | 109 | 110 | 201 | 202 | 203 |
| | serial numbers | | | | | |
| | 08/18 | 09/19 | 10/20 | 01/11-2 | 02/12-2 | 03/13-2 |
| 15.127 | 0.004 | 0.002 | 0.013 | 0.026 | 0.031 | -0.011 |
| 17.596 | 0.005 | 0.002 | 0.015 | 0.031 | 0.035 | -0.010 |
| 20.051 | 0.002 | -0.002 | 0.013 | 0.030 | 0.035 | -0.014 |
| 22.488 | -0.001 | -0.007 | 0.010 | 0.029 | 0.034 | -0.019 |
| 25.061 | -0.005 | -0.012 | 0.008 | 0.029 | 0.036 | -0.022 |



**Checked by:** RW bws

## RESULTS (CONTINUED)

| T / °C | Thermistor Channels | | | | | |
|---|---|---|---|---|---|---|
| | 204 | 205 | 206 | 207 | 208 | 209 |
| | serial numbers | | | | | |
| | 04-2 | 05-2 | 06-2 | 07-2 | 08-2 | 09-2 |
| 15.127 | -0.035 | 0.006 | -0.011 | -0.002 | -0.029 | -0.038 |
| 17.596 | -0.041 | -0.001 | -0.017 | -0.007 | -0.035 | -0.044 |
| 20.051 | -0.028 | 0.013 | -0.003 | 0.010 | -0.023 | -0.032 |
| 22.488 | -0.018 | 0.020 | 0.005 | 0.020 | -0.013 | -0.022 |
| 25.061 | -0.038 | 0.001 | -0.013 | 0.004 | -0.034 | -0.042 |

| T / °C | Thermistor Channels | | | | |
|---|---|---|---|---|---|
| | 214 | 215 | 216 | 217 | 218 |
| | serial numbers | | | | |
| | 14-2 | 15-2 | 16-2 | 17-2 | 18-2 |
| 15.127 | -0.043 | -0.001 | -0.027 | -0.030 | -0.042 |
| 17.596 | -0.048 | -0.007 | -0.033 | -0.036 | -0.048 |
| 20.051 | -0.035 | 0.008 | -0.019 | -0.023 | -0.035 |
| 22.488 | -0.024 | 0.016 | -0.010 | -0.014 | -0.025 |
| 25.061 | -0.043 | -0.002 | -0.030 | -0.034 | -0.045 |



**Checked by:** RW